
NORTH ATLANTIC TREATY
ORGANIZATION



AC/323(AVT-190)TP/866

SCIENCE AND TECHNOLOGY
ORGANIZATION



www.sto.nato.int

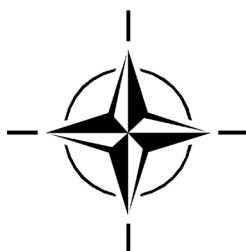
STO TECHNICAL REPORT

TR-AVT-190

Plasma Based Flow Control for Performance and Control of Military Vehicles

(Contrôle du flux à partir de plasma
pour la performance et le contrôle
des véhicules militaires)

Final report of NATO STO Task Group AVT-190.



Published August 2021

Distribution and Availability on Back Cover





STO TECHNICAL REPORT

TR-AVT-190

Plasma Based Flow Control for Performance and Control of Military Vehicles

(Contrôle du flux à partir de plasma
pour la performance et le contrôle
des véhicules militaires)

Final report of NATO STO Task Group AVT-190.

The NATO Science and Technology Organization

Science & Technology (S&T) in the NATO context is defined as the selective and rigorous generation and application of state-of-the-art, validated knowledge for defence and security purposes. S&T activities embrace scientific research, technology development, transition, application and field-testing, experimentation and a range of related scientific activities that include systems engineering, operational research and analysis, synthesis, integration and validation of knowledge derived through the scientific method.

In NATO, S&T is addressed using different business models, namely a collaborative business model where NATO provides a forum where NATO Nations and partner Nations elect to use their national resources to define, conduct and promote cooperative research and information exchange, and secondly an in-house delivery business model where S&T activities are conducted in a NATO dedicated executive body, having its own personnel, capabilities and infrastructure.

The mission of the NATO Science & Technology Organization (STO) is to help position the Nations' and NATO's S&T investments as a strategic enabler of the knowledge and technology advantage for the defence and security posture of NATO Nations and partner Nations, by conducting and promoting S&T activities that augment and leverage the capabilities and programmes of the Alliance, of the NATO Nations and the partner Nations, in support of NATO's objectives, and contributing to NATO's ability to enable and influence security and defence related capability development and threat mitigation in NATO Nations and partner Nations, in accordance with NATO policies.

The total spectrum of this collaborative effort is addressed by six Technical Panels who manage a wide range of scientific research activities, a Group specialising in modelling and simulation, plus a Committee dedicated to supporting the information management needs of the organization.

- AVT Applied Vehicle Technology Panel
- HFM Human Factors and Medicine Panel
- IST Information Systems Technology Panel
- NMSG NATO Modelling and Simulation Group
- SAS System Analysis and Studies Panel
- SCI Systems Concepts and Integration Panel
- SET Sensors and Electronics Technology Panel

These Panels and Group are the power-house of the collaborative model and are made up of national representatives as well as recognised world-class scientists, engineers and information specialists. In addition to providing critical technical oversight, they also provide a communication link to military users and other NATO bodies.

The scientific and technological work is carried out by Technical Teams, created under one or more of these eight bodies, for specific research activities which have a defined duration. These research activities can take a variety of forms, including Task Groups, Workshops, Symposia, Specialists' Meetings, Lecture Series and Technical Courses.

The content of this publication has been reproduced directly from material supplied by STO or the authors.

Published August 2021

Copyright © STO/NATO 2021
All Rights Reserved

ISBN 978-92-837-2190-1

Single copies of this publication or of a part of it may be made for individual use only by those organisations or individuals in NATO Nations defined by the limitation notice printed on the front cover. The approval of the STO Information Management Systems Branch is required for more than one copy to be made or an extract included in another publication. Requests to do so should be sent to the address on the back cover.

Table of Contents

	Page
List of Figures	vi
List of Tables	xi
Acknowledgements	xii
AVT-190 Membership List	xiii
Executive Summary and Synthèse	ES-1
Chapter 1 – Introduction: The NATO STO Task Group AVT-190	1-1
Chapter 2 – Laser and Microwave Discharge	2-1
2.1 Introduction	2-1
2.2 Laser Discharge	2-1
2.2.1 Experiment	2-1
2.2.2 Participants	2-5
2.2.3 Methodology	2-5
2.2.4 Results	2-8
2.2.5 Conclusions and Recommendations	2-15
2.3 Microwave Discharge	2-15
2.3.1 Experiment	2-15
2.3.2 Participants	2-18
2.3.3 Methodology	2-18
2.3.4 Results	2-19
2.3.5 Conclusions and Recommendations	2-22
2.4 Transfer of Microwave Energy Along a Filament Plasma Column in Air	2-23
2.4.1 Introduction	2-23
2.4.2 Experiment	2-23
2.4.3 Participants	2-25
2.4.4 Results	2-25
2.4.6 Conclusions and Recommendations	2-27
2.5 References	2-27
Chapter 3 – Numerical Modelling of SDBD Actuators in Quiescent Air	3-1
3.1 Introduction	3-1
3.2 Physical Modelling	3-1
3.2.1 Numerical Results	3-2
3.2.2 Conclusion	3-5
3.3 References	3-5

Chapter 4 – Evaluation of Force Measurement Techniques for Dielectric Barrier Discharge Actuators **4-1**

<i>Abstract</i>	4-1
4.1 Introduction	4-1
4.2 Experimental Arrangement	4-2
4.2.1 Plasma Actuator Design and Discharge Generation	4-2
4.2.2 Direct Thrust Measurements	4-4
4.3 Control Volume Analysis	4-5
4.3.1 Flow Field Measurements	4-5
4.3.2 PIV Seeding	4-7
4.3.3 Inferred Force Calculation	4-9
4.4 Results	4-10
4.4.1 Influence of the Actuator Plate Length	4-10
4.4.2 Effect of Chamber Size	4-11
4.5 Control Volume	4-12
4.5.1 Control Volume Extracted Forces	4-12
4.5.2 Comparison of Measurement Methods	4-14
4.6 Conclusions	4-15
4.7 Acknowledgements	4-16
4.8 References	4-16

Chapter 5 – Understanding SDBD Actuators: An Experimental Study on Plasma Characteristics **5-1**

<i>Abstract</i>	5-1
5.1 Introduction	5-1
5.2 Experimental Setup	5-2
5.3 Results and Discussion	5-4
5.3.1 Current Signal Measurements	5-4
5.3.2 Effect of Operating Conditions on Current Signal	5-5
5.3.3 Thrust and Power Measurements	5-6
5.3.4 Plasma Imaging	5-8
5.3.5 Spectral Analysis	5-10
5.3.6 Spectral Features of the Plasma	5-10
5.3.7 Excited Species	5-11
5.3.8 Determination of the Reduced Electric Field	5-12
5.4 Conclusions	5-14
5.5 References	5-15

Chapter 6 – Flow Control at Subsonic Speeds Using Serpentine Plasma Actuators **6-1**

<i>Abstract</i>	6-1
6.1 Introduction	6-1
6.2 Experimental Setup	6-2
6.2.1 Wind Tunnel	6-2
6.2.2 Particle Image Velocimetry	6-3
6.2.3 Plasma System	6-3

6.3	Results	6-3
6.4	Conclusion	6-6
6.5	References	6-6

Chapter 7 – Evaluation of Dielectric Barrier Discharge Actuator Substrate Materials **7-1**

<i>Abstract</i>		7-1
7.1	Introduction	7-1
7.2	Dielectric Measurements	7-4
7.2.1	Porous Dielectrics	7-6
7.3	Static Thrust Stand Measurements	7-9
7.3.1	Test Apparatus and Models	7-9
7.3.2	Humidity Effects	7-12
7.3.3	Thrust Measurements	7-13
7.4	One-Dimensional Volume Discharge	7-19
7.4.1	Electrical Measurements	7-19
7.4.2	Circuit Simulations	7-24
7.4.3	Circuit Simulation Results	7-25
7.5	Summary and Conclusions	7-28
7.6	Acknowledgements	7-30
7.7	References	7-30

Annex A: A Summary of Papers on the Topic of Special Session: NATO-RTO-AVT-190: Standardization of DBD Actuators, Delivered at the 2014 Aviation Conference (AIAA) **A-1**

List of Figures

Figure		Page
Figure 2-1	Experiment	2-2
Figure 2-2	Wind Tunnel	2-2
Figure 2-3	Sphere Model	2-3
Figure 2-4	Location of Laser Discharge	2-3
Figure 2-5	Schlieren Images at Selected Times	2-4
Figure 2-6	Flow Field Structure for Interaction of Laser Discharge with Sphere	2-5
Figure 2-7	Computational Domain	2-6
Figure 2-8	Steady Flow Mach Contours	2-6
Figure 2-9	Surface Pressure vs. Angle	2-7
Figure 2-10	Centerline Pressure vs. Time (Experiment)	2-7
Figure 2-11	Centerline Pressure vs. Time (13 mJ)	2-9
Figure 2-12	Centerline Pressure vs. Time (127 mJ)	2-9
Figure 2-13	Centerline Pressure vs. Time (258 mJ)	2-9
Figure 2-14	C_d vs. time (Mortazavi and Knight)	2-10
Figure 2-15	Point <i>A</i>	2-10
Figure 2-16	Point <i>B</i>	2-10
Figure 2-17	Point <i>C</i>	2-10
Figure 2-18	Point <i>D</i>	2-11
Figure 2-19	Filtered Rayleigh Scattering Image of 50 mJ Laser Discharge in Ambient Air	2-12
Figure 2-20	Time Evolution of the Stagnation Pressure on Axis Calculated with CEDRE	2-13
Figure 2-21	Time Evolution of the Stagnation Pressure on Axis Calculated with MISTRAL	2-13
Figure 2-22	Pressure Contours after an Energy Deposition of $E = 14.5$ mJ, during $Dt = 10$ ns, Inside a 3 mm ³ Volume, with FWHM along $z = 2$ mm, and FWHM along $r = 1.1$ mm	2-14
Figure 2-23	Experiment	2-16
Figure 2-24	Wind Tunnel	2-17
Figure 2-25	MW Discharge Apparatus	2-17
Figure 2-26	Schlieren Images (Numbers Indicate Time in μ s)	2-18
Figure 2-27	Computational Domain	2-19
Figure 2-28	Pressure Contours (Steady State)	2-19

Figure 2-29	Computed p vs. Time	2-20
Figure 2-30	Computed and Experimental p vs. Time	2-20
Figure 2-31	Pressure Contours ($t = 25 \mu\text{s}$)	2-21
Figure 2-32	Pressure Contours ($t = 42 \mu\text{s}$)	2-21
Figure 2-33	Pressure Contours ($t = 50 \mu\text{s}$)	2-21
Figure 2-34	Pressure Contours ($t = 75 \mu\text{s}$)	2-21
Figure 2-35	Electron Density ($t = 25 \mu\text{s}$)	2-22
Figure 2-36	Electron Density ($t = 42 \mu\text{s}$)	2-22
Figure 2-37	Electron Density ($t = 50 \mu\text{s}$)	2-22
Figure 2-38	Electron Density ($t = 75 \mu\text{s}$)	2-22
Figure 2-39	General Setup, Photograph of the Experiment	2-24
Figure 2-40	Side View ($yz, x = 0$ Plane) of the Intensity Map of a Multifilament Bundle	2-25
Figure 2-41	Longitudinal Current Signal Measured by the I-Dot Probe as a Function of Microwave Power in the Presence of Filament	2-26
Figure 2-42	Maximum Signal Measured by the I-Dot Probe Divided by the Maximum Signal in the Absence of Microwave Field as a Function of the Position Along the Filament Measured for $P = 100 \text{ W}$	2-26
Figure 2-43	Normalized Amplitude of the Electric Field of the TM Surface Wave as a Function of Propagation Length Calculated	2-27
Figure 3-1	Meshes Used	3-2
Figure 3-2	EHD Force	3-3
Figure 3-3	Parametric Study	3-4
Figure 3-4	Velocity Components	3-4
Figure 4-1	Schematic of DBD Plasma Actuator: Side View and Top View	4-3
Figure 4-2	Circuit Schematic Used to Generate a DBD Plasma Discharge	4-4
Figure 4-3	Experimental Setup Schematic for Direct Force Measurement; Example Readouts from the Balance Showing the Stability and Repeatability of the Direct Thrust Measurement	4-4
Figure 4-4	Convergence Plot for the X-Component of Velocity (U_x) for Two Locations in the Flow Field: Point $(x, y) = (5, 0.5) \text{ mm}$ and $(x, y) = (35, 1.5) \text{ mm}$	4-6
Figure 4-5	Relative Statistical Uncertainty as a Function of Voltage and Position for the Velocity Vector Field	4-6
Figure 4-6	Comparison Between Pitot Measurements and PIV Profiles Taken 15 mm Downstream of Exposed Electrode for an Applied Voltage of 21 kV_{pp} at 14 kHz	4-9
Figure 4-7	Schematic of Control Volume Used to Calculate Reaction Forces Induced by the Plasma Discharge	4-10
Figure 4-8	Force Measurements Over a Range of Input Voltages with Varying Actuator Plate Lengths: 14 kHz and 7 kHz	4-11

Figure 4-9	Percentage Increase in Thrust Between a Plate Length of 2.5 cm and 15 cm as a Function of Voltage	4-11
Figure 4-10	Power Dissipation as a Function of Voltage for Different Plate Lengths	4-11
Figure 4-11	Effect of a Vented vs. Unvented Chamber on the Induced Thrust	4-12
Figure 4-12	Resultant Tangential Thrust Component for a 15, 19, and 22 kVpp Input Voltage at 14 kHz as a Function of the Width for Varying Heights of the Control Volume	4-13
Figure 4-13	Forces Calculated from a Control Volume Analysis as a Function of Voltage for Various Widths of the Control Volume: Tangential Component of Force (F _x) and Normal Component of Force (F _y)	4-14
Figure 4-14	Velocity Magnitude Contour for 20 kVpp Input Driven at 14 kHz	4-14
Figure 4-15	Comparison Between Direct Force Measurements and Those Inferred from a Control Volume Analysis	4-15
Figure 4-16	Control Volume Scaling	4-15
Figure 5-1	Drawing of the DBD Actuator as Used in the Experiments	5-2
Figure 5-2	Schematic Representation of the Spectroscopy Optical Setup	5-3
Figure 5-3	Electric Circuit of the Plasma Actuator Setup for Direct Thrust and Power Measurements	5-4
Figure 5-4	Current, Measured Voltage and Reference Voltage vs. Cycle	5-4
Figure 5-5	Effect of Driven Voltage and Frequency on the Thrust Generated by the Actuator	5-7
Figure 5-6	Evolution of Normalized Thrust in Time – 25 kVpp @ 3.5 kHz	5-7
Figure 5-7	Effect of Driven Voltage and Frequency on the Power Consumption of the Actuator	5-8
Figure 5-8	Effect of Driven Voltage and Frequency on the Actuator Performance	5-8
Figure 5-9	Streamer Propagation Images During Fall and Rise Time of the Voltage Signal	5-9
Figure 5-10	Image Intensity Over Cycle Time for Voltage Amplitudes 15 kV and 7.5 kV at Atmospheric Pressure and 500 mbar	5-10
Figure 5-11	Spectrum at 385 nm to 410 nm	5-11
Figure 5-12	Spectrum at 710 nm to 790 nm	5-11
Figure 5-13	Excited Species Population Over Cycle Time for 15 kV and 2.5 kHz at Atmospheric Pressure	5-12
Figure 5-14	Reduced Electric Field Over Cycle Time for 10 kV, 2.5 kHz; 10 kV, 3.5 kHz; 15 kV, 2.5 kHz; 15 kV, 3.5 kHz	5-13
Figure 5-15	Reduced Electric Field Over Cycle Time for 7.5 kV, 2.5 kHz, 500 mbar; 7.5 kV, 3.5 kHz, 500 mbar; 5 kV, 2.5 kHz, 250 mbar; 5 kV, 3.5 kHz, 250 mbar	5-14

Figure 6-1	Pinch-Spread Effect Given by Serpentine Plasma Actuator	6-2
Figure 6-2	Velocity Contour Along the Pinch and Spread Under Quiescent Conditions (m/s)	6-4
Figure 6-3	Reynolds Stress Along the Pinch and Spread Under Quiescent Conditions (Kg/ms ²)	6-4
Figure 6-4	Average Velocity Contour for Pinch Location (m/s)	6-5
Figure 6-5	Average Velocity Contour for Spread Location (m/s)	6-5
Figure 7-1	Conventional Alternating Current	7-2
Figure 7-2	Illustration of Limited Breakdown Ionization Gap with Dielectric Material of Relative Permittivity ϵ_r and Capacitor Probe C_p	7-3
Figure 7-3	Schematic of the Circuit for: The Dielectric Constant Measurements and the Setup for the Dielectric Breakdown Strength Measurements	7-5
Figure 7-4	Small Signal Dielectric Constant and Loss Tangent at 30°C	7-7
Figure 7-5	Dielectric Constant and Loss Tangent at 120°C for Materials Studied	7-8
Figure 7-6	Leakage Current vs. Applied Electric Field from the Dielectric Breakdown Testing of the Porous Dielectrics	7-8
Figure 7-7	The Stress-Strain Curves from Mechanical Tests of the Polyimide Aerogel	7-9
Figure 7-8	Photograph of DBD Thrust Measurement Apparatus	7-10
Figure 7-9	Photograph of Typical DBD Thrust Measurement Model; Dimensional Schematic	7-11
Figure 7-10	DBD Model Thrust Data with Variable Humidity	7-13
Figure 7-11	DBD Thrust Data for Dielectric Materials	7-14
Figure 7-12	Cross Plot of Thrust in Figure 7-11 at a Constant Input Voltage, $V_s = 18$ kV, with Respect to the Effective Dielectric Thickness, t_d/ϵ_r	7-15
Figure 7-13	Method of Images for a Cylinder Above a Ground Plane	7-15
Figure 7-14	Expanded View of Right Side of Figure 7-13 Without Field Lines	7-16
Figure 7-15	Wheeler Impedance Formula vs. Effective Thickness at Constant Electrode Width ($w = 5$ mm) and Electrode Thickness (0.1 mm)	7-18
Figure 7-16	Simplified Circuit Representation of DBD Actuator	7-18
Figure 7-17	One-Dimensional Volume Discharge vs. Two-Dimensional Surface Discharge	7-20
Figure 7-18	1-D Volume Discharge Apparatus Schematic and Photograph	7-20
Figure 7-19	Example of a Volumetric DBD Discharge Viewed on Edge	7-21
Figure 7-20	Example of 1D Charge Transfer Method Cyclogram (PTFE, $t_d = 1.07$ mm, $t_a = 1.00$ mm, $f = 1$ kHz, $C_p = 22$ nF, $S1 = 12.63$, $S2 = 27.63$ nC/kV or pF)	7-22
Figure 7-21	PTFE $t_d = 1.07$ mm, $t_a = 1.00$ mm, $f = 3$ kHz, $V_s = 16$ kV _{pp}	7-23

Figure 7-22	PTFE $t_d = 1.07$ mm, $f = 3$ kHz, $V_s = 16$ kV _{pp}	7-23
Figure 7-23	Cyclogram Slope Ratio vs. Computed Surface Voltage for Different Permittivity Materials	7-24
Figure 7-24	The Circuits Used to Simulate the 1D Experiments	7-25
Figure 7-25	Typical Fitting Results Showing the Experimental Voltage and Current for the Polyimide Aerogel at 1 and 5 kHz and Values Calculated Using the 2-Diode Model	7-26
Figure 7-26	The Best-Fit Diode Breakdown Voltages and Plasma Resistances Obtained from the Circuit in Figure 7-24(b)	7-28
Figure 7-27	Trends in the Capacitances $C_{PARALLEL}$ and C_{SERIES}	7-28

List of Tables

Table		Page
Table 2-1	Experimental Conditions	2-1
Table 2-2	Location of Pressure Measurements (Deg.)	2-3
Table 2-3	List of Participants and Cases Computed	2-5
Table 2-4	Details of Grids	2-6
Table 2-5	Values of ΔE for Computations	2-8
Table 2-6	Experimental Conditions	2-16
Table 2-7	Details of Grids	2-19
Table 5-1	Statistics of Current Signal on a Symmetric DBD Actuator for Different Operating Conditions	5-5
Table 5-2	Statistics of Current Signal on an Asymmetric DBD Actuator for Different Operating Conditions	5-6
Table 5-3	Electron-Impact Excitations and References for the Corresponding Excitation Cross Sections and Quenching Rates	5-13
Table 7-1	Dielectric Materials	7-6
Table 7-2	DBD Thrust Model Dimensions	7-11
Table 7-3	The Best Fit Values Obtained from the Circuit Simulations	7-27

Acknowledgements

Two AVT-190 working group technical activities, led by Professors Doyle Knight, Rutgers University and Subrata Roy, University of Florida, are gratefully acknowledged.

The activities of the STO AVT-190 were supported by NATO CSO through the provision of meeting arrangements during bi-annual AVT Panel Business Week meetings. The support of AVT Panel Assistant Sandra Cheyne and AVT Panel Executives Andreas Schuette, Dirk Zimmer, Christoph Müller and Doug Blake are gratefully acknowledged.

AVT-190 Membership List

CHAIR

Mr. Charles SUCHOMEL
Wright Patterson Air Force Base
UNITED STATES
Email: charles.suchomel@us.af.mil

MEMBERS

Mr. Bruno Paul George CHANETZ
ONERA
FRANCE
Email: chanetz@onera.fr

Prof. Kwing-So CHOI
University of Nottingham
UNITED KINGDOM
Email: kwing-so.choi@nottingham.ac.uk

Prof. Thomas CORKE
University of Notre Dame
UNITED STATES
Email: tcorke@nd.edu

Prof. Doyle KNIGHT
Rutgers University
UNITED STATES
Email: doyleknight@gmx.com

Prof. Konstantinos KONTIS
University of Glasgow
UNITED KINGDOM
Email: kostas.kontis@glasgow.ac.uk

Mr. Jochen KRIEGSEIS
Karlsruhe Institute of Technology
GERMANY
Email: kriegseis@kit.edu

Dr. Jean LAROUR
Centre National de la Recherche Scientifique
FRANCE
Email: jean.larour@lpp.polytechnique.fr

Dr. Penelope LEYLAND
Ecole Polytechnique Fédérale de Lausanne
FRANCE
Email: penelope.leyland@epfl.ch

LtCol. Maria da Luz MADRUGA MATOS
Academia da Forca Aerea
PORTUGAL
Email: mlmadruga@academiafa.edu.pt

Dr. Rogerio PIMENTEL
DRDC Valcartier
CANADA
Email: rogerio.pimentel@drdc-rddc.gc.ca

Dr. François ROGIER
ONERA
FRANCE
Email: rogier@onera.fr

Dr. Henning ROSEMANN
DLR
GERMANY
Email: henning.rosemann@dlr.de

Dr. Subrata ROY
University of Florida
UNITED STATES
Email: subrata.roy05@gmail.com

Mr. Stephen WILKINSON
NASA Langley Research Center
UNITED STATES
Email: stephen.p.wilkinson@nasa.gov

ADDITIONAL CONTRIBUTORS

Carlo A. BORGHI
Università di Bologna
ITALY
Email: ca.borghi@unibo.it

Alain DECHAMPLAIN
Université de Laval
CANADA
Email: Alain.DeChamplain@gmc.ulaval.ca

Yves DE VILLERS
DRDC Valcartier
CANADA
Email: yves.devillers@drdc-rddc.gc.ca

Guillaume DUFOUR
ONERA
FRANCE
Email: dufour@onera.fr

Rik GEUNS
Ecole Polytechnique Fédérale de Lausanne
SWITZERLAND
Email: rikgeuns@gmail.com

Sami GOEKCE
Ecole Polytechnique Fédérale de Lausanne
SWITZERLAND
Email: samigoekce@gmail.com

Haiquan GUO
Ohio Aerospace Institute
UNITED STATES
Email: haiquan.n.guo@nasa.gov

Nicole M. HOUSER
University of Toronto
CANADA
Email: houser@utias.utoronto.ca

Yves JEAN
Université de Laval
CANADA
Email: yves.jean.2@ulaval.ca

K. KOURTZANIDIS
ONERA
FRANCE
Email: kourtzanidis@certh.gr

Philippe LAVOIE
University of Toronto
CANADA
Email: lavoie@utias.utoronto.ca

Arash NAGHIB-LAHOUTI
DRDC Valcartier
CANADA
Email: Naghieb-lahouti@alumini.utias.utoronto.ca

Gennady PLYUSHCHEV
Ecole Polytechnique Fédérale de Lausanne
SWITZERLAND
Email: gennady.plyushchev@gmail.com

Tommy RINGUETTE
Numérica Technologies
CANADA
Email: tringuet@hotmail.com

Emilie J. SIOCHI
NASA LRC
UNITED STATES
Email: Emilie.J.Siochi@nasa.gov

Tian-Bing XU
National Institute of Aerospace
UNITED STATES
Email: tbxu@nianet.org

Hossein ZARE-BEHTASH
University of Glasgow
UNITED KINGDOM
Email: Hossein.Zare-Behtash@glasgow.ac.uk

PANEL/GROUP MENTOR

Dr. Siva S. BANDA
US Air Force Research Lab
UNITED STATES
Email: siva.banda@us.af.mil

Plasma Based Flow Control for Performance and Control of Military Vehicles

(STO-TR-AVT-190)

Executive Summary

Flow Control Technologies are of interest to the general military and NATO community because of their potential to improve aerodynamic efficiency and air-sea stability and control. The basic concept in Flow Control Technologies is to effect a large change in an aerodynamic flow by a focused, carefully modulated means and with, preferably, a minimum amount of energy. Traditional flow control uses include applications such as bleed in inlets, span wise flap blowing, bumps, vortex generator devices, and spoilers for weapon bay. However, historically, most of these methods were cost and complexity expensive. Innovations changing this situation are: miniaturization of sensors and actuators, improvements in automatic controls, a host of new effectors such as synthetic jets, requiring no air supply, plasmas, new materials and integration of devices. New design options are also evolving such as electrification of the airframe, eliminating the need to duct engine bleed around the aircraft and better understanding of underlying flow phenomena physics through computation and advanced experiments. A promising option in this category uses ionized gas and electrical charge to produce momentum flux and force changes without moving parts and without changing a flight vehicles outer mold lines. It leverages the advantages of electronic/mechanical systems to affect flow control without the weight penalties and complexity of these systems. For these reasons, Task Group AVT-190 was established to conduct a research effort focused on the development and validation of theoretical models for predicting the interaction of plasma with generic aerodynamics bodies-configurations in fluid flows of interest to NATO including the effect on aerodynamic forces and moments. Specifically, discharge techniques were to be explored using Dielectric Barrier Discharges, Microwave discharges, and combined microwave-laser discharges. The specific goals to investigate were:

- Establish a common experimental database including surface pressure, forces and moments, and flow-field visualization;
- Define a matrix of test cases within the experimental database for validation of theoretical models;
- Compute the test cases;
- Evaluate the results of the computations and identify modelling strengths and weakness; and
- Recommend modifications to the theoretical models.

This report contains assessments conducted by team members from ten countries: Belgium, Canada, France, Germany, Italy, Russia Federation, Switzerland, Turkey, United Kingdom, and the United States. The contributions span academia, industry, and government laboratories. The result of the Task Group are presented in this report.

Contrôle du flux à partir de plasma pour la performance et le contrôle des véhicules militaires

(STO-TR-AVT-190)

Synthèse

Les technologies de contrôle de flux présentent un intérêt pour les forces armées et l'OTAN du fait de leur potentiel d'amélioration de l'efficacité aérodynamique, de la stabilité dans l'air ou à la mer et, du contrôle. Le concept de base des technologies de contrôle de flux consiste à effectuer un changement important dans un flux aérodynamique par des moyens concentrés, soigneusement modulés et, de préférence, avec une quantité minimale d'énergie. Les applications traditionnelles de contrôle de flux incluent notamment le prélèvement d'air dans les entrées d'air, le soufflage des volets sur l'ensemble de l'envergure, les turbulences, les générateurs de vortex et les déflecteurs pour les baies d'armement. Toutefois, historiquement, la plupart de ces méthodes étaient complexes et coûteuses. Cependant des innovations sont intervenues : miniaturisation des capteurs et des actionneurs, améliorations des commandes automatiques, une multitude de nouveaux effecteurs tels que les jets synthétiques, ne nécessitant aucune alimentation en air, les plasmas, de nouveaux matériaux et l'intégration de dispositifs. De nouvelles options de conception évoluent également, telles que l'électrification de la cellule, éliminant ainsi le besoin de canaliser le prélèvement d'air moteur autour de l'aéronef et une meilleure compréhension de la physique des phénomènes de flux sous-jacents par le biais de calculs et d'expériences avancées. Une option prometteuse dans cette catégorie utilise les gaz ionisés et la charge électrique pour produire un flux de mouvement et forcer les changements sans pièces mobiles ni modifications du profil aérodynamique des aéronefs. Elle exploite les avantages des systèmes électroniques / mécaniques pour affecter le contrôle du flux sans les inconvénients dus au poids et à la complexité de ces systèmes. Pour ces raisons, le groupe de travail AVT-190 (Technologie appliquée aux véhicules) (Applied Vehicle Technology) a été mis sur pied pour mener un effort de recherche. Celui-ci est orienté sur le développement et la validation de modèles théoriques pour prédire l'interaction du plasma avec les configurations aérodynamiques génériques dans les écoulements de fluides intéressant l'OTAN, y compris l'effet sur les forces et moments aérodynamiques. Plus précisément, des techniques de décharge devaient être explorées en utilisant des décharges de barrière diélectrique, des décharges de micro-ondes et des décharges combinées de laser et micro-ondes. Les objectifs spécifiques à étudier étaient :

- L'établissement d'une base de données expérimentale commune qui inclut la pression de surface, les forces et les moments, et la visualisation du champ d'écoulement ;
- La définition d'une matrice de tests dans la base de données expérimentale pour la validation des modèles théoriques ;
- Les calculs des tests ;
- L'évaluation des résultats des calculs et l'identification des forces et faiblesses de la modélisation ; et
- La recommandation de modifications à apporter aux modèles théoriques.

Le présent rapport contient les évaluations des membres de l'équipe provenant de dix pays : Belgique, Canada, France, Allemagne, Italie, Fédération de Russie, Suisse, Turquie, Royaume-Uni et Etats-Unis. Les contributions proviennent de l'industrie, du monde universitaire et des laboratoires nationaux. Les résultats du groupe de travail sont présentés dans ce rapport.

Chapter 1 – INTRODUCTION: THE NATO STO TASK GROUP AVT-190

Charles F. Suchomel
Air Force Research Laboratory
USA

The emergence of RTO as the organisation to co-ordinate research and technology activities over the breadth of all the NATO military environments (land, air, sea, and space) presents a unique opportunity. The core competencies embodied in the technical areas of vehicle control and optimum performance are at the heart of the mission accomplishment of all military vehicles. The experts currently active in RTO activities and in the process of solving aircraft issues and performing research in these areas have counterparts addressing analogous issues for land, sea, and space vehicles. These experts all face similar challenges, and the coordination of the different activities will have benefits that can be applied to all environments. This is especially true for emerging disciplines involving multi-physics expertise such as plasma interactions with the flow about military aircraft.

It was appropriate, therefore, to formally initiate Working Group AVT-190 to explore the use of plasma as a way to transfer energy to the atmosphere, locally, about a flight vehicle to cause and control flow interaction resulting from the deposited energy. Plasma energy discharge offers several potential advantages for performance and flight control of military vehicles compared to conventional mechanical systems (e.g., ailerons, boundary layer suction, flaperons, and rudder). First, they can be actuated virtually instantaneously, whereas mechanical systems have a finite actuation time due to their inherent mechanical inertia. Second, discharges can be focused on the surface or projected at a distance from an aerodynamic body (e.g., upstream). This is not possible with mechanical systems which are inherently affixed to the aircraft. Third, discharges can be modified in location, duration, and strength depending on the geometry and the type discharge employed. Mechanical systems are not inherently as flexible (e.g., an aileron can only be deflected about a single axis). During the exploratory phase of the working group, various applications for control and performance were explored, but it was the consensus of the group that a concerted effort to understand and to describe the fundamental physical process was more in line with the AVT charter and mandatory before these capabilities could be fully exploited.

The AVT panel approved the AVT-190 working group's objective of establishing a repeatable, systematic process to describe the fundamental physics of rapid energy transfer to air and the resulting change on local flow conditions. The group identified two subgroup activities for Plasma Flow Control (PFC) using:

- 1) Dielectric Barrier Discharge;
- 2) Microwave and combined microwave-laser discharges.

Both subgroups agreed to the following work plan:

- 1) To create common databases, using existing experimental data, to define a matrix of test cases;
- 2) To execute detailed validation of computational methods, using the test matrix, for a range of potential fluids, speed, and altitude applications of PFC;
- 3) To evaluate the results of the computations to identify modelling strengths and weaknesses; and
- 4) To identify reduced order model requirements for successful design (e.g., force and flow changes, power and weight requirements).

Execution of the AVT-190 plan proceeded smoothly until midway through the program, when unprecedented restrictions on multi-country collaborative and travel severely precluded individual/government involvement. As funding pressures increased, the size of the task group diminished, the scope of the tasks originally laid out diminished proportionately to funding restrictions, and not all tasks were done. Individual efforts that were completed, undertook tasks 1) through 3); i.e., identified computational strengths and weakness, but an overall task group assessment of reduced order model requirements for successful design was not done. At the end of the working group's activity, it was considered essential to capture the limited, high quality, work that was accomplished. This publication represents the best, under trying circumstances, by researchers in the fields of high energy electrical discharges, energetic plasma inducted flow control, and high fidelity computational aerodynamics. You are encouraged to read their contributions to the complex, fascinating, multi-disciplinary field of plasma flow control.

Laser and Microwave Discharge – D. Knight, Rutgers University, United States; J. Larour, LPP, Ecole Polytechnique, Paliseau, France.

The laser and microwave subgroup assessed the computational prediction capability of the effect of laser or microwave discharge on supersonic flow past a simplified aerodynamic body. A detailed examination of available comparison data was conducted, and two experiments were identified for the effort, namely:

- 1) The laser discharge experiment of Adelgren et al. (2005), Rutgers University;
- 2) The microwave discharge experiment of Lashkov et al. (2004).

Independent computations were done by Dr. Olga Azarova, Dorodnicyn Computing Center, Russian Academy of Sciences, and Drs. Doyle Knight and Mahsa Mortazavi, Rutgers University, as well as by Dr. Paul-Quentin Elias at ONERA and Dr. Martin Spel et R.Tech in France. All simulations were based upon a simplified model comprising the unsteady Euler equations for a perfect gas with the laser discharge modelled as an instantaneous increase in static temperature (and static pressure) in a spherical region defined by the laser focal volume. The temperature increase and peak pressure were determined on the sphere centerline due to the impact of the transmitted blast wave on the sphere. The simulations failed to accurately predict the pressure vs time history of the interaction of the laser discharge with the sphere for three different laser discharge energies. Explanations were provided for the disagreement between the simulations and the experiments and recommendations offered for future research. Flow effects of microwave energy deposition were similar to the interaction of the laser discharge with the sphere. Additionally, an experiment is reported by Dr. Jean Larour, aiming to show the coupling of microwave radiation to a multi-filament plasma column generated by powerful femtosecond laser. This leads to the amplification of longitudinal oscillations of the plasma over a distance exceeding 10 cm, giving a plasma column of interest for heating air column ahead of a supersonic body.

Numerical Modelling of SDBD Actuators in Quiescent Air – F. Rogier, ONERA, France.

In this study, numerical results obtained from modelling of SDBD plasma actuators are compared to experimental thrust measurements and to the induced velocity in quiescent air. The work presented evaluates a plasma modelling approach by comparing the results with experimental data for a 14 kHz – 21 kV actuator in a quiescent atmosphere. The study was divided into two parts: first, the numerical model is presented, and secondly, the total body force exerted by the discharge, as computed numerically, is compared with force balance measurements. Simulations were conducted for various voltages, frequencies, DBD parameters, and then compared with force measurement results and PIV measurements of the induced actuator wind in quiescent flow. The study ends by evaluating the modelling robustness to numerical and physical parameter uncertainties.

Evaluation of Force Measurement Techniques for Dielectric Barrier Discharge Actuators – Ryan Durscher and Subrata Roy, University of Florida, United States.

Despite their popularity in the recent literature, plasma dielectric barrier discharge actuator research lack a consistent thrust measurement technique. This work looked at comparing two techniques used to measure the global, plasma induced thrust with the intention of recommending remedies that facilitate direct comparison of future experimental results. A force balance was used to make a direct measurement of thrust and then compared with a control volume analysis on the data obtained through particle image velocimetry. Local velocity was measured by particle image velocimetry and was validated with a fine-tip pressure probe. The effect of varying the actuator plate length on which the induced flow acts was investigated by direct thrust measurements. Results from these tests show that the length of the actuator plate was most influential at higher voltages where the measured thrust increased as much as 20% for a six times reduction in the length of the plate. For the indirect thrust measurement, the influence of the control volume size was analyzed. When the two methods were compared, good agreement was found when the control volume size had a sufficient downstream extent. In addition, the discharge length was optically measured using visible light emission, a linear correlation was found between the discharge length and the thrust measurements for the actuator configurations studied, and the energy conversion efficiency curve for a representative actuator was determined.

Understanding SDBD Actuators: An Experimental Study on Plasma Characteristics – Pénélope Leyland, Ecole Polytechnique Fédéral De Lausanne, France/Switzerland; Rogerio Pimentel, DRDC Valcartier, Canada; Rik Geuns, Ecole Polytechnique Fédéral De Lausanne, Switzerland/Belgium.

The working mechanisms of Dielectric Barrier Discharge (DBD) plasma actuators as aerodynamic control devices are investigated experimentally on a common platform, referred to as the NATO-AVT-RTO-190 test case. A better understanding of the working principle and characteristics of DBD paves the way for more efficient and safer use of plasma actuators in aerodynamic applications. In this study, a characterization of the plasma was done by current measurements, fast-camera plasma imaging and thrust measurements. Furthermore, more advanced plasma characteristics such as reduced electric field and excited species population are found by Optical Emission Spectroscopy. The study goal is data for a common database within NATO countries which can be used for verification and validation of numerical modelling by varying the key parameters such as frequency and voltage.

Flow Control at Subsonic Speeds Using Serpentine Plasma Actuators – K. Kontis, University of Glasgow, United Kingdom.

Plasma actuators for flow control applications is fast becoming the subject of many research campaigns. A drawback of this technique is the relatively low flow speeds that the plasma induced jet exhibits. One approach to improving such actuators is to devise novel configurations that despite their low induced speeds, have improved ability to manipulate the flow characteristics. The study explores the use of a newly developed serpentine plasma actuator to a standard backwards facing step model in a low-speed wind tunnel operating at 15 m/s. The influence of the actuator on the separated shear layer is examined using PIV. The results show that due to the three-dimensional flow induced by the actuator, the shear layer exhibits different characteristics along the span wise direction. It is believed this three-dimensional flow characteristics has the ability to create greater control authority at the relatively low plasma induced velocities.

Evaluation of Dielectric Barrier Discharge Actuator Substrate Materials – S.P. Wilkinson and E.J. Siochi, NASA Langley Research Center, United States; Godfrey Sautio and Tian-Bing Xu, National Institute of Aerospace, United States; Mary Ann Meador, NASA Glenn Research Center, United States; Haiquan Guo, Ohio Aerospace Institute, United States.

A key, enabling element of a Dielectric Barrier Discharge (DBD) actuator is the choice of dielectric substrate material. While various investigators have studied the performance of different homogeneous materials, most often in the context of related DBD experiments, fundamental studies focused solely on the dielectric materials have received less attention. The purpose of this study was to conduct an experimental assessment of the body-force-generating performance of a wide range of dielectric materials in search of opportunities to improve DBD actuator performance. Materials studied included commonly available plastics and glasses as well as a custom-fabricated polyimide aerogel. Diagnostics included static induced thrust, electrical circuit parameters for 2D surface discharges and 1D volume discharges, and dielectric material properties. Lumped-parameter circuit simulations for the 1D case were conducted showing good correspondence to experimental data provided that stray capacitances are included. The effect of atmospheric humidity on DBD performance was studied and showed a large influence on thrust. The main conclusion for homogeneous, dielectric materials at forcing voltages less than that required for streamer formation, is the material chemical composition appears to have no effect on body force generation when actuator impedance is properly accounted for.

Chapter 2 – LASER AND MICROWAVE DISCHARGE

Doyle Knight
Rutgers University
UNITED STATES

Jean Larour
Laboratoire de Physique des Plasmas – LPP
Ecole Polytechnique
FRANCE

2.1 INTRODUCTION

Energy deposition for flow control in high speed flows has been a research topic of significant interest for several decades. Examples of energy deposition methods include pulsed laser or microwave discharge, spark DC discharge and electron beam. A number of review papers have summarized the technological advances and challenges afforded by this approach including Georgievsky and Levin [1], Zheltovodov [2], Knight et al. [3], Fomin et al. [4], Bletzinger et al. [5], and Knight [6].

The objective of the laser and microwave subgroup is the assessment of the computational capability for prediction of the effect of laser or microwave discharge on supersonic flow past a simplified aerodynamic body. A detailed examination of available experimental data was conducted and two experiments were identified, namely: 1) The laser discharge experiment of Adelgren et al. [7]; and 2) The microwave discharge experiment of Lashkov et al. [8].

The results of this study are described in the following sections.

2.2 LASER DISCHARGE

2.2.1 Experiment

The experiment of Adelgren et al. [7] examined the effect of the interaction of a laser discharge with a sphere at Mach 3.45. The experimental conditions are indicated in Table 2-1. The experimental configuration is shown in Figure 2-1 and the wind tunnel facility in Figure 2-2. A sphere ($D = 25.4$ mm) is mounted on a sting in the test section of the Mach 3.45 wind tunnel at Rutgers University. An Endevco pressure transducer (Model 8530C-100) is located in a 1.32 mm x 1.78 mm deep cavity within the sphere (Figure 2-3). The sphere can be rotated about a spanwise axis thereby providing pressure time history data at selected angles in the vertical plane of symmetry.

An Nd-YAG (532 nm) laser is focused upstream of the sphere model at a distance $L = D$ upstream of the stagnation point of the sphere on the centerline (Figure 2-4). The laser focal length is 250 mm and the focal region diameter is approximately 0.1 mm. The laser pulse width is 10 ns and the pulse varies from 13 mJ to 258 mJ at the laser exit as measured by an Ophir Optronics 30A-P-SH meter.

Table 2-1: Experimental Conditions.

Property	Parameter	Value
Freestream	Mach number	3.45
	Static pressure p_∞ (kPa)	13.1
	Static temperature T_∞ (K)	77.8

LASER AND MICROWAVE DISCHARGE

Property	Parameter	Value
Laser	Pulse energy Q (mJ)	13, 127 and 258
	$Q/p_{\infty} L^3$	0.0606, 0.592, 1.202
	Distance L (mm)	25.4
	Beam focal volume (mm ³)	3
	Beam focal length (mm)	250
Hemisphere cylinder	Pulse duration (ns)	10
	Diameter D (mm)	25.4

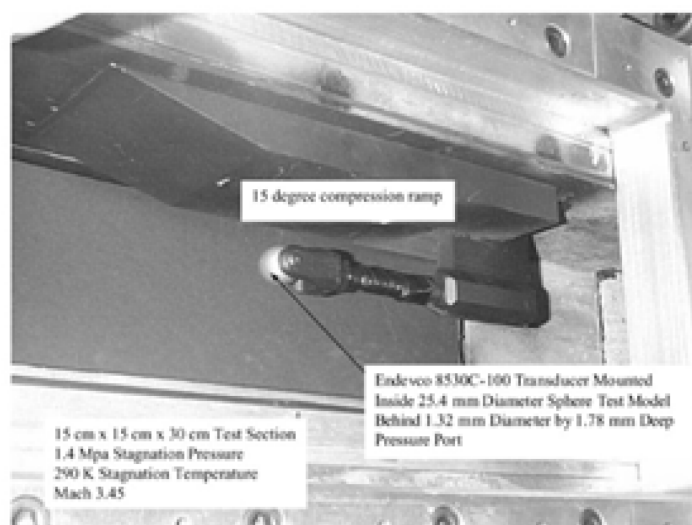


Figure 2-1: Experiment.

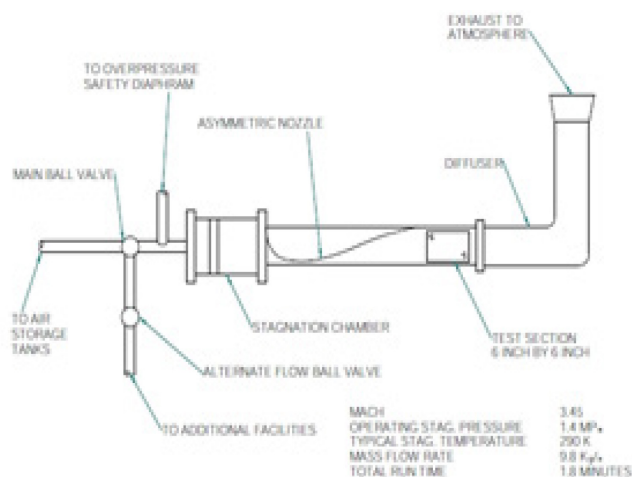


Figure 2-2: Wind Tunnel.

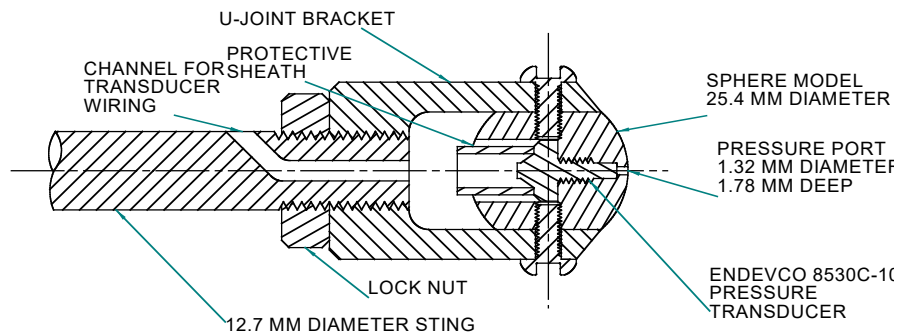


Figure 2-3: Sphere Model.

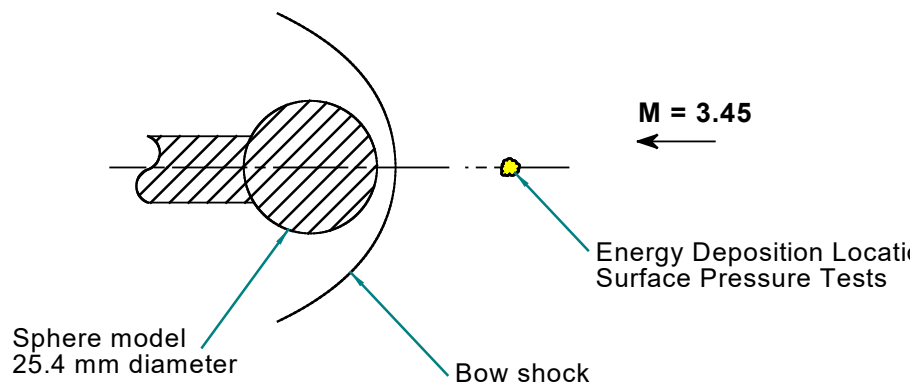


Figure 2-4: Location of Laser Discharge.

Experimental diagnostics are time history of surface pressure at selected angles in the vertical plane of symmetry indicated in Table 2-2 and Schlieren imaging. A single wind tunnel test produces the time history of surface pressure at a fixed angle. Therefore, multiple wind tunnel tests are performed at the conditions indicated in Table 2-1 to obtain the pressure vs. time over the range of angles shown. A Stanford Research Systems pulse generator is used to control the timing of the laser pulse and Schlieren imaging instrumentation.

Table 2-2: Location of Pressure Measurements (Deg.).

13 mJ	127 mJ	258 mJ	13 mJ	127 mJ	258 mJ	13 mJ	127 mJ	258 mJ
56	57	57	19	19	19	-18	-19	-18
46	47	46	11	12	10	-29	-30	-32
37	39	36	1	1	0	-42	-43	-43
28	30	29	-8	-10	-9	-56	-55	-55

An example of the flowfield structures generated by the interaction of the laser discharge with the supersonic flow pasts the hemisphere is shown in Figure 2-5. Schlieren images are displayed at $t = 0$ (i.e., the instant of the laser discharge) and at $t = 30, 60$ and $90 \mu\text{s}$ after the laser discharge. At $t = 0 \mu\text{s}$ (Figure 2-5(a)) the location of the laser discharge is indicated by the bright spot which remains in subsequent images due to saturation of the pixels in the CCD camera. The blunt body shock generated by the sphere is evident. The direction of the laser beam is indicated. At $t = 30 \mu\text{s}$ (Figure 2-5(b)), the blast wave generated by the laser discharge has propagated spherically outwards and convected with the flow. The forward portion of the blast wave has intersected the blunt body shock and a transmitted shock has impacted the sphere causing a momentary increase in pressure on the centerline. At $t = 60 \mu\text{s}$ (Figure 2-5(c)), the heated plasma has reached the blunt body shock causing a lensing forward (i.e., upstream) of the shock. At $t = 90 \mu\text{s}$, the plasma has convected past the front of the sphere and the flowfield is returning to the undisturbed structure. The entire process is illustrated schematically in Figure 2-6.

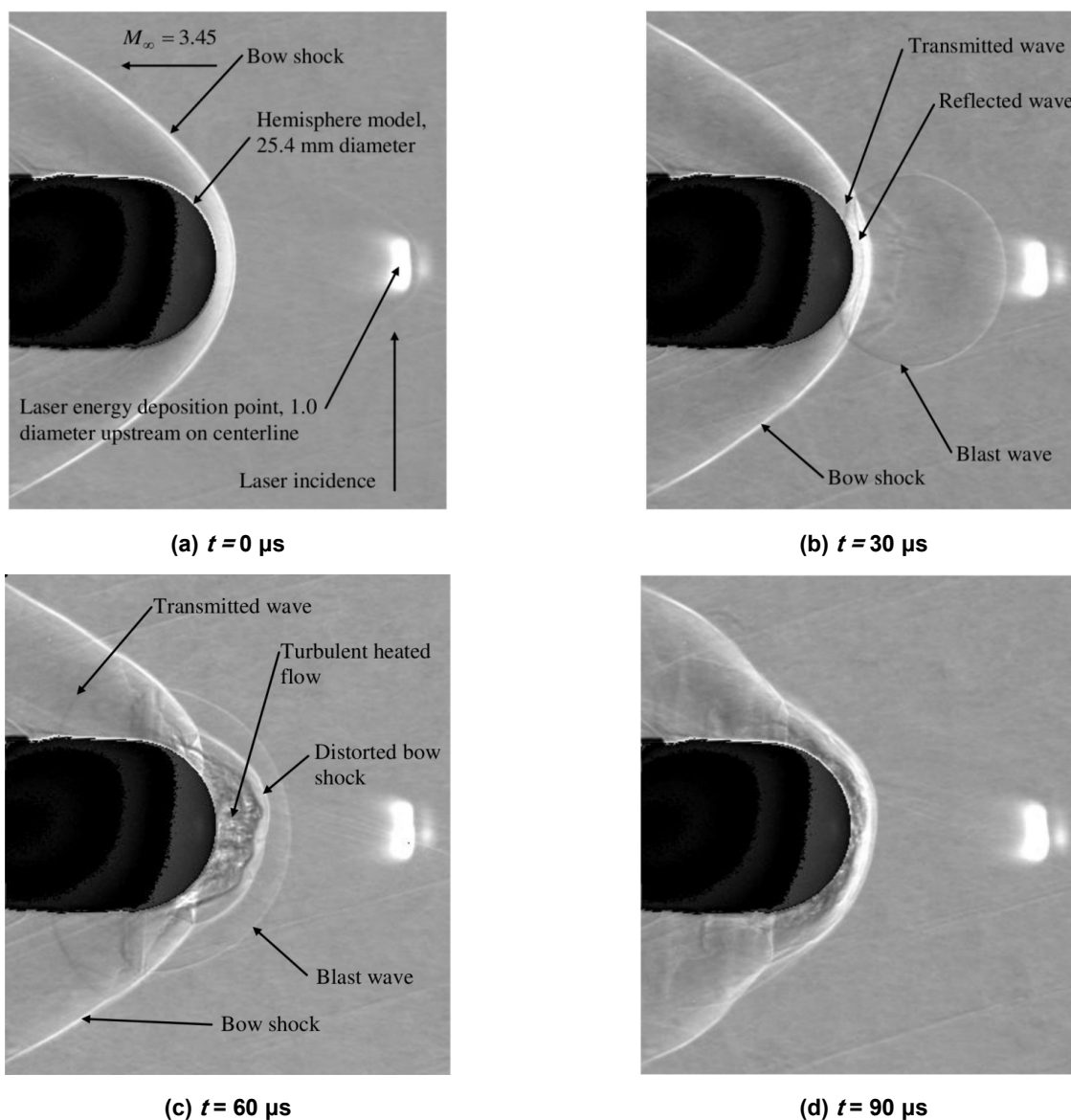


Figure 2-5: Schlieren Images at Selected Times.

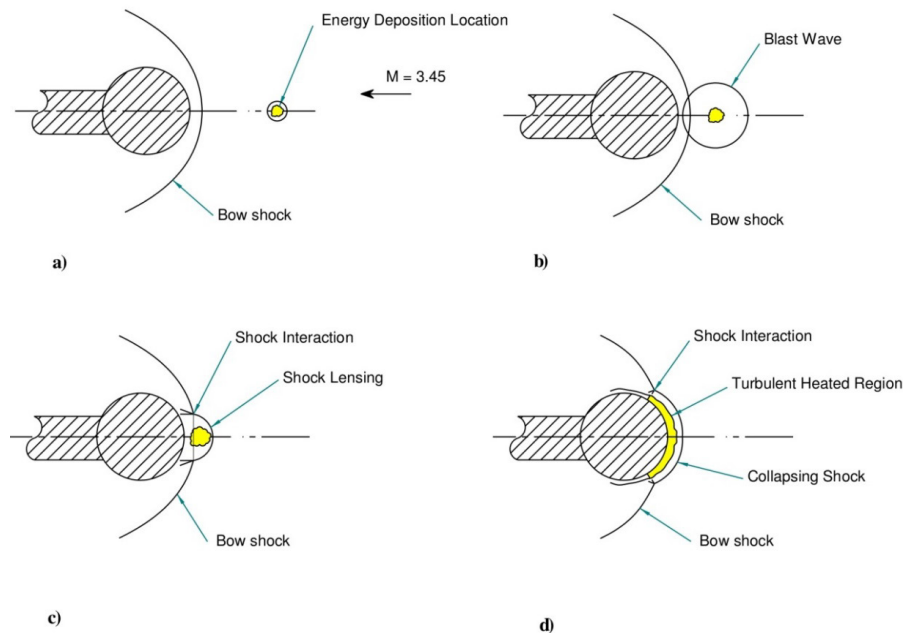


Figure 2-6: Flow Field Structure for Interaction of Laser Discharge with Sphere.

2.2.2 Participants

Computations were solicited from experts in the US and Europe for the laser discharge experiment. The list of participants and their respective organizations is presented in Table 2-3 together with the cases computed.

Table 2-3: List of Participants and Cases Computed.

Organization	Participants	Laser Energy (mJ)		
		13	127	258
Dorodnicyn Computing Center, Russian Academy of Sciences	Olga Azarova	•	•	•
Rutgers University	Mahsa Mortazavi, Doyle Knight	•	•	•
ONERA	Paul-Quentin Elias	•		
R.Tech	Martin Spel	•		

2.2.3 Methodology

The simulations by Azarova are based on the Euler equations for a compressible perfect gas. The simulation is performed using the code developed by Azarova [9]. The algorithm is second order accurate in both space and time, and is conservative for both the dependent variables and their spatial derivatives. The body is represented by a stepped shape with piecewise linear boundaries. Separate algorithms are utilized at the body surface to maintain conservation and second order spatial accuracy. Details of the computational grid are presented in Table 2-4. There are typically 500 points along the hemisphere frontal surface.

The simulations by Mortazavi and Knight are based on the Euler equations for a compressible perfect gas. The commercial code GASPex is used. The algorithm is second order accurate in space and time. The inviscid fluxes are modelled using Van Leer’s method [10] with a modified ENO limiter. Temporal integration is performed using a two-stage Runge-Kutta method. Three separate grids (coarse, medium, fine) were used. Details are presented in Table 2-4.

Table 2-4: Details of Grids.

Organization	Grid	$\Delta_{min,i}/D$	$\Delta_{min,j}/D$	No. Nodes
Dorodnicyn	Base	2.0×10^{-3}	2.0×10^{-3}	0.98×10^6
Rutgers	Coarse	6.540×10^{-4}	8.333×10^{-4}	0.270×10^6
	Medium	3.270×10^{-4}	4.167×10^{-4}	1.080×10^6
	Fine	1.645×10^{-4}	2.083×10^{-4}	4.320×10^6
ONERA	unstructured	$4 - 8 \times 10^{-4}$		6.1×10^4

The computational domain ABCDA is displayed in Figure 2-7. The line AB is the axis of symmetry. The surface BC is a slip boundary. The downstream boundary CD uses a zero normal gradient boundary condition. The outer surface DA is fixed at the freestream conditions.

Prior to the initiation of the laser discharge, the flowfield is converged to steady state. The computed Mach number contours are shown in Figure 2-8 for the simulation by Mortazavi and Knight. The computed ratio of the shock standoff distance (measured from the center of the sphere along the axis of symmetry) to the sphere diameter D is 0.6278 which is in close agreement with the experimental value of 0.60 (Adelgren et al. [7]). A similarly accurate result for the converged steady state flowfield is obtained by Azarova. The computed and experimental steady state surface pressure vs. angle θ (measured in the vertical plane of symmetry) is displayed in Figure 2-9. Excellent agreement between the computation and experiment is achieved.

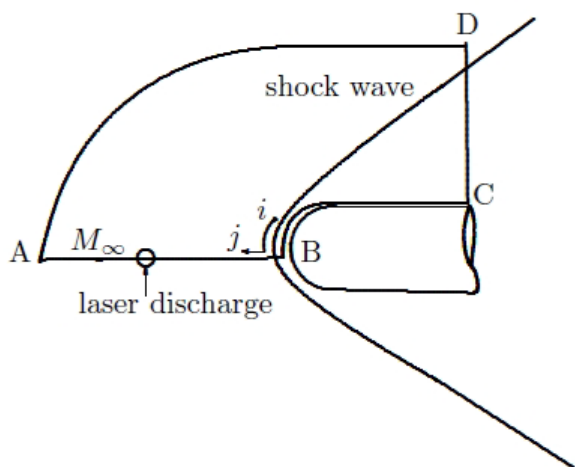


Figure 2-7:Computational Domain.

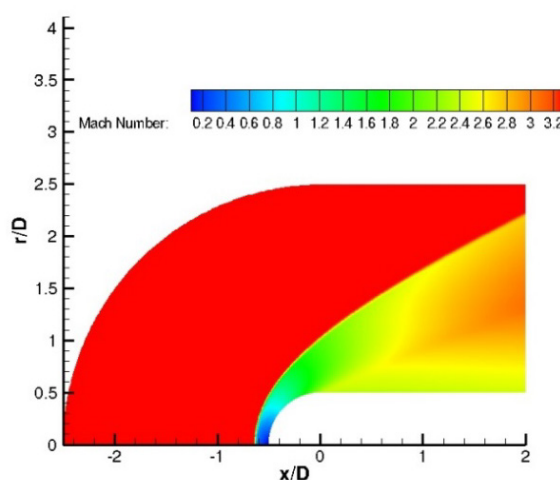


Figure 2-8:Steady Flow Mach Contours.

The laser discharge is modelled as an instantaneous modification to the converged steady state flowfield at a location one diameter upstream of the stagnation point of the sphere and on the axis of symmetry. This is justified since the duration of the laser spark (10 ns) is small compared to the development time of the flowfield during the interaction of the laser-generated plasma with the sphere (typically, 120 μs). The static temperature is modified according to:

$$T = T_{\infty} + \Delta T \text{ for } r \leq r_o \text{ and } T = T_{\infty} \text{ for } r > r_o$$

The density and velocity are unchanged, and the static pressure is determined by the Ideal Gas Law. Therefore, the additional energy added to the flowfield is:

$$\Delta E = \rho_{\infty} c_v \Delta T V$$

where ρ_{∞} is the freestream density, c_v is the specific heat at constant volume and V is the volume of the sphere. With the above modification to the previously converged steady state, the flowfield is integrated in time to examine the effect of the heated region (the plasma) on the sphere.

A principal challenge for the simulation is the determination of the values of ΔT and r_o for a given laser energy discharge. It is widely recognized that only a fraction of the laser energy pulse (as measured at the laser exit) is absorbed by the gas with the remainder reflected or transmitted. Additionally, the laser discharge results in formation of excited vibrational modes and thermochemical reactions. Since the simulations assume a perfect gas, the fraction of the discharge energy resulting in the heating of the gas (i.e., increasing the translational-rotational temperature) must be determined by comparison with experimental data. Examining the experimental centerline pressure vs. time in Figure 2-10, it is evident that the initial pressure peak (due to the impingement of the transmitted blast wave on the sphere centerline) increases monotonically with laser discharge energy. It is particularly noteworthy that the minimum pressure on the sphere centerline is insensitive to the laser discharge energy. Therefore, the magnitude of the initial pressure peak was chosen as the experimental data point for determination of the value of ΔT (and hence ΔE) for each laser discharge experiment.

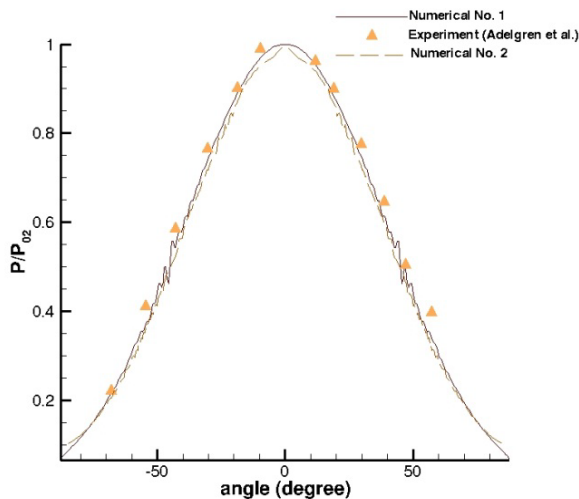


Figure 2-9: Surface Pressure vs. Angle.

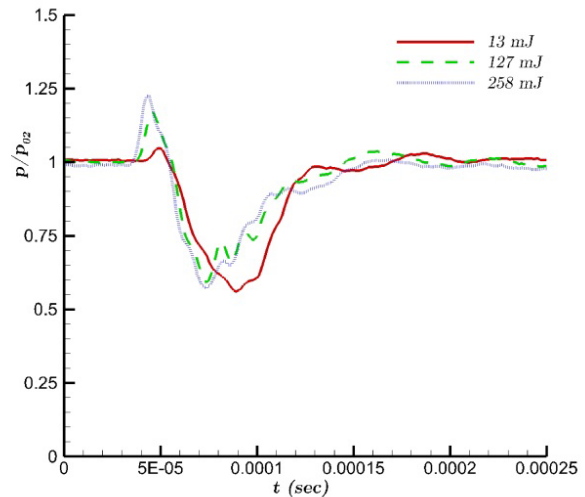


Figure 2-10: Centerline Pressure vs. Time (Experiment).

The value for r_o can be estimated from the beam focal volume of 3 mm^3 (Table 2-1). This implies $r_o = 0.895 \text{ mm}$ ($r_o/D = 0.0352$). The values chosen are $r_o/D = 0.0352$ (Azarova) and $r_o/D = 0.05$ (Mortazavi and Knight).

In the simulations by Elias at ONERA (Palaiseau, France), the effect of single or repetitive linear energy depositions in front of a supersonic blunt body is computed using the CEDRE flow solver. The CFD Code models the effect of a laser-induced energy deposition, as obtained for example using the long filaments created by a femtosecond laser. Adelgren's results were simulated for laser energy 13 mJ.

In the simulations by Spel at R.Tech company, a French partner of ONERA, the effect of single or repetitive linear energy depositions in front of a supersonic blunt body is computed using the MISTRAL flow solver [11] dedicated to re-entry studies. Adelgren's type results were simulated for laser energy 14.5 mJ.

2.2.4 Results

The values of ΔE required to achieve agreement with the experimental first pressure peak are displayed in Table 2-5. It is noted that the values obtained by Azarova are more than an order of magnitude larger than Mortazavi and Knight. This may be attributable to the sensitivity of the computed first peak pressure to the grid refinement (see Table 2-4).

Table 2-5: Values of ΔE for Computations.

Experiment	Dorodnicyn Computing Center	Rutgers University	ONERA
Q (mJ)	ΔE (mJ)	ΔE (mJ)	ΔE (mJ)
13	2.769	0.1405	13 (LTA gas)
127	13.081	0.7366	
258	21.930	1.1249	

The computed and experimental centerline pressure vs. time is displayed in Figure 2-11, Figure 2-12, and Figure 2-13 for 13 mJ, 127 mJ and 258 mJ cases, respectively. The vertical axis is $\Delta p/p_{02}$ where p_{02} is the stagnation pressure on the sphere centerline in the steady state and $\Delta p = p_0 - p_{02}$ where p_0 is the instantaneous pressure on the sphere centerline. The horizontal axis is the dimensionless time $\tau = t U_\infty/D$ which represents the relative convective time for the flow. The magnitude of the initial pressure peak is accurately matched by all simulations as the method for determination of the value ΔT for the initial condition of the laser discharge. The time series of the computed and experimental centerline pressures are matched at the time point of the first peak in the experimental pressure.

Comparison of the computed and experimental centerline pressure vs. time provides several important conclusions. First, the computed duration of the interaction is significantly less than the experiment for all laser discharge energy levels. Second, a strong shock wave appears in the computations subsequent to the impact of the transmitted blast wave at $\tau \approx 1.5$. The strength of this second shock wave increases with the laser discharge energy. The second shock does not appear, however, in the experiment for any case.

Comparison of the computed centerline pressure for the two separate simulations provides additional conclusions. First, there is significant disagreement for the computed peak pressure of the second shock at $\tau \approx 1.5$. Second, there is significant disagreement for the computed minimum pressure occurring just prior to the second shock.

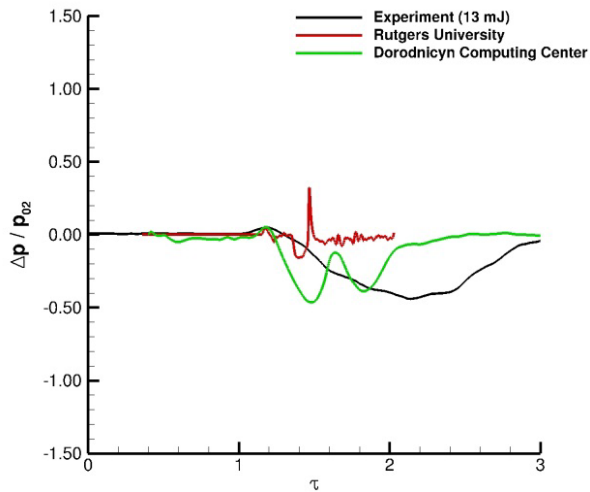


Figure 2-11: Centerline Pressure vs. Time (13 mJ).

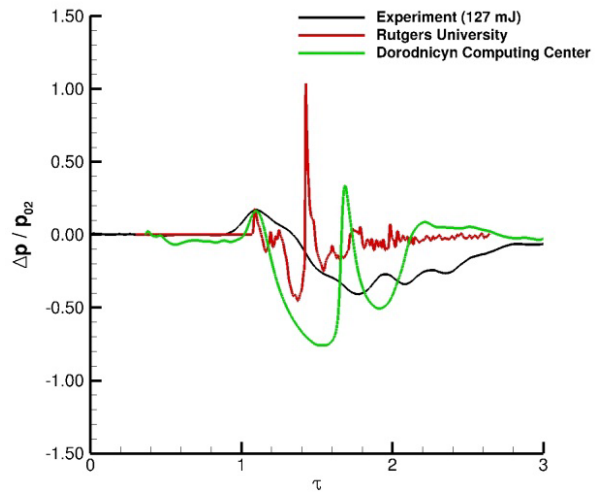


Figure 2-12: Centerline Pressure vs. Time (127 mJ).

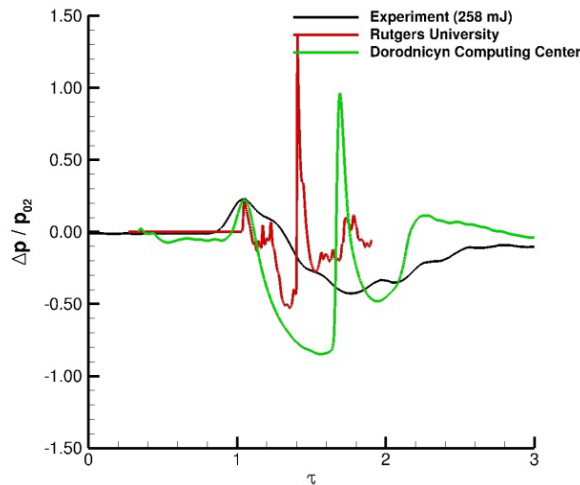


Figure 2-13: Centerline Pressure vs. Time (258 mJ).

Notwithstanding the differences between the computations and experiment evident in the centerline pressure vs. time, the relationship between the instantaneous drag coefficient C_d based upon the pressure on the sphere frontal surface and the flowfield structure can be qualitatively described in Figure 2-14 to Figure 2-18. The computed C_d vs. time for $\Delta T/T_\infty = 9$ is shown in Figure 2-14. Four points labelled *A* through *D* are identified. At point *A* the drag coefficient value is halfway between the undisturbed value and the first peak associated with the impact of the transmitted blast wave on the sphere centerline. The heated region (plasma) has just reached the blunt body shock (Figure 2-15). At point *B* the transmitted blast wave has impacted the sphere centerline causing the initial

peak pressure. The heated region has interacted with the blunt body shock wave resulting in a lensing forward (upstream) of the shock (Figure 2-16). A stagnation point has appeared upstream of the sphere centerline due to the lower Mach number of the heated region relative to the freestream flow. At point *C* the heated region has completely passed through the blunt body shock wave and the lensing effect has reached its maximum upstream position (Figure 2-17). This interaction generates a rarefaction wave which reduces the pressure on the sphere centerline. At point *D* the blunt body shock has begun to return to its steady state position as the heated region convects past the sphere (Figure 2-18).

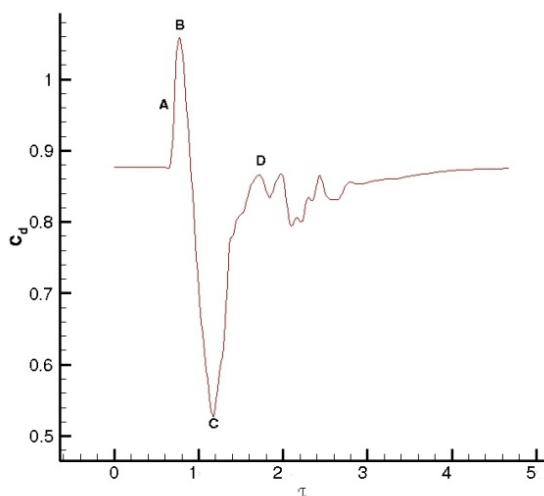


Figure 2-14: C_D vs. Time (Mortazavi and Knight).

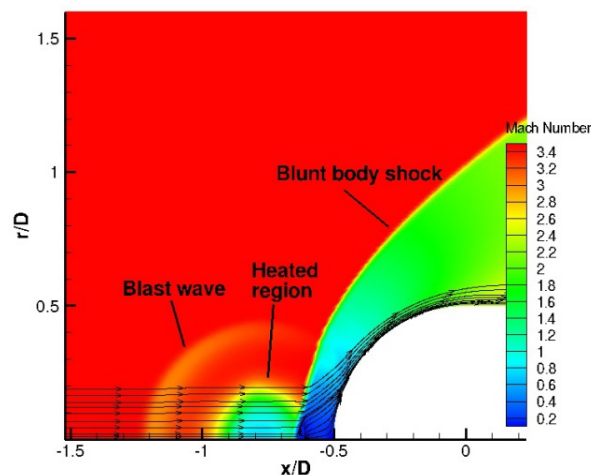


Figure 2-15: Point A.

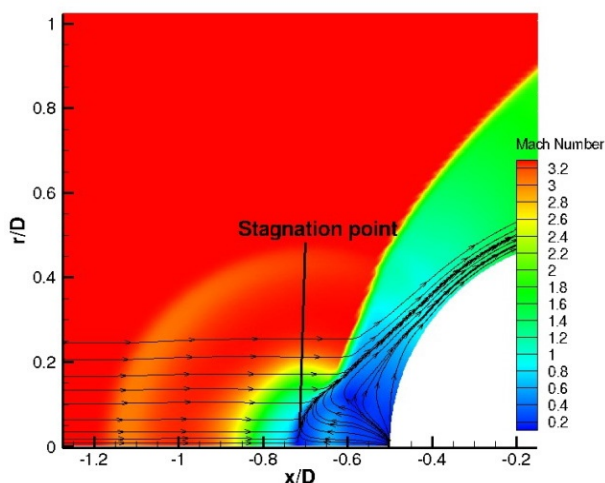


Figure 2-16: Point B.

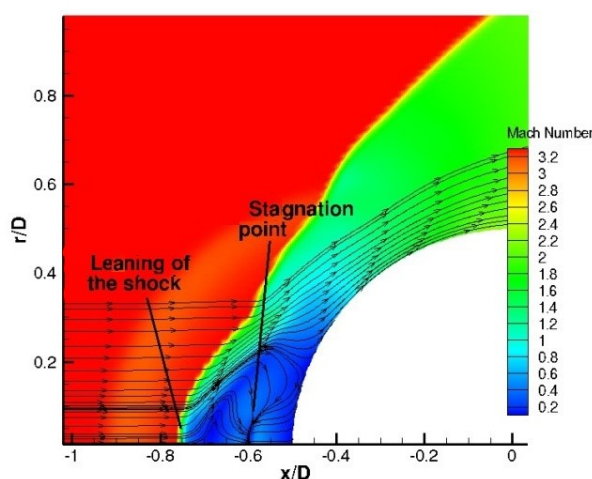


Figure 2-17: Point C.

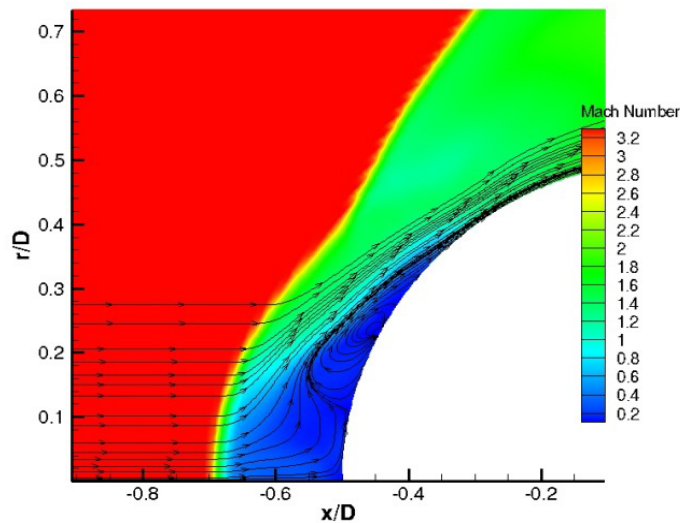


Figure 2-18: Point *D*.

The imaging of Figure 2-19 shows a spherical development of the shock, even if the hot core is non spherical. That point is discussed later in Section 2.2.5.

Very similar behavior is obtained for time dependence of stagnation pressure on axis computed by CEDRE at 13 mJ (Figure 2-20) and by MISTRAL at 14,5mJ (Figure 2-21). With MISTRAL too, Figure 2-22 shows pressure contours after an energy deposition of $E=14.5$ mJ, during $Dt = 10$ ns, inside a 3 mm³ volume, with FWHM along $z = 2$ mm, and FWHM along $r = 1.1$ mm. The air flow is at $M=3.45$ and $T_0 = 79$ K. Plots are performed 5, 15, 25 and 40 μ s after the laser breakdown.

CEDRE simulations are also available for a wide variety of deposited energy in Ref. [12]. Single energy depositions show that significant transient drag reductions are obtained, due to the interaction of the heated core, created by the energy release, with the bow shock. When the deposition is repeated, cumulative effects are important and quasi-steady or unsteady flow regimes are obtained, depending on the power and repetition frequency. This behavior is similar to that obtained with supersonic spiked blunt bodies, acting like a laser spike. This system can lead to 15% – 20% fuel savings, depending on the energy deposition efficiency.

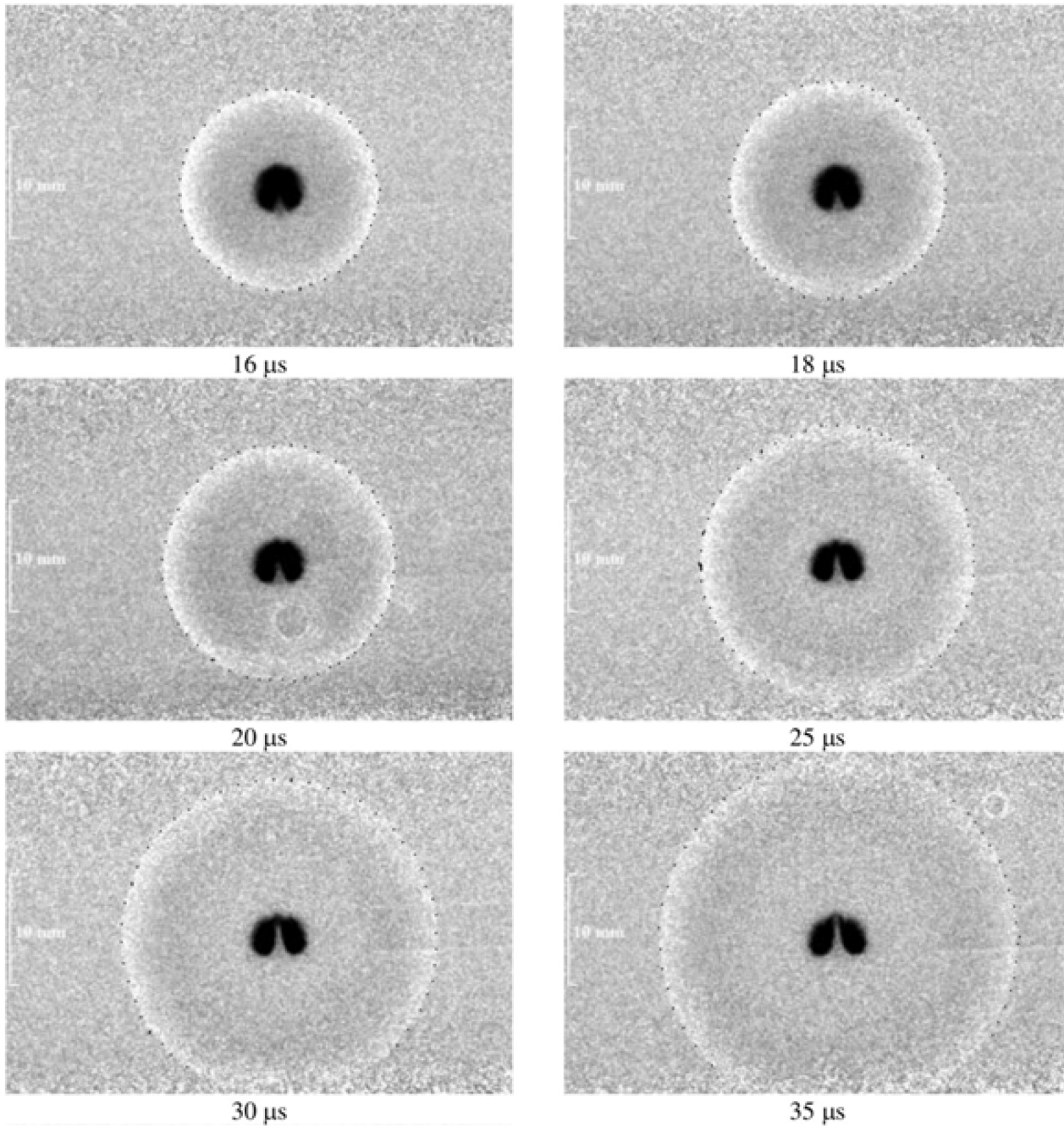


Figure 2-19: Filtered Rayleigh Scattering Image of 50 mJ Laser Discharge in Ambient Air [13].

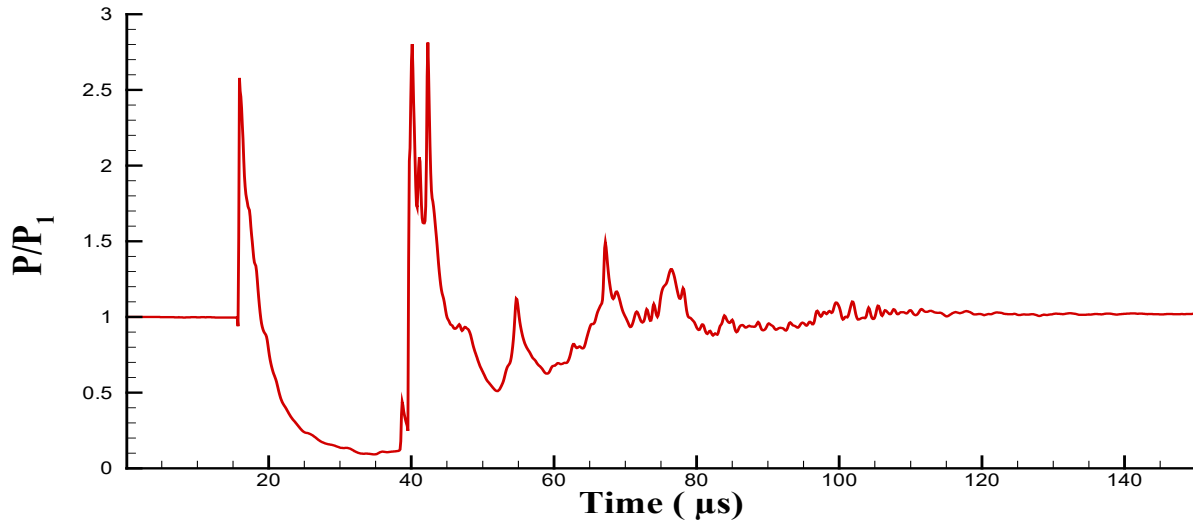


Figure 2-20: Time Evolution of the Stagnation Pressure on Axis Calculated with CEDRE. The laser energy deposition $\Delta E = 13$ mJ starts at $t = 0$.

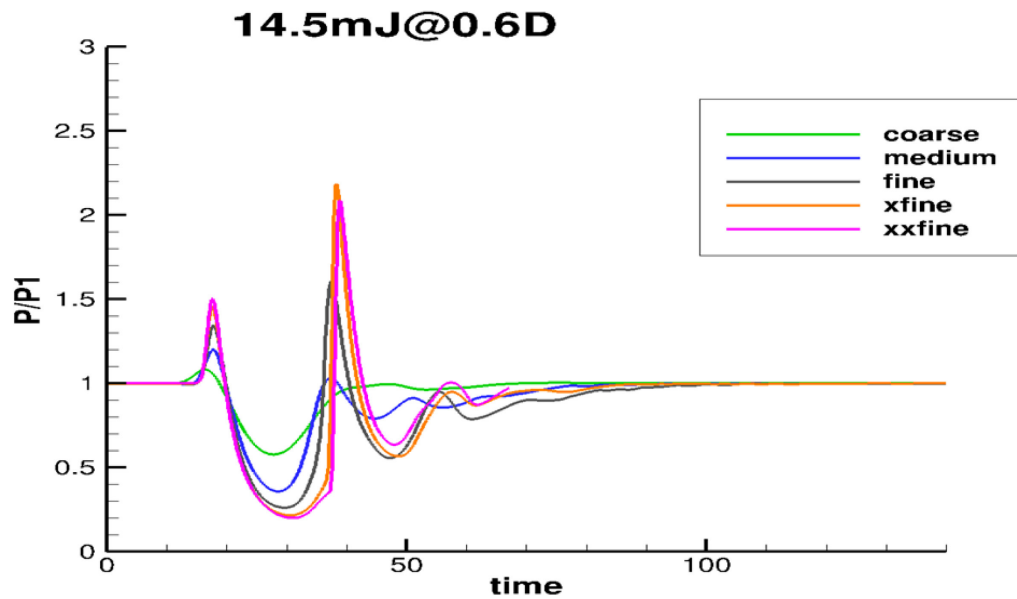


Figure 2-21: Time Evolution of the Stagnation Pressure on Axis Calculated with MISTRAL. The laser energy deposition starts at $t = 0$. The sensitivity to the mesh refinement is indicated from very fast simulation to the more detailed one.

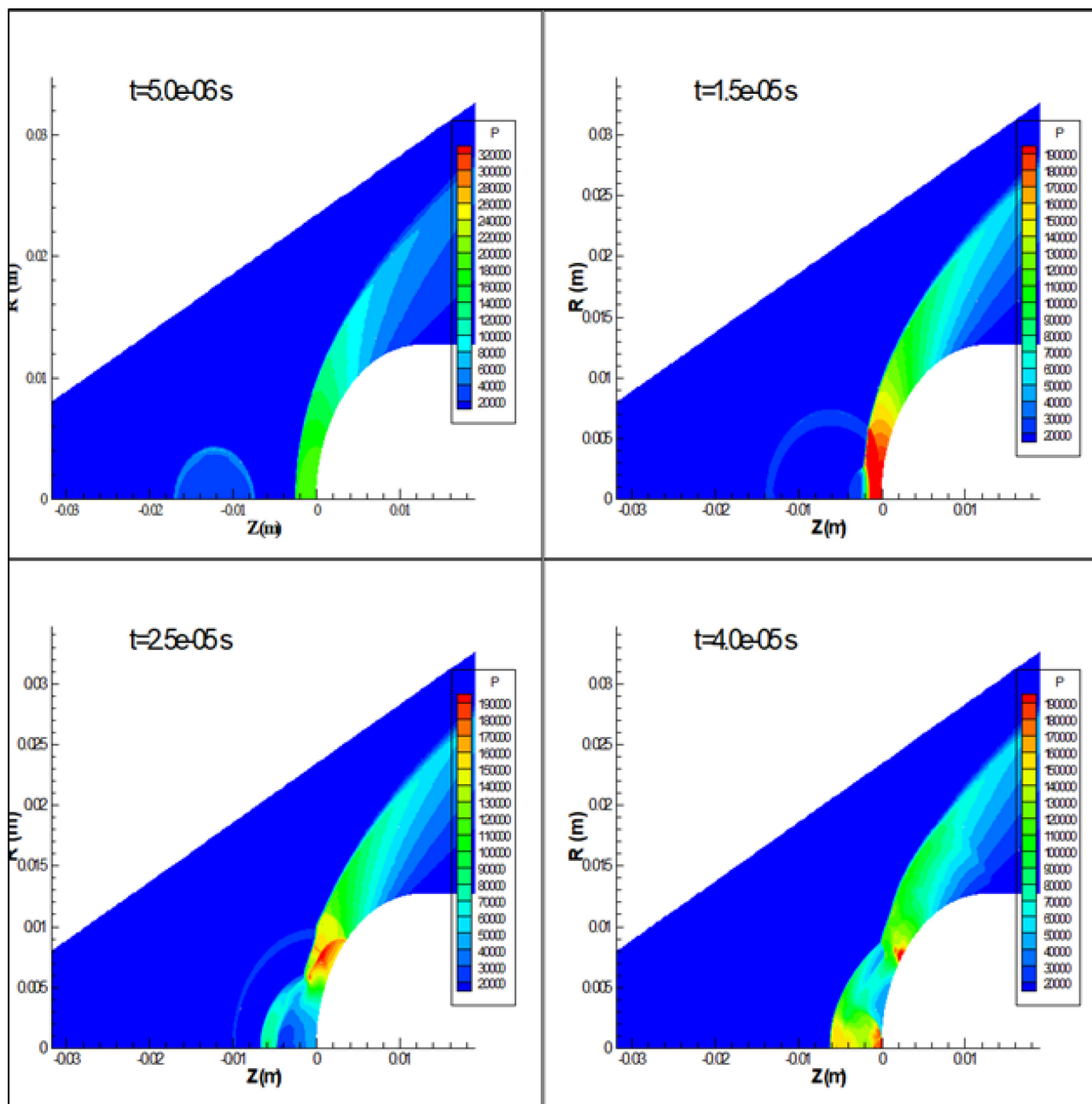


Figure 2-22: Pressure Contours after an Energy Deposition of $E = 14.5$ mJ, during $Dt = 10$ ns, Inside a 3 mm^3 Volume, with FWHM along $z = 2$ mm, and FWHM along $r = 1.1$ mm. The air flow is at $M=3.45$ and $T_0 = 79$ K. Plots are performed 5, 15, 25 and 40 μs after the laser breakdown.

2.2.5 Conclusions and Recommendations

The present study focused on the simulation of a laser discharge upstream of a sphere in supersonic flow and the interaction of the heated region (plasma) with the flow field of the sphere. Two independent computations were performed based upon a simplified model comprising the unsteady Euler equations for a perfect gas with the laser discharge modelled as an instantaneous increase in static temperature (and static pressure) in a spherical region defined by the laser focal volume. The instantaneous temperature increase ΔT was determined by matching the initial peak pressure on the sphere centerline due to the impact of the transmitted blast wave on the sphere.

The simulations fail to accurately predict the pressure vs. time history of the interaction of the laser discharge with the sphere for three different laser discharge energies ranging from 13 mJ to 258 mJ. Two possible explanations may be offered for the disagreement. First, the assumption of perfect gas is questionable. It is well known that a portion of the absorbed laser energy is channeled into vibrational excitation and thermochemical reactions. Neither effect is represented in the perfect gas simulation. In particular, the extremely small fraction of laser discharge energy required to match the initial peak pressure for the finest grid simulations of Mortazavi and Knight (e.g., ranging from 0.436% to 1.081%) suggests the heated region (plasma) generated by the laser discharge is not in thermochemical equilibrium. Second, the topological model of the laser discharge as a spherical region of uniform temperature increase is far too simple. The structure of the plasma evolution for a 50 mJ laser discharge in ambient air is shown in Figure 2-19 [13]. The structure evolves into a toroidal vortex whose axis is aligned with the direction of the incident laser beam. In the experiment of Adalgren et al. [7], the incident laser beam was directed perpendicular to the freestream flow thus resulting in a non-spherical plasma interacting with the sphere.

It is therefore evident that the perfect gas Euler equation modelling of the laser discharge as an initially spherical region of heated gas subsequently interacting with the sphere (or likely any other aerodynamic body) is incapable of a priori accurate prediction of the time-dependent surface pressure and drag. The following recommendations are presented:

- Fully three-dimensional, viscous, thermochemically non-equilibrium models of laser discharge in quiescent air be developed and validated through comparison with experimental data including spatial and temporal measurements of thermochemical states (translational-rotational temperature, vibrational temperature), species and flowfield velocity.
- Experiments be developed for detailed measurements of spatial and temporal development of surface pressure for simplified geometries (e.g., cone, hemisphere cylinder).

2.3 MICROWAVE DISCHARGE

2.3.1 Experiment

The experiment of Lashkov et al. [8] examined the effect of the interaction of a microwave discharge with a hemisphere cylinder at Mach 2.1. The experimental conditions are indicated in Table 2-6. The experimental configuration is shown in Figure 2-23 and the wind tunnel arrangement in Figure 2-24. A hemisphere cylinder is mounted on a sting in the test section of the Mach 2.1 wind tunnel at St Petersburg State University. A pressure transducer is located on the hemisphere centerline and provides a time history of surface centerline pressure.

Table 2-6: Experimental Conditions.

Property	Parameter	Value
Freestream	Mach number	2.1
	Static pressure p_∞ (Torr)	26.0
	Static temperature T_∞ (K)	154
Microwave	Electric field E_o (kV/cm)	2.3
	Wavelength λ (cm)	3.33
	Frequency (GHz)	9.0
	Pulse duration (μ s)	2.0
	Focal point x_o (cm)	-3.5
Hemisphere-cylinder	Diameter D (mm)	20

A microwave beam is focused at a distance $x_o = 3.5$ cm upstream of the stagnation point. The microwave pulse is generated by a 10 GHz klystron connected to a waveguide and beamed to a parabolic mirror within the test section which focuses the beam to the position upstream of the hemisphere cylinder (Figure 2-25). Experimental diagnostics are time history of surface pressure at the hemisphere centerline and Schlieren imaging.

An example of the flow field structures due to the interaction of the microwave-generated plasma with the hemisphere cylinder is shown in Figure 2-26. Schlieren images are displayed at six successive instants of time subsequent to the microwave discharge. At $t = 30 \mu$ s the plasma has reached the blunt body shock and begun to deform the shock wave. At $t = 45 \mu$ s the plasma has partially penetrated the shock causing a lensing forward of the shock wave. At later times the shock lensing effect continues until the plasma has completely passed through the shock wave and convected downstream. The effect is qualitatively similar to the interaction of the laser discharge with the sphere.

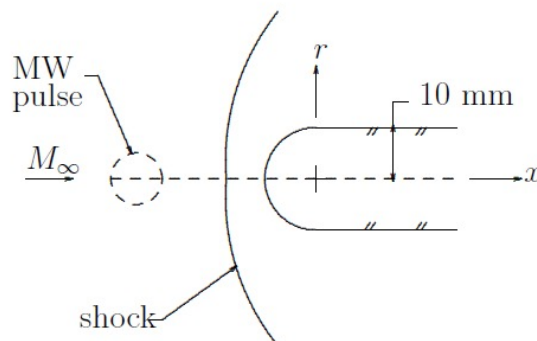


Figure 2-23: Experiment.

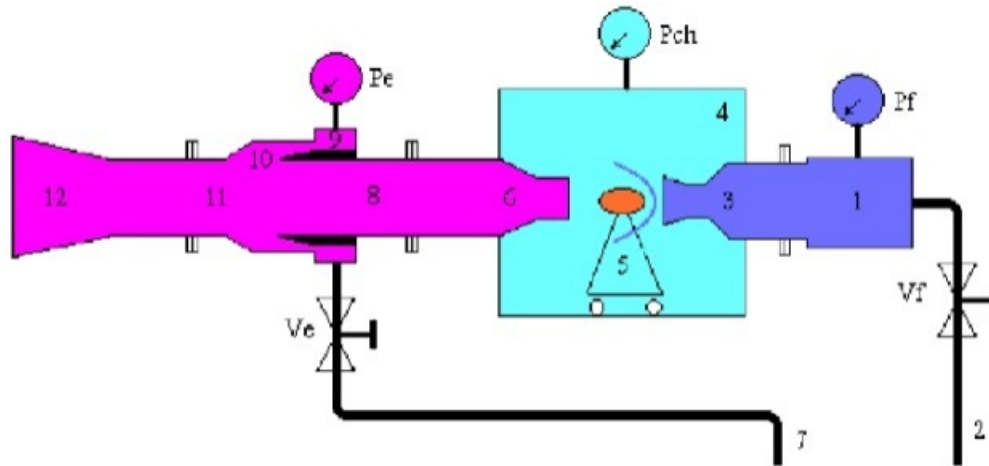


Figure 2-24: Wind Tunnel.

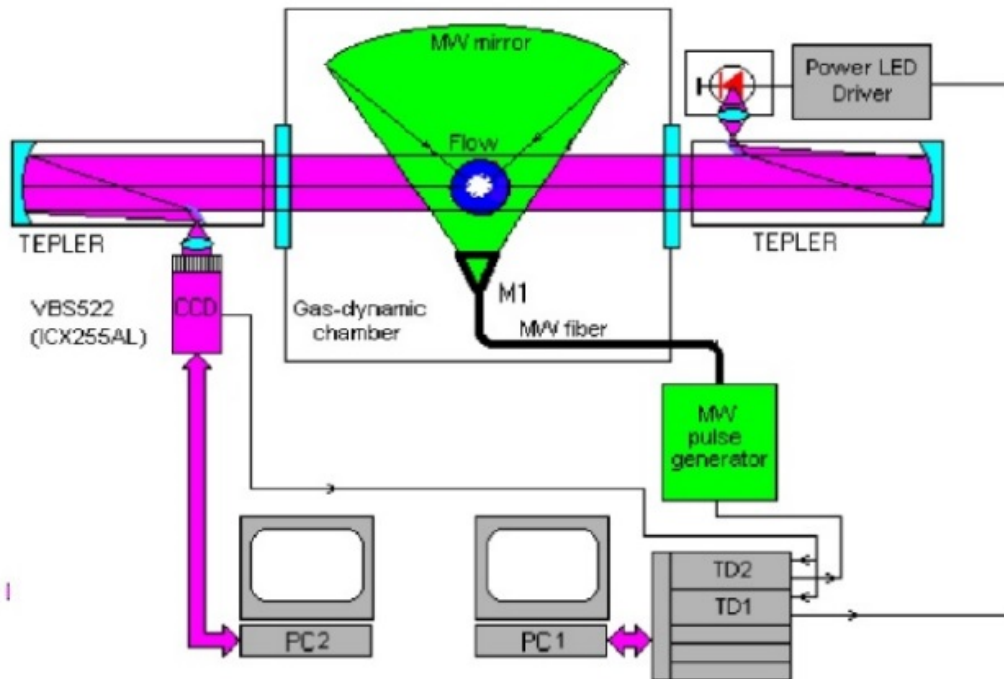


Figure 2-25: MW Discharge Apparatus.

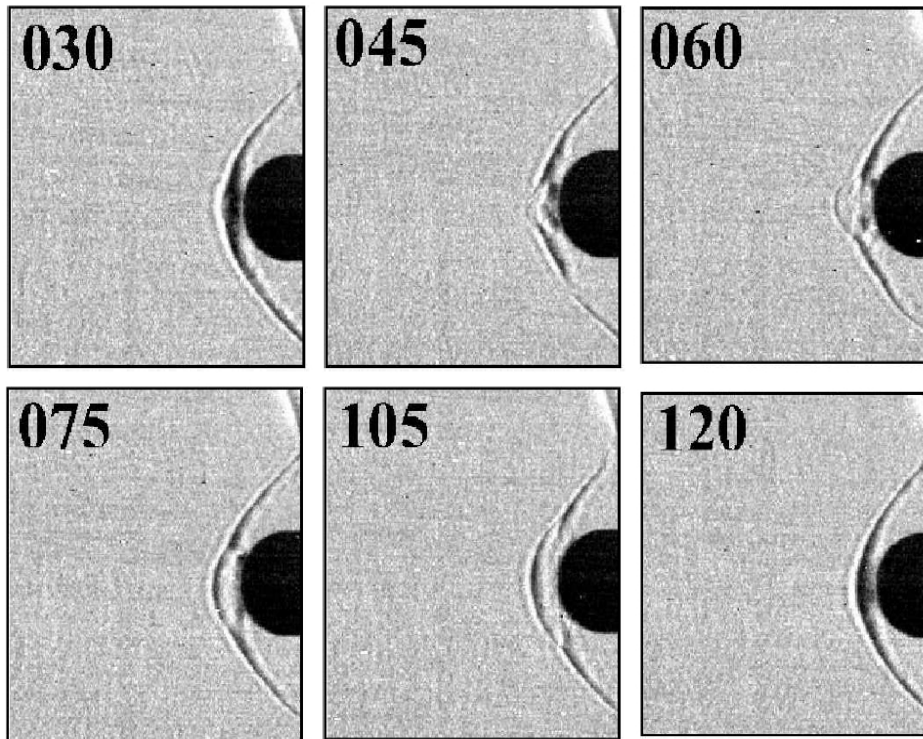


Figure 2-26: Schlieren Images (Numbers Indicate Time in μs).

2.3.2 Participants

Simulation of the experiment was performed by Rutgers University (Doyle Knight).

2.3.3 Methodology

The simulations are based on a fully three-dimensional non-equilibrium gas dynamic model for microwave energy deposition in air. The flow is assumed inviscid and non-heat conducting. The thermochemistry model includes 23 species and 238 reactions. Complete details of the governing equations, thermochemistry model and reactions are presented in Ref. [14]. The algorithm uses Roe's method for the inviscid fluxes with extension to multiple species and second order accurate reconstruction. Temporal integration is performed using a second order accurate Runge-Kutta method. The code was developed at Rutgers University and is written in C++ utilizing Message Passing Interface (MPI).

The computational domain ABCDA is displayed in Figure 2-27. The line AB is the axis of symmetry. The outer surface BC is fixed at the freestream conditions. The downstream boundary CD uses a zero normal gradient boundary condition. The body surface DA is a slip boundary. Simulations were performed for two separate grids to assess the computational accuracy. Details are presented in Table 2-7.

Prior to the initiation of the microwave discharge, the flow field is converged to steady state. The computed pressure contours are shown in Figure 2-28. The computed ratio of standoff distance (measured from the center of the hemisphere along the axis of symmetry) to the hemisphere diameter D is in excellent agreement with experiment.

Table 2-7: Details of Grids.

Quantity	Grid No. 1	Grid No. 2
No. grid points along body	276	550
No. grid points normal to body	90	180
Total no. of grid points	24,840	99,000
Δr_{min} (cm)	4.00×10^{-2}	2.00×10^{-2}
Δr_{max} (cm)	4.00×10^{-2}	2.00×10^{-2}
Δs_{min} (cm)	1.13×10^{-2}	0.57×10^{-2}
Δs_{max} (cm)	5.86×10^{-2}	2.95×10^{-2}

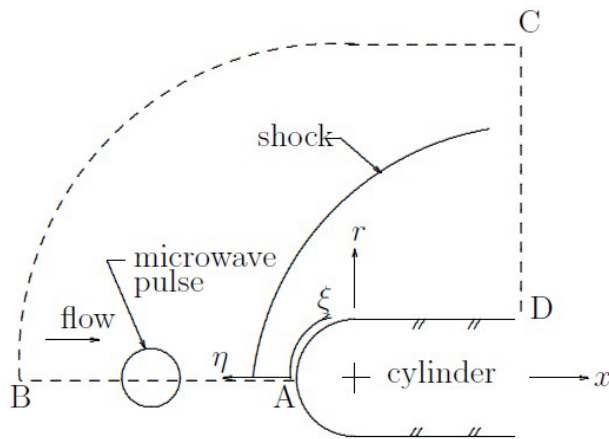


Figure 2-27: Computational Domain.

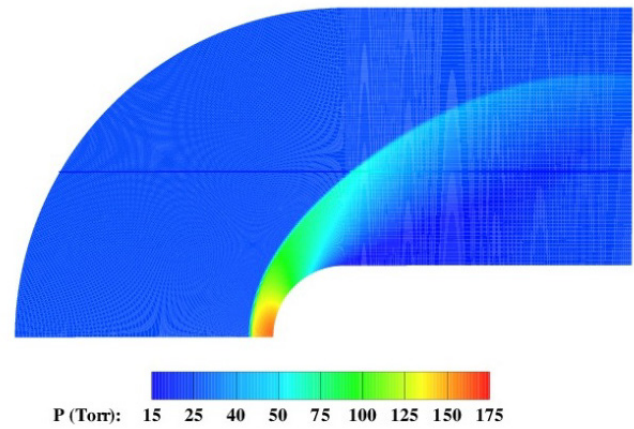


Figure 2-28: Pressure Contours (Steady State).

The microwave discharge is modelled as a spatially and temporally variable electric field $E(x,t)$ defined by:

$$E(x,t) = E_o \cos k(x-x_o) \cos kr \text{ for } kr \leq \pi/2 \text{ and } -\pi/2 \leq k(x-x) \leq \pi/2 \text{ and } t \leq \tau_o$$

and zero otherwise where $k = 2\pi/\lambda$ and λ is the microwave wavelength. The spatial form of the electric field conforms to the experimental measurements of Kolesnichenko et al. [15] for a single microwave-generated plasma.

2.3.4 Results

The computed centerline pressure vs. time is displayed in Figure 2-29. The frequency bandwidth of the computation is significantly greater than the pressure transducer, and therefore the computed pressure time series was filtered in accordance with the transducer manufacturer's recommendation (i.e., filtered at one-fifth of the natural frequency of 150 kHz). The filtered computed centerline pressure vs. time is displayed in Figure 2-30 for the two simulations together with the experimental data. Good agreement is obtained between the computation and experiment.

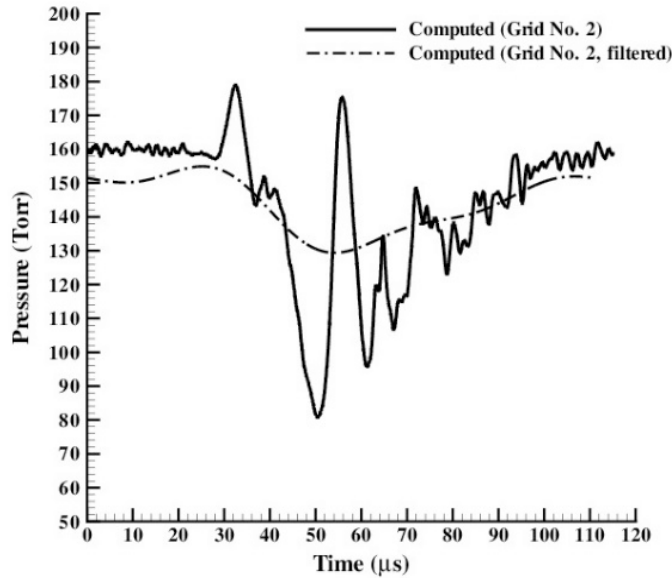


Figure 2-29: Computed p vs. Time.

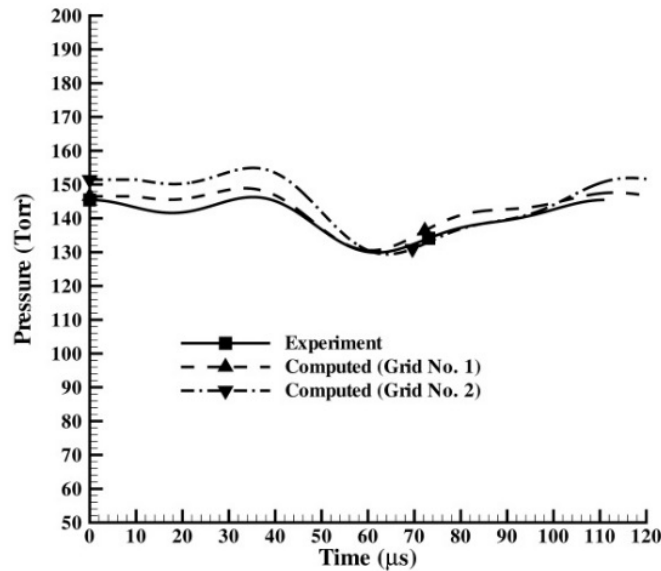


Figure 2-30: Computed and Experimental p vs. Time.

Computed pressure contours at selected times are displayed in Figure 2-31 to Figure 2-34. At $t = 25 \mu\text{s}$ the blast wave generated by the microwave discharge has reached the blunt body shock (Figure 2-31). At $t = 42 \mu\text{s}$ the plasma has begun penetration of the blunt body shock causing a lensing forward of the shock (Figure 2-32). A high pressure region forms immediately ahead of the hemisphere centerline due to the impact of the transmitted blast wave on the hemisphere. At $t = 50 \mu\text{s}$ the plasma has fully penetrated the blunt body shock and formed a

recirculation region (toroidal vortex), moving the stagnation point off the hemisphere surface and reducing the surface pressure (Figure 2-33). At $t = 75 \mu\text{s}$ the plasma has convected along part of the hemisphere and the shock has relaxed to its initial location (Figure 2-34). The flow structures are similar to the interaction of the laser discharge with a blunt body.

Computed electron density contours at selected times are shown in Figure 2-35 to Figure 2-38. At $t = 25 \mu\text{s}$ the peak electron density is $5.0 \times 10^{11} \text{ cm}^{-3}$ (Figure 2-35). This time point is $23 \mu\text{s}$ subsequent to the termination of the microwave discharge. A similar peak electron density is evident at $t = 42 \mu\text{s}$ where the plasma has begun penetration of the blunt body shock wave (Figure 2-36). The size of the plasma (somewhat arbitrarily defined as an electron concentration above 10^{11} cm^{-3}) decreases rapidly as it completely penetrates the blunt body shock due to compression (Figure 2-37 and Figure 2-38) and gradually reduces thereafter due to recombination.

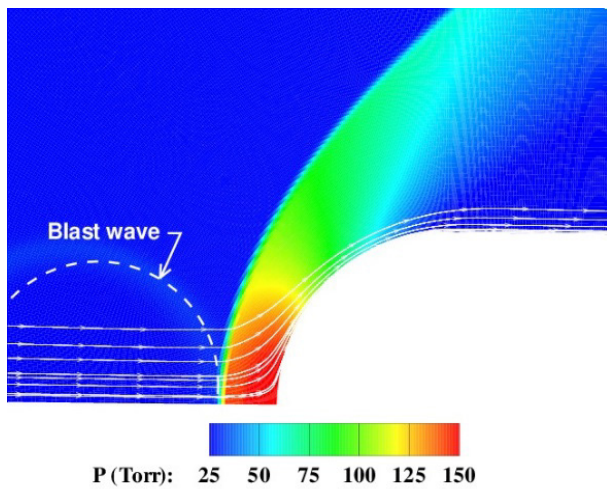


Figure 2-31: Pressure Contours ($t = 25 \mu\text{s}$).

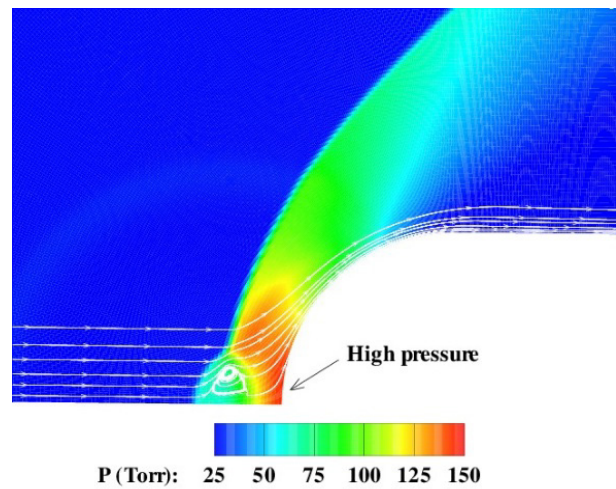


Figure 2-32: Pressure Contours ($t = 42 \mu\text{s}$).

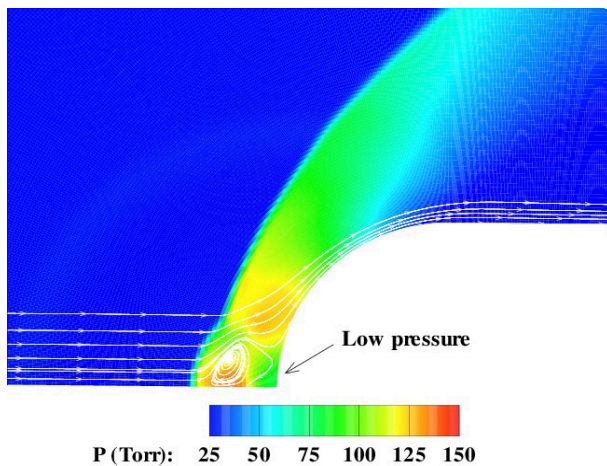


Figure 2-33: Pressure Contours ($t = 50 \mu\text{s}$).

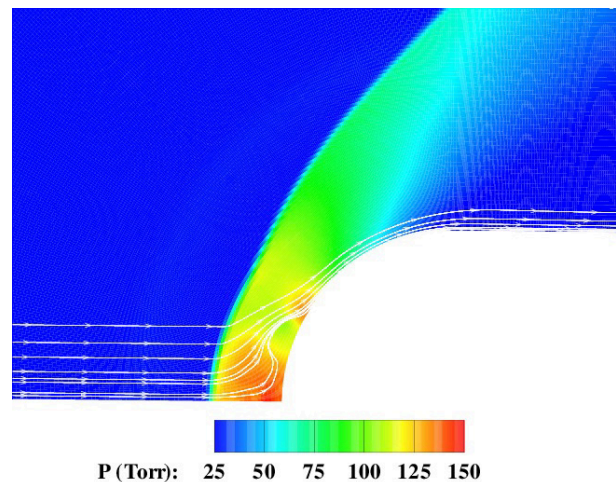


Figure 2-34: Pressure Contours ($t = 75 \mu\text{s}$).

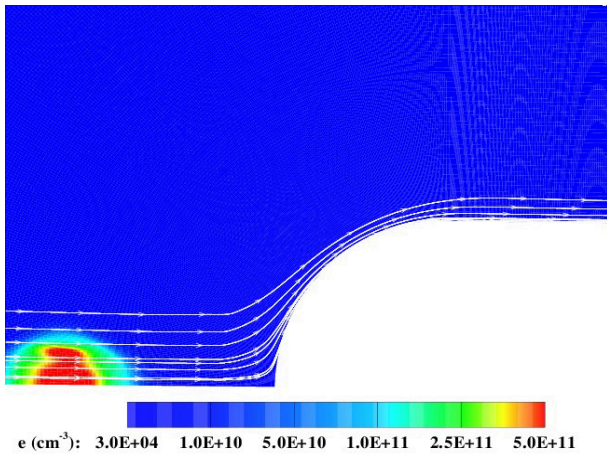


Figure 2-35: Electron Density ($t = 25 \mu\text{s}$).

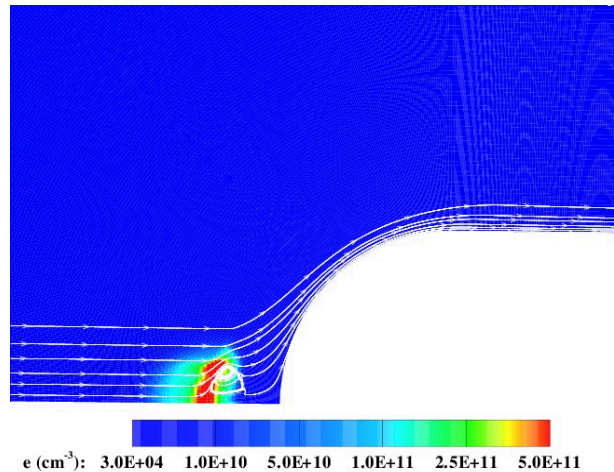


Figure 2-36: Electron Density ($t = 42 \mu\text{s}$).

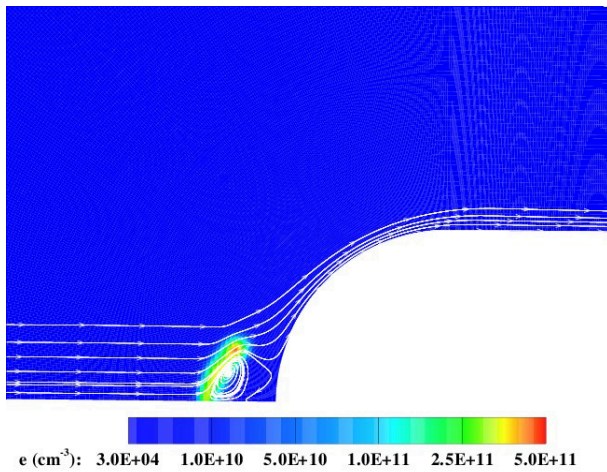


Figure 2-37: Electron Density ($t = 50 \mu\text{s}$).

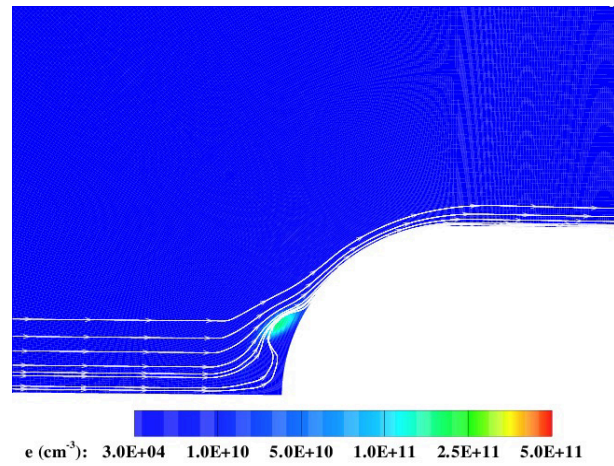


Figure 2-38: Electron Density ($t = 75 \mu\text{s}$).

2.3.5 Conclusions and Recommendations

A fully three-dimensional non-equilibrium simulation of the interaction of a microwave-generated plasma with a hemisphere cylinder at Mach 2.1 was performed. Good agreement is observed between the computed and experimental centerline surface pressure. Qualitative agreement is also achieved in the flow field structure development in time.

The comparison between computation and experiment is limited, however, to a single point pressure time history and Schlieren imaging. The following recommendations are presented:

- Detailed experimental diagnostics of the interaction of a microwave-generated plasma with simple geometric bodies is needed. Important measurements include panoramic surface pressure, and temporally and spatially resolved spectroscopic data.

- Further development of simulation capability is needed to include coupling of the electromagnetic radiation with the non-equilibrium fluid dynamics using Maxwell's equations, and species diffusion and Lorentz forces in the governing equations.

2.4 TRANSFER OF MICROWAVE ENERGY ALONG A FILAMENT PLASMA COLUMN IN AIR

2.4.1 Introduction

A sufficiently intense femtosecond laser pulse can propagate in air in the form of a filamentary pulse that maintains a high intensity over several hundreds of meters [16]. This nonlinear propagation regime results from a complex interplay between diffraction, the optical Kerr effect, high-field ionization, plasma defocusing and other nonlinear effects. A column of weakly ionized plasma, of free electron density $n_e \sim 10^{17} \text{ cm}^{-3}$, is left in the wake of the filamentary pulse. This plasma column can lead to many applications. It is the source of a forward oriented conical emission of pulsed THz radiation [17]. It can form a low-jitter fast spark gap [18]. It can also trigger and guide meter long electric discharges [19], allowing contactless transfer of large currents [20]. In turn, long-lived guided discharges can act as virtual antennas [21] or could improve the aerodynamics of fast-moving object through atmosphere [12], [22].

Considering that, in a supersonic flow, the energy deposition ahead is a promising way to create an aerodynamic rod and to mitigate the shock around an object, according to Sections 2.2 and 2.3, it appears that realistic conditions of flight would demand to upscale the conditions, namely the energy deposited and the size of the heated volume, as given in Table 2-1 and Table 2-6. Laser induced filamentary ionization of air is essentially dependent of the instant power and the practical cases are obtained in reducing the pulse duration, the laser energy in the pulse remaining rather modest. Options for delivering more energy, and creating a significant heated volume, might be to couple a nanosecond IR laser beam to femtosecond laser filaments [23] or to superimpose a microsecond electrical discharge to femtosecond laser filaments [24]. The latter case involves a pole wearing electrical feeding wire and electrode. For pure Microwave (MW) excitation, the geometry proposed in Figure 2-24 and Figure 2-25 includes an antenna and a large mirror which are out of the blunt body; such an assembly can sit close to the walls of a wind tunnel while heating an elongated volume in the main flow but is not compatible with free flight.

2.4.2 Experiment

The coupling of a long-duration energetic MW pulse to a linear plasma column was then considered to energize the air flow inward. The concept was developed of a device installed at the nose of a flying body, made of a transparent axial zone, allowing the femtosecond laser beam to pass through and to focus on a line, and of a coaxial compact MW applicator, the laser and the MW source being hidden in the body. Prior to test a device in a wind tunnel, it has been planned to install the MW applicator and the laser beam in quiet atmospheric air. The objective of the experiment was to demonstrate the transfer of microwave energy along a filament plasma column in air. Preliminary tests of feasibility were performed, using CST Microwave studio[®] (2010 edition) to model the MW applicator, the pre-plasma column being described using a Drude model. First insight was that an efficient coupling was obtained for a mm-size or more column under 2.4 GHz excitation, due to surface waves propagating over five wavelengths or so. The hydrodynamics numerical simulation was not in the scope of the work.

In the experimental conditions, an oscillating RF electric field excites an electromagnetic TM wave with maximum electric field amplitude located at the interface between a small section of a multi-filament plasma column and the non-ionized external medium [25], [26]. This surface wave propagates out of the excitation region, allowing the transfer, over a significant distance, of microwave energy to the plasma in the form of longitudinal oscillations. The propagation distance should reach several meters in the case of lower-frequency electromagnetic waves. Guided propagation of microwave radiation by filaments using a different approach has been discussed previously both theoretically [27], [28], [29] and experimentally [30], [31], [32]. It is suggested that a self-sustained plasma antenna could be realized if sufficient microwave or VHF power is injected.

Figure 2-39 shows the experimental arrangement. The plasma channel is created by filamentation of intense laser pulses at 800 nm. Such laser pulses with 200 mJ energy and adjustable duration between 50 fs and 1 ps are delivered by a multi-terawatt CPA laser source (ENSTAmobile) at a rate of 10 Hz. When focused in air with a lens of 5 m focal length, they create a bundle of ionized filaments merging into a cylindrical plasma of average density $n_e \sim 10^{17} \text{ cm}^{-3}$, roughly 1 mm in diameter and 1 – 2 m in length (see Figure 2-40) [33]. A microwave field is delivered to a small section of the plasma using a well-known source called *surfatron* [34]. The surfatron consists of a commercial microwave generator (magnetron) emitting continuously at 2.45 GHz with a maximum power of 500 W (GMP 12 KED by SAIREM S.A.). The microwave is injected as a TM mode via a capacitive coupler in a 40 mm long, annular brass cavity surrounding the filament bundle, itself contained in a fused silica tube. Transfer of microwave to the plasma region occurs via a leak in the annular cavity, an oscillating longitudinal E-field being imposed across the launching gap. The diameter of the surfatron hole is 6 mm. In our experiment, the microwave radiation was produced continuously, while the laser operated in single-pulse mode. No provision was made to synchronize the time of arrival of the laser pulse with a cycle of the microwave field. To measure the transfer of microwave energy to the filament plasma, we detected the induced longitudinal electronic currents in the plasma by using a fast I-dot probe placed outside the surfatron cavity, at a distance D . The I-dot probe allows the contactless measurement of longitudinal currents in the plasma [35]. It was connected with a shielded 50- Ω cable to an oscilloscope of 10-GHz bandwidth. No signal was detected by the I-dot probe in the absence of laser filament, even at maximum microwave power.

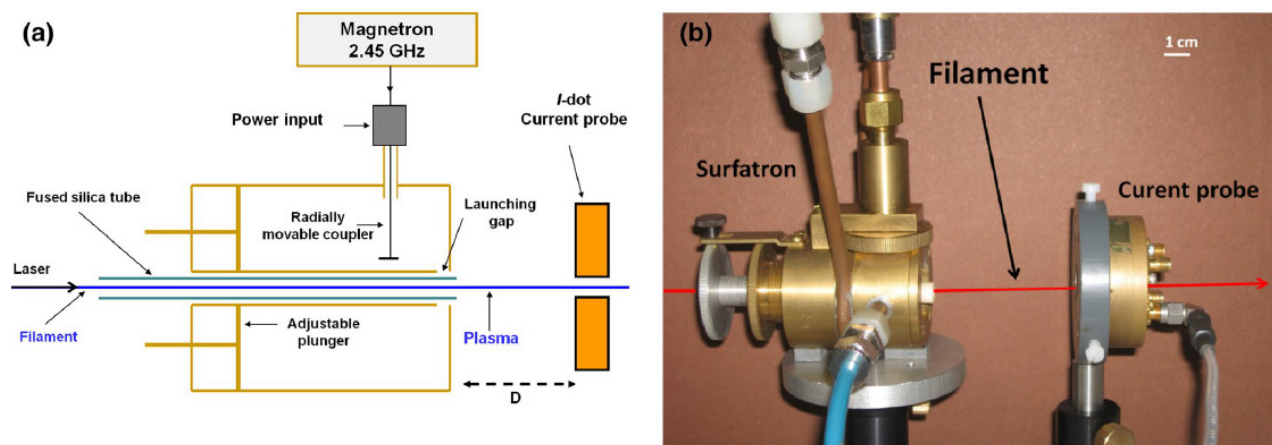


Figure 2-39: (a) General Setup, (b) Photograph of the Experiment.

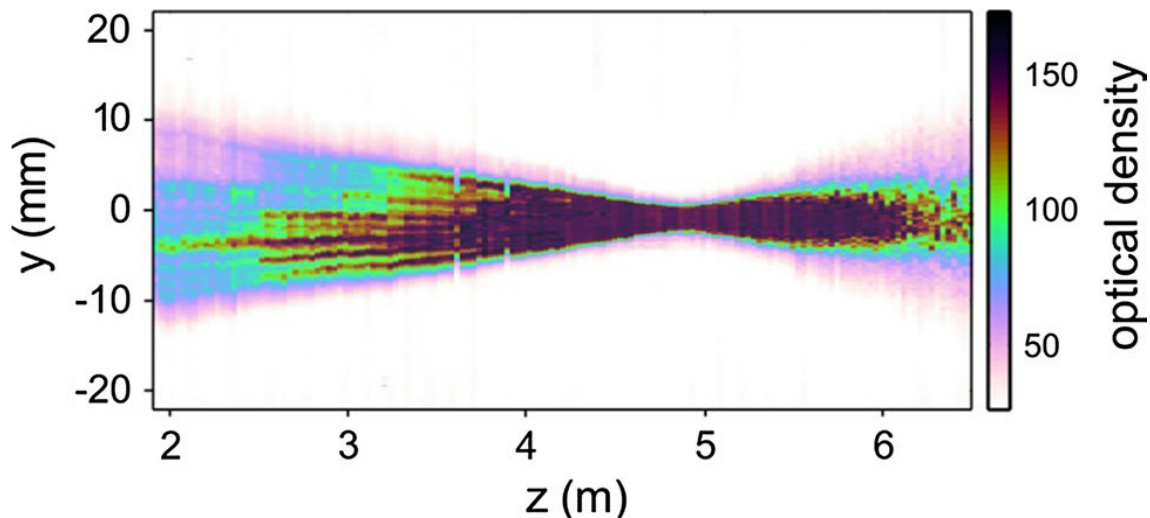


Figure 2-40: Side View (yz , $x = 0$ Plane) of the Intensity Map of a Multifilament Bundle. The laser is impinging from the left. Dark colors (color scale > 100) correspond to ionized regions.

2.4.3 Participants

The experiment was performed at the Laboratoire d'Optique Appliquée (LOA), a laboratory of Ecole Nationale Supérieure des Techniques Avancées and Ecole Polytechnique, in Palaiseau, France, jointly with the Laboratoire de Physique des Plasmas (LPP) of Ecole Polytechnique, Palaiseau, France.

2.4.4 Results

Figure 2-41 presents the signals registered in the presence of the filaments by the I-dot probe for different microwave powers at a fixed position $D = 6.3$ cm. Since there is no synchronization between the laser pulse and the surfatron, different laser shots arrived randomly in the cavity at different phases of the microwave field. We have selected from a large number of shots the highest signals recorded for a given microwave value. They correspond to the arrival of the pulse at the positive or negative peak of a microwave cycle. The weak signal recorded in the absence of microwave (black curve) corresponds to the longitudinal oscillation that is imparted to the plasma during its formation, due to the ponderomotive force of the laser pulse [17]. We have measured the maximum signal detected by the I-dot probe as a function of distance D . The maximum signal divided by the maximum signal in the absence of microwave field is plotted in Figure 2-42 for a microwave injected power of $P = 100$ W. It shows an amplification of the longitudinal current over a length longer than 15 cm beyond the exit of the surfatron.

To interpret the flow of excitation along the filament, we consider the propagation of a surface-guided TM wave. It is then possible to see the influence of the plasma column radius. Figure 2-43 shows the calculated attenuation of the electric field component for two typical radii of the plasma. Here $v_e = 15 \times 10^{12} \text{ s}^{-1}$. The first case: $a = 100 \text{ }\mu\text{m}$, models a single filament. The second case $a = 450 \text{ }\mu\text{m}$ models a bundle of focused filaments and corresponds to the realistic case of our experimental conditions. The amplitude of the propagating microwave field calculated for a mm diameter plasma is similar to the experimental curve of Figure 2-42 and supports the hypothesis of a surface wave coupling. Assuming a perfect coupling for $a = 450 \text{ }\mu\text{m}$, we find $n_{\text{eff}} = 1.015 - 0.3203i$ and the magnitude of the longitudinal component of the electric field of the TM_0 mode at the interface is found to be $E_z = 1.2 \text{ kV/cm}$ for 100W of microwave power.

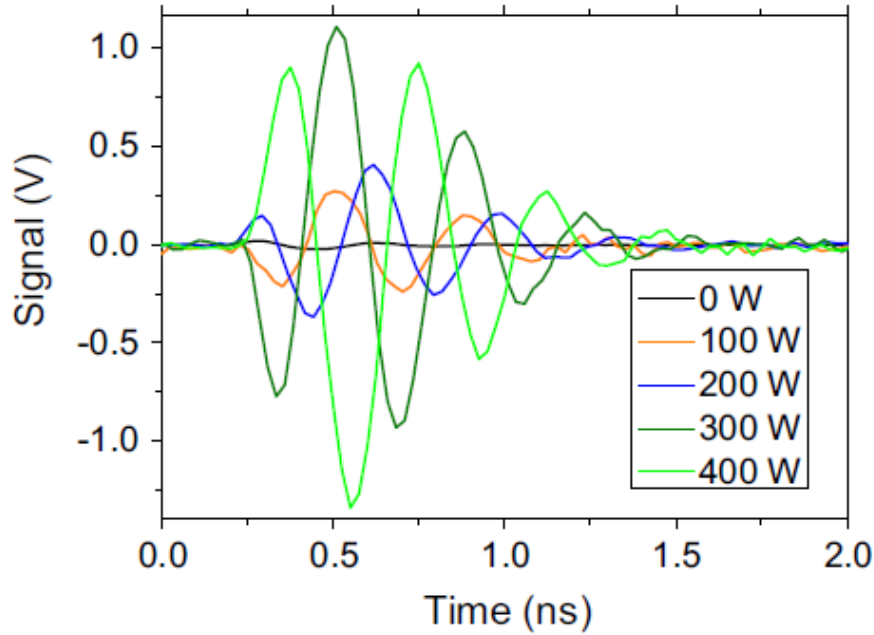


Figure 2-41: Longitudinal Current Signal Measured by the I-Dot Probe as a Function of Microwave Power in the Presence of Filament. The probe is placed away from the surfatron exit (D = 6.3cm).

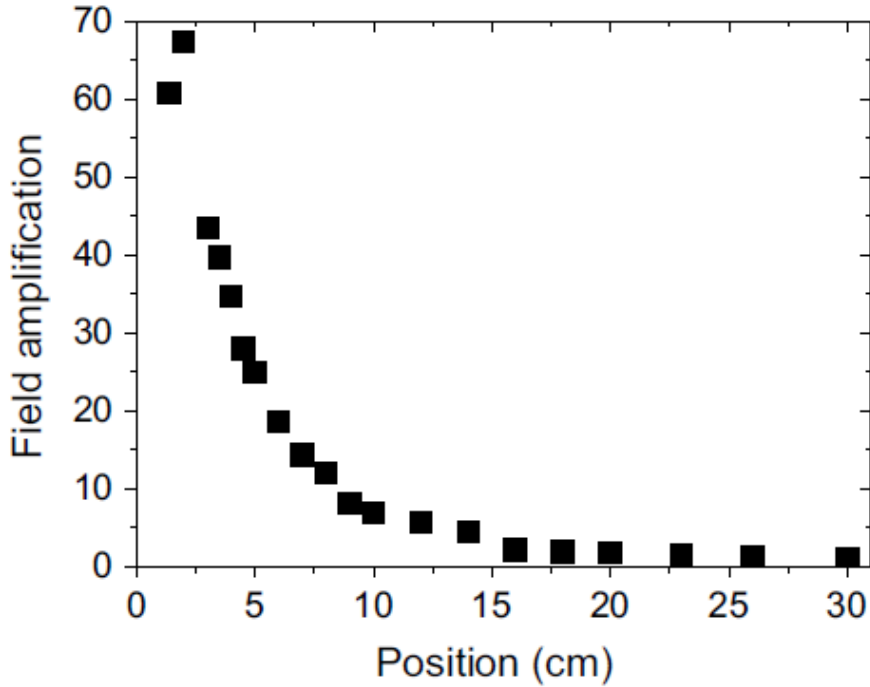


Figure 2-42: Maximum Signal Measured by the I-Dot Probe Divided by the Maximum Signal in the Absence of Microwave Field as a Function of the Position Along the Filament Measured for P = 100 W.

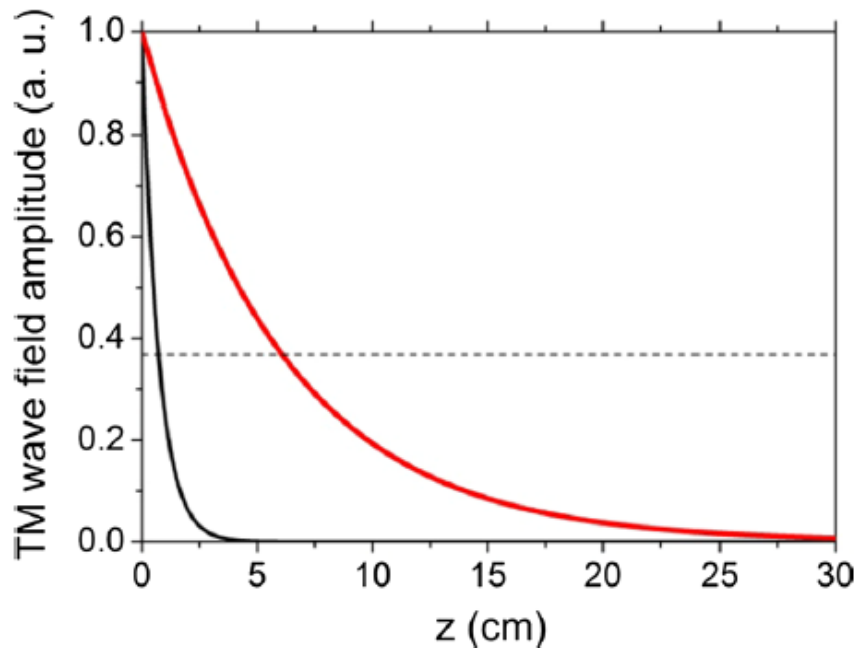


Figure 2-43: Normalized Amplitude of the Electric Field of the TM Surface Wave as a Function of Propagation Length Calculated with: $n_e = 10^{17} \text{ cm}^{-3}$; $n_0 = 1$; $\nu_e = 15 \times 10^{12} \text{ s}^{-1}$. In black $a = 100 \text{ } \mu\text{m}$ (attenuation length of 7 mm). In red $a = 450 \text{ } \mu\text{m}$ (attenuation length of 6 cm). The dashed horizontal line indicates the attenuation length defined at $1/e$.

2.4.6 Conclusions and Recommendations

In conclusion [33], evidence was shown of the coupling of MW radiation to a multi-filament plasma column and its propagation out of the excited region of the plasma in the form of a TM wave. This leads to the amplification of longitudinal oscillations of the plasma over a distance exceeding 10 cm, giving a plasma column of interest for heating air ahead a supersonic body. This transfer could reach several meters if lower frequency is injected in a larger plasma radius.

The surfatron device being compatible with installation in the nose of the body, further tests are recommended in a wind tunnel. At present, powerful ultrashort lasers are expensive and hard to handle; however the laser beam might be introduced in the body through a supporting pole. A planned evolution of these lasers to much more compact size could allow to embark them.

2.5 REFERENCES

- [1] Georgievsky, P. and Levin, V. (1988). Supersonic Flow Over Bodies in the Presence of External Energy Input, *Journal of Technical Physics*, Vol. 14, No. 8, pp. 684-687 (in Russian).
- [2] Zheltovodov, A. (2002). Development of the Studies on Energy Deposition for Application to the Problems of Supersonic Aerodynamics, Preprint No. 10-2002, Khristianovich Institute of Theoretical and Applied Mechanics, Novosibirsk, Russian Federation.

- [3] Knight, D., Kuchinsky, V., Kuranov, A., and Sheikin, E. (2003). Survey of Aerodynamic Flow control at High Speed Using Energy Deposition, AIAA Paper No. 2003-0525, American Institute of Aeronautics and Astronautics, Reston, VA, USA.
- [4] Fomin, V., Tretyakov, P., and Taran, J.-P. (2004). Flow Control Using Various Plasma and Aerodynamic Approaches (Short Review), *Aerospace Science and Technology*, Vol. 8, No. 5, pp. 411-421.
- [5] Bletzinger, P., Ganguly, B., Van Wie, D., and Garscadden, A. (2005). Plasmas in High Speed Aerodynamics, *Journal of Physics D: Applied Physics*, Vol. 38, No. 4, pp. R33-R57.
- [6] Knight, D. (2008). Survey of Aerodynamic Drag Reduction at High Speed by Energy Deposition, *Journal of Propulsion and Power*, Vol. 24, No. 6, pp. 1153-1167.
- [7] Adelgren, R., Yan, H., Elliott, G., Knight, D., Beutner, T., and Zheltovodov, A. (2005). Control of Edney IV Interaction by Pulsed Laser Energy Deposition, *AIAA Journal*, Vol. 4, No. 2, pp. 256-269.
- [8] Lashkov, V., Mashek, I., Anisimov, Y., Ivanov, V., Kolesnichenko, Y., Ryvkin, M., and Gorynya, A. (2004). Gas Dynamic Effect of Microwave Discharge on Supersonic Cone-Shaped Bodies, AIAA Paper No. 2004-0671, American Institute of Aeronautics and Astronautics, Reston, VA, USA.
- [9] Azarova, O. (2009). A Minimum Stencil Difference Scheme for Computing Two-Dimensional Axisymmetric Flows: Examples of Pulsating Flows with Instabilities, *Journal of Computational Mathematics and Mathematical Physics*, Vol. 49, No. 4, pp. 734-753.
- [10] Van Leer, B. (1982). Flux Vector Splitting for the Euler Equations, *Lecture Notes in Physics*, Vol. 170, pp. 507-512.
- [11] Scott, T., Dieudonné, W., and Spel, M. (2004). MISTRAL: CONUS Debut Flow Field and Heat Transfer Calculations, 34th AIAA Fluid Dynamics Conference and Exhibit, AIAA-2004-2423.
- [12] Elias, P.-Q. (2015). Numerical Simulations on the Effect and Efficiency of Long Linear Energy Deposition Ahead of a Supersonic Blunt Body: Toward a Laser Spike, *Aerospace Lab. 10*, 03.
- [13] Adelgren, R. (2002). Localized Flow Control with Energy Deposition, PhD Thesis, Department of Mechanical and Aerospace Engineering, Rutgers University – New Brunswick, New Jersey, USA.
- [14] Knight, D., Kolesnichenko, Y., Brovkin, V., Khmara, D., Lashkov, V., and Mashek, I. (2009). Interaction of Microwave-Generated Plasma with a Hemisphere Cylinder at Mach 2.1, *AIAA Journal*, Vol. 47, No. 12, pp. 2996-3010.
- [15] Kolesnichenko, Y., Brovkin, V., Leonov, S., Krylov, A., Lashkov, V., Mashek, I., Gorynya, A., and Ryvkin, M. (2001). Investigation of AD-Body Interaction with Microwave Discharge Region in Supersonic Flows, AIAA Paper No. 2001-0345, American Institute of Aeronautics and Astronautics, Reston, VA, USA.
- [16] Couairon, A. and Mysyrowicz, A. (2007). Femtosecond Filamentation in Transparent Media, *Phys. Rep.* 441, 47.

- [17] D'Amico, C., Houard, A., Franco, M., Prade, B., Mysyrowicz, A., Couairon, A., and Tikhonchuk, V.T. (2007). Conical Forward THz Emission from Femtosecond-Laser-Beam Filamentation in Air, *Phys. Rev. Lett.* 98, 235002.
- [18] Arantchouk, L., Houard, A., Brelet, Y., Carbonnel, J., Larour, J., André, Y.-B., and Mysyrowicz, A. (2013). A Simple High-Voltage High Current Spark Gap with Subnanosecond Jitter Triggered by Femtosecond Laser Filamentation, *Appl. Phys. Lett.* 102, 163502.
- [19] Rodriguez, M., Sauerbrey, R., Wille, H., Wöste, L., Fujii, T., André, Y.-B., Mysyrowicz, A., Klingbeil, L., Rethmeier, K., Kalkner, W., Kasparian, J., Salmon, E., Yu, J., and Wolf, J.-P. (2002). Triggering and Guiding Megavolt Discharges by Use of Laser-Induced Ionized Filaments, *Opt. Lett.* 27, 772.
- [20] Houard, A., D'Amico, C., Liu, Y., André, Y.-B., Franco, M., Prade, B., Mysyrowicz, A., Salmon, E., Pierlot, P., and Cléon, L.-M. (2007). High Current Permanent Discharges in Air Induced by Femtosecond Laser Filamentation, *Appl. Phys. Lett.* 90, 171501.
- [21] Brelet, Y., Houard, A., Point, G., Prade, B., Arantchouk, L., Carbonnel, J., André, Y.-B., Pellet, M., and Mysyrowicz, A. (2012). Radiofrequency Plasma Antenna Generated by Femtosecond Laser Filaments in Air, *Appl. Phys. Lett.* 101, 264106.
- [22] Johnson, L.A. and Sprangle, P. (2015). Guiding Supersonic Projectiles Using Optically Generated Air Density Channels, *J. Appl. Phys.* 118, 123301.
- [23] Zhou, B., Akturk, S., Prade, B., André, Y.-B., Houard, A., Liu, Y., Franco, M., D'Amico, C., Salmon, E., Hao, Z.Q., Lascoux, N., and Mysyrowicz, A. (2009). Revival of Femtosecond Laser Plasma Filaments in Air By Nanosecond, *Laser Opt. Express* 17, 11450-6.
- [24] Arantchouk, L., Honnorat, B., Thouin, E., Point, G., Mysyrowicz, A., and Houard, A. (2016). Prolongation of the Lifetime of Guided Discharges Triggered in Atmospheric Air by Femtosecond Laser Filaments up to 130 μ s, *Appl. Phys. Lett.* 108, 173501.
- [25] Alshershby, M., Lin, J., and Hao, Z. (2012). Modeling of Sommerfeld Surface Waves Propagating on a Single Wire of Laser Plasma Filaments, *Appl. Phys. B* 108, 859.
- [26] Kandidov, V.P., Shlenov, S.A., and Kosareva, O.G. (2009). Filamentation of High-Power Femtosecond Laser Radiation, *Quantum Electron* 39, 205.
- [27] Musin, R., Shneider, M.N., Zheltikov, A.M., and Miles, R.B. (2007). Guiding Radar Signals by Arrays of Laser-Induced Filaments: Finite-Difference Analysis, *Appl. Opt.* 46, 5593.
- [28] Shneider, M.N., Zheltikov, A.M., and Miles, R.B. (2010). Long-Lived Laser-Induced Microwave Plasma Guides in the Atmosphere: Self-Consistent Plasma-Dynamic Analysis and Numerical Simulations, *J. Appl. Phys.* 108, 033113.
- [29] Alshershby, M., Lin, J., and Hao, Z. (2012). Numerical Analysis of Guiding a Microwave Radiation Using a Set of Plasma Filaments: Dielectric Waveguide Concept, *J. Phys. D Appl. Phys.* 45, 065102.

- [30] Châteauneuf, M., Payeur, S., Dubois, J., and Kieffer, J.-C. (2008). Microwave Guiding in Air by a Cylindrical Filament Array Waveguide, *Appl. Phys. Lett.* 92, 091104.
- [31] Bogatov, N.A., Kuznetsov, A.I., Smirnov, A.I., and Stepanov, A.N. (2009). Channeling of Microwave Radiation in a Double Line Containing a Plasma Filament Produced by Intense Femtosecond Laser Pulses in Air, *Quantum Electron.* 39, 985.
- [32] Zvorykin, V.D., Levchenko, A.O., Shutov, A.V., Solomina, E.V., Ustinovskii, N.N., and Smetanin, I.V. (2012). Long-Distance Directed Transfer of Microwaves in Tubular Sliding-Mode Plasma Waveguides Produced by KrF Laser in Atmospheric Air, *Phys. Plasmas* 19, 033509.
- [33] Prade, B., Houard, A., Larour, J. et al. Transfer of Microwave Energy Along a Filament Plasma Column in Air. *Appl. Phys. B* 123, 40 (2017). <https://doi.org/10.1007/s00340-016-6616-4>.
- [34] Point, G., Brelet, Y., Houard, A., Jukna, V., Milián, C., Carbonnel, J., Liu, Y., Couairon, A., and Mysyrowicz, A., (2014). Superfilamentation in Air, *Phys. Rev. Lett.* 112, 223902.
- [35] Moisan, M., and Zakrzewski, Z. (1991), Plasma Sources Based on the Propagation of Electromagnetic Surface Waves, *J. Phys. D Appl. Phys.* 24, 1025.

Chapter 3 – NUMERICAL MODELLING OF SDBD ACTUATORS IN QUIESCENT AIR

François Rogier
ONERA, FRANCE

3.1 INTRODUCTION

Numerical results obtained from modelling of SDBD plasma actuators are compared to experimental thrust measurements as well as to the induced velocity in quiescent air. The work presented aims to test a plasma modelling approach proposed in Boeuf, [1] and to compare it with the experimental ones obtained in Refs. [2], [3] for a 14 kHz – 21 kV actuator in a quiescent atmosphere. In the first section, the chosen numerical model is presented. In the second section, the total body force exerted by the discharge as computed numerically is shown and compared with force balance measurements. In this part, other simulations are also presented for various voltages, frequencies and DBD parameters and compared with experimental results. In a quiescent flow, PIV measurements of the induced actuator wind, and computational results obtained by CFD are also presented and analyzed. Finally, the effects of the numerical and physical parameters are studied in order to evaluate the robustness of the modelling.

3.2 PHYSICAL MODELLING

The model uses a fine description of the plasma while keeping the kinetic scheme simple. Air chemistry is highly complex and involves many species and reactions, (see Ref. [4]) so that the computational complexity required for a complete description would be too large and would contain too much uncertainty. Hence, we follow the approach of J.P Boeuf [1], [4], and use a simplified scheme that is nevertheless complex enough to results in a relevant behavior of the body force with respect to the discharge parameters. The scheme consists of solving the momentum equations for a set of simplified species composed of positive ions (+), negative ions (-) and electrons (e). The body force exerted by the discharge on the flow is then given by $\mathbf{F} = \mathbf{qE}$, where \mathbf{q} is the local charge deposited by the plasma and \mathbf{E} the electric field. The boundary conditions taken into account are secondary emission of electrons at the dielectric surface or a prescribed value of the minimal density. The kinetic scheme involves different reactions, like recombination, ionization and attachment. The main characteristic times of these processes are related to the Electric field. For example, the ionization frequency increases strongly with the electric field (varying from ps to ns), and so does the electron transport time step (which can also plummet to ps). The diffusion phenomenon also typically depends on the electric field and the Maxwell time relaxation depends on the charge density and can be predominant in some situations. Hence, the simulation has to deal with these small typical times and also with the SDBD period whose value is about 10 kHz. In terms of characteristic lengths, we may compare the geometry of the SDBD (from cm to 100 μm), and the Debye length – to capture the dielectric relaxation time step – which is micrometric. The integration of all these different scales require a small time step and a small step size that leads to highly multiscale simulations. As for the numerical methods used, the system of equations is solved using a second order explicit finite volume scheme and the Poisson equation is solved using a finite element method. Due to the large mobility of the electrons, a semi-implicit scheme has been written in order to reduce the CPU time, and the electron motion is treated separately from the heaviest species. In addition, a coupled structured/unstructured mesh strategy has been developed in order to improve the quality of the resolution close to the tip of the anode where the electric field strength is at its highest and where the electric charge is created.

An SDBD actuator with the following set of parameters was used to obtain the numerical results for comparison in the experiments. The relative dielectric permittivity was 3, the thickness of the dielectric was about $r = 3 \text{ mm}$. The anode was **70 mm** thick and **5 cm** long and the cathode was **20 cm** long. As shown in Figure 3-1, the mesh is refined near the tip of the anode in order to have a good resolution in the body force. Typically, **50 to 80 %** of the cells lay in the structured zone. The size of the computational domain selected was large enough to avoid electrostatic perturbations due to the boundary of the computational domain.

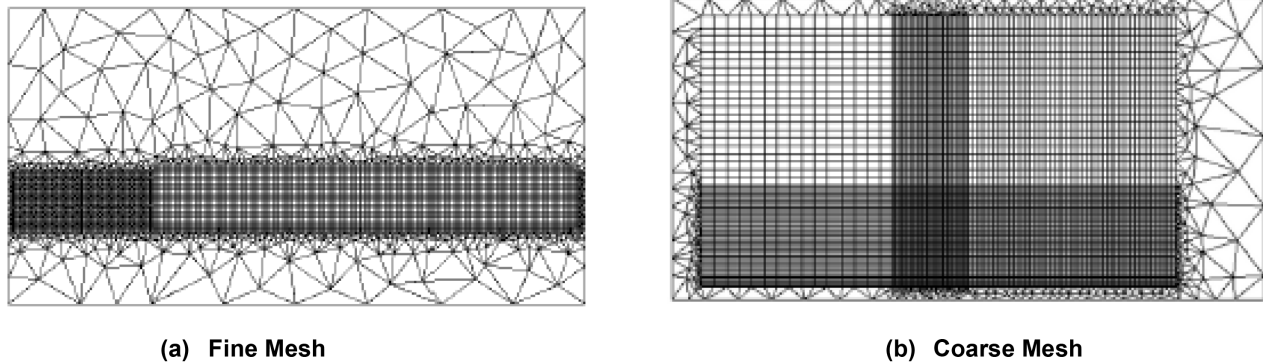


Figure 3-1: Meshes Used.

3.2.1 Numerical Results

Simulating about four periods is enough to reach a periodical regime corresponding to the SDBD actuator period. The time-averaged force is defined by:

$$\mathbf{F}_T(x) = \frac{1}{T} \int_0^T \mathbf{f}(s + \Delta t, x) ds$$

where Δt is a time offset after which all the computed quantities. The maximum of the parallel force is located near the upper electrode tip where the strength of the electrostatic field is the highest. The value of its maximum is about 120 kN/m^3 but it exponentially decreases with the distance to the anode tip and can be considered as zero outside a region of 1 mm in width and 1 mm in height (see Figure 3-1). This differs from other authors who find this non-zero force region to be twice as long and high.

Nevertheless, as expected, the main component of the force is parallel to the dielectric surface and as a consequence, the discharge pushes the gas molecules along the dielectric surface.

For evaluation purposes, the force has been integrated over the whole computational domain A , and its time variation has been plotted over one period (see Figure 3-2).

$$\mathbf{F}_{\text{vol}}(t) = \int_A \mathbf{f}(s + \Delta t, x) dx$$

From 0 to T the positive ions are generated by ionization, so the space charge is positive and the force is directed along the Electric field near the tip of the anode. So, the main component of the force is parallel to the dielectric surface.

From T to T +e the Electrostatic field is screened by a high density of ions during a short time (e # some μs) that stops the ionization and the force decreases to zero.

From T +e to T when the applied potential goes to Vmax, the positive charge deposited at the dielectric surface creates an intense electric field inducing a negative parallel force during a short time. The formation of a negative volume force precedes the streamer regime; then, the ionization of electrons and secondary electrons emission generates negative ions that go to the anode in successive waves.

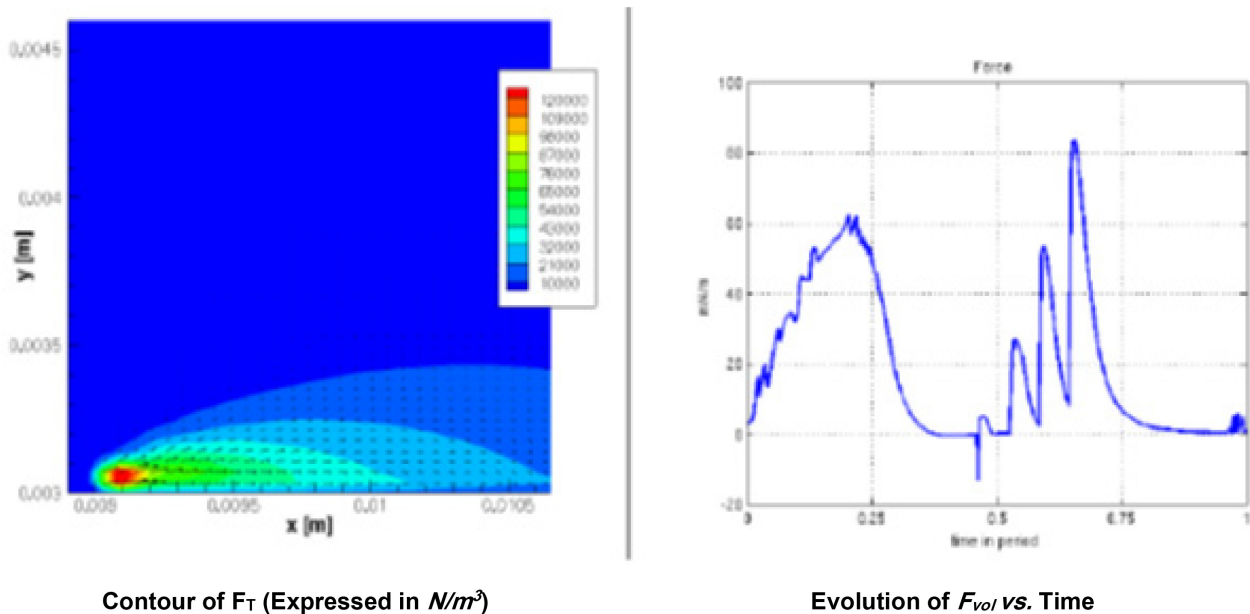


Figure 3-2: EHD Force.

The computed value for this setup is about 19 mN/m and the experimental value given in Ref. [4] is approximately 20 mN/m. Hence, the discrepancy between measurement and modelling is less than 1 mN/m, which is a good estimation, given the low level of complexity of the modelling. Simulations with fine and coarse meshes showed a small difference between the results of the total force (less than 5%) while the computational time proved to be significantly lower. In consequence, all the simulations have been performed with the coarse mesh.

A parametric study of the total force variation with respect to the operating voltage V_0 has been performed. The frequency is set to $F = 14$ kHz. Figure 3-3 shows the total body force for voltages ranging from 14 kV to 28 kV. We observed a small discrepancy of the total body force (less than 1 mN/m) for voltages around $V_0 \approx 21$ kV and a larger one for low voltages. In the range of high voltages (larger than 26 kV), the body force reaches a threshold. This phenomenon has been noticed by many experimentalists in other configurations: for example, the induced velocity does not increase with the voltage for high enough voltage. This fact has also been noted by the group of J.P. Boeuf, [1], [4] which suggests that the induced velocity will eventually reach a limit.

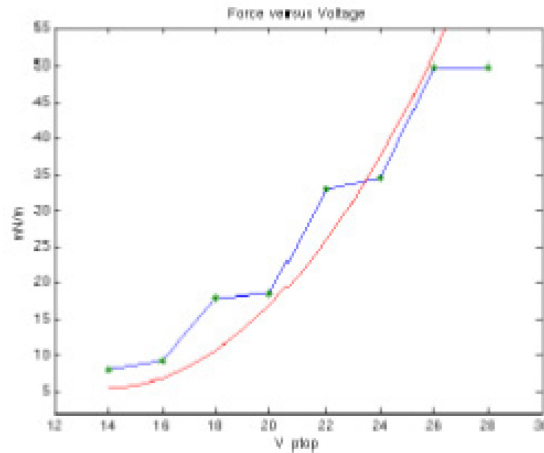
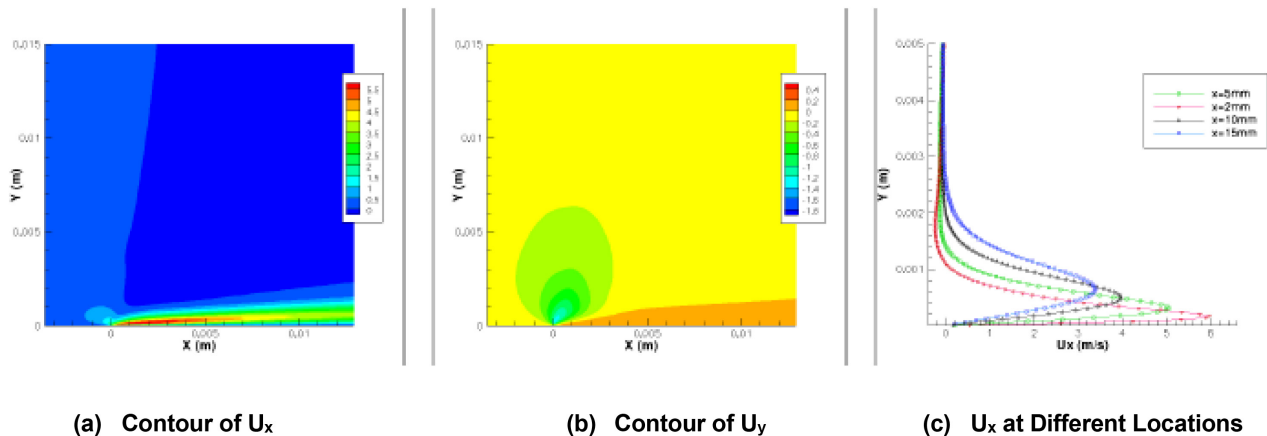


Figure 3-3: Parametric Study.

Flow computations performed with the body force provided by our numerical model are presented, corresponding to typical flat plate experimental cases. To that end, the force computed by the plasma modelling was introduced as a source term in a CFD solver. The simulations are performed with the in-house CFD code of ONERA, CEDRE. The total force is averaged over one period and this mean value is constantly applied as a source term during the simulation. The convergence of the solution toward a steady state is reached after about 0.5 s of physical time. We have performed two computations, firstly assuming the flow as laminar and secondly using a turbulent $k - \omega$ model, which better describes the wall jet nature of the flow, based on the numerical experiments of Kourtzanidis [3]. We have observed here too, that the main effect of the turbulence is a change in the velocity profiles of the flow's boundary layer, especially downstream from the actuator's position. The turbulent boundary layer is, as expected, thicker and corresponds better to experimental results, while the maximum velocity tends to be slightly smaller. Near the actuator's anode, the turbulent effects are almost negligible, possibly due to the time scales concerning the evolution of the boundary layer and the wall jet formation itself. A more adapted turbulent model, i.e., a transitional one, as well as one more refined in both time and space simulations (towards maybe a LES simulation) could spread more light on these scales that are hard to capture. We present the parallel, U_x , and perpendicular component, U_y , of the induced velocity in Figure 3-4.



(a) Contour of U_x

(b) Contour of U_y

(c) U_x at Different Locations

Figure 3-4: Velocity Components.

It can be observed that the maximum of the parallel velocity is very close to the anode, which is located at $x = 5$ mm where the maximum value is more than 7 m/s. It corresponds to an acceleration of the flow due to the body force, which is very large near the exposed electrode. The perpendicular velocity is negative and its maximum amplitude is -1.8 m/s, which is reached a little over the exposed electrode. This corresponds to the region of suction. Figure 3-4(c) shows the profile of the parallel velocity at different locations.

3.2.2 Conclusion

A numerical investigation of the body force induced by a plasma actuator has been carried out on a standardized configuration proposed in the AVT-190 group. The results have shown a good estimation of the total body force compared with measurements for a large range of operating voltages and for some values of the working frequency. The description of the body force variations in time and in space by numerical simulation shows a good correlation with the observations noticed in many experimental works. Nevertheless, some differences such as the presence of a negative force for a 14 kHz SDBD actuator, have been noted via a prediction tool and validated with measurements by Roy and Durscher (see Chapter 4 of the present report) who showed that the maximum parallel velocity reached at 15 mm from the anode tip, is approximately 5 m/s, which is somewhat larger than the computed one [6].

3.3 REFERENCES

- [1] Boeuf, J., Lagmich, Y., and Pitchford, L. Contribution of Positive and Negative Ions to the Electrohydrodynamic Force in a Dielectric Barrier Discharge Plasma Actuator Operating in Air, *Journal of Applied Physics*, Vol. 106, No. 2, 2009, 023115.
- [2] Durscher, R. and Roy, S. Force Measurement Techniques and Preliminary Results Using Aerogels and Ferroelectrics for Dielectric Barrier Discharge Actuators, 42nd AIAA Plasmadynamics and Lasers Conference, 27 – 30 June 2011, Honolulu, Hawaii, USA.
- [3] Kourtzanidis, K. Numerical Simulation of Plasma Actuators for Flow Control, 51ST AIAA Aerospace Sciences Meeting, Texas, USA 2013-0134, 2013.
- [4] Kossyi, I. A., Yu Kostinsky, A., Matveyev, A.A., Silakov, V.P. Kinetic Scheme of the Non-Equilibrium Discharge in Nitrogen-Oxygen Mixtures, *Plasma Sources Science and Technology*, Vol. 1(3), 1992, pp. 207-220.
- [5] Lagmich, Y., Callegari, T., Pitchford, L.C., and Boeuf, J.P. Model Description of Surface Dielectric Barrier Discharges for flow Control, *Journal of Physics D: Applied Physics*, Vol. 41, No. 9, 2008, 095205.
- [6] Durscher, R. and Roy, S. Evaluation of Thrust Measurement Techniques for Dielectric Barrier Discharge Actuators, *Experiments in Fluids*, Vol. 53, No. 4, 2012, pp. 1165-1176.



Chapter 4 – EVALUATION OF FORCE MEASUREMENT TECHNIQUES FOR DIELECTRIC BARRIER DISCHARGE ACTUATORS

Ryan Durscher and Subrata Roy

University of Florida
UNITED STATES

ABSTRACT

Despite their popularity in the recent literature, plasma actuators lack a consistent study to identify limitations, and remedy thereof, of various thrust measurement techniques. This paper focuses on comparing two different experimental techniques commonly used to measure the global, plasma induced thrust. A force balance is used to make a direct measurement of the thrust produced, which is then compared with a control volume analysis on data obtained through particle image velocimetry. The local velocity measured by particle image velocimetry is also validated with a fine-tip pressure probe. For the direct thrust measurements, the effect of varying the actuator plate length upon which the induced flow acts is investigated. The results from these tests show that the length of the actuator plate is most influential at higher voltages with the measured thrust increasing as much as 20% for a six times reduction in the length of the plate. For the indirect thrust measurement, the influence of the control volume size is analyzed. When the two methods are compared against each other, good agreement is found when the control volume size has a sufficient downstream extent. Also, the discharge length is optically measured using visible light emission. A linear correlation is found between the discharge length and the thrust measurements for the actuator configurations studied. Finally, the energy conversion efficiency curve for a representative actuator is also presented.

4.1 INTRODUCTION

The Dielectric Barrier Discharge (DBD) plasma actuator, in general, consists of an asymmetric electrode arrangement (one exposed and one encapsulated) separated by a dielectric medium. The application of an alternating, high voltage signal results in a surface-mode discharge along the dielectric. At (or near) atmospheric pressures, the discharge is comprised of microdischarges, which form discrete channels between the electrode and dielectric surface (Gibalov and Pietsch 2000 [1]; Kogelschatz 2003 [2]; Xu 2001 [3]). The expansion of the discharge along the dielectric surface results in a charge deposition, which in turn reduces the local electric field and extinguishes the microdischarge. Collectively, the discharge is completely extinguished twice per period as evident by the light emission and discharge current (Enloe et al. 2004 [4]). As the ionized particles within the microdischarges propagate along the dielectric surface, momentum is transferred to the surrounding neutral particles through a poorly understood collisional mechanism. Macroscopically, however, the net separated space charge within the plasma interacts with the electric field resulting in an electrohydrodynamic body force acting on the working gas resulting in an acceleration of the fluid. By virtue of Newton's third law, an equal and opposite force is imparted to the actuator. Experiments have shown this momentum exchange to be cyclic with the magnitude of the force varying depending on the polarity of the exposed electrode (Debien et al. 2012 [5], Enloe et al. 2008b [6]; Enloe et al. 2009 [7]; Font et al. 2011 [8]).

The plasma actuator has been used as a flow control mechanism in various aerodynamic applications such as turbine blades (Ramakumar and Jacob 2005 [9]; Rizzetta and Visbal 2008 [10]), landing gears (Thomas et al. 2005 [11]), airfoils (Little et al. 2010 [12]; Post and Corke 2004 [13]), turbulent jets (Labergue et al. 2007 [14]),

and an assortment of conical flows (e.g., flat plate boundary layers (Gibson et al. 2012 [15]; Grundmann and Tropea 2009 [16]; Roth et al. 2000 [17]; Schatzman and Thomas 2010 [18]), cylinder vortex shedding (Jukes and Choi 2009 [19]; Thomas et al. 2008 [20]), etc.). In order to improve the fluidic authority of the actuators, numerous parametric studies have been undertaken which have focused on various aspects (e.g., applied voltage/frequency, dielectric material, electrode arrangement) of the actuator (Abe et al. 2008 [21]; Borghi et al. 2008 [22]; Corke et al. 2007 [23]; Forte et al. 2007 [24]; Hoskinson and Hershkowitz 2010 [25]; Hoskinson et al. 2008 [26]; Jolibois and Moreau 2009 [27]; Roth and Dai 2006 [28]; Thomas et al. 2009 [29]). Characterizing the resulting induced thrust is therefore pivotal for understanding the influence of various control parameters in improving the actuator authority.

Several methods have been employed for measuring the plasma induced thrust. Typically, a simplified approach is used to either measure the net thrust directly using a high resolution (~mg) force balance or calculate it indirectly based on the velocity field extracted using techniques such as pitot probes, Particle Image Velocimetry (PIV), and Laser Doppler Velocimetry (LDV). Specifically, the latter approach relies on a control volume analysis of the measured flow field to determine the net thrust produced (Baughn et al. 2006 [30]; Hoskinson et al. 2008 [31]; Kotsonis et al. 2011 [32]; Kriegseis 2011a [33]; Debien et al. 2012 [34]). Recently, more complicated methods have also been investigated that resolves the plasma body force spatially by applying the Navier-Stokes momentum equations to PIV data (Kotsonis et al. 2011 [32]). However, a basic study aimed at the limitations of the simplified direct or indirect measurements is lacking. For example, the near wall flow as a result of actuation gives rise to a self-induced drag (Font et al. 2010 [33]), for which the plate size would likely have a significant impact on the measured thrust. The plate size, however, is not typically reported in the literature. Also, how does the calculated thrust vary with the size of control volume, and how does it compare with the direct measurement? In literature, a comparison between the two methods is often met with mixed results. Hoskinson et al. (2008 [31]) reported a factor of two difference in the calculated thrust between the two techniques (attributed to simplifications made), while Kotsonis et al. (2011 [32]) showed a reasonable agreement between the two methods.

This paper focuses on characterizing some limitations of the aforementioned direct and control volume inferred experimental techniques used to measure the net, induced thrust for a basic Single Dielectric Barrier Discharge (SDBD) actuator. In particular, the influence of the plate size on the direct thrust measurement is investigated. Similarly, the thrust is indirectly determined from a control volume analysis of the flow field obtained through PIV. Here, the influence of the control volume size on the calculated thrust is analyzed by comparing with the plate size-independent direct thrust data. Also, the discharge length is optically measured using visible light emission. A functional relationship between the measured discharge length and the measured thrust is studied. The local velocity measured by the PIV technique is also validated with pitot tube measurements at different locations. The paper is organized in the following manner. Section 4.2 describes the experimental setup for the tests conducted. This includes a discussion of the direct thrust measuring arrangement, PIV details, and the control volume analysis. Section 4.4 presents the results for the aforementioned investigations, while conclusions are drawn in Section 4.6.

4.2 EXPERIMENTAL ARRANGEMENT

4.2.1 Plasma Actuator Design and Discharge Generation

A cross-sectional schematic of the DBD plasma actuator used in these experiments is shown in Figure 4-1(a). The actuator consists of two thin (70 μm) copper electrodes placed asymmetrically on either side of the dielectric material with no horizontal gap between the two electrodes. The dielectric in this case was a 3-mm-thick (t) sheet of acrylic, which has a nominal relative dielectric constant of 3. The width, w, of the upper electrode was 0.5 cm

while the lower electrode's width is 2 cm. Both electrodes have a length, l , of 12 cm. Three layers of vinyl electrical tape (178- μm thick) covered the encapsulated electrode to avert an unwanted discharge on the lower surface. Similarly, an 84- μm -thick piece of Kapton was placed on the opposite side of the exposed electrode preventing the occurrence of a discharge. The actuator depicted in Figure 4-1(b) shows the dimensions of the dielectric used in the actuator plate length tests, where the effect on the thrust was investigated by shortening the actuator's plate length, L .

In order to ionize the surrounding air, the exposed and encapsulated electrodes were each supplied with high voltage signals that were 180° out of phase. A congruent powering scheme has previously been used by Thomas et al. [20]. The sinusoidal input signals were generated using an arbitrary waveform generator (Tektronix AFG3022B). These signals were further amplified by a dual output audio amplifier (QSC RMX 2450) which was then stepped up using high voltage transformers (Corona Magnetics, Inc. CMI 5523) (Figure 4-2). Actuators were tested with total voltages ranging from 14 to 28 kV_{pp} at two distinct frequencies 7 and 14 kHz.

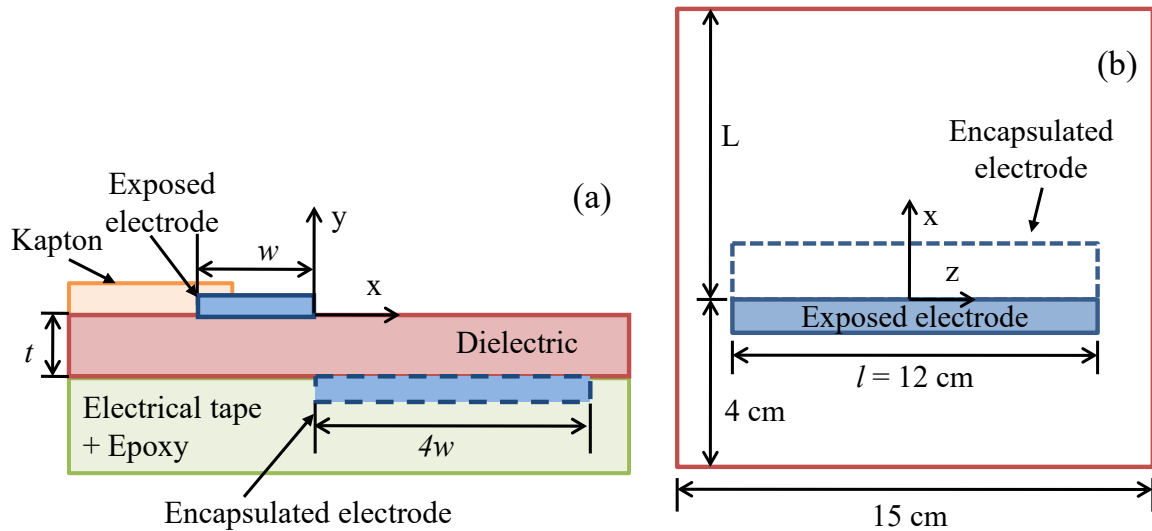


Figure 4-1: Schematic of DBD Plasma Actuator: (a) Side View and (b) Top View (Not Drawn to Scale).

The voltage and current supplied to the actuators were monitored using high voltage (Tektronix P6015A) and current probes (Pearson Electronic 2100). In order to calculate the delivered power, the voltage and current waveforms were captured using a digitizing oscilloscope (Tektronix DPO3014). In a single acquisition, the oscilloscopes captured 1 million points for each waveform at a sampling rate of 250 MSA s^{-1} . For each input voltage, 10 acquisitions were recorded. This corresponds to 280 and 560 periods over which the calculated power is averaged for 7 and 14 kHz waveforms, respectively. The total power, P , delivered to the plasma actuator was considered to be a linear superposition of the power supplied to each electrode. The average real power was numerically calculated by multiplying the instantaneous voltage, V_i , by the instantaneous current, I_i , and then summing and dividing by the total number of samples, N . Indices 1 and 2 in Equation 4-1 correspond to the respective circuit branches in Figure 4-2.

$$P = \frac{1}{N} \left(\sum_{i=1}^N V_{1,i} I_{1,i} + \sum_{i=1}^N V_{2,i} I_{2,i} \right) \quad (4-1)$$

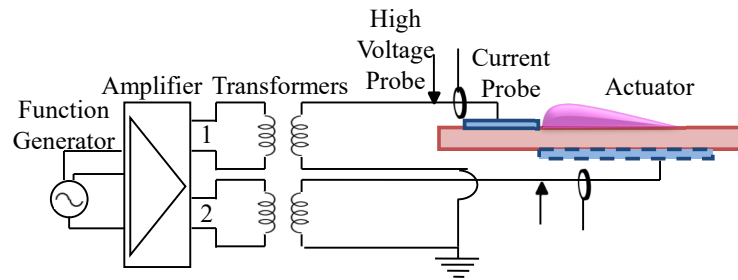


Figure 4-2: Circuit Schematic Used to Generate a DBD Plasma Discharge.

4.2.2 Direct Thrust Measurements

Direct force measurements were obtained using an Ohaus precision balance (Adventurer™ Pro AV313C). The actuators were mounted to the scale by an acrylic stand which protruded through a small opening in a Faraday cage, Figure 4-3(a). The cage was constructed using aluminium (3.18-mm thick) and was used to shield the balance from any electromagnetic interference due to the high electric fields required to generate the plasma discharge. An example output from the balance is shown in Figure 4-3(b) for various voltages. The maximum uncertainty associated with a given measurement is estimated to be within 4% (to 95% confidence), based on repeated measurements (at a constant voltage) and the scale’s inherent uncertainty. Furthermore, the error in the thrust measurement due to the scale’s cross-axis sensitivity was investigated and found to be negligible. This was determined by orienting the actuator on the mass balance to measure the z-component of the force (referring to Figure 4-1). In such an arrangement, the scale would be affected by both x and y components in the cross-axis direction. Given that the z-component should be zero for a linear actuator, a registered thrust reading by the balance should presumably be a result of its sensitivity to cross-axis forces. No thrust was measured as the balance read zero over the entire range of input voltages.

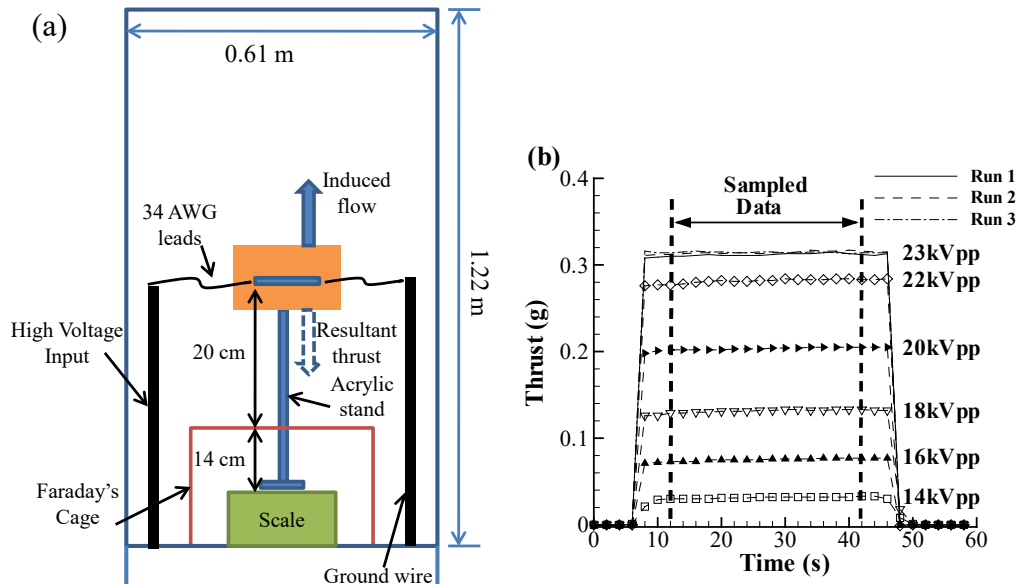


Figure 4-3: (a) Experimental Setup Schematic for Direct Force Measurement; (b) Example Readouts from the Balance Showing the Stability and Repeatability of the Direct Thrust Measurement (14 kHz Input Frequency).

4.3 CONTROL VOLUME ANALYSIS

4.3.1 Flow Field Measurements

Two-component Particle Image Velocimetry (PIV) was used to generate time-averaged, spatially resolved data of the induced flow due to the plasma actuator. These averaged vector fields were then used for the control volume analysis. The plasma actuator geometry is similar to that described previously (Figure 4-1) however the dielectric plate upon which the actuator was built was much larger. The dimensions of the plate are 30 cm x 30 cm with the electrodes placed in the center. The actuator was set up in the same quiescent chamber as described above.

An Nd:YAG, dual cavity pulsed 532 nm laser (New Wave Research Solo PIV II 30) was used to generate a light sheet along the centerline of the actuator normal to the span. This illuminated the vaporized Ondina oil used to seed the chamber (see Section 4.3.2 PIV Seeding). *LaVision*'s adjustable light sheet optics allowed for fine adjustments to the waist of the laser sheet, which had an estimated thickness of 1 mm. The time separation (dt) between laser pulses was adjusted accordingly depending on the induced flow velocity. In general, the dt was set to maintain a maximum particle displacement of 5 to 7 pixels, with the value ranging from 48 μ s to 22 μ s (voltage/velocity dependent). *LaVision*'s ImagerPro X 4M (2048 x 2048 pixels) camera fitted with a 105 mm lens was used to capture the PIV images. The field of view for each image was approximately 48 mm x 48 mm (x, y).

LaVision's DaVis 7.2 PIV software package was used to calibrate, capture, pre-process, process and post-process the PIV images. Image calibration was performed with a 40 mm x 40 mm, two-tiered calibration plate. In processing the PIV data, the local average intensity was subtracted from the raw images in order to increase the relative contrast between the particles and the background. Furthermore, a local particle intensity correction was applied in which the particle intensities are normalized over a window of 4 pixels, allowing smaller particles to contribute more effectively in the correlation (Westerweel, 1994 [37]). Having masked the surface of the actuator, each image pair was then subjected to a cross-correlation multi-grid process. The correlation process consisted of an initial pass with a 32 x 32 pixel² interrogation window with a 50% overlap, followed by two refining passes with 16 x 16 pixel² windows again with 50% overlaps. For the initial pass a 1:1 Gaussian weight was applied to the integration windows, while a 2:1 was applied on the refining passes. This resulted in a vector field resolution of 0.19 mm. Outliers were detected and removed using a recursive spatial outlier detection [37] in between multi-grid passes as well as on the final vector field.

For each input voltage, 300 image pairs were taken at a repetition rate of 7.2 Hz. Typical convergence plots of the tangential velocity component (U_x) are shown in Figure 4-4(a) and Figure 4-4(b) for two locations in the vector field. The first point, $(x, y) = (5, 0.5)$ mm, is representative of the region of high velocity near the discharge, Figure 4-4(a), while the second position, $(x, y) = (35, 1.5)$, is characteristic of the fully developed wall jet, Figure 4-4(b). The relative statistical uncertainty for these two points is shown in Figure 4-5 as calculated from:

$$\text{Rel. Uncertainty} = \frac{t_{N-1,95\%} \bar{\sigma}_x}{\bar{U}_x} \quad (4-2)$$

where $t_{N-1,95\%}$ is the t estimator ($N-1$ degrees of freedom, 95% confidence interval), $\bar{\sigma}_x$ is the standard deviation of the mean velocity, and \bar{U}_x mean velocity (x -component).

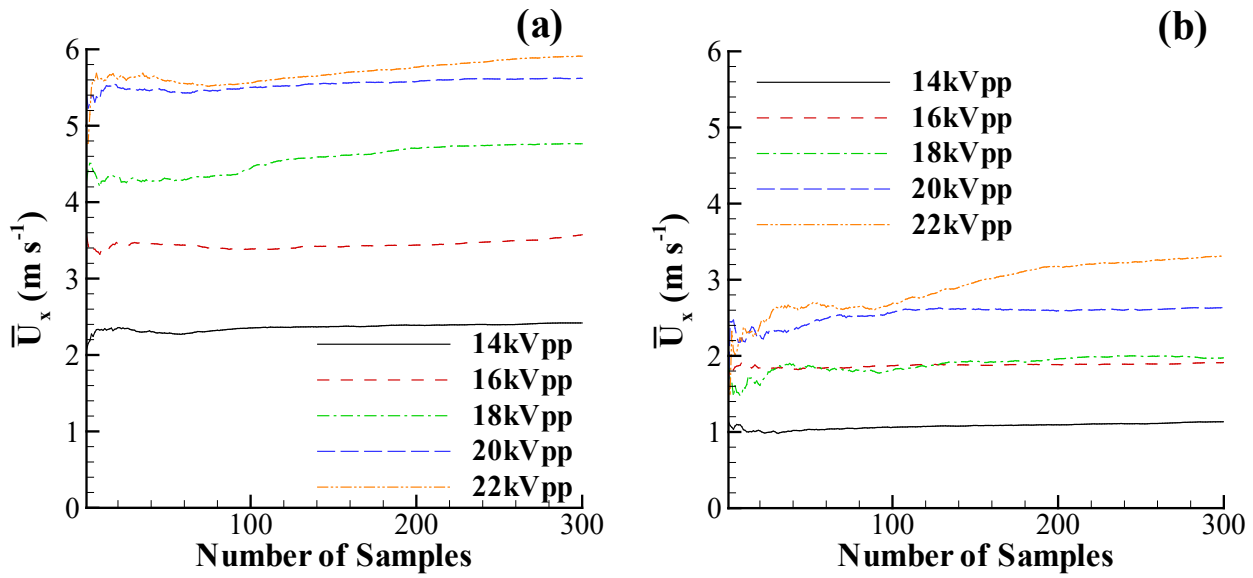


Figure 4-4: Convergence Plot for the X-Component of Velocity (U_x) for Two Locations in the Flow Field: (a) Point $(x, y) = (5, 0.5)$ mm and (b) $(x, y) = (35, 1.5)$ mm.

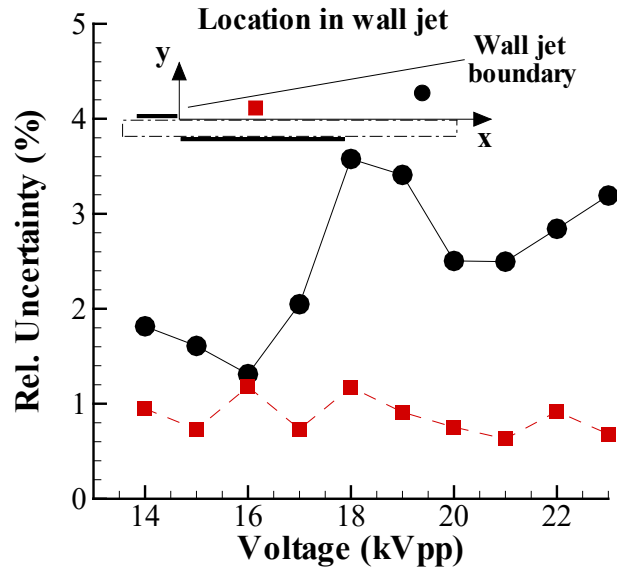


Figure 4-5: Relative Statistical Uncertainty as a Function of Voltage and Position for the Velocity Vector Field. Red squares correspond to point $(x, y) = (5, 0.5)$ mm, while black circles represent $(x, y) = (35, 1.5)$ mm.

4.3.2 PIV Seeding

In general, the fluid dynamic response accuracy of the seeding particles can be estimated by the Stokes number:

$$St = \frac{\tau_p U_{ref}}{L_{ref}} \quad (4-3)$$

where τ_p particle is the relaxation time of the particle, U_{ref} is the characteristic reference velocity (typically the freestream velocity), and L_{ref} is the characteristic reference length. A Stokes number, $St \geq 1$ indicates the particle will poorly follow the flow, while a Stokes number approaching zero ($St \rightarrow 0$) implies a perfect tracer. The particle relaxation time in a constant accelerating flow is:

$$\tau_p = \frac{d_p^2(\rho_p - \rho_f)}{6\pi\rho_f\nu_f\phi} \quad (4-4)$$

where d_p is the particle's diameter, ρ_p the particle density, ρ_f the fluid density, and ν_f the kinematic viscosity of the fluid. The value of ϕ is dependent on the particle Reynolds number but may be taken as one ($\phi = 1$) for Stokesian drag at low Reynolds numbers. In general, the dynamics of a suspended particle are much more complicated [38]. However, Equation 4-3 provides a reasonable estimation of the particles' response.

For plasma actuation, however, consideration of the electrodynamic influence on the particles is warranted due to the presence of large electric fields required to initiate a breakdown of the air. In doing so the PIV images may be broken into two regions:

- 1) The discharge volume itself;
- 2) The far-field away from the vicinity of the discharge.

Within the discharge volume, a charging of particle could result in a combination of fluidic and Coulombic forces influencing the particles paths. In the far-field, however, the dielectrophoretic force due to polarization would likely be prevalent. This force may be approximated by considering a dielectric sphere of radius r_p and relative dielectric constant $\epsilon_{r,p}$ being placed into a dielectric fluid with a relative permittivity of $\epsilon_{r,f}$. The force on a dipole neutral particle is then:

$$\vec{F}_{dipole} = 2\pi\epsilon_0\epsilon_{r,f}Kr_p^3\nabla\vec{E}^2 \quad (4-5)$$

where K is the Clausius-Mossotti factor given by:

$$K = \frac{\epsilon_{r,p} - \epsilon_{r,f}}{\epsilon_{r,p} + 2\epsilon_{r,f}} \quad (4-6)$$

Here, only the static case is considered, which is sufficient for illustrative purposes. Considering Stokesian drag (F_{Stokes}) as above, for the dielectrophoretic force to be considered negligible it should be significantly less than the shear force on the tracer particle ($F_{dipole} \ll F_{Stokes}$). The frictional force based on Stokes' law is given by:

$$F_{Stokes} = 6\pi\rho_f\nu_f r_p V_p \quad (4-7)$$

where V_p is the particle's velocity.

For the experiments outlined in this text, Ondina oil was used as the fluidic tracer particle. The oil was vaporized using a TSI atomizer (Model 9302) which, when pressurized at 25 psi, produces a droplet with a mean diameter of $\sim 0.8 \mu\text{m}$. Assuming Stokesian drag and air as the working fluid ($\rho_f = 1.184 \text{ kg m}^{-3}$, $\nu_f = 15.68\text{E-}6 \text{ m}^2 \text{ s}^{-1}$), substituting the particle's diameter and density ($\rho_p = 854 \text{ kg m}^{-3}$) into Equation 4 gives a relaxation time of $1.63\text{E-}6 \text{ s}$. Assuming a characteristic velocity of 5 m s^{-1} and a reference length of 1 mm , Equation 4-3 gives a Stokes number of $8.2\text{E-}3$ (or $\text{St} \ll 1$). Furthermore, the dipole neutrality of Ondina may be verified by considering the two regions considered above (the plasma volume and the far-field). First consider the far-field in which the dipole force on the particle is given by Equation 4-5. In this analysis the electric field will be taken as $3,000 \text{ kV m}^{-1}$ (or 30 kV cm^{-1} the breakdown field for air at atmospheric pressure). Additionally, for simplification, consider the gradient of the electric field in Equation 4-5 to scale with the particle's diameter such that:

$$\nabla E^2 \approx \frac{E^2}{d_p} \quad (4-8)$$

The exact value of the relative dielectric constant for Ondina was not reported by the manufacture, so a value of 4 (typical for oils) is assumed. Taking air again as the working fluid, Equation 4-5 gives a force due to polarization of the particle of $4.0 \times 10^{-11} \text{ N}$. Similarly, applying Equation 4-7, the Stokes drag on the particle becomes $7.0 \times 10^{-10} \text{ N}$. Although F_{Stokes} is only an order of magnitude higher than F_{dipole} , Equation 4-8 was taking as the worst-case scenario. The polarization force is therefore considered negligible. Hence, it is reasonable to assume that Ondina is dipole neutral and, thus, relatively unaffected by the high electric field near the actuators.

Additionally, the charge carried in the plasma volume due to tracer particle charging would likely influence the conductive current, and therefore result in a different power consumption when seeding particles were present. For these experiments no observable changes in consumed power were noted. This argument, however, is not absolute and further consideration of the seeding particles concentration is required. On average the atomizer was ran for approximately 10 seconds to seed the 0.45 m^3 quiescent chamber. Based on the specified flow rate of the atomizer and particle volume, a particle concentration of $9 \times 10^{15} \text{ m}^{-3}$ was estimated. Relative to the ion concentration of a weakly ionized plasma generated in a DBD actuator ($\sim 10^{21} \text{ m}^{-3}$) the seed particle density is ~ 5 -6 orders of magnitude smaller, indicating a substantial change in the discharge current may not be prevalent. To investigate the influence of particle charging on the induced velocity, the PIV velocity profiles were compared against measurements obtained using a glass pitot probe. The probe was constructed out of a modified glass Pasteur pipet with an inner and outer diameter of 1.2 and 1.5 mm , respectively. The pressure measurements were made using a Furness Controls FCO332 differential manometer calibrated to $\pm 25 \text{ Pa}$ with a $\pm 10 \text{ V}$ output. Each data point represents the average of 120 voltage reading recorded at a sampling rate of 15 Hz using a National Instruments data acquisition module (PCI-6133). The differential pressure, ΔP , measurements were converted to velocities using Equation 4-9 where ρ is the air density. Here the air density was taken as 1.184 kg m^{-3} which corresponds to a laboratory temperature of $25 \text{ }^\circ\text{C}$.

$$U_x = \sqrt{2\Delta P / \rho} \quad (4-9)$$

Reasonably good agreement is seen between the two data sets giving some indication that particle charging may be negligible in the current experimental setup. The slight difference between the two profiles height and magnitude could be attributed to the relatively large area of integration of the inner diameter of the pitot probe used (see Figure 4-6). Further experiments will be carried out using a smaller probe in future efforts.

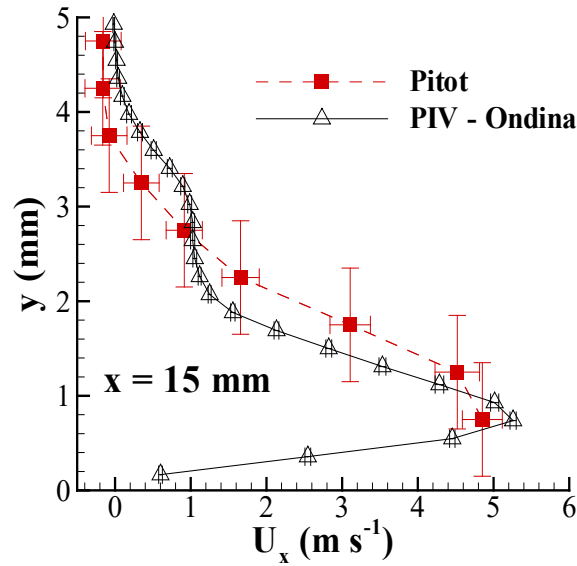


Figure 4-6: Comparison Between Pitot Measurements and PIV Profiles Taken 15 mm Downstream of Exposed Electrode for an Applied Voltage of 21 kV_{pp} at 14 kHz. The vertical error bars on the pitot measurements indicate the inner diameter of the probe used.

4.3.3 Inferred Force Calculation

The rectangular control volume as depicted in Figure 4-7 was applied to the time-averaged velocity field generated from the PIV measurements. The net thrust, T_x and T_y , produced by the actuator (normalized by the electrode length) is determined from the conservative form of the momentum equations assuming time independence. The net thrust produced would be the summation of the plasma induced body force (F_p), the wall shear stress (F_s), and pressure differential acting within and on the control volume. Given the control volume boundaries are significantly removed from the bulk plasma, a constant pressure assumption may be made, in which the net thrust in the x-direction would be equal to $T_x = F_{x,p} - F_s$. In this analysis, however, we are only interested in the net thrust imparted to the dielectric, therefore the control volume used is drawn accordingly to negate such distinctions. To emphasize the negation of wall shear stress, the control volume shown in Figure 4-7 is drawn to extend below the dielectric where the velocity field is zero.

$$T_x = -\int_{y_0}^H \rho U_{x,left}^2 dy + \int_{x_0}^W \rho U_{x,top} U_{y,top} dx + \int_{y_0}^H \rho U_{x,right}^2 dy \quad (4-10)$$

$$T_y = -\int_{y_0}^H \rho U_{y,left} U_{x,left} dy + \int_{x_0}^W \rho U_{y,top}^2 dx + \int_{y_0}^H \rho U_{y,right} U_{x,right} dy \quad (4-11)$$

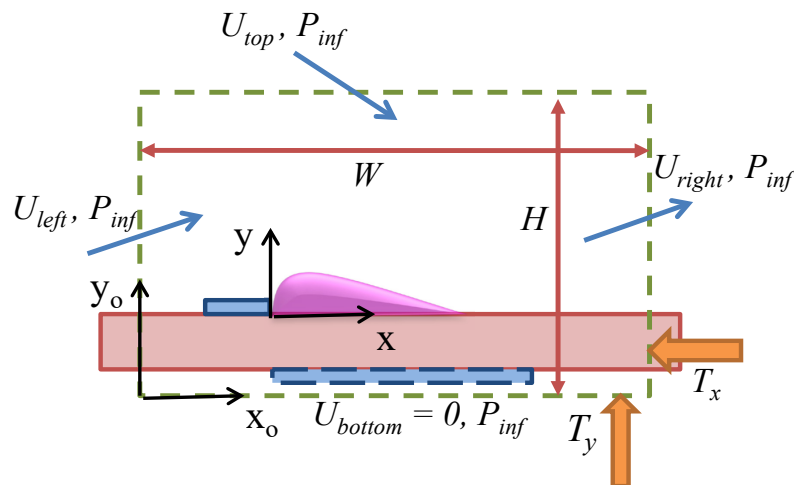


Figure 4-7: Schematic of Control Volume Used to Calculate Reaction Forces Induced by the Plasma Discharge.

4.4 RESULTS

4.4.1 Influence of the Actuator Plate Length

In order to evaluate the effect of the actuator's plate length (L), shown in Figure 4-8(b), different plate lengths were tested. The same actuator was used throughout the experiments with the plate length, L , being reduced each time. Lengths corresponding to 15, 10, 5, and 2.5 cm were investigated over a range of voltages. A plate length of 15 cm was chosen as to mimic the plate length of the actuator used in the control volume analysis. A limiting length of 2.5 cm was imposed to avoid the possibility of arcing around the dielectric substrate, since the encapsulated electrode itself is 2 cm wide. 10 and 5 cm were chosen arbitrarily as incremental lengths.

The results of this study, presented in Figure 4-8, indicate that there is little variation in the resultant force regardless of the length of the plate for lower input voltages. This trend does not hold, however, as the voltage increases. At the higher voltages investigated, an increase in thrust is observed as the actuator's plate length is decreased. This increase is independent of the two frequencies investigated. At the maximum voltages tested a difference of 5 and 7 mN/m was measured between plate lengths of 15 and 2.5 cm for 14 and 7 kHz, respectively. This corresponds to a ~20% increase in measured thrust in both cases (Figure 4-9). Such a large discrepancy could prove problematic when trying to compare between different researchers' results.

Since the longer plate lengths ($L = 15$ and 10 cm) converge to a single value, it is believed that these lengths provide a more accurate representation of the true net thrust (= plasma force – viscous drag) produced. The velocity profile for the larger plates will have a significantly longer length to develop over allowing plateauing of the resulting viscous drag, and also providing a more comparable flow field with that of the PIV experiments. By reducing the plate size, one is reducing the net viscous drag component for the same actuator setup. As an alternative, however, it is plausible that a shortening of the dielectric plate affects the surface charge accumulation and thus the electric field and induced force on the fluid. The surface charge has been shown to persist several centimeters downstream of actuator. Regardless of the exact mechanism, Figure 4-10 verifies that the power consumption and thus power delivered to plasma load remain constant regardless of the plate length.

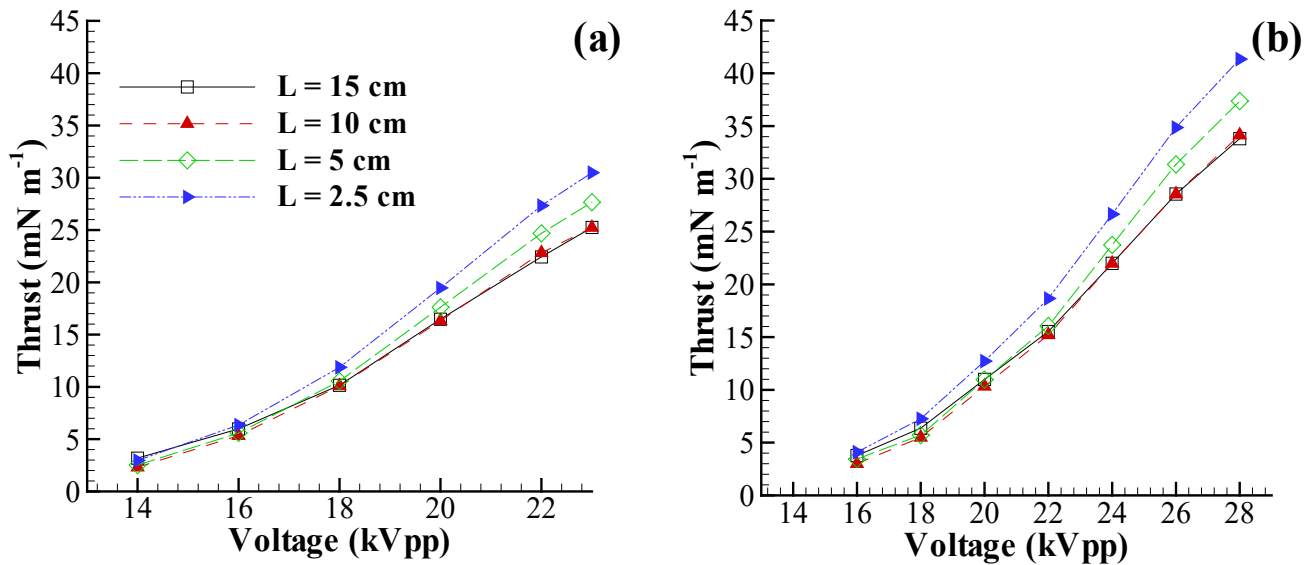


Figure 4-8: Force Measurements Over a Range of Input Voltages with Varying Actuator Plate Lengths: (a) 14 kHz and (b) 7 kHz.

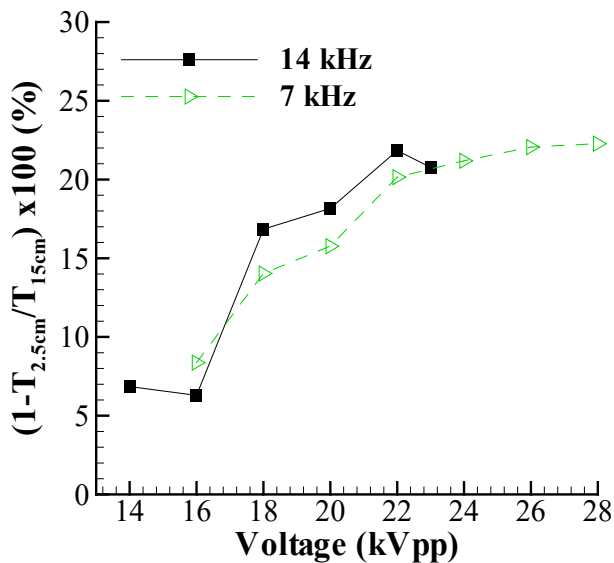


Figure 4-9: Percentage Increase in Thrust Between a Plate Length of 2.5 cm and 15 cm as a Function of Voltage.

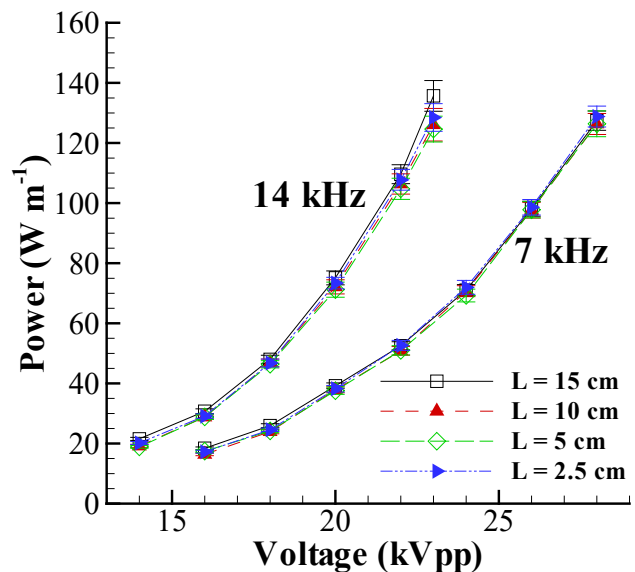


Figure 4-10: Power Dissipation as a Function of Voltage for Different Plate Lengths.

4.4.2 Effect of Chamber Size

As stated previously the chamber in which the scale is housed is only slightly vented to prevent potentially dangerous amounts of ozone from continuously spreading into the laboratory. As a consequence, one could argue that for particularly long runs of the actuator that the air chemistry inside of the chamber is being

modified. To test this argument, two tests were carried out over a range on input voltages. In one case the 0.74 m² door to the chamber was closed during testing, while it was left wide open in the other. The measured thrust from these tests are shown in Figure 4-11, where “not vented” and “vented” correspond to the door being closed and open, respectively. As one can see, the resultant thrust was nearly identical regardless of ventilation. This result would likely change if the volume of the quiescent of chamber was reduced, though the results seem indifferent for the current experimental setup.

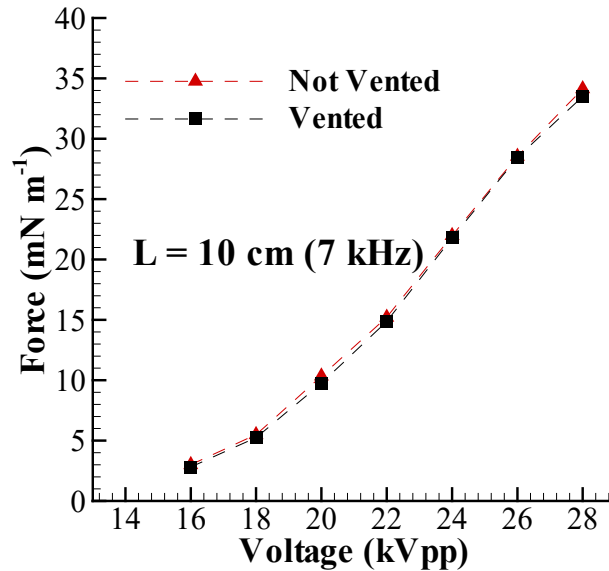


Figure 4-11: Effect of a Vented vs. Unvented Chamber on the Induced Thrust. The plate length was 10 cm and the input frequency was 7 kHz.

4.5 CONTROL VOLUME

4.5.1 Control Volume Extracted Forces

In order to extract the reaction forces on the control volume, the integrals on the right-hand side of Equation 4-10 and Equation 4-11 were numerically integrated in MATLAB using the time-averaged PIV data. Both composite trapezoidal rule (a 2nd order accurate method) and composite Simpson’s rule (3rd order accurate) integration schemes were applied. While both methods yielded nearly identical outcomes, the following results were obtained using the trapezoidal rule. It was found that the starting x-location, x_0 , in the integrals had little influence on the resultant force calculated as long as it was chosen behind the edge of the exposed electrode (i.e., $x_0 < x = 0$, referring to Figure 4-7). The starting y-location, y_0 , was chosen arbitrarily below the dielectric material such that $y_0 < 0$ (Figure 4-7). The starting locations used were: -5.0 mm and -0.1 mm corresponding to x_0 and y_0 , respectively. Also, it is pertinent to note that a constant fluid density (ρ) is assumed. This assumption was also made by Hoskinson et al. [31] based on prior experimental data from Enloe et al. [39]. In this prior work it was estimated that the density fluctuations near the actuator were less than 2% of ambient. Again, the air density was taken as 1.184 kg m⁻³.

Figure 4-12 depicts a plot of the tangential force component, T_x , and how it varies with the width (W) and the height (H) of the control volume (referring to Figure 4-7). The applied voltage was 15, 19, and 22 kV_{pp} at an input

frequency of 14 kHz. Although not shown, the normal force component (T_y) exhibits similar characteristics. The plot indicates that the force is independent of the height above the dielectric surface in which the control volume is taken beyond a given point (10 mm for these cases). This point corresponds to the total encapsulation of the induced wall jet's boundary layer. The boundary layer created by the jet increases with both applied voltage and downstream location. However, for the range of voltages investigated the boundary layer was less than 10 mm thick for the given field of view. More important than the height of the control volume is its width, as Figure 4-12 reveals. The calculated thrust is highly dependent on the point at which the control volume ends. If the width is too small the thrust may be grossly over predicted as compared to a much wider control volume.

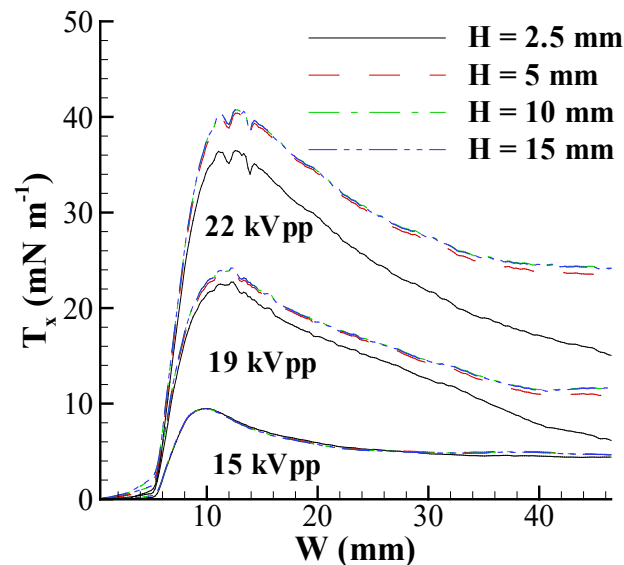


Figure 4-12: Resultant Tangential Thrust Component for a 15, 19, and 22 kV_{pp} Input Voltage at 14 kHz as a Function of the Width (W) for Varying Heights (H) of the Control Volume.

The tangential and normal force components are plotted in Figure 4-13(a) and Figure 4-13(b), respectively, over the range of input voltages investigated. At each voltage, the force was extracted for five different control volume widths from data similar to Figure 4-12. The vertical dashed lines in Figure 4-14 correspond to control volume widths of 10, 20, 30, 40, and 45 mm. The height of the control volume chosen was 10 mm, which for reasons previously discussed is a suitable choice. Over the range of supplied voltages, the same trend holds, in that the resultant tangential force has a strong dependency on the width of the control volume. This dependence becomes more pronounced at higher voltages. The calculated forces do begin to converge, however, as the downstream extent of the control is increased. Based on the current results a downstream extent of ~ 35 mm is necessary to provide consistent results. This convergence/asymptotic behavior can also be seen in Figure 4-12.

The normal force component deviates from this trend with its values remaining approximately constant as the width of the control volume is increased, Figure 4-13(b). The exception, however, to this observation is the smallest control volume plotted ($W = 10$ mm). Regardless, the magnitude of the normal component is significantly less than that of the tangential. The large disparity between the normal and tangential components is in line with other reports. Due to such a large difference between the two components, it is assumed that the normal component will have a negligible impact on the direct force measurement and there should be a reasonably good agreement between the two measurement techniques (direct and control volume inferred).

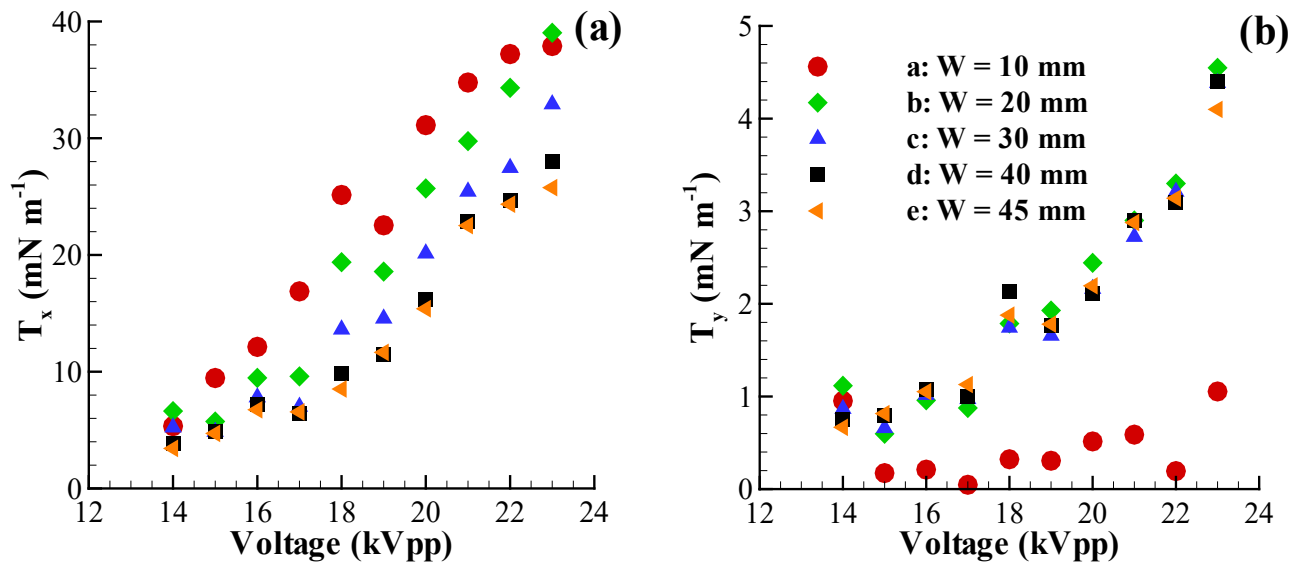


Figure 4-13: Forces Calculated from a Control Volume Analysis as a Function of Voltage for Various Widths of the Control Volume: (a) Tangential Component of Force (F_x) and (b) Normal Component of Force (F_y).

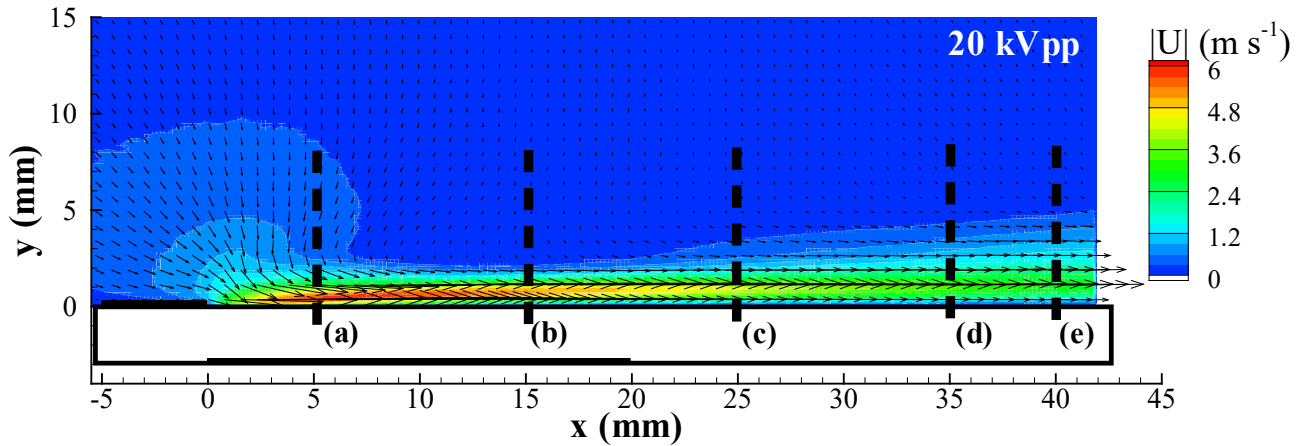


Figure 4-14: Velocity Magnitude Contour for 20 kV_{pp} Input Driven at 14 kHz. The dashed lines labelled (a) through (e) correspond to control volume widths ($W = x - x_0$) of 10, 20, 30, 40, and 45 mm, respectively.

4.5.2 Comparison of Measurement Methods

A comparison between the control volume analysis and the direct force measurement is shown in Figure 4-15. Two different control volume widths ($W = 40$ and 20 mm) are presented, as well as the direct force measurements with an actuator plate length of 10 cm (note that the difference between $L = 10$ and 15 mm was negligible). Results indicate that the measured and inferred forces are in good agreement over the entire voltage range for the wider (40 mm) control volume. Results also show that if the control volume is of insufficient size, that thrust may be over predicted and eludes that there is a minimum length downstream of the actuator that the

control volume needs to consider. That length however is directly tied to the applied voltage as there is a decent agreement for the smaller control volume width at lower input voltages. Based on these results a downstream extension of ~35 mm is recommended.

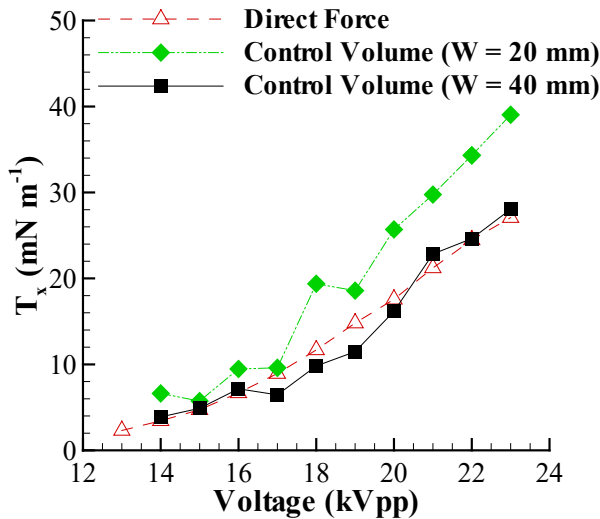


Figure 4-15: Comparison Between Direct Force Measurements and Those Inferred from a Control Volume Analysis. The driving frequency was 14 kHz.

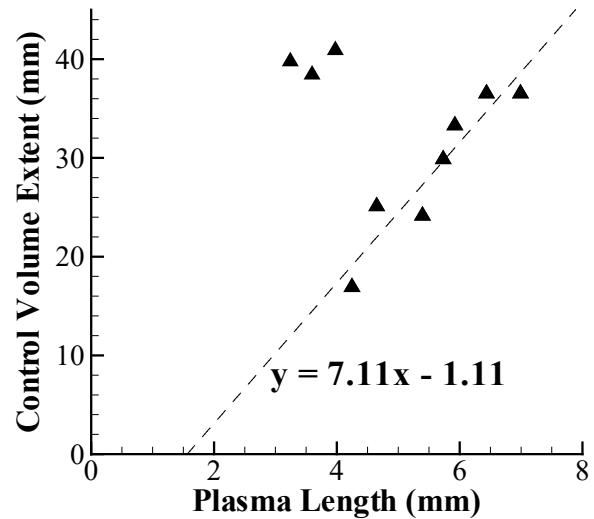


Figure 4-16: Control Volume Scaling.

In order to determine the minimum control volume size requirement, the direct thrust data (Figure 4-8(a) for a plate length of 10 cm) were matched against the thrust verse control volume width curves (examples shown in Figure 4-12). A near linear relationship was observed between the necessary control volume width and voltage. A similar linear trend has been observed by other researchers in terms of the plasma’s downstream extension. To further examine this, the plasma’s length was determined from photographs obtained using a Nikon D90 digital camera. The color images were first converted to grayscale, then binarized using a threshold value of 0.7. A tracing algorithm then mapped out the plasma extension and an average value was then determined. Plotting the necessary/minimum control volume extent verse the plasma length an approximate linear scaling relation, as shown in Figure 4-16 was obtained. This provides an approximation for the minimum control volume size necessary to produce accurate thrust estimates from inferred measurements.

4.6 CONCLUSIONS

The effect of varying the plate length upon which the plasma induced wall jet acted was investigated using a direct force balance. At the upper range of the voltages investigated, an increase in thrust was observed as the plate length was decreased. The thrust was nearly identical for 10- and 15-cm lengths, but an increase in thrust of 20 % was observed as the plate length was reduced to 2.5 cm (a four to six times reduction). Based on these findings, the plate’s length is an important consideration when making comparisons with reported experimental data. PIV measurements were also made on a single DBD actuator at various voltages. These measurements provided time-averaged data sets of the induced flow field. The velocity fields were then subjected to a control volume analysis to infer the resultant thrusts acting on a rectangular volume. The results of the analysis indicated a strong dependency on the size of the considered volume with a particular emphasis on the width of it. When

compared with the direct thrust measurements, the calculated tangential thrust agreed well regardless of the input voltage if the control volume extended far enough downstream. Also, the discharge length was optically measured using visible light emission. A linear correlation was found between the plasma length and the measured thrust for the actuator configurations studied. A suitable control volume size was also recommended based on the plasma length. Finally, to complete the device characterization, the energy conversion efficiency curve for a representative actuator is also plotted.

4.7 ACKNOWLEDGEMENTS

This work was sponsored in part under Air Force Office of Scientific Research Grants #FA9550-09-1-0372 and #FA9550-09-1-0615 monitored by Dr. Doug Smith and Charles Suchomel.

4.8 REFERENCES

- [1] Gibalov, V.I., Pietsch, G.J., The Development of Dielectric Barrier Discharges in Gas Gaps and on Surfaces, *J Phys D Appl Phys* 33(20):2618, 2000.
- [2] Kogelschatz, U., Dielectric-barrier discharges: their history, discharge physics, and industrial applications. *Plasma Chem Plasma Process* 23, 2003, pp. 1-46. doi:10.1023/A:1022470901385
- [3] Xu, X., Dielectric Barrier Discharge – Properties and Applications, *Thin Solid Films* 390(1-2), 2001, pp. 237-242.
- [4] Enloe, C.L., McLaughlin, T.E., Vandyken, R.D., Kachner, K.D., Jumper, E.J., Corke, T.C., Mechanisms and Responses of a Single Dielectric Barrier Plasma Actuator: Plasma Morphology, *AIAA J* 42(3), 2004, pp. 589-594.
- [5] Debien, A., Benard, N., David, L., Moreau, E., Unsteady Aspect of the Electrohydrodynamic Force Produced by Surface Dielectric Barrier Discharge Actuators, *Appl Phys Lett* 100(1), 013901, 2012. doi: 10.1063/1.3674308.
- [6] Enloe, C.L., McHarg, M.G., McLaughlin, T.E., Time-Related Force Production Measurements of the Dielectric Barrier Discharge Plasma Aerodynamic Actuator, *J Appl Phys* 103(7):073302, 2008b.
- [7] Enloe, C.L., McHarg, M.G., Font, G.I., McLaughlin, T.E., Plasma Induced Force and Self-Induced Drag in the Dielectric Barrier Discharge Aerodynamic Plasma Actuator. In: 47th AIAA Aerospace Sciences Meeting Including the New Horizons Forum and Aerospace Exposition, AIAA 2009-1622, 2009.
- [8] Font, G.I., Enloe, C.L., Newcomb, J.Y., Teague, A.L., Vasso, A.R., McLaughlin, T.E., Effects of Oxygen Content on Dielectric Barrier Discharge Plasma Actuator Behavior, *AIAA J* 49(7), 2011, pp. 1366-1373. doi:10.2514/1.55031.
- [9] Ramakumar, K., Jacob, J.D., Flow Control and Lift Enhancement Using Plasma Actuators, In: 35th AIAA Fluid Dynamics Conference and Exhibit, AIAA 2005-4635, 2005.
- [10] Rizzetta, D.P., Visbal, M.R., Plasma-Based Flow-Control Strategies for Transitional Highly Loaded Low-Pressure Turbines, *J Fluids Eng* 130(4):041104, 2008.

- [11] Thomas, F.O., Kozlov, A., Corke, T.C., Plasma Actuators for Landing Gear Noise Reduction, In: 11th AIAA/CEAS Aeroacoustics Conference (26th AIAA Aeroacoustics Conference), AIAA 2005-3010, 2005.
- [12] Little, J., Nishihara, M., Adamovich, I., Samimy, M., High-Lift Airfoil Trailing Edge Separation Control Using a Single Dielectric Barrier Discharge Plasma Actuator, *Exp Fluids* 48, 2010, pp. 521-537. doi:10.1007/s00348-009-0755-x.
- [13] Post, M.L., Corke, T.C., Separation Control on High Angle of Attack Airfoil Using Plasma Actuators, *AIAA J* 42(11), 2004, pp. 2177-2184.
- [14] Labergue, A., Moreau, E., Zouzou, N., Touchard, G., Separation Control Using Plasma Actuators: Application to a Free Turbulent Jet, *J Phys D Appl Phys* 40(3), 2007, p. 674.
- [15] Gibson, B.A., Arjomandi, M., Kelso, R.M., The Response of a Flat Plate Boundary Layer to an Orthogonally Arranged Dielectric Barrier Discharge Actuator, *J Phys D Appl Phys* 45(2):025202, 2012.
- [16] Grundmann, S., Tropea, C., Experimental Damping of Boundary-Layer Oscillations Using DBD Plasma Actuators, *Int J Heat Fluid Flow* 30(3), 2009, pp. 394-402.
- [17] Roth, J.R., Sherman, D.M., Wilkinson, S.P., Electrohydrodynamic Flow Control with a Glow-Discharge Surface Plasma, *AIAA J* 38(7), 2000, pp. 1166-1172.
- [18] Schatzman, D.M., Thomas, F.O., Turbulent Boundary-Layer Separation Control with Single Dielectric Barrier Discharge Plasma Actuators, *AIAA J* 48(8), 2010, pp. 1620-1634.
- [19] Jukes, T.N., Choi, K.-S., Long Lasting Modifications to Vortex Shedding Using a Short Plasma Excitation, *Phys RevLett* 102, 254501, 2009.
- [20] Thomas, F.O., Kozlov, A., Corke, T.C., Plasma Actuators for Cylinder Flow Control and Noise Reduction, *AIAA J* 46(8), 2008, pp. 1921-1931.
- [21] Abe, T., Takizawa, Y., Sato, S., Kimura, N., Experimental Study for Momentum Transfer in a Dielectric Barrier Discharge Plasma Actuator, *AIAA J* 46(9), 2008, pp. 2248-2256.
- [22] Borghi, C.A., Carraro, M.R., Cristofolini, A., Neretti, G., Electrohydrodynamic Interaction Induced by a Dielectric Barrier Discharge, *J Appl Phys* 103(6):063304, 2008.
- [23] Corke, T.C., Post, M.L., Orlov, D.M., SDBD Plasma Enhanced Aerodynamics: Concepts, Optimization and Applications, *Prog Aerosp Sci* 43(7-8), 2007, pp. 193-217.
- [24] Forte, M., Jolibois, J., Pons, J., Moreau, E., Touchard, G., and Cazalens, M., Optimization of a Dielectric Barrier Discharge Actuator by Stationary and Non-Stationary Measurements of the Induced Flow Velocity: Application to Flow Control, *Exp Fluids*, Vol. 43, 2007, pp. 917-928.
- [25] Hoskinson, A.R., Hershkowitz, N., Differences Between Dielectric Barrier Discharge Plasma Actuators with Cylindrical and Rectangular Exposed Electrodes, *J Phys D Appl Phys* 43(6), 065205, 2010.

- [26] Hoskinson, A.R., Hershkowitz, N., Ashpis, D.E., Force Measurements of Single and Double Barrier DBD Plasma Actuators in Quiescent Air, *J Phys D Appl Phys* 41(24), 245209, 2008.
- [27] Jolibois, J., Moreau, E., Enhancement of the Electromechanical Performances of a Single Dielectric Barrier Discharge Actuator, *Dielectr Electr Insulation IEEE Trans* 16(3), 2009, pp. 758-767.
- [28] Roth, J.R., Dai, X., Optimization of the Aerodynamic Plasma Actuator as an Electrohydrodynamic (EHD) Electrical Device, In: 44th AIAA Aerospace Sciences Meeting and Exhibit, AIAA 2006-1203, 2006.
- [29] Thomas, F., Corke, T., Iqbal, M., Kozlov, A., Schatzman, D., Optimization of Dielectric Barrier Discharge Plasma Actuators for Active Aerodynamic Flow Control, *AIAA J* 47(9), 2009, pp. 2169-2178.
- [30] Baughn, J.W., Porter, C.O., Peterson, B.L., McLaughlin, T.E., Enloe, C.L., Font, G.I., Baird, C., Momentum Transfer for an Aerodynamic Plasma Actuator with an Imposed Boundary Layer, In: 44th AIAA Aerospace Sciences Meeting, AIAA 2006-168, 2006.
- [31] Hoskinson, A.R., Hershkowitz, N., Ashpis, D.E., Force Measurements of Single and Double Barrier DBD Plasma Actuators in Quiescent Air, *J Phys D Appl Phys* 41(24): 245209, 2008.
- [32] Kotsonis, M., Ghaemi, S., Veldhuis, L., Scarano, F., Measurement of the Body Force Field of Plasma Actuators, *J Phys D Appl Phys* 44(4):045204, 2011.
- [33] Kriegseis, J., Performance Characterization and Quantification of Dielectric Barrier Discharge Plasma Actuators. Ph.D thesis, TU Darmstadt, 2011a.
- [34] Debien, A., Benard, N., David, L., Moreau, E., Unsteady Aspect of the Electrohydrodynamic Force Produced by Surface Dielectric Barrier Discharge Actuators, *Appl Phys Lett* 100(1):013901, 2012, doi:10.1063/1.3674308
- [35] Kotsonis, M., Ghaemi, S., Veldhuis, L., Scarano, F., Measurement of the Body Force Field of Plasma Actuators, *J Phys D Appl Phys* 44(4):045204, 2011.
- [36] Font, G.I., Enloe, C.L., McLaughlin, T.E., Plasma Volumetric Effects on the Force Production of a Plasma Actuator, *AIAA J* 48(9), 2010, pp. 1869-1874. doi:10.2514/1.51660.
- [37] Westerweel, J., Efficient Detection of Spurious Vectors in Particle Image Velocimetry Data, *Exp Fluids* 16, 1994, pp. 236-247. doi:10.1007/BF00206543.
- [38] Durscher, R., Roy, S., Evaluation of Thrust Measurement Techniques for Dielectric Barrier Discharge Actuators, *Exp Fluids* 53, 2012, pp. 1165-1176. doi :10.1007/s00348-012-1349-6.
- [39] Enloe, C.L., Font, G.I., McLaughlin, T.E., Orlov, D.M., Surface Potential and Longitudinal Electric Field Measurements in the Aerodynamic Plasma Actuator, *AIAA J* 46(11), 2008a, pp. 2730-2740.

Chapter 5 – UNDERSTANDING SDBD ACTUATORS: AN EXPERIMENTAL STUDY ON PLASMA CHARACTERISTICS

Pénélope Leyland

Ecole Polytechnique Fédérale de Lausanne
SWITZERLAND/FRANCE

Rogério Pimentel

DRDC
CANADA

Rik Geuns

Ecole Polytechnique Fédérale de Lausanne
SWITZERLAND /BELGIUM

ABSTRACT

The working mechanisms of Dielectric Barrier Discharge (DBD) plasma actuators foreseen as aerodynamic control devices are investigated experimentally on a common platform, referred to as the NATO-AVT-RTO-190 test case. A better understanding of the working principle and characteristics of DBD paves the way for more efficient and safe use of plasma actuators in aerodynamic applications. In this study, a characterization of the plasma is done by current measurements, fast-camera plasma imaging and thrust measurements. Furthermore, more advanced plasma characteristics such as reduced electric field and excited species population are found by Optical Emission Spectroscopy. The overall goal of this research is to contribute to generate a common database within NATO countries which can also be used for numerical verification and validation by varying the key parameters such as frequency and voltage.

5.1 INTRODUCTION

At low flow speeds, DBD actuators driven by AC waveforms (AC-DBD) have shown to be efficient due to the production of an ionic wind close to the wall, adding momentum to the boundary layer. Recent reviews by Corke et al. [1] and Moreau et al. [2] describe these effects in detail. At higher flow velocities, this equivalent wall jet does not seem to produce significant effects. In a previous study at EPFL, Pavon et al. [3], [4] investigated the interaction between an AC-DBD actuator mounted on a NACA 3506 profile in transonic flow, where no significant effect of the actuator on the shock wave buffeting and strength was observed. However, a strong effect on the discharge plasma state was produced with increasing flow velocities.

Alternatively, studies have been performed on nanosecond pulsed actuators (ns-DBD), showing effects for transonic flows at very high voltage levels [5], [6]. For these actuators, the working mechanism is believed to be the generation of compression waves that emerge from the surface, adding pulsed energy to the flow. Little et al. [7] and Grech et al. [8] have investigated the application of ns-DBD actuators to delay separation for lower flow velocities, up to $u_\infty = 62$ m/s, where the generated compression wave acts as an active trip at pre-stall angles of attack. The plasma produced here is essentially a streamer discharge regime propagating along the surface of the dielectric.

From these considerations, the relevance of understanding the plasma regimes and transitions in such DBD is clear. In order to further develop safe and effective applications of DBD, research on the characterization of these plasmas needs to be performed. The NATO STO AVT-190 working group has suggested a standard DBD setup to investigate the basic characteristics of these plasmas and to evaluate the thrust and relative power

produced, with respect to different input voltages and frequencies from AC or nanosecond pulsed power supplies. The effects of ambient pressure were also investigated at EPFL by placing the DBD in a low-pressure chamber where the pressure levels of the air can be modulated.

In this work, spectroscopy and plasma imaging were performed under different operating conditions (i.e., voltage amplitude, voltage frequency and ambient pressure) at EPFL. Thrust and power measurements were performed for different voltages and frequencies at atmospheric pressure at Laval University (ULaval) in collaboration with DRDC Valcartier.

5.2 EXPERIMENTAL SETUP

The proposed test case considers a DBD setup of copper electrodes on an acrylic type dielectric, PMMA, set up as in Figure 5-1. The thickness of the dielectric plate equals 3 mm and suitable silicon based glue is used to attach the copper electrodes.

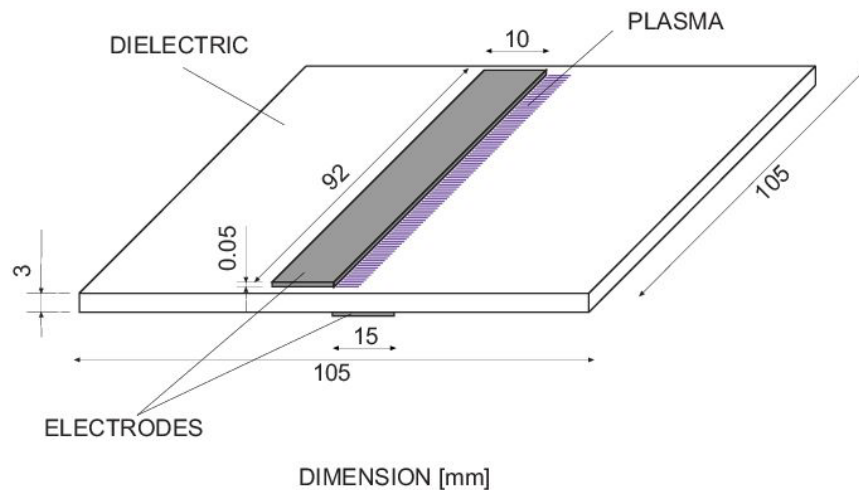


Figure 5-1: Drawing of the DBD Actuator as Used in the Experiments.

In the experiments at EPFL for the dedicated AVT-190 testcase, high voltage is supplied to the actuator by a PM04015-H-CE TREK high voltage function generator (600 VA max) which provides ± 10 kV in AC or DC mode. The TREK power generator is used in amplifier mode, being triggered by a pulse signal from a SCF-AL-018 Rohde and Schwarz function generator. The sine waveform is used for the experiments.

Use of a nanosecond pulse in-house designed generator was also considered, however, the thickness of the dielectric and the design of the AVT-190 test case was not suitable for this kind of plasma generation, for which the plasma characteristics are quite different from those generated by an A/C generator. Indeed, both represent the highly non-equilibrium plasma characteristics of such air plasmas, where the A/C generated DBD plasma represents a complete cycle of discharge physics from the semi-permanent surface microdischarge through the glow discharge to the avalanche process with streamers in the rise and fall times. Whereas the nanosecond pulse generated plasma produces essentially the streamer/avalanche filamentary process, and for similar voltage/frequencies to the A/C conditions would have required a much thinner dielectric.

In order to be able to measure the plasma characteristics at different ambient pressures, the DBD actuator is installed in a low-pressure chamber. A vacuum pump is used to set the pressure in the chamber. Three different pressures are used during the experiments, namely atmospheric pressure, 500 mbar and 250 mbar. The pressure is measured using a MKS Baratron 626A pressure gauge (1-1000 mbar).

A Princeton Instruments Acton SP2750 spectrometer coupled to an ICCD PI-MAX2 fast camera is used for time-resolved spectroscopy. Light emission originating from the plasma is collected through a converging lens with a focal length of 50 mm and captured by a row of 16 fibres. The light is diffracted using a grating of 600 g/mm. At high spectral ranges, a high-pass filter (> 400 nm) is used to filter out the lower wavelengths and avoid second order spectra. The whole optical system is schematically represented in Figure 5-2. The setup is calibrated in intensity using a Labsphere integrating sphere.

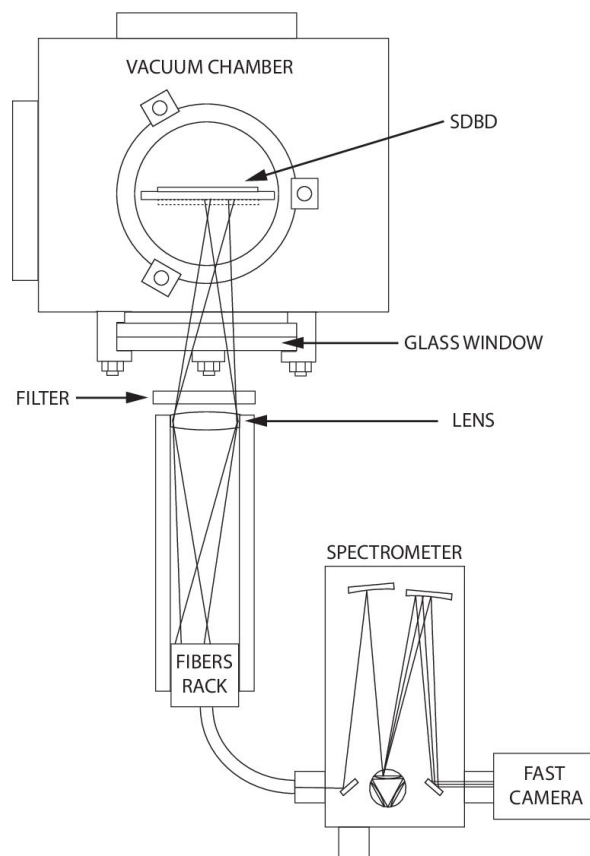


Figure 5-2: Schematic Representation of the Spectroscopy Optical Setup.

A fast current transformer, Bergoz FCT-016-10:1-WB, is used to measure the current signal over time. The frequency response of this coil equals 700 mHz. Data are retrieved from a LeCroy Wavesurfer 454 oscilloscope with a temporal resolution of 4 ns.

At ULaval, thrust measurements were obtained using a precision balance Ohaus Adventurer Pro AV313C (0.001 g precision). For power supply, a combination of an audio amplifier QSC RX2450 with a Corona Magnetic Inc. transformer was used. Detail of the electric circuit used in the experiment is shown in Figure 5-3.

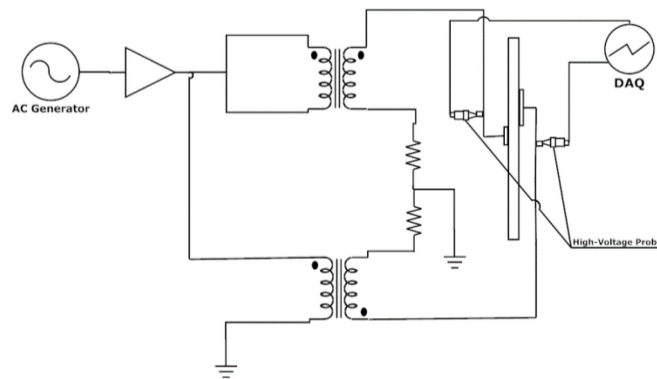


Figure 5-3: Electric Circuit of the Plasma Actuator Setup for Direct Thrust and Power Measurements.

5.3 RESULTS AND DISCUSSION

5.3.1 Current Signal Measurements

Current signal measurements are performed to identify the power consumption by the plasma. Also, these measurements provide useful information about the time span in which streamers are present. In Figure 5-4, a typical DBD current curve is shown. For reference, the measured high voltage signal generated by the amplifier (red line) is plotted together with the reference voltage from the function generator (blue line). While voltage is decreasing, the current disturbances start at about 30% of the cycle and end at approximately 50%. This is referred to as fall time, whereas rise time indicates an increasing voltage. In case of a symmetric DBD actuator, the positive peaks during rise time are similar to the negative peaks during fall time.

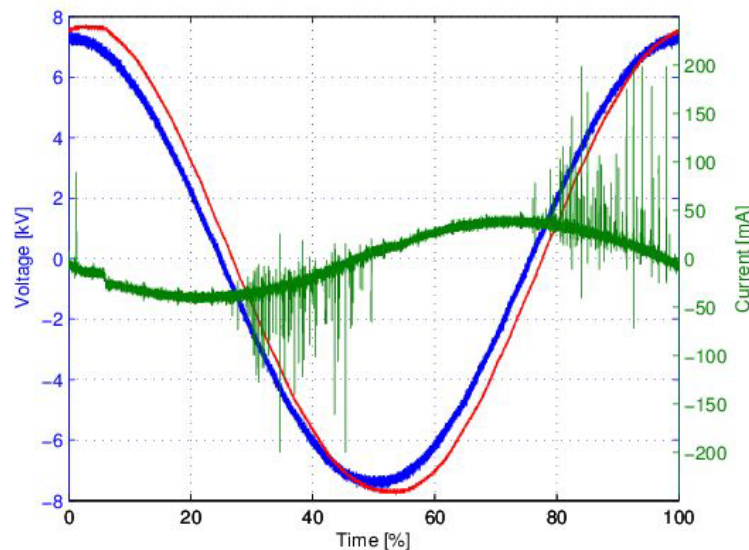


Figure 5-4: Current (Green), Measured Voltage (Red) and Reference Voltage (Blue) vs. Cycle. Measurements are performed at atmospheric pressure, 15 kV and 2.5 kHz.

The current signal encounters ringing, induced by the external electric circuit, which also slightly disturbs the voltage signal [9]. In Figure 5-4, this induces small positive peaks during fall time and negative peaks during the rise time of the voltage signal. The capacitance of the DBD actuator changes with varying current, leading to a change in impedance of the electric circuit and disturbance of the voltage signal.

5.3.2 Effect of Operating Conditions on Current Signal

Under different operating conditions investigated, i.e., voltage amplitude, frequency and operating pressure, the current signal differs. Investigating this current signal reveals properties of the plasma. The amplitude and duration of the peaks is of interest, as it gives an indication of the power consumed. As noise is present in the signal measurements, only peaks which are higher than four times the standard deviation of the current signal are taken into account. The integral of these peaks is calculated. Also, the duration and starting time of the streamers are derived from the current signal in Table 5-1 the aforementioned values are presented.

Table 5-1: Statistics of Current Signal on a Symmetric DBD Actuator for Different Operating Conditions. Measurements Performed at Atmospheric Pressure.

		Unit	10 kV	15 kV
2.5 kHz	Integrated negative peaks	mA · μ s	37.4	136.9
	Number of negative peaks		13.0	39.8
	Duration of signal	μ s	77.8	101.1
	Start of signal	μ s	127.6	109.6
2.5 kHz	Integrated negative peaks	mA · μ s	51.2	182.3
	Number of negative peaks		27.9	79.0
	Duration of signal	μ s	56.1	73.0
	Start of signal	μ s	94.8	79.6

An increase in voltage amplitude leads to an increase of the mean amplitude of the current peaks. Also, the plasma formation starts earlier with rising voltage amplitude and the power consumption has a longer duration. A possible explanation for this is that the breakdown voltage which is needed to initiate plasma generation has been reached earlier in the voltage cycle. Another observation is that the current peaks end when the maximum voltage is reached.

An increase in voltage frequency also increases the mean value of the peaks. On the other hand, it decreases the duration of the plasma streamers and shifts the starting point towards the beginning of the cycle. This can be related to the new shape of the higher frequency signal. As frequency becomes higher, cycle duration becomes shorter and the voltage slope is steeper. Due to this, the breakdown voltage will be reached earlier.

Another set of experiments was conducted using the same DBD actuator on which one electrode (15 mm width) was covered by dielectric tape. The results of these measurements are listed in Table 5-2. As one electrode is covered, the DBD actuator is not symmetric any longer. This leads to a current signal which is not similar during rise and fall time of the voltage signal.

Table 5-2: Statistics of Current Signal on an Asymmetric DBD Actuator for Different Operating Conditions. Measurements performed at atmospheric pressure. Integrated peaks and number of peaks considers positive peaks for the rise time and negative peaks for the fall time.

		Unit	10 kV Fall	10 kV Rise	15 kV Fall	15 kV Rise
2.5 kHz	Integrated peaks	$\text{mA} \cdot \mu\text{s}$	-3.5	31.1	-32.1	103.5
	Number of peaks		5.5	17.6	32.3	53.9
	Duration of signal	μs	47.0	82.4	89.0	96.5
	Start of signal	μs	149.5	321.7	116.9	312.0
3.5 kHz	Integrated peaks	$\text{mA} \cdot \mu\text{s}$	-1.0	52.2	-36.2	180.0
	Number of peaks		2.7	30.2	37.7	95.3
	Duration of signal	μs	32.3	70.1	62.2	72.8
	Start of signal	μs	103.8	231.8	88.5	220.8

5.3.3 Thrust and Power Measurements

For the thrust and power measurements, the asymmetric DBD actuator with covered electrode is used (uncovered and covered electrodes have widths of 5 and 15 mm respectively, the length of both electrodes is equal to 155 mm). The thrust and power consumption results are normalized by unit length of electrodes. A sinusoidal waveform was used during the experiments. The operating conditions during the tests were as follows:

- Temperature: 24.0 ± 0.5 °C.
- Pressure: 100.5 ± 0.5 kPa.
- Humidity: $45.8 \pm 2.5\%$.

In Figure 5-5 the results of normalized thrust for different driven voltage (10 to 30 kV_{pp}) and frequency (3.5, 7 and 14 kHz) are presented. In this figure it is shown that thrust generated by the actuator increases as the driven frequency or voltage increases.

Thrust was obtained from 5 independent measurements after the precision balance stabilized (after about 1 second). Standard deviation of the measurements was below 2%. Typical thrust measurements obtained with the precision balance are shown in Figure 5-6.

The power consumption also increases with driven frequency or voltage, as can be seen in Figure 5-7. From this figure, it can be found that, during the experiments at driven frequencies of 3.5, 7.0 and 14.0 kHz, the normalized power consumption followed the power-law function with a power exponent varying from 3.4 to 4.0.

In Figure 5-8, the thrust/power performance parameter is presented. The results suggested that an optimal condition for operating the DBD plasma actuator exists. For this test case, this optimal is found to be approximately 20 kV_{pp}. From this figure, it can be concluded that the lower frequency (3.5 kHz) is more efficient compared to the higher frequencies tested (7 and 14 kHz) in terms of thrust to power ratio.

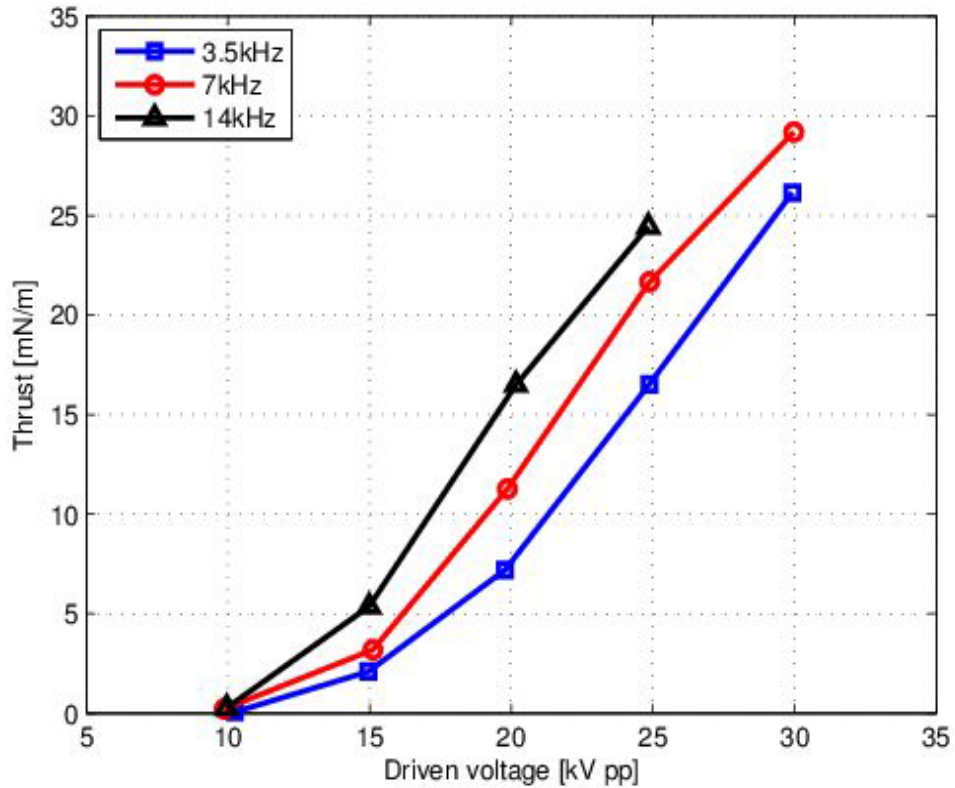


Figure 5-5: Effect of Driven Voltage and Frequency on the Thrust Generated by the Actuator.

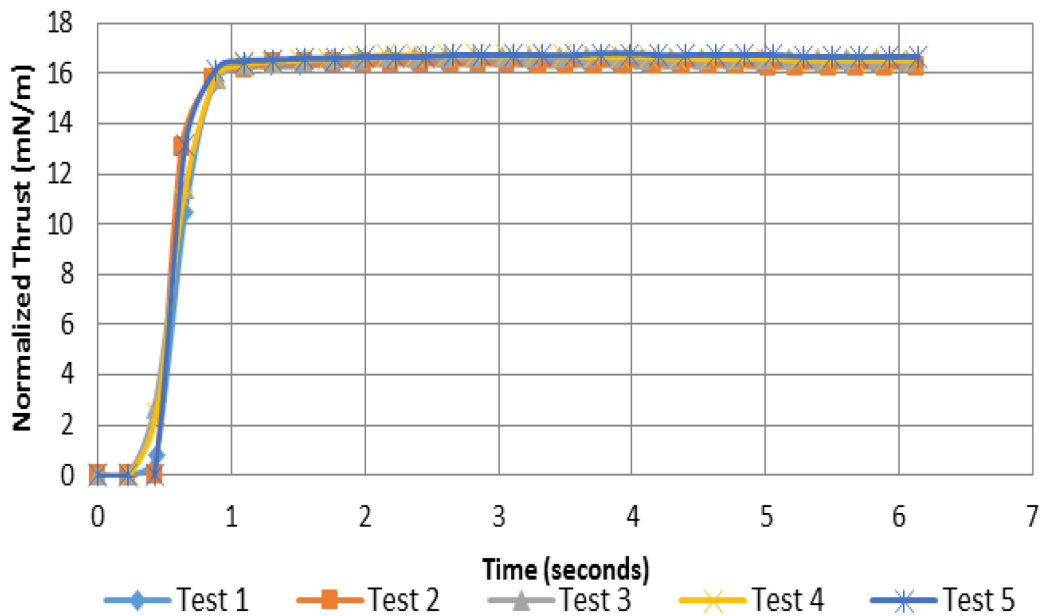


Figure 5-6: Evolution of Normalized Thrust in Time – 25 kV_{pp} @ 3.5 kHz.

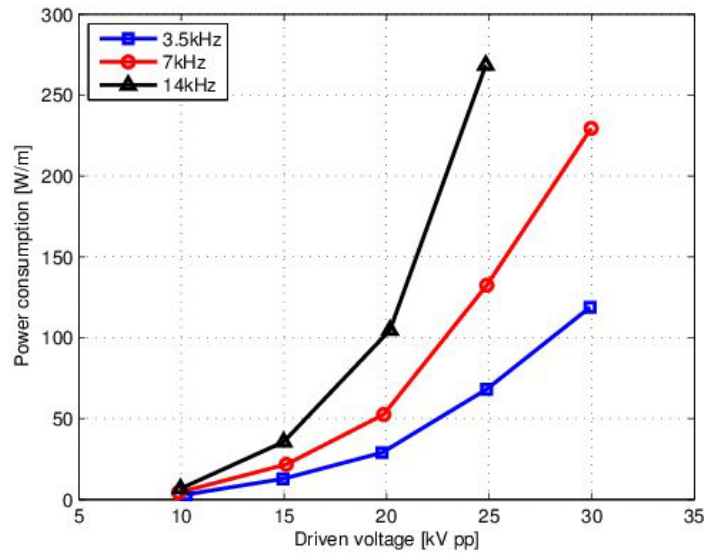


Figure 5-7: Effect of Driven Voltage and Frequency on the Power Consumption of the Actuator.

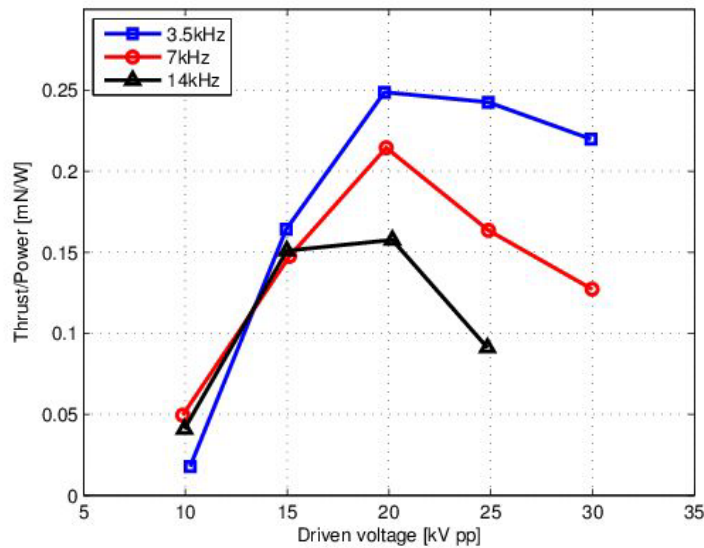


Figure 5-8: Effect of Driven Voltage and Frequency on the Actuator Performance.

5.3.4 Plasma Imaging

In order to better understand the development and propagation of streamers in the air gap between the electrodes, time-resolved synchronized plasma imaging has been performed. Resulting images show a clear distinction between the two phases in Figure 5-4 during rise and fall time of the voltage signal. In Figure 5-9, examples of images during rise and fall time of the signal are shown. During rise time of the voltage signal (pictures (d),

(e) and (f)), the streamers clearly originate at the upper electrode and propagate through the air gap towards the lower electrode. During fall time of the signal (pictures (a), (b) and (c)), this structure is less clear. Here, the propagation of the streamers is far less pronounced. The plasma extends over a length of about 4 mm during rise time, whereas it only extends over about 1 mm during fall time. Nevertheless, both rise and fall time streamers seem to originate at the upper electrode.

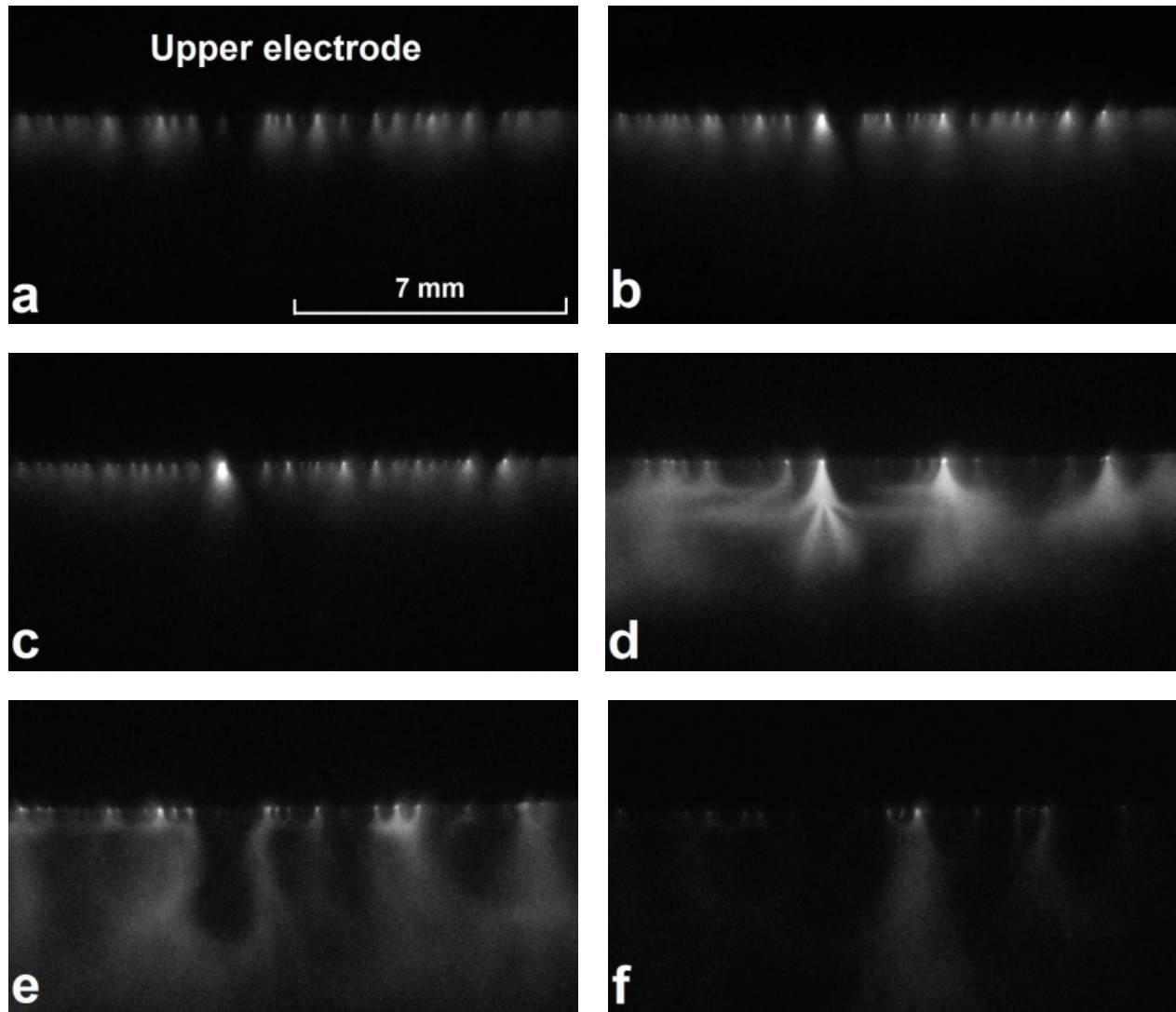


Figure 5-9: Streamer Propagation Images During Fall (a), (b), (c); and Rise (d), (e), (f); Time of the Voltage Signal. Pictures (a), (b) and (c) correspond to 30, 40 and 50 % of cycle time respectively. Pictures (d), (e) and (f) correspond to 80, 90 and 100 %.
Voltage amplitude and frequency are 15 kV and 2.5 kHz respectively.
Measurements performed at atmospheric pressure.

The difference in streamer mechanisms during rise and fall time of the voltage signal is further elaborated in Figure 5-10, where the light intensity of the plasma images is plotted against time for two different ambient pressures and voltages. A first observation is that the light emission during rise time of the signal is higher than

the light emission during fall time in both cases. The peak values for intensity are comparable, which indicates that the maximum light intensity is of the same order for a constant ratio of voltage over pressure. The light emission is initiated earlier at atmospheric pressure and higher voltage compared to the measurements performed at lower voltages. This observation is in agreement with the duration and starting time of the current signal measurements presented in Table 5-2. Furthermore, in Figure 5-10, two sets of image intensities are plotted using the same conditions for voltage, frequency and ambient pressure. The alignment of the curves is nearly exact, indicating a high repeatability of plasma imaging in terms of intensity.

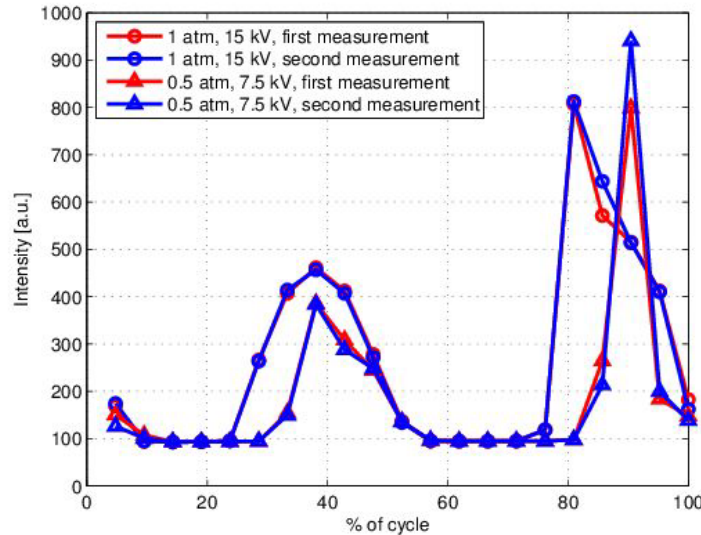


Figure 5-10: Image Intensity Over Cycle Time for Voltage Amplitudes 15 kV and 7.5 kV at Atmospheric Pressure and 500 mbar. All measurements performed at 2.5 kHz.

5.3.5 Spectral Analysis

Excited species are produced in the plasma, mostly by transfer of energy between energetic electrons and molecules (or atoms). These excited species can de-excite to a state possessing a lower energy, either by colliding with another molecule (quenching) or by radiative decay, i.e., by the release of a photon. The spectrum of this light depends on the electronic structures of the upper and lower states, and therefore allows the unambiguous identification of excited species by analyzing the spectrum of the light. The light spectrum emitted by the DBD was analyzed in this study using a spectrometer coupled to a fast camera, as described in the experimental setup.

5.3.6 Spectral Features of the Plasma

Two main regions of the spectral intensities are identified as significant for such discharges: the zone between 380 to 410 nm, and the one between 700 – 785nm. For the first range, the most intense part of the spectrum emitted by the plasma is due to the transition $N_2(C^3\Pi_u - B^3\Pi_g)$, i.e., the Second Positive System (SPS) of nitrogen. Besides this transition, also the transition $N_2^+(B^2\Sigma_u^+ - X^2\Sigma_g^+)$, the first negative system of $N_2^+N_2^+$, was clearly identified. It reveals the presence of the ion $N_2^+N_2^+$. Both transitions can be seen in Figure 5-11. The spectrum is recorded using light emission collected from 4000 cycles (accumulations). For the second zone, the

first positive system of nitrogen (FPS), $N_2^+(B^3\Pi_g - A^3\Sigma_u^+)$, and atomic lines due to oxygen and argon were also identified, as shown in Figure 5-12. However, these transitions were much weaker. In order to obtain the same order of intensity as in Figure 5-11, more than 100,000 accumulations were needed.

5.3.7 Excited Species

The spectra recorded were analyzed with an in-house spectral code, able to simulate the spectrum from several spin-allowed transitions of diatomic molecules and some atomic transitions. The determination of the intensities of the rotational lines from the spectra of diatomic molecules is computed following Whiting [10]. The emission coefficients are taken from Gilmore [11]. The location of the rotational lines is computed by the method outlined by Hornkohl [12]. Lambda doubling was neglected apart for the first positive system. The population of excited species was assumed to be at rotational equilibrium but not at vibrational or electronic equilibrium. The vibrational level specific spectra were therefore computed independently. The simulated spectra were fitted to the experimentally recorded spectra using the least square method, which allowed the accurate determination of the population densities of excited species. The resulting excited species populations for the same conditions as Figure 5-11 are shown in Figure 5-13.

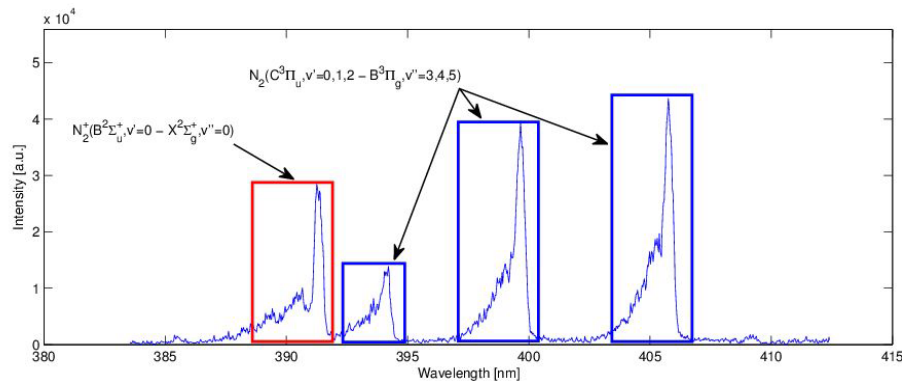


Figure 5-11: Spectrum at 385 nm to 410 nm. Voltage and frequency are respectively 15 kV and 2.5 kHz. Measurement performed at atmospheric pressure.

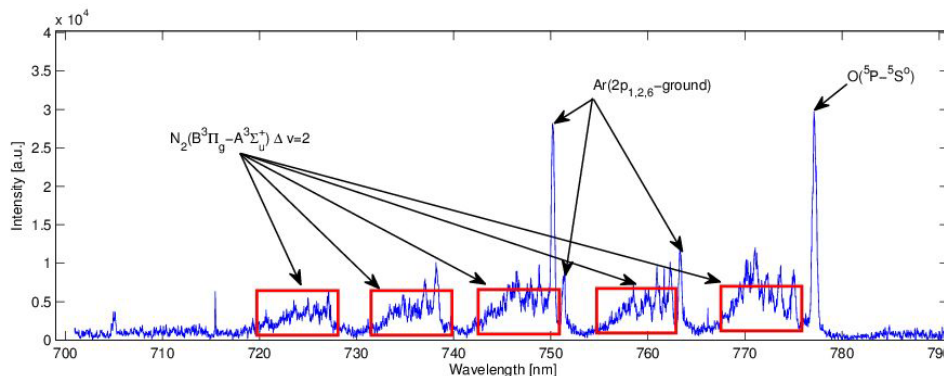


Figure 5-12: Spectrum at 710 nm to 790 nm. Voltage and frequency are respectively 15 kV and 2.5 kHz. Measurement performed at atmospheric pressure.

5.3.8 Determination of the Reduced Electric Field

If the excited species are assumed to be produced only by electron impacts from the ground state and de-excited only by spontaneous radiative decay and two-body collisional de-excitation (quenching), it is possible to determine the average reduced electric field of the plasma. With these assumptions, the evolution of the populations of excited species can be described by the relation given in Equation 5-1.

$$\frac{dn_i}{dt} = n_e X_i K_i \left(\frac{E}{N} \right) - \frac{n_i}{\tau_i} \quad (5-1)$$

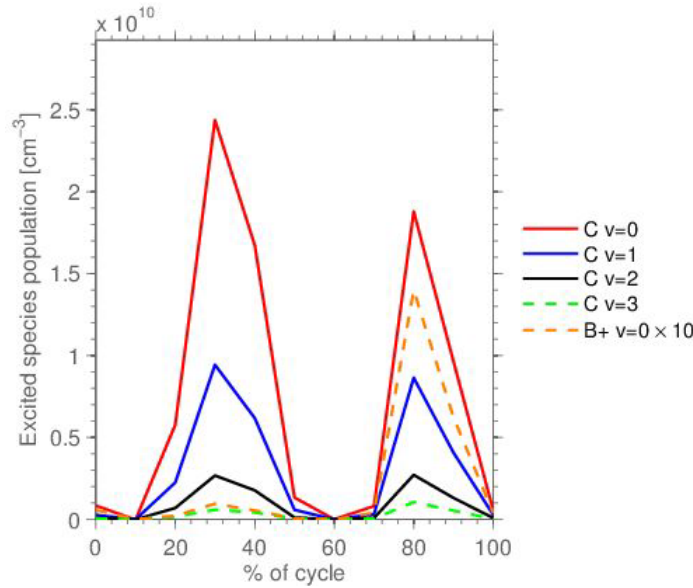


Figure 5-13: Excited Species Population Over Cycle Time for 15 kV and 2.5 kHz at Atmospheric Pressure. C v = 0,1,2,3 and B+ v = 0 represent excited species population density of states $N_2(C^3\Pi_u; \nu = 0; 1; 2; 3)$ and $N_2^+(B^2\Sigma^+_u; \nu = 0)$ states respectively.

In equation 5-1, $K_i(E/N)$ is the production rate for the electron-impact excitation process i , which depends on $E/NE/N$. X_i is the target gas density. τ_i is the total lifetime of the excited state i , calculated as:

$$\tau_i = 1/\tau_0^i + Q_{N_2}^i N_2 + Q_{O_2}^i O_2,$$

where τ_0^i is the radiative lifetime of the species i and Q_x^i is the quenching rate of the i^{th} state by the quencher X . From Equation 5-1, Equation 5-2. is obtained.

$$0 = n_e X_i K_i \left(\frac{E}{N} \right) - \frac{n_i}{\tau_i} \quad (5-2)$$

The experimental determination of the reduced electric field can be performed by comparing the relative population of two different excited species. By dividing Equation 5-2 for two different excited species, an equation in which only the reduced electric field is unknown is obtained. The production rates for the excitation process are computed using Equation 5-3.

$$K_i \left(\frac{E}{N} \right) = \frac{2e}{m} \int_0^\infty \varepsilon \sigma_i^e F_0 d\varepsilon \quad (5-3)$$

In Equation 5-3, $\varepsilon = mv^2 / (2e)$ is the kinetic energy of the electron, F_0 is the Electron Energy Distribution Function (EEDF), which is computed using for example the Boltzmann solver Bolsig+ [13] and σ_i^e is the excitation cross section. The references corresponding to the excitation cross sections and quenching rates of the excited species used in this study are shown in Table 5-3. The resulting plots for reduced electric field strength for atmospheric and low pressure are shown in Figure 5-14 and Figure 5-15 respectively.

Full details of the collisional – radiative model derived here can be found in the thesis of Sami Goekce [20].

Table 5-3: Electron-Impact Excitations and References for the Corresponding Excitation Cross Sections and Quenching Rates.

Process	Reference for E-impact	Reference for Quenching
$N_2(X^1\Sigma_g^+) + e \rightarrow N_2(B^3\Pi_g) + e$	Tabata 2006 [14]	Piper 1992 [15]
$N_2(X^1\Sigma_g^+) + e \rightarrow N_2(C^3\Pi_u) + e$	Tabata 2006 [14]	Dilecce 2007 [16] Pancheshnyi 1992 [17]
$N_2(X^1\Sigma_g^+) + e \rightarrow N_2^+(B^2\Sigma_u^+, v = 0) + 2e$	Tabata 2006 [14]	Valk 2010 [18]
$Ar(\text{ground}) + e \rightarrow Ar(2p_1) + e$	Boffard 2007 [19]	Sadeghi 2001 [20]

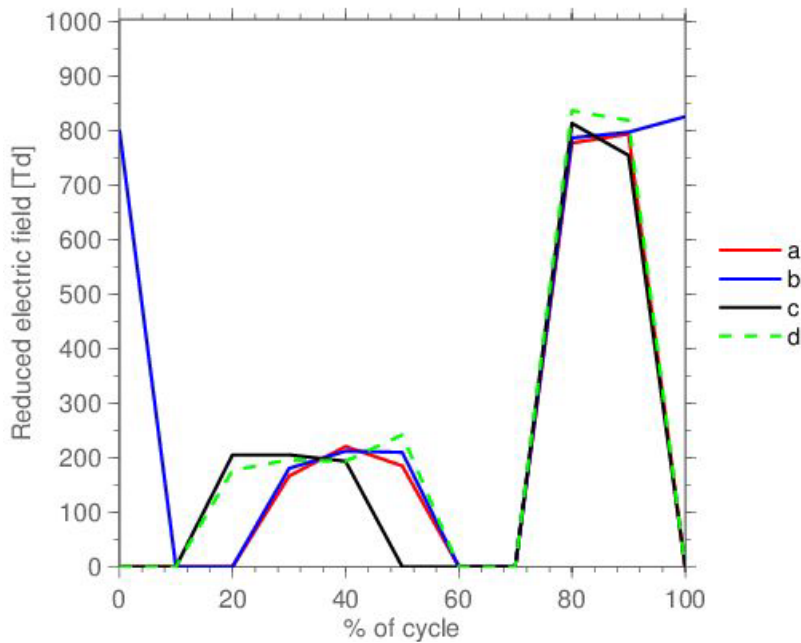


Figure 5-14: Reduced Electric Field Over Cycle Time for (a) 10 kV, 2.5 kHz; (b) 10 kV, 3.5 kHz; (c) 15 kV, 2.5 kHz; (d) 15 kV, 3.5 kHz. Measurements performed at atmospheric pressure.

In Figure 5-14, the electric field differs during rise and fall time of the voltage signal. During the rise time, the reduced electric field is approximately 800 Td, whereas during fall time, it only reaches about 200 Td. This behavior is observed for all measured conditions. Furthermore, at the highest voltage (15 kV), the breakdown electric field value is reached earlier in the cycle. This corresponds to the current signal measurements in Table 5-2 and image intensity in Figure 5-10. However, this behavior is only observed during fall time. A different trend is observable in Figure 5-15, where the electric field value starts increasing earlier in the cycle during rise time for the cases with highest voltage over pressure ratio.

It is clearly seen by these studies that in order to accurately investigate the reduced electric field and electron density behavior with respect to the plasma regimes and voltage cycle, a complete parametric study needs to be performed, thereby ranging voltage, frequency and ambient pressure independently.

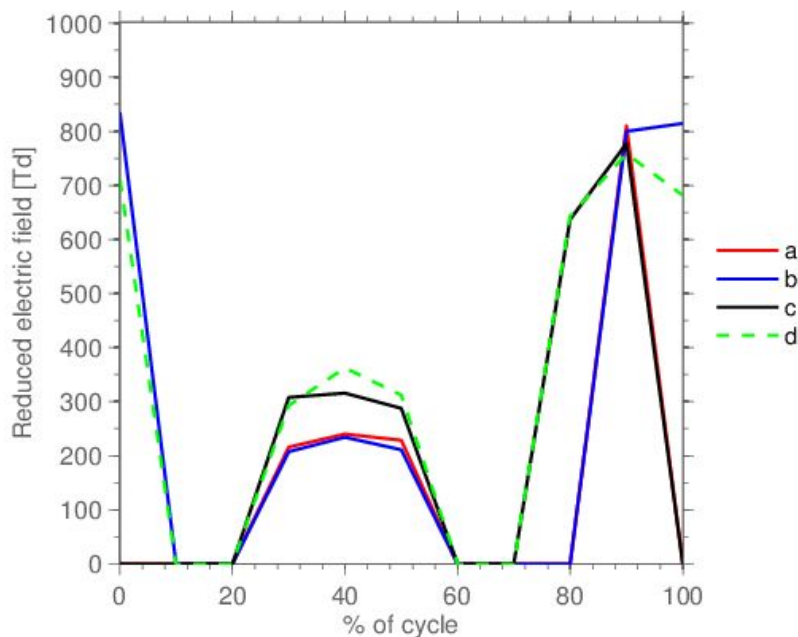


Figure 5-15: Reduced Electric Field Over Cycle Time for (a) 7.5 kV, 2.5 kHz, 500 mbar; (b) 7.5 kV, 3.5 kHz, 500 mbar; (c) 5 kV, 2.5 kHz, 250 mbar; (d) 5 kV, 3.5 kHz, 250 mbar.

5.4 CONCLUSIONS

Plasma characteristics of the NATO-AVT-RTO-190 AC-DBD test case were analyzed experimentally. Current signal measurements revealed information about the strength, duration and starting time of the plasma for different voltages and frequencies. A higher voltage or frequency shifts the starting point of the plasma towards the beginning of the cycle, as the breakdown voltage is reached earlier. The number of current peaks increases with rising voltage or frequency.

Thrust and power consumption measurements were performed for different driven voltages and frequencies. The results showed that the thrust generated by the actuator increases as the driven frequency or voltage increases. An optimal condition for operating the DBD plasma actuator exists, and pushing for higher voltage levels is not necessary.

Detailed fast-camera imaging and spectroscopy allows understanding of the plasma's transitions and characteristics, as well as their temporal evolution with respect to different operating conditions of voltage, frequency and ambient pressure. From Optical Emission Spectroscopy, the excited species in the plasma are detected and the reduced electric field is calculated. These are in agreement with trends noticed during current measurements and plasma imaging.

5.5 REFERENCES

- [1] Corke, T., Enloe, C., and Wilkinson, S. Dielectric Barrier Discharge Plasma Actuators for Flow Control, *Annual Review of Fluid Mechanics*, Vol. 42, No. 1, Jan. 2010, pp. 505-529.
- [2] Moreau, E., Louste, C., and Touchard, G. Electric Wind Induced by Sliding Discharge in Air at Atmospheric Pressure, *Journal of Electrostatics*, Vol. 66, No. 1-2, Jan. 2008, pp. 107-114.
- [3] Pavon, S., Dorier, J.L., Hollenstein, C., Ott, P., and Leyland, P. Effects of High-Speed Airflows on a Surface Dielectric Discharge, *Journal of Physics D: Applied Physics*, Vol. 40, No. 6, 2007.
- [4] Pavon, S., Ott, P., Leyland, P., Dorier, J.L., and Hollenstein, C. Effects of a Surface Dielectric Barrier Discharge on Transonic Flows Around an Airfoil, *AIAA 2009-649*, 47th AIAA Aerospace Sciences Meeting, Orlando, FL, USA, 2009.
- [5] Roupasov, D.V., Nikipelov, A.A., Nudnova, M.M., and Starikovskii, A.Y. Flow Separation Control by Plasma Actuator with Nanosecond Pulsed-Periodic Discharge, *AIAA Journal*, Vol. 47, No. 1, 2009.
- [6] Starikovskii, A.Y., Nikipelov, A.A., Nudnova, M.M., and Roupasov, D.V. SDBD Plasma Actuator with Nanosecond Pulse-Periodic Discharge, *Plasma Sources Sci. Technol.*, Vol. 18, No. 3, 2009.
- [7] Little, J., Takashima, K., Nishihara, M., Adamovich, I., and Samimy, M. High lift Airfoil Leading Edge Separation Control with Nanosecond Pulse Driven DBD plasma Actuators, *AIAA 2010-4256*, 5th AIAA Flow Control Conference, Chicago, IL, USA, 2010.
- [8] Grech, N., Peschke, P., and Leyland, P. Investigation of Flow Separation Control by Nanosecond Pulsed Dielectric Barrier Discharge Actuators, *Progress in Flight Physics Volume 6: Selected papers of the EUCCAS 2013 5th European Conference for Aeronautics and Space Sciences*, Munich, Germany, 2013, 2014.
- [9] Pavon, S., *Interaction Between a Surface Dielectric Barrier Discharge and Transonic Airflows*, EPFL thesis, Vol. 4201, 2008.
- [10] Whiting, E.E. and Center, A.R.. *Computer Program for Determining Rotational Line Intensity Factors for Diatomic Molecules*, National Aeronautics and Space Administration, 1973.
- [11] Gilmore, F.R., Laher, R.R., and Espy, P.J. Franck-Condon Factors, r-Centroids, Electronic Transition Moments, and Einstein Coefficients for Many Nitrogen and Oxygen Band Systems, *Journal of Physical and Chemical Reference Data*, Vol. 21, No. 5, 1992, pp. 1005-1107.
- [12] Hornkohl, J.O., Parigger, C.G., and Nemes, L. Diatomic Hönl-London Factor Computer Program, *Appl Opt*, Vol. 44. 18, June 2005, pp. 3686-3695, PMID: 15989043.

- [13] Hagelaar, G.J.M. and Pitchford, L.C. Solving the Boltzmann Equation to Obtain Electron Transport Coefficients and Rate Coefficients for Fluid Models, *Plasma Sources Science and Technology*, Vol. 14, No. 4, Nov. 2005, pp. 722-733.
- [14] Tabata, T., Shirai, T., Sataka, M., and Kubo, H. Analytic Cross Sections for Electron Impact Collisions with Nitrogen Molecules, *Atomic Data and Nuclear Data Tables*, Vol. 92, No. 3, May 2006, pp. 375-406.
- [15] Piper, L.G. Energy transfer Studies on $N_2(X\ 1\Sigma^+g, v)$ and $N_2(B\ 3\Pi_g)$, *The Journal of Chemical Physics*, Vol. 97, No. 1, July 1992, pp. 270-275.
- [16] Dilecce, G., Ambrico, P.F., and Benedictis, S.D. New $N_2(C\ 3\Pi_u, v)$ Collision Quenching and Vibrational Relaxation Rate Constants: PG Emission Diagnostics of High-Pressure Discharges, *Plasma Sources Science and Technology*, Vol. 16, No. 1, Feb. 2007, pp. S45-S51.
- [17] Pancheshnyi, S.V., Starikovskaia, S.M., and Starikovskii, A.Y. Measurements of Rate Constants of the $N_2(C^3\Pi_u, v = 0)$ and $N_2+(B^2\Sigma_g^+ u, v = 0)$ Deactivation by N_2 , O_2 , H_2 , CO and H_2O Molecules in Afterglow of the nanosecond Discharge, *Chemical Physics Letters*, Vol. 294, No. 6, Sept. 1998, pp. 523-527.
- [18] Valk, F., Aints, M., Paris, P., Plank, T., Maksimov, J., and Tamm, A., Measurement Of Collisional Quenching Rate of Nitrogen States $N_2(C^3\Pi_u, v = 0)$ and $N_2^+ B_2$, *J. Phys. D: Appl. Phys.*, Vol. 43, No. 38, Sept. 2010, pp. 385202.
- [19] Boffard, J.B., Chiaro, B., Weber, T., and Lin, C.C. Electron-Impact Excitation of Argon: Optical Emission Cross Sections in the Range of 300 – 2500nm, *Atomic Data and Nuclear Data Tables*, Vol. 93, No. 6, Nov. 2007, pp. 831-863.
- [20] Sadeghi, N., Setser, D.W., Francis, A., Czarnetzki, U., and Döbele, H.F., Quenching Rate Constants for Reactions of $Ar(4p'[1/2]0, 4p[1/2]0, 4p[3/2]2, \text{ and } 4p[5/2]2)$ Atoms with 22 reagent Gases, *The Journal of Chemical Physics*, Vol. 115, No. 7, Aug. 2001, pp. 3144-3154.
- [21] Goekce. S. Plasma Diagnostics and Modelling of Nanosecond Pulsed Surface Dielectric Barrier Discharge Actuators. EPFL, Lausanne, 2014. Doi: 10.5075/epfl-thesis-6282.

Chapter 6 – FLOW CONTROL AT SUBSONIC SPEEDS USING SERPENTINE PLASMA ACTUATORS

K. Kontis

University of Glasgow
UNITED KINGDOM

ABSTRACT

The use of plasma actuators for flow control applications is fast becoming the subject of many research campaigns. A drawback of this technique is the relatively low flow speeds that the plasma induced jet exhibits. One method of enhancing the influence of such actuators, is to devise novel actuator configurations that despite their low induced speeds still have the ability to considerably manipulate the flow characteristics. The objective of the current study is to apply the newly developed serpentine plasma actuator to a standard backwards facing step model in a low-speed wind tunnel operating at 15 m/s. The influence of the actuator on the separated shear layer is examined using PIV. The results show that due to the three-dimensional flow induced by the actuator, the shear layer exhibits different characteristics along the span wise direction. It is believed that using plasma actuators with three-dimensional flow characteristics has the ability to create greater control authority at the relatively low plasma induced velocities.

6.1 INTRODUCTION

The Single Dielectric Barrier discharge (SDBD) plasma actuator consists of two electrodes flush-mounted on the opposite faces of a dielectric plate: one is exposed to the flow and the other is placed under the body's surface and insulated by a dielectric material [1], [2]. A high AC voltage is applied to the exposed electrode using a particular waveform, usually sine or square waveforms. This results in a weakly ionized region above the dielectric, referred to as surface non-thermal plasma discharge. The electrochemical interactions between air and plasma lead to complex plasma kinetic phenomena resulting in production of a wall tangential jet flow due to a self-sustaining process involving high rate of collisions between neutral and charged particles. Ramakumar and Jacob [3] showed, in their experiments with quiescent flow, that sine waveforms perform better than square and sawtooth waveforms in terms of plasma induced velocities; this is also confirmed by Jolibois and Moreau [4] which discourages the use of high-sloped waveforms such as square or sawtooth. The high AC applied ionizes the atmospheric air adjacent to the exposed electrode creating plasma which, due to the electric field gradient, results in a body force inducing airflow along the actuator surface.

Balcon et al. [5] in a study on plasma actuators performed in absence of flow, evaluated the time required by the plasma induced airflow to reach a stationary state (using a fixed 1 kHz sine wave at an amplitude of 20 kV); PIV flow investigation aimed to an evaluation of turbulent kinetic energy, have shown that for short unsteady actuations (< 100 m/s) a vortex is created and convected downstream and after 400 m/s the flow can be considered in a steady state.

Most of the literature refer to experiments aimed at delaying separation on general aviation aerofoils and turbine blades, particular interest is given to unsteady actuation of plasma devices specifically by varying the frequency and duty cycle. Huang et al. [6] applied an SDBD actuator on a turbine blade for separation control for Reynolds number ranging from 10000 to 100000, both steady and unsteady actuation were studied. Steady actuation resulted in a decrease of the separation bubble size proportional to the voltage increase. Unsteady excitation

caused vortical structures that are thought to bring more momentum to the fluid, hence helping to withstand adverse pressure gradients. The optimal forcing frequency was found corresponding to a Strouhal number $St = 1$ and this was confirmed by the improved pressure coefficient on the aerofoil's suction side for $St = 1$. Benard et al. [7] studied both steady and unsteady actuation on a NACA 0015 aerofoil in a free stream velocity of 20 m/s, resulting in a Reynolds number, based on the chord length of approximately 2.6×10^5 . For a steady actuation the results showed an increase in the stall angle between 1° and 2° (linearly with the increasing voltage amplitude), an increase of CL at baseline post-stall angles of attack (reaching + 60% at 15°) and good CD reduction for higher voltage values (reaching a reduction of -37% at 15°) showing CD to be more sensitive to frequency. Similar advantageous findings have been reported elsewhere [8], [9].

Interesting new designs of plasma actuators have been developed and tested recently in order to increase the actuation authority on the flow. Roy et al. [10], [11], [12] designed serpentine shaped actuators, as shown in Figure 6-1 and tested them in quiescent flow, also comparing different serpentine shapes with the straight actuator case. The results were also validated by simulations and showed a remarkable increment in the introduction of vortical structures, due to their peculiar pinch – spread effect. A complex three-dimensional corkscrew structure is produced and a noticeable plume expands from the pinch section of the actuator at an angle ranging from 38° to 43° .

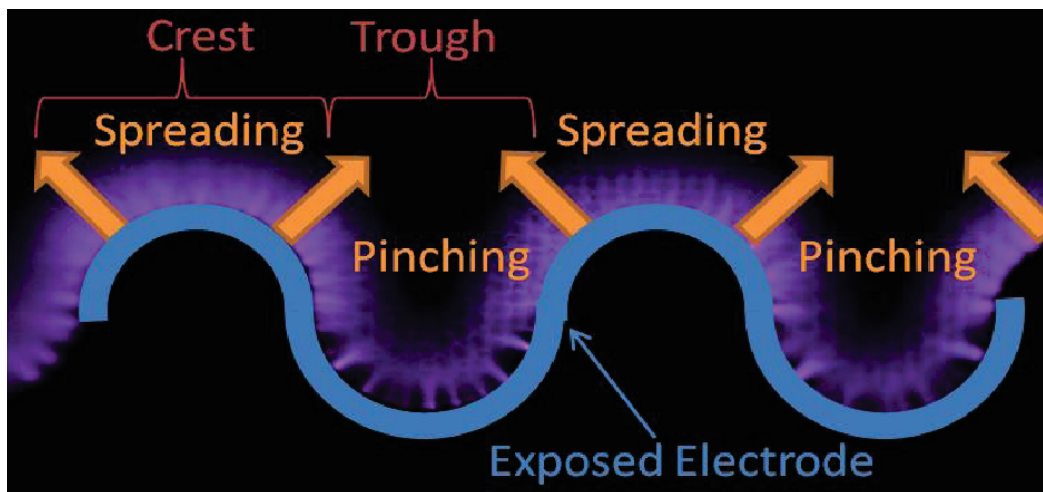


Figure 6-1: Pinch-Spread Effect Given by Serpentine Plasma Actuator [13].

The purpose of this experimental campaign is to apply the aforementioned serpentine plasma actuator to a backwards facing step model in a low-speed wind tunnel and examine the three-dimensional influence the plasma induced jet has on the shear layer characteristics.

6.2 EXPERIMENTAL SETUP

6.2.1 Wind Tunnel

Experiments are conducted in an open-return wind tunnel with a total working section of 5.5 m in length, cross section of $0.9 \text{ m} \times 0.9 \text{ m}$, and maximum operating speed of 20 m/s with a nominal free stream turbulence of 0.5%. Cross-wire measurements were conducted at a specific measurement location with a free stream

velocity of 15 m/s to determine the boundary layer height at this location. A backwards facing step was then introduced at this location, 3.5 m from the tunnel entrance, equal to the boundary layer height (h) of 65 mm.

6.2.2 Particle Image Velocimetry

The PIV system used for the experiments uses a pulsed Nd:YAG laser (Litron Lasers, model Nano L PIV). It is a double oscillator laser system, providing a laser beam at a wavelength of 532 nm. The system is composed of a power supply, the laser box, and an adjustable laser arm. The movable arm allows the laser beam to be positioned in the preferred location within the wind tunnel. At the end of the laser arm, a cylindrical lens is mounted, expanding the laser into a thin sheet of approximately 1 mm thick. The camera used to capture the consecutive images is a LaVision Imager ProX 2M CCD camera. It uses a KAI-2001 interline-CCD sensor sized 1600×1200 pixels (each being a square of side $7.4 \mu\text{m}$) with a dynamic range of 14 bits. A total of 400 image pairs were collected for each test case. The recorded image pairs are initially divided into 32×32 pixel interrogation windows and then processed with a cross-correlation algorithm using the DaVis 7.2 software, the interrogation windows are then refined to 16×16 pixel squares.

For the actuator in quiescent conditions, a Δt of $430 \mu\text{s}$ was selected, whereas for the actuator with free stream flow the Δt was reduced to $31 \mu\text{s}$. The time intervals were calculated by the software depending on the camera resolution, the image field of view, and an allowable particle displacement of 5 pixels. To create tracer particles a TSI six-jet atomizer model 9307-6 was used. The seeder is capable of creating particles with a diameter of approximately 1 microns [14].

6.2.3 Plasma System

High voltage is generated using a Voltcraft 3610 power supply connected to a circuit board which can output a variety of signals. A shielded connector block by National Instruments is used to connect the circuit board to a computer, using a PCI-6713 analog output card. LabView is used to control the driving frequency, modulation frequency, duty cycle, phase, and signal shape of the system, which has a maximum output of 30 kHz at 0 to 100 % DC. The final output is connected to a Minipulse 6 transformer, capable of 30 kHz output at voltages up to $40 \text{ kV}_{\text{p-p}}$ (peak-to-peak voltage). The voltage and frequency of the output signal are measured with a high voltage probe LeCroy PPE 20 kV, while a current probe in the transformer is used to measure current. The experiments with the serpentine actuator were performed at $16 \text{ kV}_{\text{p-p}}$.

6.3 RESULTS

Figure 6-2(a) and Figure 6-2(b) show the time-averaged velocity contours corresponding to the PIV laser sheet placed along the pinch and spread regions of the actuator, respectively. The actuator in this figure is placed on the step, however there is no free stream flow. It is clear that at the pinch location, the induced flow has a stronger upwards component compared to the spread region. This is because at this location, the induced jet from opposite sides collide head-on and the interaction leads to an upward motion of the flow.

The turbulence Reynolds stress, R_{xy} is an important dynamic quantity affecting the mean flow since it is responsible for a major part of the momentum transfer due to turbulent fluctuations. The Reynolds stress is not only an indicator of the r.m.s. velocities but also related to vorticity which has strong influence on mixing, making it a suitable parameter to analyze. The calculated Reynolds stresses are provided in Figure 6-3 for the quiescent actuator along the pinch and spread locations. In Figure 6-3(a) two dominant areas of high R_{xy} are identifiable, the first is tangential to the step and the other region is pointing away from the step upwards on at an approximately 40° angle.

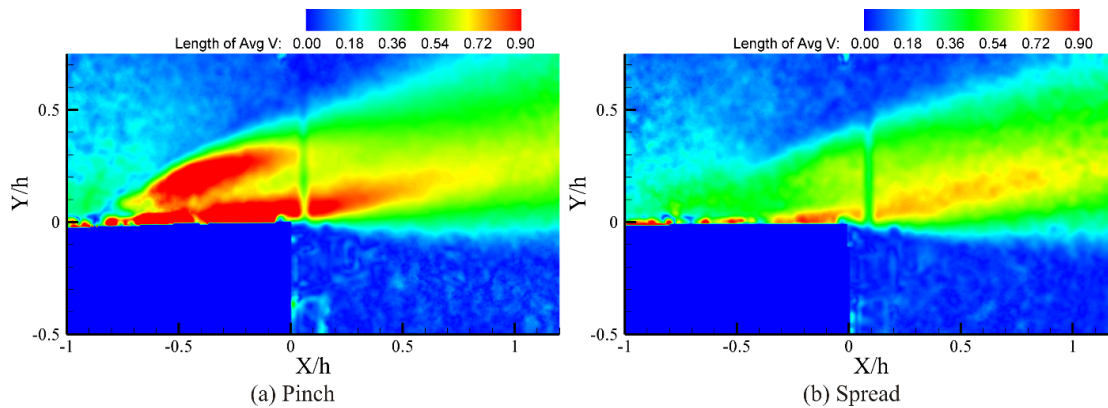


Figure 6-2: Velocity Contour Along the (a) Pinch and (b) Spread Under Quiescent Conditions (m/s).

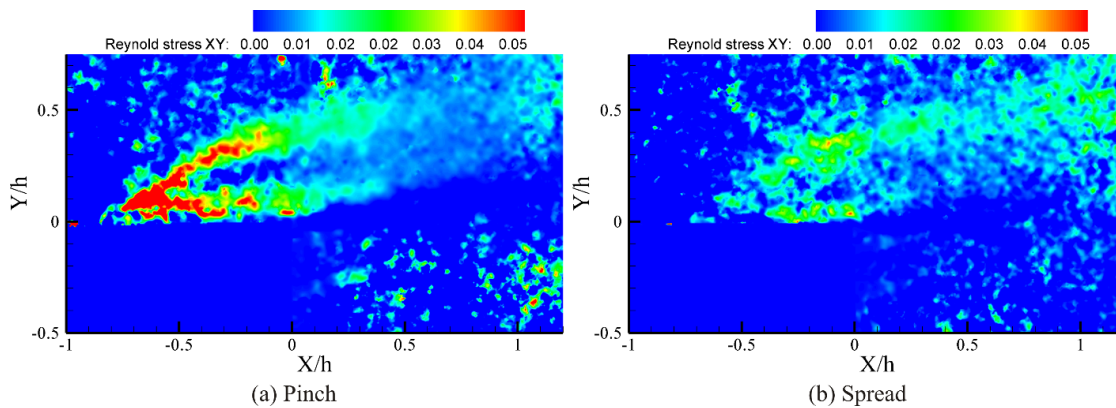


Figure 6-3: Reynolds Stress Along the (a) Pinch and (b) Spread Under Quiescent Conditions (Kg/ms²).

Figure 6-4 displays the time-averaged velocity contours during the operation of the wind tunnel with the plasma actuator off, actuator on, and also the difference in velocity between the off and on cases in Figure 6-4(c). Here, the flow is left to right and the laser sheet is illuminating the pinch portion of the actuator. The same results are presented for when the laser sheet is positioned over the spread portion of the actuator in Figure 6-5. Examining the velocity contours in Figure 6-4(a) and Figure 6-4(b) and Figure 6-5(a) and Figure 6-5(b), it is difficult to identify the influence of the plasma actuator. Examining the difference between the actuator off and on cases, it is evident that the pinch portion of the actuator has a greater influence upstream of the step leading edge, Figure 6-4(c), whilst the spread portion influence more the separated shear layer downstream.

At the pinch location, see Figure 6-4(c), an upwards vectored jet is produced, forcing the incoming flow away from the wall, which explains the strong influence upstream of the step leading edge. The three-dimensional nature of the serpentine induced jet leads to the generation of streamwise vortices. According to Riherd and Roy [15] these vortices can lead to the generation of boundary layer streaks, a type of transient instability mechanism capable of achieving large energy growth over finite time scales, which are initiated by streamwise vorticity. It is suggested by the authors that these streaks can be used to provide a means of flow control or to induce transition from laminar to turbulent flow.

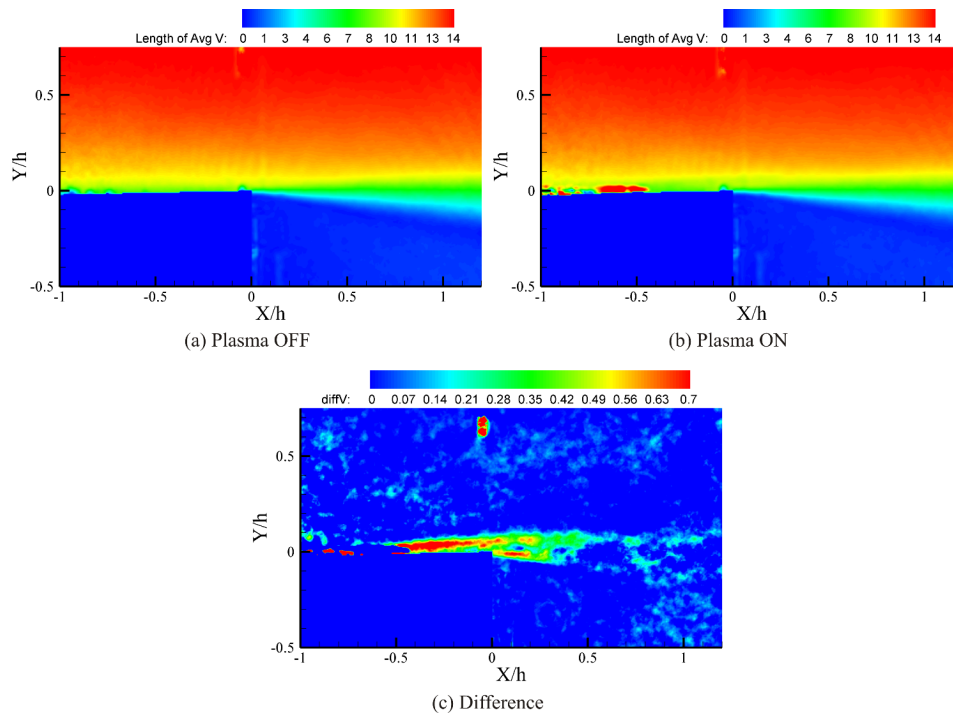


Figure 6-4: Average Velocity Contour for Pinch Location (m/s).

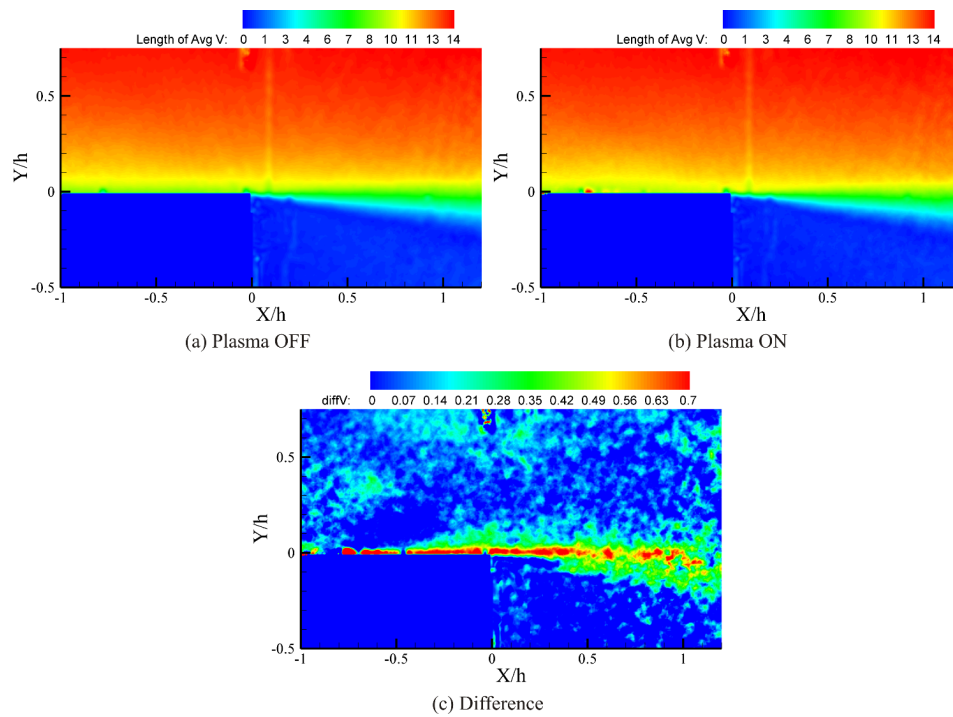


Figure 6-5: Average Velocity Contour for Spread Location (m/s).

6.4 CONCLUSION

The present investigation examines the application of a three-dimensional serpentine plasma actuator, as an active flow control device, to manipulate the flow over a backwards facing step. The serpentine actuator is characterized by two regions, namely the pinch, and the spread. At the pinch location, the induced jet from opposing sides collide and a strong upwards jet is created. At the spread location, because there is no cancelling effect of the induced jet from opposite sides of the actuator, a greater streamwise influence is achieved.

Further studies are underway to understand in greater detail the influence of such three-dimensional actuators on the flow properties, such as the flow reattachment downstream of the step as well as the vertical structures inside the recirculation bubble.

6.5 REFERENCES

- [1] Corke, T.C., Enloe, C.L. and Wilkinson, S.P., Dielectric Barrier Discharge Plasma Actuators For Flow Control, *Annual Review of Fluid Mechanics* 42, pp. 505-529, 2010.
- [2] Erfani, R., Zare-Behtash, H. and Kontis, K., Plasma Actuator: Influence of Dielectric Surface Temperature, *Experimental Thermal and Fluid Science* 42, pp. 258-264, 2012.
- [3] Ramakumar, K. and Jacob, J.D., Flow Control and Lift Enhancement Using Plasma Actuators, 35th Fluid Dynamics Conference, Toronto, AIAA-2005-4635, 2005.
- [4] Jolibois, J. and Moreau, E., Enhancement of the Electromechanical Performances of a Single Dielectric Barrier Discharge Actuator, *IEEE Transactions on Dielectrics and Electrical Insulation* 16, pp. 758-767, 2009.
- [5] Balcon, N., Benard, N. and Moreau, E., Formation Process of the Electric Wind Produced by a Plasma Actuator, *IEEE Transactions on Dielectrics and Electrical Insulation* 16, pp. 463-469, 2009.
- [6] Huang, J., Corke, T.C. and Thomas, F.O., Unsteady Plasma Actuators for Separation Control of Low-Pressure Turbine Blades, *AIAA Journal* 44, pp. 1477-1515, 2006.
- [7] Benard, N., Jolibois, J. and Moreau, E., Lift and Drag Performances of an Axisymmetric Airfoil Controlled by Plasma Actuator, *Journal of Electrostatics* 67, pp. 133-139, 2009.
- [8] Little, J., Nishihara, M., Adamovich, I. and Samimy, M., High-lift Airfoil Trailing Edge Separation Control Using a Single Dielectric Barrier Discharge Plasma Actuator, *Experiments in Fluids* 48, pp. 521-537, 2010.
- [9] Mabe, J.H., Calkins, F.T., Wesley, B., Wozidlo, R., Taubert, L. and Wagnanski, I., Single Dielectric Barrier Discharge Plasma Actuators for Improved Airfoil Performance, *Journal of Aircraft* 46, pp. 847-855, 2009.
- [10] Durscher, R.J. and Roy, S., Induced Flow From Serpentine Plasma Actuators Acting in Quiescent Air, 49th AIAA Aerospace Sciences Meeting including the New Horizons Forum and Aerospace Exposition, Orlando, AIAA-2011-957, 2011.
- [11] Wang, C.C., Durscher, R.J. and Roy, S., Three-Dimensional Effects of Curved Plasma Actuators in Quiescent Air, *Journal of Applied Physics* 109, pp. 083305, 2011.

- [12] Riherd, M. and Roy, S., Numerical Investigation of Serpentine Plasma Actuators for Separation Control at Low Reynolds Number, 41st AIAA Fluid Dynamics Conference and Exhibit, Hawaii, AIAA-2011-3990, 2011.
- [13] Durscher, R.J., Characterization of Novel and Conventional Dielectric Barrier Discharge Actuators, PhD Thesis, University of Florida, USA, 2012.
- [14] Zare-Behtash, H., Kontis, K., Gongora-Orozco, N. and Takayama, K., Shock Wave-Induced Vortex Loops Emanating From Nozzles With Singular Corners, Experiments in Fluids 49, pp. 1005-1019, 2010.
- [15] Riherd, M. and Roy, S., Serpentine Geometry Plasma Actuators for Flow Control, Journal of Applied Physics 114, pp. 083303, 2013.



Chapter 7 – EVALUATION OF DIELECTRIC BARRIER DISCHARGE ACTUATOR SUBSTRATE MATERIALS

S.P. Wilkinson and E.J. Siochi
NASA Langley Research Center
UNITED STATES

Mary Ann Meador
NASA Glenn Research Center
UNITED STATES

Godfrey Sauti and Tian-Bing Xu
National Institute of Aerospace
UNITED STATES

Haiquan Guo
Ohio Aerospace Institute
UNITED STATES

ABSTRACT

A key, enabling element of a Dielectric Barrier Discharge (DBD) actuator is the dielectric substrate material. While various investigators have studied the performance of different homogeneous materials, most often in the context of related DBD experiments, fundamental studies focused solely on the dielectric materials have received less attention. The purpose of this study was to conduct an experimental assessment of the body-force-generating performance of a wide range of dielectric materials in search of opportunities to improve DBD actuator performance. Materials studied included commonly available plastics and glasses as well as a custom-fabricated polyimide aerogel. Diagnostics included static induced thrust, electrical circuit parameters for 2D surface discharges and 1D volume discharges, and dielectric material properties. Lumped-parameter circuit simulations for the 1D case were conducted showing good correspondence to experimental data provided that stray capacitances are included. The effect of atmospheric humidity on DBD performance was studied showing a large influence on thrust. The main conclusion is that for homogeneous, dielectric materials at forcing voltages less than that required for streamer formation, the material chemical composition appears to have no effect on body force generation when actuator impedance is properly accounted for.

7.1 INTRODUCTION

Alternating current Dielectric Barrier Discharge (DBD) actuators are flow control devices that convert electrical to kinetic energy within a weakly ionized plasma over a dielectric surface. An illustration of a typical device operated with sinusoidal AC voltage is shown in Figure 7-1. The cyclical interaction between the alternately charged electrodes, dielectric surface and ionized air at the excitation frequency produces a zero-net-mass surface jet and a corresponding opposing mechanical reaction force on the model. Various other modes of operation are possible based on short duration, high amplitude voltage pulse technology [1], [2], and DC bias fields [3] but are not discussed further in this report. The alternating current DBD actuator, henceforth referred to as simply a DBD actuator, has shown promise for a variety of flow control applications, particularly in the boundary layer separation and aeroacoustic noise control areas. Excellent reviews of the DBD actuator are available and provide more detailed background information [4], [5].

With nearly two decades of in-depth study of the DBD actuator since its first modern study in aeronautics in 1995 [6], operation of the DBD actuator is now largely understood. The basic functioning of the electrical and fluid mechanical energy conversion mechanisms, actuator geometry requirements, sensitivities to gas composition and thermodynamic properties, electrical operating characteristics, numerical modelling methods, and much of the fundamental plasma chemistry is reasonably well understood. What is currently lacking are details of plasma chemical processes and dielectric surface interactions that are either difficult to access

experimentally or are currently beyond the reach of practical numerical simulation capabilities. The current effort is a step towards identifying specifically where such knowledge gaps exist with the long-range goal of providing seed information for improvements in DBD technology.

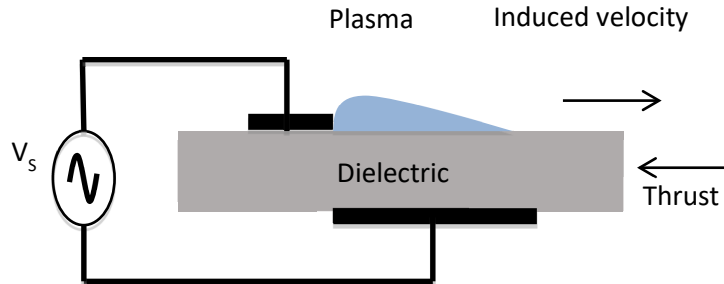


Figure 7-1: Conventional Alternating Current.

The extent to which DBD performance can be improved is based on its underlying physics. The DBD is a threshold device in the sense that energy must be expended initially simply to ionize the working gas, usually air. No direct flow control benefit is derived from that initial energy expenditure, at least in a momentum augmentation sense. Only after ionization has occurred, are charged particles available to do work on the surrounding non-ionized gas via the local electric fields. It has been shown from measurements of electrical input power and induced momentum flux that the thermodynamic efficiency of the DBD actuator is actually very small, by at least one estimate less than 0.1% [7]. This finding should be viewed with respect to the desired aeronautical applications. For high Reynolds number flight, the area of primary interest to NASA, a rough order of magnitude energy analysis shows that for a typical large transport aircraft, the average power required to overcome viscous drag is only about 1/4 watt/cm² of total wetted surface area. (Estimate based on Boeing 737-200 at cruise conditions, operating weight 31600 kg, total wetted area 769 m², viscous drag assumed to be one-half of total drag, speed 216 m/s, and L/D = 18). Due to the low DBD thermodynamic efficiency, the required total energy input could easily exceed the object of the control, at least in the viscous drag case, if applied on an area wide basis. Proposed applications of the DBD are, therefore, generally discrete, local inputs such as those applicable to separation or noise control.

Another often cited metric of DBD performance is the interaction parameter [8] based on energy density available in a DBD electric field compared to that in the flow:

$$Z_{EHD} = \frac{\epsilon_0 E_{cath}^2}{2\rho U^2} \quad (7-1)$$

where ϵ_0 is the permittivity of free space, E_{cath} electric field at the cathode, ρ air density, and U induced velocity. For expected electric field values, Ref. [8] estimates maximum induced velocities in the approximate range of 2-10 m/s, consistent with numerous laboratory observations. This estimate, along with the low electrical to kinetic conversion efficiency, further restricts DBD flow control options. Therefore, widespread application of DBD technology on high Reynolds number aircraft will require a significant increase in thermodynamic efficiency or discovery of creative applications for which energy input is not an overriding issue.

In the DBD actuator, the fundamental role of the dielectric is to enable a self-limiting discharge by preventing formation of conductive, gaseous, discharge channels between the electrodes that would circumvent the DBD electrohydrodynamic (EHD) forcing property. In terms of classical DC, low-pressure discharge tube terminology, the desired discharge is in the glow discharge region between corona formation and glow-to-arc transition [9]. The externally imposed voltage causes dielectric polarization resulting in the appearance of surface charge on the exposed dielectric. The instantaneous magnitude of this charge depends upon the relative permittivity of the dielectric, the ionization physics in the gap including charge deposition on the surface and the time history of the excitation. This is illustrated in Figure 7-2 for the classical, one-dimensional case of a partially filled capacitor. Under the influence of the external power supply, V_s , the dielectric material of relative permittivity ϵ_r polarizes forming alternating positive and negative charge layers on its surfaces.

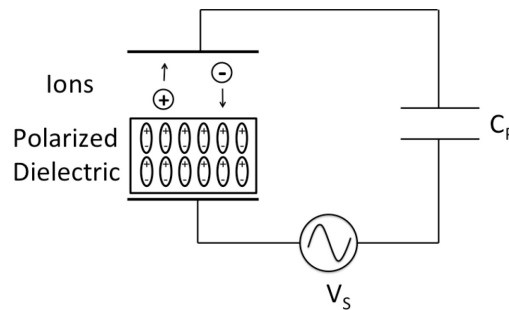


Figure 7-2: Illustration of Limited Breakdown Ionization Gap with Dielectric Material of Relative Permittivity ϵ_r and Capacitor Probe C_p .

The electric field due to the surface charge is responsible for the initial ionization of the air gap and the subsequent motion of the charge particles. The magnitude of the initial surface charge is determined by the relative permittivity of the dielectric material and the applied voltage. For the one-dimensional case shown, the surface charge prior to gas breakdown can be derived [10] in terms of capacitance and applied voltage:

$$C = \frac{Q}{V} = \frac{\epsilon_0 A}{t_a + \frac{t_d}{\epsilon_r}} \quad (7-2)$$

where C is capacitance, Q charge, V applied voltage, A plate area, t_a air gap thickness and t_d dielectric thickness. For a fixed geometry (i.e., t_a , t_d and A), for the pre-breakdown case, the charge on the capacitor plates is solely dependent upon the relative permittivity. Following breakdown, charge deposition onto the surface [11], [12] and remnant polarization from the previous AC cycle (memory effect [13]) also contribute to the surface charge. In addition to polarization and charge deposition, dynamic charged particle effects, such as Secondary Electron Emission (SEE) due to ion bombardment are also a possibility although for the energy levels encountered in atmospheric DBD work, this may not be a significant effect. The Stolletow constant for air, the minimum energy required to create an ion-electron pair, is 81 eV/ion-electron pair [9]. SEE data for glasses [14] indicate a secondary electron yield of 2 or 3 electrons per incident electron with energy in the range of 300-450 eV. It is not clear whether this is close enough for a measurable effect in typical DBD work. The preface to the SEE data table in Ref. [14] states that the SEE data is very sensitive to surface contamination so various controlled dielectric surface coatings could be an effective way to examine the relative importance of the SEE effect. Other possible effects include those related to:

- Surface energy (hydrophilic vs. Hydrophobic materials);
- Surface conductivity (including semiconductor effects [15]);
- Catalytic coatings [16];
- Humidity and water absorption [17], [18];
- Material electronegativity; and possibly others.

The dielectric loss tangent plays an important role in dielectric heating, energy efficiency and physical durability of the material. This is an important research area for DBD material engineering. The data for small signal measurements will be reported in Section 7.2.

A related topic is partial discharges in high voltage dielectrics wherein the gas within microscopic voids in the material and breaks down leading to excessive heating and material failure [19]. The subject of nanoporous dielectrics (aerogels) and micro-porous dielectrics (foams) is also discussed.

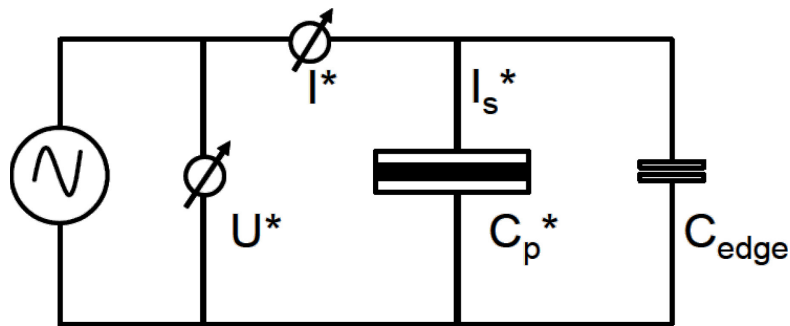
The goal of this study was to attempt to explain performance differences among various, common dielectric materials. Where the data cannot be readily explained, opportunities exist for research and discovery with the potential for improvement of DBD actuator materials and/or actuator performance. The materials investigated in this study were those commonly found in DBD literature such as polymer plastics, glass and one case of boron nitride ceramic. We also had the unique opportunity to study newly developed polyimide aerogel materials [20], [21], for DBD application. Aerogels have dielectric constants close to unity and, as such, limit dielectric heating. Silica aerogel was previously examined in Ref. [22] and it was found to have a potentially very high saturation thrust associated with formation of plasma streamers. In the current experiments, however, we did not have sufficient power supply voltage to reach the plasma streamer saturation state.

In addition to the basic dielectrics, we also initially intended to look at various surface coatings. The most notable example in that category is the work reported by Fine and Brickner [16] which showed that a coating of photocatalytic nanoparticle titanium oxide can greatly increase the thrust of a DBD actuator. However, that work could not be replicated in two different laboratories (NASA Langley under the current study, and Princeton University by Profs. R. Miles and M. Post (personal communication)). What was found, however, is that atmospheric humidity can have a large, variable effect on DBD surface coatings, thus, the focus was shifted to study of humidity effects? Future investigations of surface coatings or infused layers with electrical properties may nonetheless be useful as suggested by their role in static charge elimination on dielectric surfaces [23]. Numerous coating options are available including anionic and cationic surfactants such as Sodium Dodecyl Sulfate (SDS), sodium dodecylbenzenesulfonate (SDBS) and cetrimonium bromide (CTAB), and antioxidants such as α -tocopherol (vitamin E) and 2,2-diphenyl-1-picrylhydrazyl (DPPH).

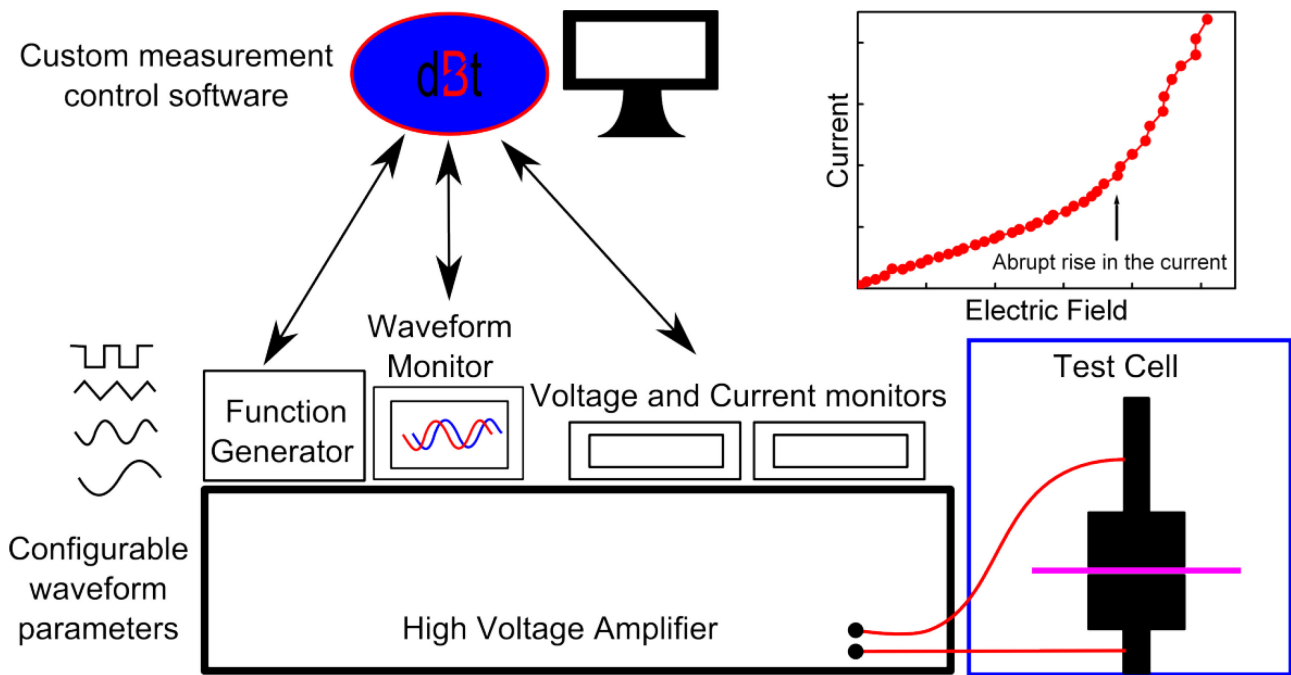
7.2 DIELECTRIC MEASUREMENTS

Real and imaginary permittivity measurements in the frequency range $10^2 - 10^6$ Hz and temperature range 30 – 120°C were carried out using the combination of a Novocontrol Broadband Dielectric Converter (BDC) and Solartron SI1260 Impedance Gain / Phase Analyzer with a Novocool temperature controller. Data capture was managed by Novocontrol WinDETA software. Measurement samples were mounted in a Novocontrol BDS 1200 sample cell. Room temperature measurements were also made for samples mounted in a custom built PTFE lined cell to help determine and correct for sample cell related stray capacitances. All dielectric measurements were small signal measurements with an excitation voltage on the order of 1 V.

Figure 7-3(a) shows the basic setup for a dielectric measurement.



(a) Dielectric Constant Measurement.



(b) Dielectric Breakdown Test.

Figure 7-3: Schematic of the Circuit for: (a) the Dielectric Constant Measurements and (b) the Setup for the Dielectric Breakdown Strength Measurements.

Dielectric breakdown was established by monitoring the rise in the current through the dielectric.

An excitation signal produced by the generator is applied to the sample and the complex voltage U^* and the current I^* as well as the phase shift between the current and the voltage are measured. The complex parallel capacitance of the sample C_p^* is then:

$$C_p^* = -\frac{iI^*}{\omega U^*} - C_{edge} \quad (7-3)$$

where C_{edge} denotes the edge effects. For accurate measurements of the relatively low dielectric constants of the porous dielectrics, the edge correction was carried out using:

$$C_{corr} = C_{meas} - (C_{stray} + C_{edge}) \quad (7-4)$$

C_{stray} was estimated by carrying out the measurements in different sample cells. C_{edge} was determined using the following:

$$C_{edge} = C_0 \frac{2d}{\pi D} \left[\ln \frac{8\pi D}{d} - 3 + z(x) \right] \quad (7-5)$$

where $C_0 = \epsilon_0 \pi \frac{(D/2)^2}{d}$ is the empty cell capacitance and $z(x) = (1+x) \ln(1+x) - x \ln x$ with $x = t/d$, D the sample diameter, d the sample thickness, t the electrode thickness, and $\epsilon_0 = 8.85 \times 10^{-12}$ F/m the permittivity of free space. The corrected dielectric constant is then $\epsilon_{corr} = \frac{C_{corr}}{C_0}$.

7.2.1 Porous Dielectrics

The dielectric breakdown strengths were measured for the porous dielectrics, polyetherimide microfoam and polyimide aerogels. The setup for dielectric breakdown testing consisted of a Philips PM5138A function generator, TREK 10/10B voltage amplifier (10 kV, 10 mA), Keithley 2000 digital multimeter current monitors, and Hipotronics TF-2-50 2 (50 mm) diameter brass electrodes. Data capture was made using custom LabVIEW based dBt software. The tests were carried out according to ASTM D149 [24]. Mechanical tests were also carried out for the robust polyimide aerogel. Tensile tests were conducted using an Instron 5848 Microtester. The tensile test specimens had a gauge length of 10.00 mm, 5.08 mm width (~30 um thickness) and were strained at 10 mm/min. The tensile test was based on ASTM D638 [25] and ASTM D1708 [26].

Table 7-1 is a full listing of the dielectric materials studied including their chemical composition information. The materials chosen included some commonly used dielectrics as well as novel formulations and porous materials. Recently it has been shown in the literature that silica aerogels can act as dielectrics for DBD actuators with high saturation thrusts [22]. More robust polyimide aerogels were used in the current study.

Table 7-1: Dielectric Materials. (Aerogel: 50% ODA / 50% DMBZ and BPDA with POSS crosslinks.)

Trade (Common) Name	Chemical Name or Class	Unit Formula
Glass	Silica, Silicon Dioxide	SiO ₂ +Na ₂ O+CaO
Teflon® (PTFE)	Polytetrafluoroethylene	C ₂ F ₄
Plexiglass® (Acrylic, PMMA)	Polymethylmethacrylate	C ₅ O ₂ H ₈
Lexan®	Polycarbonate	C ₁₈ H ₂₀ O ₃

Trade (Common) Name	Chemical Name or Class	Unit Formula
ULTEM™	Polyetherimide	C ₃₇ H ₂₄ O ₆ N ₂
PEEK	Polyetheretherketone	C ₂₁ H ₁₈ O ₃
Kapton®	Polyimide	C ₂₄ H ₂₀ N ₂ O ₅
Boron Nitride	Ceramic	BN
Nylon-6,6	Polyamide	C ₁₂ H ₂₂ N ₂ O ₂
FVMQ	Fluorosilicone Elastomer	C ₉ H ₂₂ O ₃ F ₃ Si ₃
Microfoam (PEI)	Polyetherimide	C ₃₇ H ₂₄ O ₆ N ₂
Aerogel	Polyimide	(see caption)

Figure 7-4(a) and Figure 7-5(a) show the dielectric constants of the materials studied at 30 and 120°C, respectively and the frequency range of interest for DBD actuators. The aerogel and microfoam have very low and non-dispersive dielectric constants that are close to 1. Glass has the highest and most frequency dependent dielectric constant. The remainder of the dielectrics show largely non-dispersive dielectric constants between the porous dielectrics and the glass. At 120°C, the dielectric constants of the aerogel and microfoam remain largely unchanged while those of PMMA and glass change very significantly. The aerogel and microfoam are polyimides, polymers with high glass transition temperatures (T_g) and thus have low sensitivity of the dielectric constant to the temperature. Ion mobility in the glass is expected to be the main contributor to the very high and dispersive dielectric constant [27]. Figure 7-4(b) and Figure 7-5(b) show the loss tangents of the materials. Again, the glass shows the highest loss while the PI aerogel and PTFE show the lowest. It should be noted though that the loss of the microfoam is slightly higher than that of both PTFE and the PI aerogel which indicates a slightly conductive matrix for the microfoam.

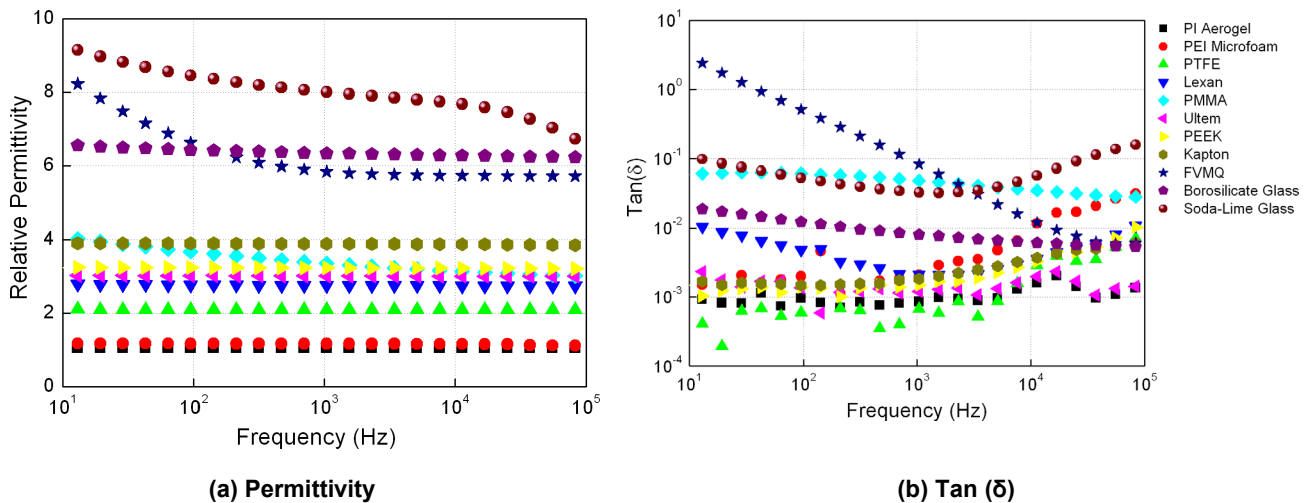


Figure 7-4: Small Signal Dielectric Constant and Loss Tangent at 30°C.

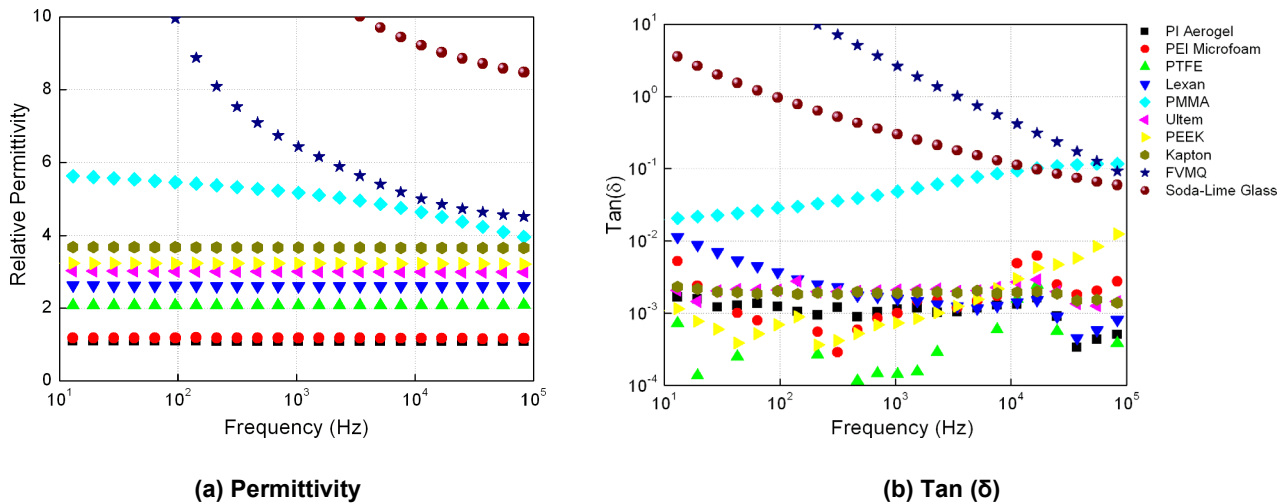


Figure 7-5: Dielectric Constant and Loss Tangent at 120°C for Materials Studied.

Figure 7-6 shows the leakage current as a function of applied electric field for the high voltage breakdown tests of the porous dielectrics. The leakage current for the microfoam rises rapidly with the increasing electric field making it unsuitable for DBD applications. This is a result of the slight conductance of the foam matrix and internal breakdown within the relatively large pores. For the aerogels, the pore size is small enough such that internal breakdown does not occur [28] allowing the current to rise steadily. Two formulations of aerogel were tested, a flexible aerogel containing hydrophilic chemical groups (ODA and BPDA with POSS crosslinks) and a more hydrophobic composition (50% ODA / 50% DMBZ and BPDA with POSS crosslinks). For the aerogel with the hydrophilic groups, dielectric breakdown occurs at an electric field of about 10 kV/mm as indicated by the abrupt rise in the leakage current (Figure 7-6, PI Aerogel 1). The hydrophobic aerogel remained insulating to the limit of the breakdown testing and this formulation was used in subsequent mechanical and DBD testing.

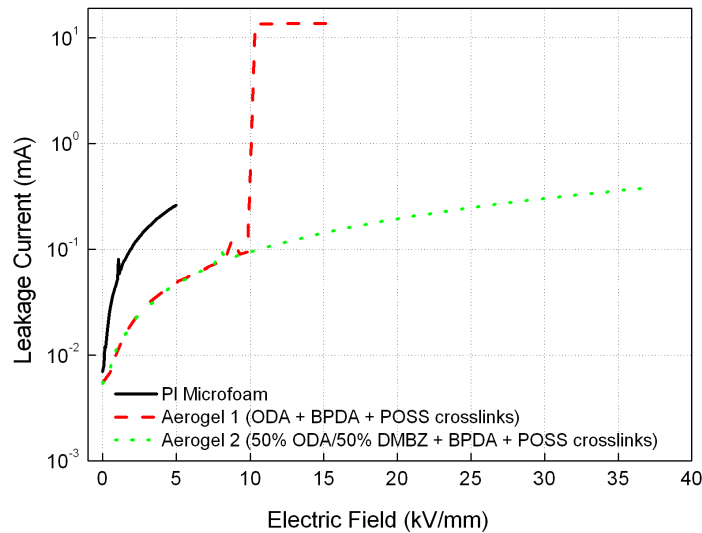


Figure 7-6: Leakage Current vs. Applied Electric Field from the Dielectric Breakdown Testing of the Porous Dielectrics.

Figure 7-7 shows the tensile properties of a series of the hydrophobic aerogel specimens. It can be seen that unlike the highly brittle and friable silica aerogels used in Ref. [22], this material is highly robust with the strain at break of 10%. Thus, this material can act as a high saturation thrust, low mass and robust DBD dielectric.

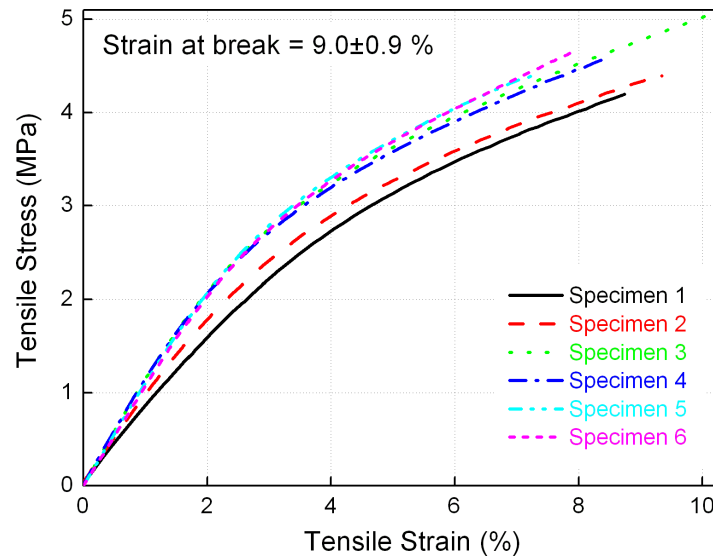


Figure 7-7: The Stress-Strain Curves from Mechanical Tests of the Polyimide Aerogel.

7.3 STATIC THRUST STAND MEASUREMENTS

7.3.1 Test Apparatus and Models

Performance characterization of the dielectric materials was conducted using two methods: static thrust measurements discussed in this section (7.3) and, one-dimensional volume-discharges using the charge transfer method discussed in Sections 7.2 and 7.5. A photograph of the thrust stand is shown in Figure 7-8.

An electronic mass balance was used to measure DBD thrust force. It had a full scale rating of 310 grams and a resolution of 0.1 milligram. The device body was of all metal construction and was electrically grounded (including the metal platen). No additional shielding was required to avoid EMI effects from the high voltage power supply and plasma. The acrylic plastic enclosure's volume was 61 x 61 x 71.1 cm (24 x 24 x 28 inch) with 9.5 mm (3/8-inch) wall thickness and allowed adequate distance between the DBD actuator and sidewalls of the enclosure to avoid significant electrostatic induction force errors. The red corner posts shown in Figure 7-8 are electrical grade GP03 fiberglass 90-degree structural angle assembled with nylon machine screws. The floor is 19 mm (3/4 inch) thick wood Medium Density Fiberboard (MDF). The ground plane was aluminium foil bonded to 3 mm (0.12 inch) thick acrylic plastic sheet. Its main function was to provide additional protection for the grounded force balance in the event that the energized model would fall. Its effect on the electric field distribution within the enclosure was not examined. The model standoff post was 12.5 mm (0.492 inch) square acrylic mounted in a plastic foam block.

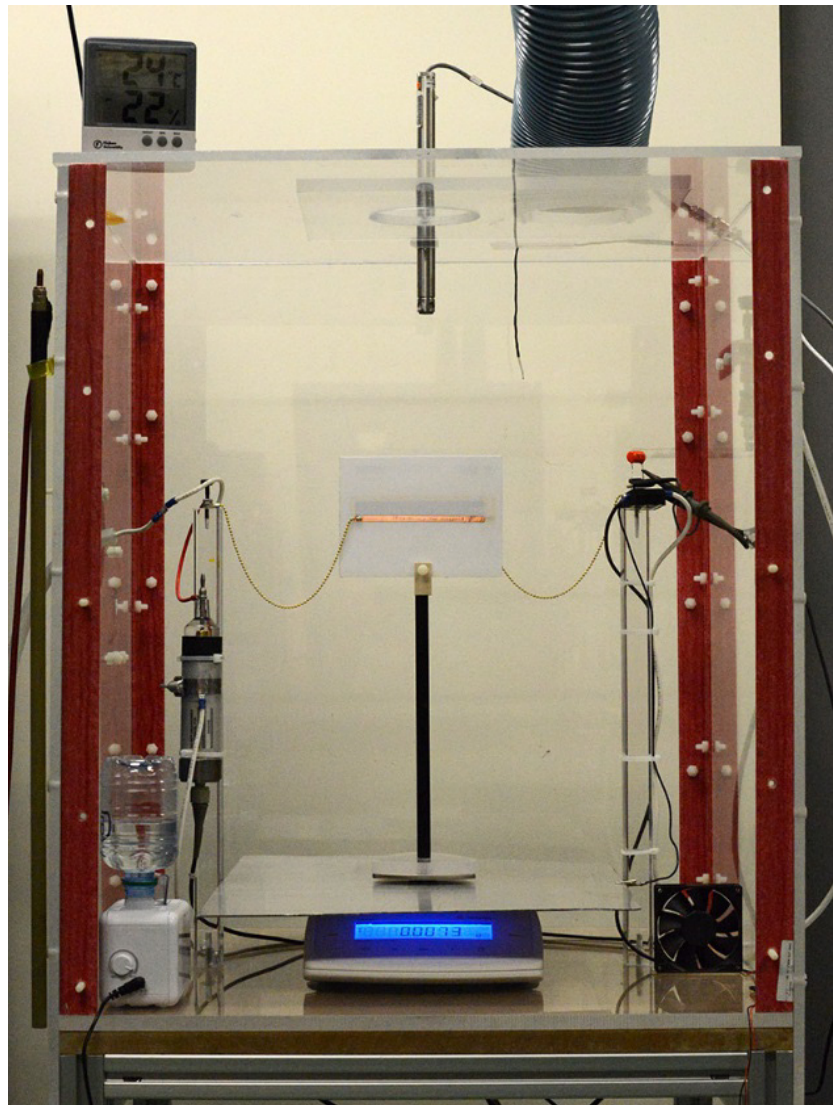


Figure 7-8: Photograph of DBD Thrust Measurement Apparatus.

A photograph of a typical DBD actuator used for thrust measurement is shown in Figure 7-9(a) and critical dimensions are described in Figure 7-9(b) and Table 7-2. The dielectric thickness varied with material as supplied by the manufacturer. Only manufacturer's stock thicknesses were used and no attempt was made to alter the thickness out of concern for modifying the surface properties. The electrodes were 0.075 mm (0.003 inch) copper adhesive tape (including adhesive). The exposed electrode was 5 mm (0.197 inch) wide and the buried electrode 15 mm (0.591 inch) wide with zero overlap. Scotch™ 130C electrical splicing tape was used to prevent plasma breakdown on the backside of the models. Power leads, consisting of #3 yellow brass ball chain (3/32 inch diameter, 94 balls/foot) or #27 AWG (American Wire Gage) (7 twisted strands of #35 AWG tinned copper wire with a flexible, soft plastic jacket of unknown material) were soft-soldered to the copper electrodes. The ball chain exhibits very high impedance, on the order of 500 MOhm, when measured with a typical low voltage bench resistance meter. In operation, however, there is little or no discernible difference in the charge transfer cyclogram between the ball chain and solid wire indicating a similar lack of difference in the induced

thrust. The reason is most likely that the multiple contact resistances due to the individual brass balls and connecting wire links breakdown microscopically under high voltage thereby substantially lowering the overall resistance. This could be verified by measuring the high voltage impedance of the chain under vacuum however such test was not conducted. It does, however, raise a caution if the ball chain were to be used for comparing thrust data at different ambient pressures.

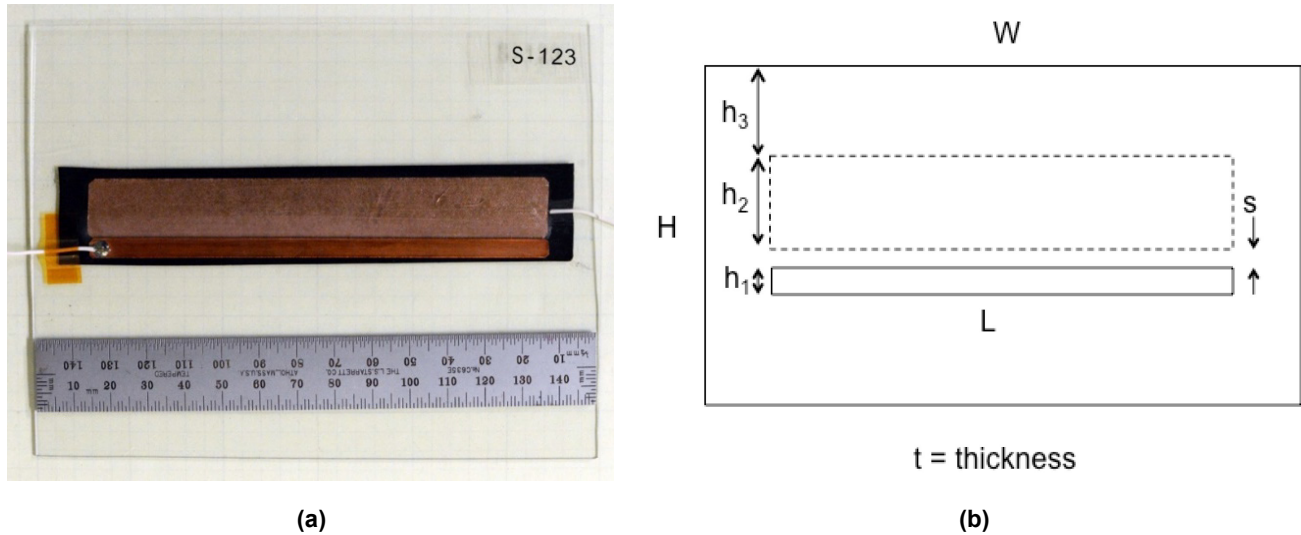


Figure 7-9: (a) Photograph of Typical DBD Thrust Measurement Model; (b) Dimensional Schematic.

Table 7-2: DBD Thrust Model Dimensions.

Model	Material	H	W	t	h1	h2	h3	L	s	Plasma Initiation kV _{pp} /kHz
S108	Acrylic (PMMA)	124	197	2.0	5	15	61	150	0	6.3/5
S109	Polycarbonate (Lexan)	120	203	2.3	5	15	60	150	0	6.6/5
S110	Ultem	120	153	3.2	5	15	60	124	0	6.9/5
S111	PEEK	116	153	3.1	5	15	58	120	0	7.6/5
S113	Glass	104	153	1.2	5	15	57	120	0	5.6/5
S114	PTFE (Teflon)	120	153	3.3	5	15	60	113	0	8.6/5
S118	Boron Nitride	102	152	7.3	5	15	50	120	0	7.3/5

Supply voltage was recorded with a Tektronix model P6015 high voltage probe mounted inside of the test enclosure on the left-hand tether post in Figure 7-8. Current was measured using two methods. One was with a current monitor transformer (Pearson Electronics, Model 2100) with a high frequency cut off rating of 20 MHz (-3dB) and a sensitivity of 1 volt/amp. It was situated on the left side of the test enclosure in Figure 7-8 where

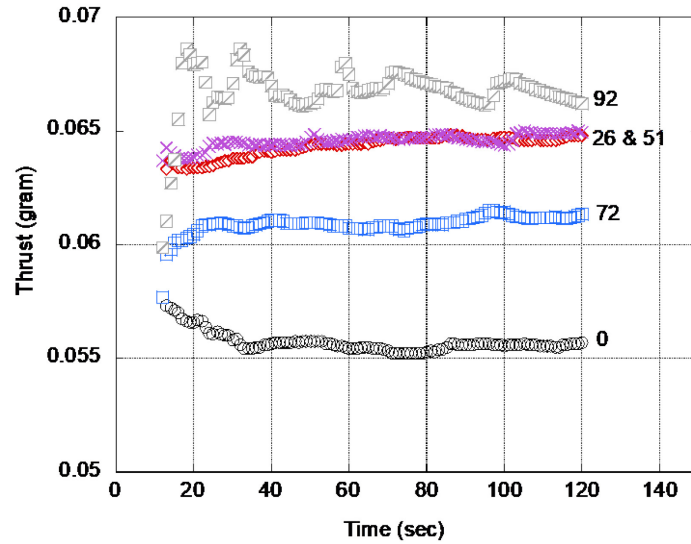
the power lead passes through the acrylic wall. The second method was to use the probe capacitor and charge transfer method described in Section 7.4.

Accuracy of DBD thrust measurements using a mass balance was a concern throughout the test process. Ashpis and Laun [29] have identified numerous sources of error that can alter thrust measurements and need to be accounted for including: new model plasma burn-in duration, time between measurements (i.e., model rest period), data settling time after a voltage change, exposed electrode distance upstream from model edge, dielectric polarization remnant effects, mechanical forces due to lead wire elasticity, ion wind effects from corona on lead wires, electrostatic induction forcing due to capacitive coupling surroundings, electrode size and placement inaccuracies, measures to prevent undesired regions of plasma breakdown (corona dopes and tapes), power supply impedance matching issues, and variable, uncontrolled atmospheric humidity.

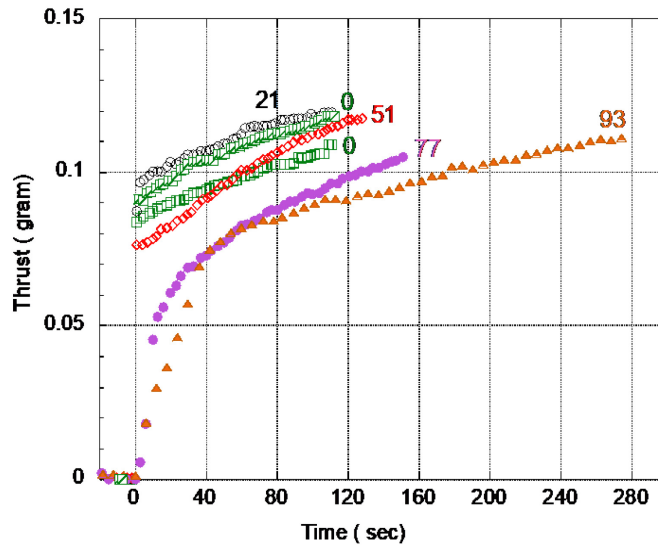
7.3.2 Humidity Effects

The last item, humidity, is of particular concern since it can affect DBD performance via multiple pathways, i.e., through charge effects on polar water molecules, charge effects on water impurities, plasma chemistry reactions involving water, modification of air density (binary gas), water adsorption/absorption effects on the dielectric, surface condensation, and dielectric surface conductivity. Also, depending on how the humidity is created, an airborne dispersion of microscopic water droplets can be created with uncertain effects on the plasma and DBD thrust measurements. Humidification methods, other than naturally occurring atmospheric humidity, include thermal evaporation and various methods of atomization including jet nebulizers and ultrasonic humidifiers. Kwok [30] has shown that a small charge can be imparted even to distilled water droplets depending on the atomization method used.

To demonstrate the difficulty with humidity, two dielectric materials were tested having widely different water retention properties, PTFE and Nylon 6,6. PTFE has an extremely low water absorption rate, < 0.01% weight gain for 24-hour immersion per ASTM D-570 [31]. It's also has one of the lowest surface energies of all polymer plastics. Nylon 6,6 on the other hand is known for its hygroscopic nature with an ASTM D-570 water weight gain of about 3% and a surface energy at least double that of PTFE. Figure 7-10(a) shows the PTFE DBD thrust response for five levels of humidity created by ultrasonic humidification in the test enclosure (Figure 7-8). The 0% relative humidity case was obtained by displacing the room air in the test enclosure with a steady flow of dry air from a dual regenerative desiccant drier (Hankison Model DHW7) with a specified output dew point temperature of -70 deg F. Prior to thrust measurement, the dry airflow was stopped and the enclosure sealed. For the conditions described in the caption, the thrust levels are seen to increase with increasing humidity. The erratic appearance of the 92% case is most likely related to surface condensation. Figure 7-10(b) shows the Nylon 6,6, case for the same electrical input conditions. In this case, increasing humidity tends to reduce thrust except for the RH = 21% case. Also note that the pre-run and post-run 0% cases did not repeat well for reasons most likely related to insufficient drying time. The continual rise in thrust with time for the Nylon dielectric is an additional notable difference and no explanation can be offered at this time. The lesson from this test, besides the fact that Nylon is probably a poor DBD dielectric choice, is that humidity has a major impact on DBD performance affecting both trend and amplitude. Control of humidity in DBD testing is an essential requirement where high accuracy results are required.



(a) PTFE



(b) Nylon 6,6

Figure 7-10: DBD Model Thrust Data with Variable Humidity. Both models excited with step input of 20 kV_{pp}, 1 kHz (sine). (a) 1.07 mm thick PTFE dielectric; (b) 0.97 mm thick nylon 6,6 dielectric. For the nylon case only, 0-1 denotes the pre-run 0% humidity and 0-2 post-run 0% humidity.

7.3.3 Thrust Measurements

Thrust measurements, scaled with respect to electrode length, are shown in Figure 7-11 for eight different dielectric materials covering nearly an order of magnitude in thickness and permittivity as indicated in the legend. (These data were acquired prior to the humidity testing discussed above and accurate humidity data was

not recorded. Testing was conducted in a climate-controlled laboratory with seasonal relative humidity variations typically in the range of 30 – 50 %.) In log-log coordinates, the curves are approximately parallel to each other. This suggests that the plasma and surface charge growth responsible for the increase in thrust behave in the same fashion independently of the chemical composition of the dielectric material.

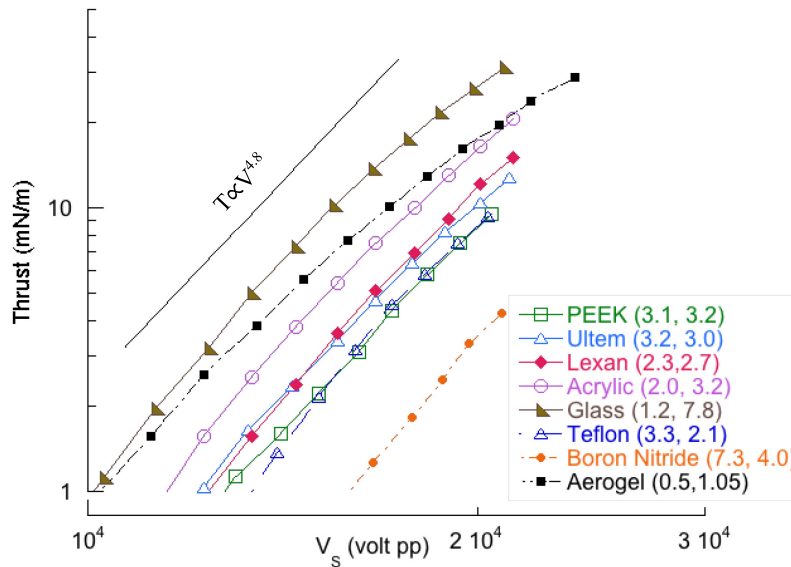


Figure 7-11: DBD Thrust Data for Dielectric Materials. Frequency = 5 kHz (Sine Input). The number pairs in the legend refer to the material thickness in millimeters and dielectric coefficient respectively. Solid line $T \propto V^{4.8}$ is for reference.

Figure 7-12 shows a cross plot of the thrust data in Figure 7-11 at a constant voltage of 18 kV with respect to the 1D effective thickness, t_d/ϵ_r in semi-log coordinates. The 18 kV is simply convenient value that vertically intersects all of the thrust curves. Figure 7-12 shows that the thrust varies as the inverse log of the effective thickness, t_d/ϵ_r .

The most probable cause of this semi-logarithmic behavior is the variation in circuit impedance with dielectric thickness and permittivity. This conjecture can be assessed by examining theoretical formulations of the pre-breakdown impedance of an asymmetric actuator or the closely related symmetric case. A simple and exact solution is available for the canonical case of a small diameter cylinder above a conducting plane in a region of constant dielectric constant using the method-of-images [32], [35], a graphical method for solving Poisson’s equation. The relevant physical case would be that of a circular wire on an aerogel dielectric with unity dielectric constant. As will be shown below, this model captures the semi-logarithmic behavior shown in Figure 7-12 thereby largely proving the circuit impedance effect.

Figure 7-13 shows a symmetric, two-dimensional slice of the electric field distribution along a wire suspended above a plane obtained using the method-of-images [35]. A rectangular, shaded region of thickness t_d is shown to demarcate the physical boundaries of a dielectric with unity dielectric constant ($\epsilon_r = 1$), for example an aerogel. Since such a dielectric does not bend the electric field lines at the air-dielectric interface, as would higher valued permittivity materials, it does not affect the solution.

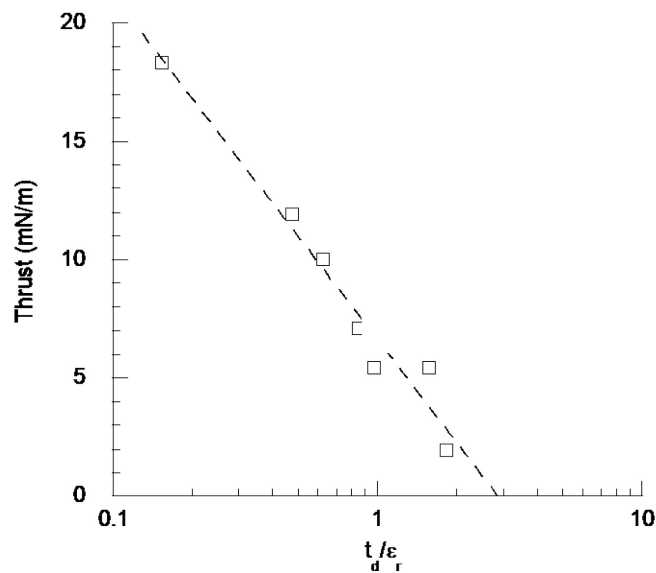


Figure 7-12: Cross Plot of Thrust in Figure 7-11 at a Constant Input Voltage, $V_s = 18$ kV, with Respect to the Effective Dielectric Thickness, t_d/ϵ_r .

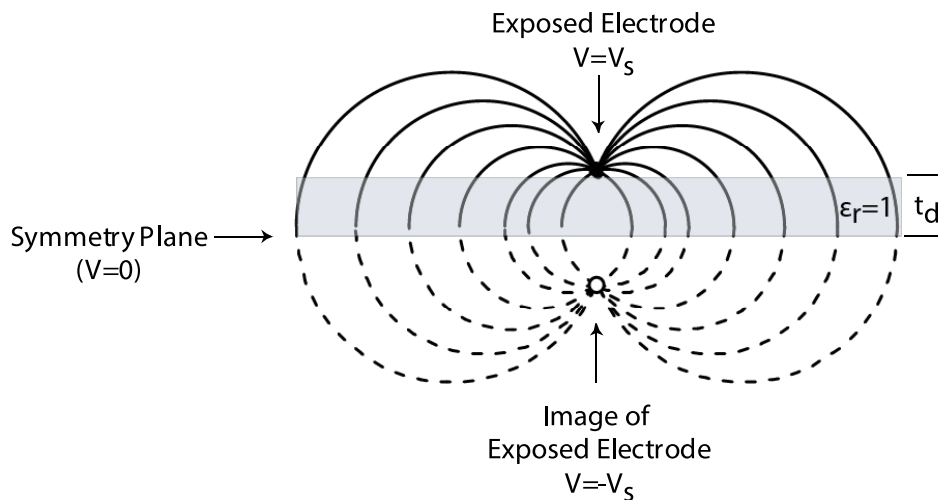


Figure 7-13: Method of Images for a Cylinder Above a Ground Plane.

The top, exposed electrode of radius r is shown as a filled circle on the upper surface of the dielectric. The image electrode is shown below the line of symmetry by an equal distance as an open circle. The E-field flux lines are represented by circles with centers on the line of symmetry and passing through the top electrode and its image.

Figure 7-14 shows one-half of the method-of-images geometry portrayed in Figure 7-12 with the flux lines removed for clarity. The potential at any point with respect to the symmetry plane ($V = 0$), in this case V_p on the upper surface of the dielectric, can be obtained by integrating the electric fields emanating from the two electrodes and using the principle of superposition. Both Attwood (Ref. [32], pages 85-88; 141-145) and Hyatt

(Ref. [35], pages 150-155, 390-393) present the derivation in detail. Assuming that the electrodes' diameter and the distance to the evaluation point P are each much less than the dielectric thickness, the surface volatge at point P is approximated by the expression:

$$V_p = \frac{\rho_s}{2\pi\epsilon} \ln \frac{r_2}{r_1} \approx \frac{\rho_s}{2\pi\epsilon} \ln \left(\frac{2t_d}{r_1} \right) \quad (7-6)$$

where ρ_s is the lineal charge density on the electrode due to the applied voltage, V_s , and ϵ is the permittvity of the medium, assumed to be unity in this case.

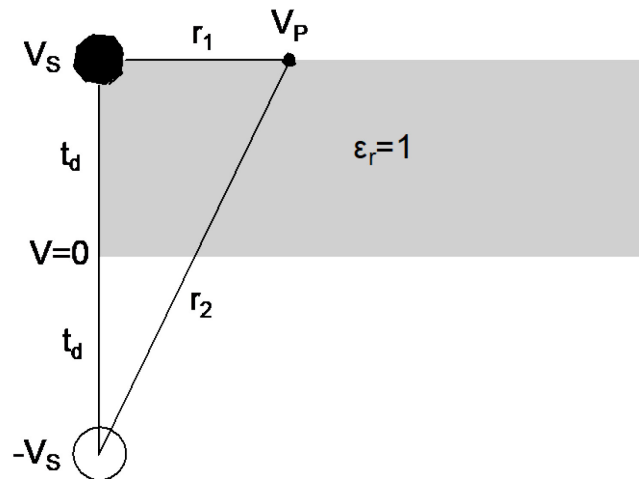


Figure 7-14: Expanded View of Right Side of Figure 7-13 Without Field Lines.

Equation 7-6 shows that for a fixed location on the dielectric surface close to the upper electrode (r_1), the voltage V_p increases logarithmically with dielectric thickness. As V_p increases, however, the voltage difference $\Delta V = V_s - V_p$ decreases. Since the voltage difference, ΔV , drives the momentum transfer between the ionized gas particles and the neutral gas, a thicker dielectric tends to reduce induced thrust logarithmically at constant input votage. Following Attwood's development [32], the origin of the logarithmic response is ultimately the integration of the $E \propto 1/r$ radial electric field required for derivation of the potential field. Figure 7-12 clearly shows an inverse logarithmic response to the dielectric thickness. While this derivation has been for the case of unity dielectric constant, the results clearly apply to the general case of non-unity dielectric constant as shown by the correlation to the effective thickness t_d/ϵ_r in Figure 7-12. The effective thickness term appears explicitly in the expression for the capacitance of parallel plate capacitor, $C \propto \epsilon_r / t_d$ or the capacitive impedance $Z \propto 1/C \propto t_d/\epsilon_r$ and appears to be a useful correlating parameter in the general case. This result establishes that thrust level variations shown in Figure 7-11 are due to pre-breakdown circuit impedance. More specifically, it shows that the thrust variation at constant input voltage is due to dielectric polarization, the physical mechanism for the impedance variation. Ref. [34] presents a derivation of the exact solution for the potential between concentric cylinders that also shows the logarithmic radial variation.

Wheeler [33] has investigated the characteristic impedance of printed circuit board traces, also referred to as strip lines or microstrips that could also function as symmetric DBD actuators. Some of the original DBD work used exactly that construction technique [6]. Wheeler developed a lengthy, approximate expression for the

characteristic impedance of the microstrip in terms of its geometry and the dielectric constant of the circuit board material. Based on equations 10, 13 and 21 in Ref. [33], the characteristic impedance is:

$$\frac{Z}{Z_0} = \frac{0.113}{\sqrt{\epsilon_r + 1}} \ln \left\{ 1 + \left(\frac{4t_d}{w_{eff}} \right) \left[\left(\frac{14 + 8/\epsilon_r}{11} \right) \left(\frac{4t_d}{w_{eff}} \right) + \sqrt{\left(\frac{14 + 8/\epsilon_r}{11} \right)^2 \left(\frac{4t_d}{w_{eff}} \right)^2 + \frac{1 + 1/\epsilon_r}{2} \pi^2} \right] \right\}$$

$$w_{eff} = w + t \frac{\left(1 + \frac{1}{\epsilon_r} \right)}{2\pi} \ln \left(\frac{4e}{\sqrt{\left(\frac{t}{t_d} \right)^2 + \left(\frac{1}{\pi \left(\frac{w}{t} + \frac{11}{10} \right)} \right)^2}} \right) \quad (7-7)$$

where Z is the characteristic impedance, Z_0 impedance of free space (377 ohm), ϵ_r dielectric constant, t_d dielectric thickness, w_{eff} microstrip effective width, w actual microstrip width, t microstrip thickness and e natural logarithm base.

Figure 7-15 shows a plot of Wheeler's characteristic impedance ratio, Z/Z_0 , with respect to effective dielectric thickness, t_d/ϵ_r , for a constant electrode width and thickness of the materials tested in this study. The plot shows that the actuator impedance is linearly related to the effective thickness for the range of values studied so that the same logarithmic thrust response to dielectric thickness would be expected. A similar, approximate argument can be made for the characteristic impedance of a planar transmission line (Ref. [35], p. 392). At constant inductance and neglecting the resistivity and conductance of the dielectric material, the capacitance is proportional to the reciprocal of the square of the characteristic impedance (Ref. [35], p. 385). For an asymmetric DBD actuator, the capacitance would be one-half of that value. This supports the finding that the effective dielectric thickness properly correlates the thrust differences due to pre-breakdown impedance variation.

Another approach to assessing the thrust curves in Figure 7-11 is to consider the DBD actuator as a capacitive voltage divider [34] and as shown in Figure 7-16. The plasma is modelled as lumped-parameter capacitive and resistive elements, C_a and R_a that will assume different values depending on whether the plasma is on or off. The high AC voltage is denoted by V_s . In the current discussion, the plasma is assumed to be on.

The capacitance C_d represents the capacitor formed by the exposed and buried electrodes across the dielectric material. V_d is the voltage on the virtual electrode of the exposed dielectric surface and the difference $\Delta V = V_s - V_d$ is the potential difference that drives the plasma particles to produce the DBD thrust. Capacitance C_p is a constant and is used for charge transfer measurements. For the current discussion, it is considered it to be a short circuit, i.e., $C_p = \infty$, that effectively removes it from the circuit. Solving the voltage divider for V_d yields:

$$\frac{V_d}{V_s} = \frac{X_d}{X_a + X_d} \tag{7-8}$$

where X_d and X_a are the complex impedances of the dielectric and air plasma respectively. X_a can be expressed algebraically in terms of the parallel components C_a and R_a but for current purposes, that step is not necessary. The key observation is that, if the role of the dielectric in thrust production is desired, that implies a relationship between the surface potential (V_d) and the air plasma impedance (X_a) with the supply voltage (V_s), and the dielectric impedance (X_d), held constant. In other words, to prove or disprove a plasma-surface interaction effect on thrust, data must be compared at constant dielectric impedance and supply voltage. This is essentially the same conclusion arrived at using the impedance arguments based on the method-of-images and Wheeler’s characteristic impedance formula.

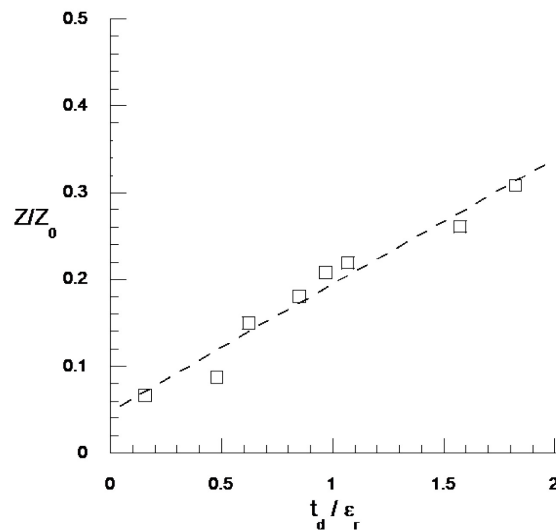


Figure 7-15: Wheeler Impedance Formula [33] vs. Effective Thickness at Constant Electrode Width ($w = 5 \text{ mm}$) and Electrode Thickness (0.1 mm).

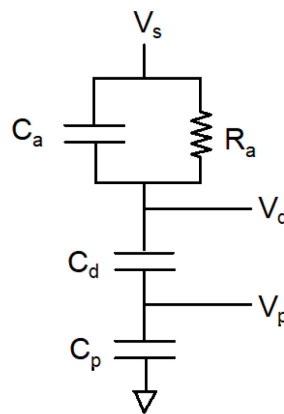


Figure 7-16: Simplified Circuit Representation of DBD Actuator.

7.4 ONE-DIMENSIONAL VOLUME DISCHARGE

7.4.1 Electrical Measurements

As noted in the Introduction, the 1D volume discharge may offer a simple alternative to the asymmetric DBD geometry in a search for DBD plasma-surface interaction effects. The goal of the current 1D work was to develop such experimental capability, along with related data analysis methods, in order to explore its diagnostic value for DBD materials study. Figure 7-17 illustrates the similarities between 1D and 2D cases. As in the 2D case, when the 1D geometry is operated at a sufficiently high voltage, ionization occurs in the air gap and the resulting plasma is commonly referred to as a volume discharge. For the surface discharge, the plasma initiates at the exposed electrode edge and sweeps across the dielectric surface above the buried electrode, varying the overall device capacitance due to both spatial and temporal plasma mechanisms [12]. The volume discharge has a much faster temporal variation associated with multiple, discrete microdischarges [36] but a much smaller spatial variation restricted to one dimension as the plasma expands and contracts within the small air gap.

The 1D case has a simple, exact solution to Poisson's equation describing the pre-breakdown electric field in the air gap that simplifies analysis (e.g., Ref. [35], and other basic textbooks under partially filled capacitor). The disadvantage of the 1D case is that, due to symmetry, there is no mean, induced momentum flux to use as a diagnostic indicator. In addition, the equilibrium plasma chemistry conditions in the confined space may differ from the asymmetric 2D case where a steady supply of fresh replenishment air is available. Furthermore, the confined space geometry is subject to various plasma instabilities leading to patterned discharge phenomena [36]. Nonetheless, the electron and ion energies for the 1D and 2D cases should be similar for same frequency and voltage. By comparing voltage and current relationships for the 1D case for different dielectric materials, it may be possible to detect plasma-surface interaction effects. Also, the 1D case can be readily modelled using commonly available analog circuit simulation software as will be discussed below.

For the 1D case in Figure 7-17(a), an algebraic expression for voltage on the exposed dielectric surface can be easily derived using Laplace's equation and a capacitive voltage divider. The capacitance of the partially filled capacitor is a commonly used example in many electrical engineering textbooks (e.g., Ref. [35], page 148) and the pre-breakdown voltage on the dielectric surface can be shown to be:

$$\frac{V_a}{V_s} = \frac{1}{1 + \frac{t_a}{t_{eff}}} \quad (7-9)$$

where t_{eff} is the effective thickness, $t_{eff} = t_d/\epsilon_r$, t_d is the dielectric thickness, ϵ_r is the relative permittivity of the dielectric material.

A schematic representation and photograph of the 1D test apparatus is shown in Figure 7-18. The large brass electrodes were re-purposed components from the dielectric breakdown tester (Section 7.2.1) and are not the optimal design for this application due to the extensive fringe electric fields at the edges. As shown below, however, the rapid radial decline in electric field outside of the electrodes effectively confines the plasma to the air gap. Lower profile electrodes with guard rings to minimize edge fringe effects may be an improvement but were not investigated. The levelling platen used to create a uniform height air gap is an essential requirement. In order to avoid plasma breakdown in small backside gaps due to thickness non-uniformities of the dielectric material, the top surface of the lower brass electrode was coated with silicone dielectric grease (Permatex Dielectric Tune Up Grease, p/n 22058) and pressed firmly into place to act as a temporary viscous adhesive and fill any gaps. A pin on

the bottom of the lower electrode maintains its coaxial relation to the upper electrode. A 1 mm pitch threaded adjusting nut was rotated around the stationary threaded rod to raise and lower the upper electrode in order to precisely set the air gap. Electrical power was applied through the quick-connect cables shown in Figure 7-18. An example of the device in operation is shown in Figure 7-19.

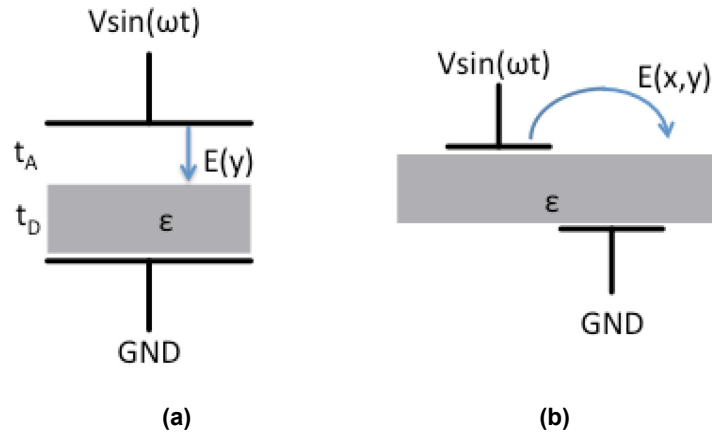


Figure 7-17: (a) One-Dimensional Volume Discharge vs. (b) Two-Dimensional Surface Discharge.

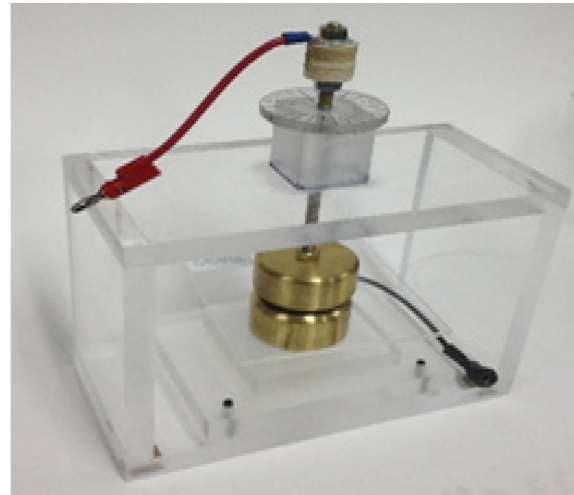
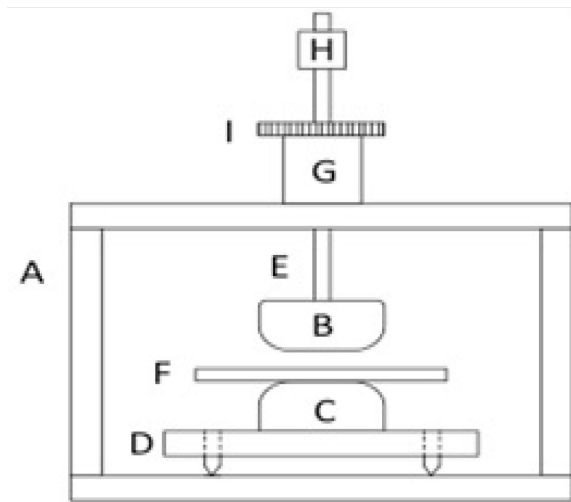


Figure 7-18: 1-D Volume Discharge Apparatus Schematic and Photograph. (a) Acrylic plastic frame; (b) and (c), brass electrodes; (d) set screw leveling platen; (e) brass threaded rod; (f) test specimen; (g) smooth bore alignment block; (h) rotation knob; (i) threaded nut and rotation position indicator. The brass electrodes are 50.8 mm in diameter.

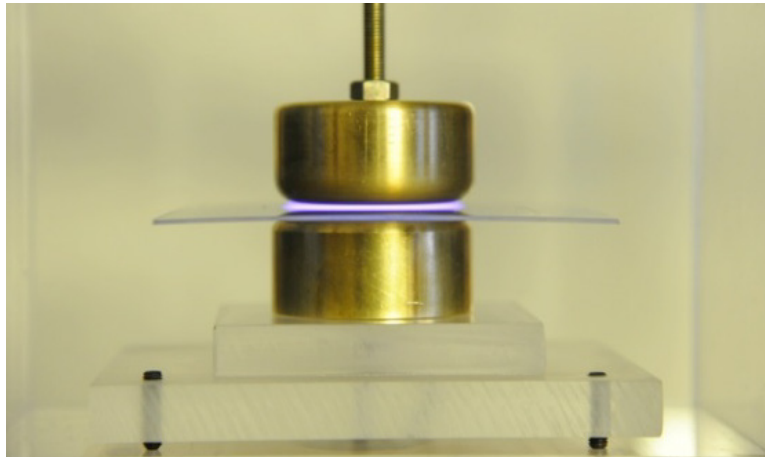


Figure 7-19: Example of a Volumetric DBD Discharge Viewed on Edge. The dielectric is 1 mm thick acrylic plastic and the air gap is 1 mm. $f = 1$ kHz, $V = 20$ kV_{pp}.

An effective way to characterize the 1D volume discharge is to use the charge transfer method, described in Ref. [37] and the basis of the circuit simulations to follow in this section. This method allows transfer of charge from a physically inaccessible location, in this case on the dielectric surface, to an accessible location, a series probe capacitor. The method is based on the principle that the total charge in a circuit of series-connected capacitors is constant and is given by the simple relation $Q = CV$ where C and V are the relevant capacitance and voltage respectively. A simplified DBD actuator circuit including the charge transfer probe capacitor is shown in Figure 7-16 as previously discussed. The parallel elements C_a and R_a represent the plasma and vary periodically with time as the plasma ignites and extinguishes twice per cycle. Charges on capacitors C_a and C_d are not easily accessible to measurement. By adding series capacitor, C_p , however, the charge is transferred to an accessible location and easily measured by recording voltage V_p across known probe capacitor C_p . In the current case, C_p is a large-valued (i.e., low impedance) capacitor relative to the actuator capacitances C_a and C_d . For the actuators used in this study, C_a and C_d are typically in the low tens of picofarads and the probe capacitor, C_p , was selected as 22 nanofarads or approximately 2000 times lower impedance than the actuator so as not to significantly load or alter the DBD circuit.

An example of the resulting charge transfer waveform for the volume discharge case is shown in Figure 7-20. The cyclogram is plotted from phased-averaged voltage waveforms over 128 oscilloscope sweeps. The charge value is linearly related to the probe voltage by $Q = C_p V_p$ where C_p has a fixed value of 22 nF. The capacitance of the actuator can easily be determined from the slope of cyclogram charge-voltage waveform for the plasma-on and plasma-off segments of the cycle, $C = dQ/dV_s = d(C_p V_p)/dV_s$. Slope values, S1 and S2, as shown in the figure, are provided in the caption. The area enclosed by the cyclogram is equal to the energy dissipated per AC activation cycle. The product of the energy per cycle and the excitation frequency is the dissipated power.

The 1D and 2D DBD discharges differ somewhat in charging characteristics. In both cases, charge transfer occurs by three methods:

- 1) Dielectric polarization, i.e., the usual capacitor charging mechanism irrespective of plasma formation;
- 2) Discrete microdischarges [36];
- 3) Charge deposition to and from the plasma to the dielectric surface and exposed electrode [12].

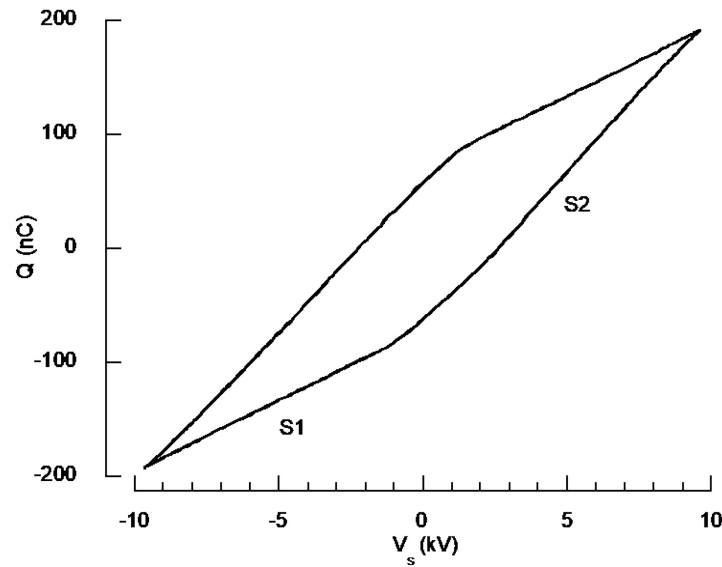


Figure 7-20: Example of 1D Charge Transfer Method Cyclogram (PTFE, $t_d = 1.07$ mm, $t_a = 1.00$ mm, $f = 1$ kHz, $C_p = 22$ nF, $S1 = 12.63$, $S2 = 27.63$ nC/kV or pF).

The role of the microdischarges is much more evident in the 1D case than in the 2D case. Figure 7-21 and Figure 7-22 show brief segments of the total current and charge history for a rising input voltage. In the 1D case, charge transfer due to discrete microdischarges is clearly evident as small steps in the accumulated charge and, furthermore, are seen to exactly coincide with the spikes in the total current measured with a current transformer on the high voltage side close to the actuator. This observation is consistent with prior investigations of the 1D volume discharge [36]. In the 2D actuator case, the influence of the discrete microdischarges is not as evident although some stepwise features in the charge curve seem to be related to spikes in the total current. The microdischarge phenomenon is relevant to plasma behavior in the presence of water vapor (humidity) as described by Falkenstein and Coogan [38]. They show by photographic observation of discrete microdischarges in a volume discharge that the dielectric capacitance increases with the addition of water. Since the surface discharge does not exhibit the same discrete microdischarge behavior, it is not clear that same mechanism applies. From Figure 7-12, an increase in dielectric capacitance equates to a reduction in effective thickness and one would expect the thrust to increase. As shown in Figure 7-10, however, change in thrust with water vapor depends upon the dielectric material's water absorption rate.

A series of 1D tests with different dielectric materials in a variety of thicknesses, air gap widths, input voltages and frequencies was conducted as an adjunct to the 2D actuator thrust measurements to see if any unexplained differences between materials existed that could be the basis for future DBD dielectric material studies.

Figure 7-23 shows a plot of the ratio of cyclogram plasma-off segment (S1) and plasma-on (S2) segment with respect to computed surface voltage ratio from Equation 7-9 for a range of materials. Since the cyclogram slopes are proportional to capacitance, taking the ratio of the plasma-off and plasma-on slopes effectively removes the influence of the pre-breakdown circuit impedance and displays only the increase in capacitance due to the plasma. As seen, such procedure correlates all of the materials and thicknesses into a single power law. From Equation 7-9, an increase in abscissa, V_d / V_s corresponds to an increase in the effective thickness, t_d / ϵ_r . Therefore, increased effective thickness leads to reduce plasma induced capacitance. This is the same mechanism responsible for the reduction in thrust in the 2D case with increasing effective thickness as shown in Figure 7-11. Based on these

results, it can be concluded, therefore, that changes in capacitance due to plasma formation in either the 1D or 2D cases occurs independently of the chemical composition of the different materials. When actuator impedance is properly accounted for, there is no evidence of any surface-plasma interaction such as secondary electron emission or catalytic effects that contribute to plasma induced capacitance. The chemical composition and structure of the material appear to have little or no impact on charge transfer characteristics when the overall circuit impedance is accounted for.

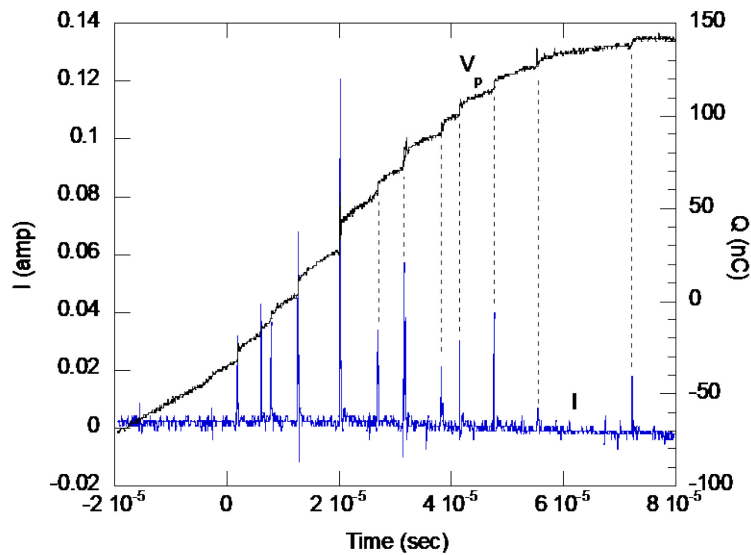


Figure 7-21: PTFE $t_d = 1.07$ mm, $t_a = 1.00$ mm, $f = 3$ kHz, $V_s = 16$ kV_{pp}.

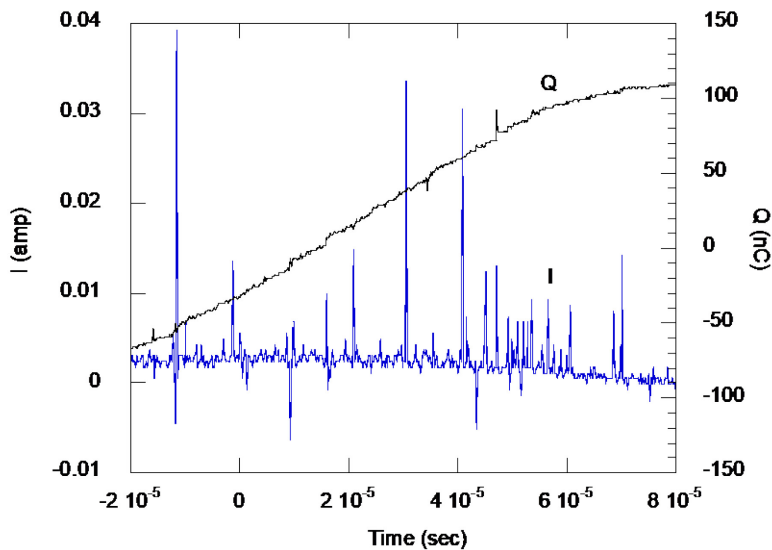


Figure 7-22: PTFE $t_d = 1.07$ mm, $f = 3$ kHz, $V_s = 16$ kV_{pp}.

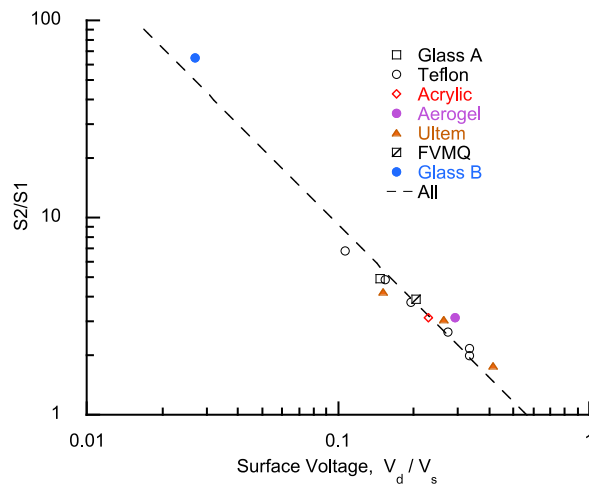


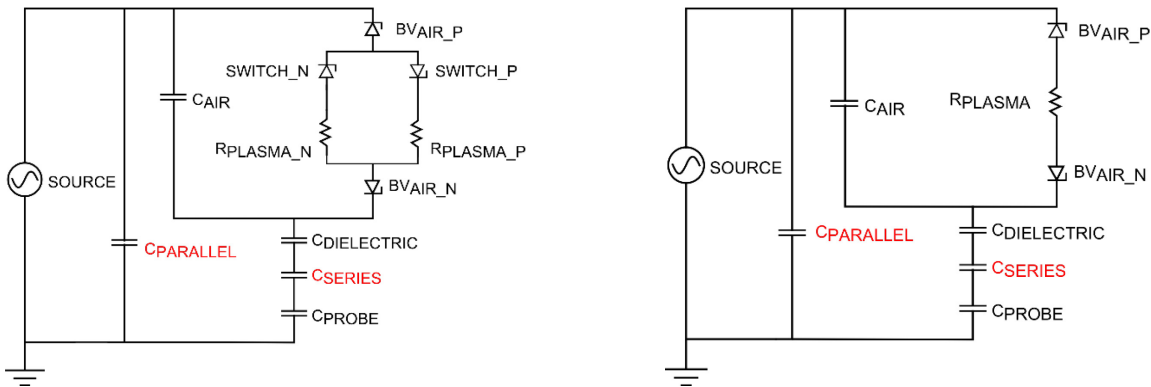
Figure 7-23: Cyclogram Slope Ratio vs. Computed Surface Voltage (Equation 7-9) for Different Permittivity Materials. $t_a = 1.00$ mm, $f = 1$ kHz, $V_s = 20$ kV_{pp}.

7.4.2 Circuit Simulations

To further analyze the 1D test data, circuit simulations were made to model the dielectric materials, test environment and plasma. Figure 7-24 shows the two circuits used to model the 1D experiments. These are based on the simple circuit in Figure 7-16 with additional elements added to account for the interaction of the test article with its surroundings as well as for the plasma formation. Dielectric breakdown of the air in the 1D gap was modelled with the 2 back-to-back zener diodes. The reverse breakdown voltages started at $3 \text{ kV} \times \text{gap}$ in mm. In the circuit in Figure 7-24(a) (4-diode model), two additional diodes SWITCH_P and SWITCH_N were used to model asymmetry of the discharge and plasma properties in the forward and reverse directions, the reverse breakdown voltage of these diodes was set to 100 kV, higher than the voltage range of the experiments. The plasma resistance is allowed to be different in the positive and negative going half cycles of the ac waveform. The circuit in Figure 7-24(b) (2-diode model) assumes the discharge is symmetrical and thus only a single plasma resistance is used and the values of the dielectric breakdown voltages ($B_{\text{VAIR_P}}$ and $B_{\text{VAIR_N}}$) are made the same. The voltage across the probe capacitance and total current in the simulations were compared to experiment. Optimization of the values of the circuit elements to match the calculated data to the experiments was made using CIRCOPT, a Python-based program developed for this work, that uses the simulation engines in the Quite universal circuit simulator (Qucs) [39] and LTSpice [40] as back ends. In the simulations, the measured (small signal) properties of the dielectric and air gap were used as starting inputs. The procedure for the optimization as implemented by CIRCOPT was as follows:

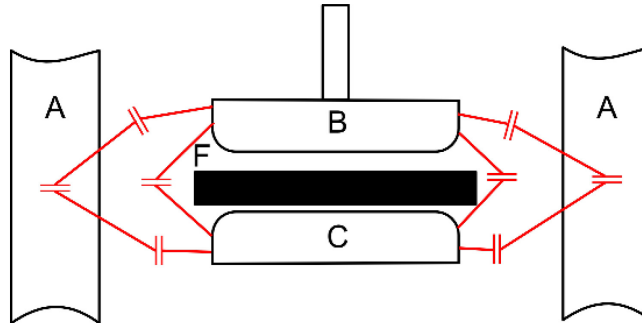
- 1) Obtain template netlist.
- 2) Substitute current parameter values into the template.
- 3) Pass it to the circuit simulator.
- 4) Wait on the result or kill the circuit simulator if there is no convergence in a set time.
- 5) Parse the data, if any, from the circuit simulator.
- 6) Calculate the merit function.
- 7) Set the next set of parameter values.

- 8) Repeat the above until the termination criterion has been reached. There were two termination criteria: no changes in the merit function or a fixed number of iterations being reached.
- 9) To compare fitting of the data by models with different numbers of parameters (the 2- and 4-diode models), the Akaike information criterion (AIC) [41] was used. The AIC deals with the trade-off between the goodness of fit of the model and the complexity of the model.
- 10) Standard deviations of the best-fit parameters were estimated using the Bootstrap method [42].
- 11) The parameter value optimization in CIRCOPT was made using the Scipy algorithms Nelder-Mead [43] and Powell [44].



(a) 4-Diode Model.

(b) 2-Diode Model.



(c) 1D Geometry with Stray Capacitances Indicated.

Figure 7-24: The Circuits Used to Simulate the 1D Experiments. The circuit elements were chosen to represent the dielectric material (F) as well as the test fixture (B, C) and its surroundings (A). These extraneous capacitances are captured as the circuit elements $C_{PARALLEL}$ and C_{SERIES} .

7.4.3 Circuit Simulation Results

Best-fit curves and AIC values showed that, in the 1D case, there is no significant asymmetry and both the 2- and 4-diode models appeared to fit the data equally well. Therefore, only results from the simpler 2-diode model will be discussed further.

Figure 7-25 shows experimental and calculated voltages and current at 1 kHz, Figure 7-25(a), Figure 7-25(c), Figure 7-25(e); and 5 kHz, Figure 7-25(b), Figure 7-25(d), Figure 7-25(f), for the polyimide aerogel. It can be seen

that the model fits both the current and the voltage quite well at both frequencies. Similar results were also observed at the other test frequencies. The contribution of the various circuit branches to the total current is shown in Figure 7-25(e) and Figure 7-25(f). A steady sine current, with amplitude similar to the current through the air, flows through the parallel capacitance. The current through the air capacitance rises and falls with the formation of the plasma. This is due to changes in the impedance of the plasma branch upon breakdown.

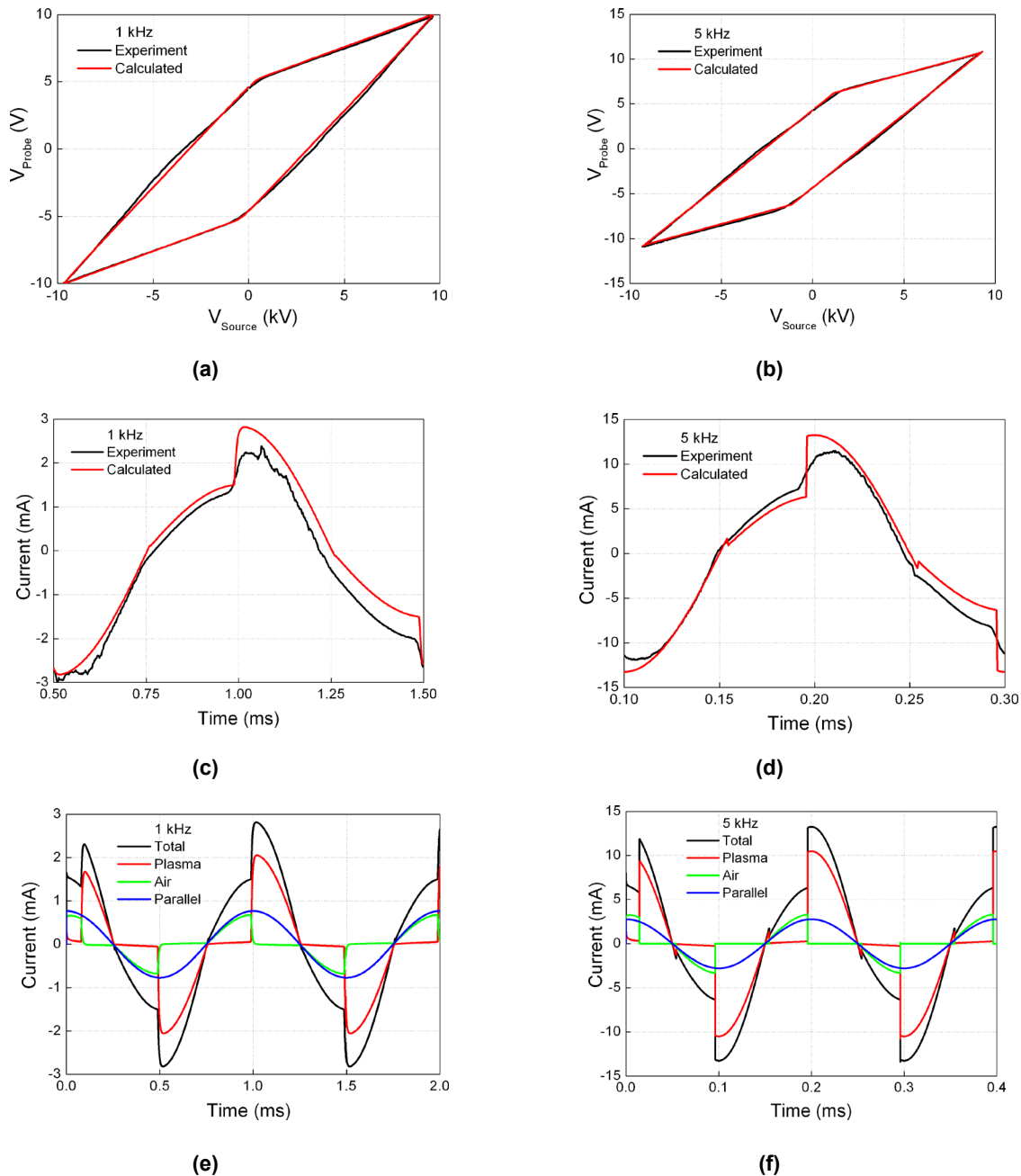


Figure 7-25: Typical Fitting Results Showing the Experimental Voltage and Current for the Polyimide Aerogel at 1 and 5 KHz and Values Calculated Using the 2-Diode Model Figure 7-24(b).

A full set of the best-fit parameters values from the circuit simulations and optimization is given in Table 7-3.

Table 7-3: The Best Fit Values Obtained from the Circuit Simulations.

Material (td mm)	Frequency (kHz)	BV (kV)	R _{PLASMA} (kΩ)	C _{DIELECTRIC} (pF) /ε _{DIELECTRIC}	C _{PARALLEL} (pF)	C _{SERIES} (pF)
Aerogel (0.43)	1	2.90	107	51.1/1.26	12.6	104
	2	2.84	36	48.5/1.20	13.2	109
	4	2.77	37	48.9/1.21	11.4	130
	5	2.64	0.03	48.6/1.20	9.5	138
PTFE (1.04)	1	2.26	1.77	34.7/2.08	13.4	86
	2	2.18	2.53	33.8/2.03	13.1	105
	4	2.18	0.02	33.2/1.99	11.8	175
	5	2.18	0.44	33.2/1.99	11.0	226
Acrylic (0.94)	1	2.84	0.51	59.4/3.22	13.1	122
	2	2.60	0.03	59.6/3.23	12.4	123
	4	2.38	21.4	51.8/2.80	13.5	166
	5	2.26	1.13	55.0/2.98	12.0	139
FVMQ (1.47)	1	3.13	6.90	68.7/5.83	8.9	173
	2	2.92	12.5	72.1/6.12	7.5	165
	4	2.61	16.1	68.5/5.81	3.3	195
	5	2.49	0.45	68.6/5.82	0.017	197
Glass (1.37)	1	3.27	37.8	108/8.57	3.3	185
	2	2.70	0.06	101/8.01	5.2E-6	218
	4	2.26	0.029	103/8.17	10.11	212
	5	2.18	0.006	104/8.20	2.8E-4	205

Note: Kept fixed in the analysis and optimization were the diameter of the air gap and dielectric (50.8 mm), the thickness of the air gap ($t_a = 1.0$ mm) and hence the capacitance of the air gap $C_{AIR} = 17.38$ pF ($\epsilon_{AIR} = 1$). The probe capacitance was allowed to vary slightly in the region around the 22 nF nominal value $21 \text{ nF} \leq C_{PROBE} \leq 23 \text{ nF}$. No significant deviation was observed, and the best fit values were within a few percent of the nominal value.

Figure 7-26 shows the best-fit reverse breakdown voltage of the zener diodes, Figure 7-26(a), and the plasma resistance, Figure 7-26(b). The breakdown voltages lie in a narrow range and all decrease slightly with increasing frequency as expected. The plasma resistances vary by several orders of magnitude. This is in spite of the very small standard deviations in the best-fit parameter values calculated using the Bootstrap method and which may be in part due to the symmetry of the waveforms. Values of R_{PLASMA} above 500 kΩ caused significant rounding of the voltage cyclograms that is inconsistent with the experimental observations thus placing an upper bound. Figure 7-27 shows the ratios of the capacitances $C_{PARALLEL}$ and C_{SERIES} to C_{AIR} and $C_{DIELECTRIC}$ respectively. $C_{PARALLEL}$ is about $0.6 \times C_{AIR}$ while C_{SERIES} is mostly $\sim 2 \times C_{DIELECTRIC}$. Note that there

were no values of C_{AIR} and $C_{DIELECTRIC}$ that could be used to absorb $C_{PARALLEL}$ or C_{SERIES} thus simplifying the circuit while remaining consistent with the known properties of the materials. The capacitance C_{SERIES} may be a combination of the contributions of the test setup as well as nonlinearity of the permittivity of the dielectric at the 1D test voltages which are much greater than the 1V where the material dielectric constants were measured.

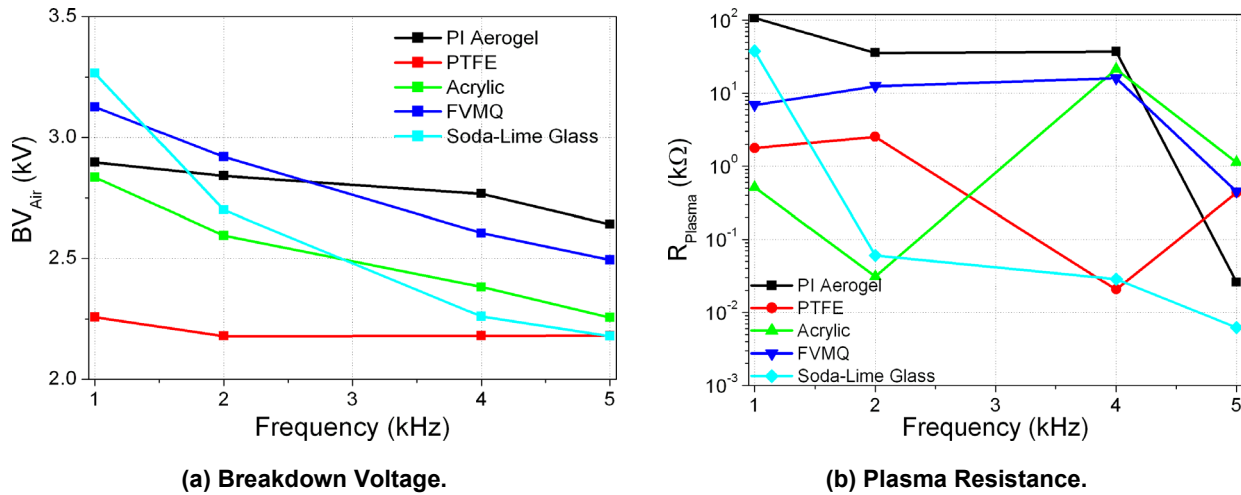


Figure 7-26: The Best-Fit Diode Breakdown Voltages and Plasma Resistances Obtained from the Circuit in Figure 7-24(b). Estimates of the standard deviations of the parameters computed using the Bootstrap method were very small.

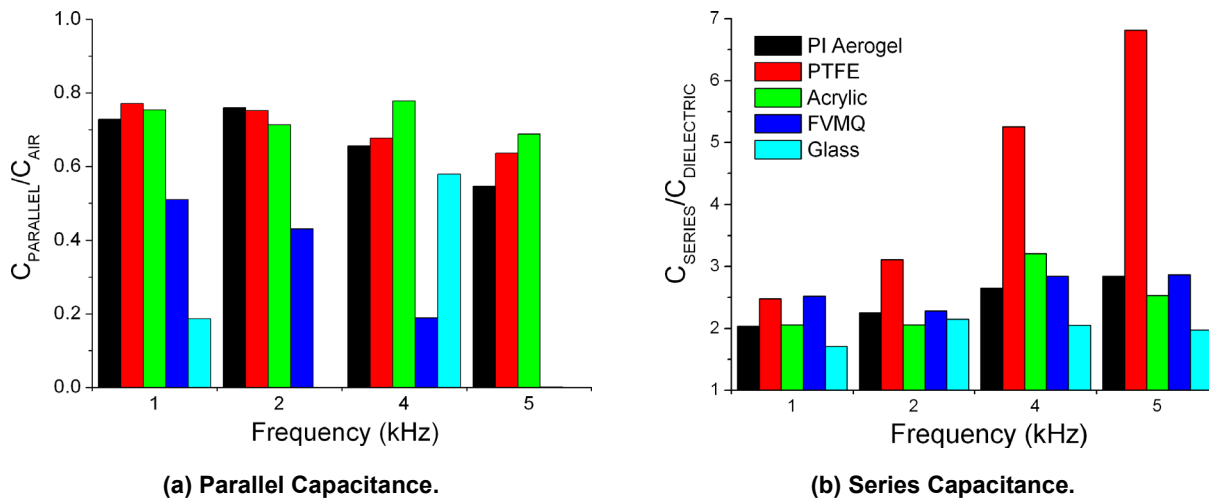


Figure 7-27: Trends in the Capacitances $C_{PARALLEL}$ and C_{SERIES} .

7.5 SUMMARY AND CONCLUSIONS

A cross-disiplinary study of DBD actuator dielectric materials was conducted in search of material optimization opportunities to improve DBD actuator performance. The rationale was to study a variety of existing dielectric

materials, along with new polyimide aerogels, seeking to explain differences in performance based on both volume and surface properties. The primary diagnostic methods employed were static thrust stand measurements of asymmetric, surface-discharge actuators and charge transfer studies on one-dimensional volume-discharge actuators. Low voltage dielectric property measurements (permittivity and loss tangent) were conducted in accordance with ASTM standards. Open-source circuit simulation software was configured to find optimal, lumped-parameter values for simplified circuit representations of the 1D volume discharge showing good correspondence to experiment data provided that stray capacitance is accounted for.

The induced thrust for a range of relative dielectric permittivities and thicknesses covering nearly an order of magnitude was found to scale semi-logarithmically with the effective dielectric thickness (ratio of thickness to dielectric constant) at constant input voltage. The semi-logarithmic behavior was shown to be predicted by an approximate, method-of-images analysis of the pre-breakdown capacitance from which it was concluded that thrust depends primarily on DBD circuit impedance, all other factors held constant. For the range of input voltages tested ($< 20 \text{ kV}_{pp}$), this finding effectively rules out any significant role of plasma-surface interactions, such as secondary electron emission from the dielectric or surface catalytic effects, in DBD thrust production. Based in this finding, it is concluded that chemical composition and structure of the material has no significant effect on DBD performance, at least for the range of input energies tested.

In the course of the studies, it became apparent that normal levels of atmospheric humidity can have a significant effect on DBD performance when accurate thrust measurements are required, as, for example, in the case of CFD code-validation studies. This became most apparent in our observation of a wide variation of DBD thrust readings when testing surface coatings such as photocatalytic titanium oxide and various surfactants and antioxidants. This necessitated the postponement of the surface coating portion of the study pending development of proper humidity control and testing protocol. Humidity tests on uncoated PTFE and Nylon were conducted showing large variations in both thrust levels and trends. This behavior is presumably due to the large difference in water absorption rate for the PTFE and Nylon and helps to identify requirements for future research in this area.

An extensive study of one-dimensional volume discharges was conducted, both experimentally and analytically, using the charge transfer cyclogram (Lissajous) method. The charge transfer method circumvents error-prone thrust measurements at the expense of a different model geometry (1D vs. 2D), lack of mean, directed momentum transfer, and possibly creating different microdischarge physics within the air gap (patterned discharges, discharge instabilities). It provides, however, a simple, alternative method by which to study dielectric materials, surface coatings, and ambient gas properties under discharge energy levels very close to the 2D surface-discharge case. The key finding of the current study was that the cyclogram plasma-on to plasma-off slope ratio (S_2/S_1), indicative of the increase in air gap charge due to the plasma, varies logarithmically with the effective dielectric thickness (t_d/ϵ_r) and independently of the chemical composition of the dielectric material. This finding shows that the charge increase depends only on the effective dielectric thickness, and not the dielectric material's chemical composition and that the slope variation is solely a pre-breakdown capacitive impedance effect.

The 1D cyclogram data was analyzed using analog, SPICE3-based [39], [40], open-source, circuit simulation software in order to find the effective plasma resistances and capacitances that best fit the experimental waveforms. In order to match the simulations to the experiment, it was necessary to include iteration on stray capacitance between the 1D electrodes, and between the individual electrodes and the laboratory surroundings. The search procedure resulted in good reproduction of experimental waveforms. This finding suggests that the fitting method can become the basis for development of a semi-empirical plasma actuator design method. The requirement for inclusion of stray capacitance has implications for the 2D surface-discharge thrust measurement case. It is likely

that different laboratory apparatuses will have different stray capacitances and, therefore, different thrust readings based on the overall circuit response to the excitation voltage. This represents a source of uncertainty when comparing 2D surface-discharge thrust data between different laboratories, even on identical models with important implications for acquisition of CFD code-validation data.

7.6 ACKNOWLEDGEMENTS

This work was funded under the NASA Aeronautics Research Mission Directorate (ARMD) 2011 Phase 1 and 2012 Phase 2 Seedling Fund awards. The authors would like to acknowledge Mr. Cameron Butler (University of Virginia) for his contributions to the dBt dielectric break down test software.

7.7 REFERENCES

- [1] Takashima, K., Zuzeeq, Y., Lempert, W.R., and Adamovich, I.V. Characterization of Surface Dielectric Barrier Discharge Plasma Sustained by Repetitive Nanosecond Pulses. AIAA Paper 2010-4764.
- [2] Likhanskii, A.V., Shneider, M.N., Macheret, S.O., and Miles R.B. Modelling of Dielectric Barrier Discharge Plasma Actuators Driven by Repetitive Nanosecond Pulses. 2007 Physics of Plasmas 14, 073501.
- [3] Opaits, D.F. Dielectric Barrier Discharge Plasma Actuator for Flow Control, Final Report, NASA CR 2012-217655, September 2012.
- [4] Moreau, E. Airflow Control by Non-Thermal Plasma Actuators, J. Phys D: Appl. Phys., V. 40, N. 3, 2007, pp. 605-636.
- [5] Corke, T.C., Enloe, C.L., and Wilkinson, S.P. Dielectric Barrier Discharge Plasma Actuators for Flow Control, Ann. Rev. Fluid Mech. V. 42, 2010, pp: 505-529.
- [6] Roth, J.R., Sherman, D.M., and Wilkinson, S.P. Boundary Layer Flow Control with A One Atmosphere Uniform Glow Discharge Surface Plasma, AIAA Paper 1998-0328.
- [7] Zito, J.C., Durscher, R.J., Soni, J., Roy, S., and Arnold, P.A. Flow and Force Inducement Using Micron Size Dielectric Barrier Discharge Actuators, Appl. Phys. Lett. 100, 193502, 2012.
- [8] Macheret, S.O., Shneider, M.N., and Miles, R.B. Magnetohydrodynamic and Electrohydrodynamic Control of Hypersonic Flows of Weakly Ionized Plasmas, AIAA J., Vol. 42, No. 7, July 2004, pp. 1378-1387.
- [9] Roth, J.R. Industrial Plasma Engineering, Volume 1 – Principles, Institute of Physics Publishing, Bristol and Philadelphia, ISBN 0-7503-0318-2, 1995, p. 149.
- [10] Hayt, W.H. Jr. Engineering Electromagnetics, 5th Ed., McGraw-Hill, Inc., ISBN 0-07-027406-1, 1989, pp. 147-150.
- [11] Enloe, C.L., McLaughlin, T.E., Gregory, J.W., Medina, R.A., and Miller, W.S. Surface Potential and Electric Field Structure in the Aerodynamic Plasma Actuator, AIAA Paper 2008-1103, Jan. 2008.

- [12] Enloe, C.L., Font, G.I., McLaughlin, T.E., and Orlov, D.M. Surface Potential and Longitudinal Electric Field Measurements in the Aerodynamic Plasma Actuator, *AIAA J.*, Vol. 46, No. 11, November 2008, pp. 2730-2740.
- [13] Massines, F., Ben Gadri, R., Rabehi, A., Decomps, Ph., Segur, P., and Mayoux, Ch. Mechanisms of a Glow Discharge at Atmospheric Pressure Controlled by Dielectric Barrier, *Journal of Applied Physics*, Vol. 83, No. 6, March 1998, pp. 2950-2957.
- [14] *Handbook of Chemistry and Physics*, Lide, D.R. ed., 73rd Edition, Special Student Edition, 1992-1993, CRC Press, ISBN 0-8493-0566-7, page 12-110.
- [15] Starikovskiy, A., and Miles, R. Dielectric Barrier Discharge Control and Flow Acceleration Enhancement by Diode Surface, *AIAA Paper 2013-0754*, 2013.
- [16] Fine, N., and Brickner, S. Plasma Catalysis for Enhanced-Thrust Single Dielectric Barrier Discharge Plasma Actuators, *AIAA Journal*, vol.48 no.12, 2010, pp. 2979-2982.
- [17] Anderson, R., and Roy, S. Preliminary Experiments of Barrier Discharge Plasma Actuators Using Dry and Humid Air, *AIAA Paper 2006-369*, 2006.
- [18] Benard, N., Balcon, N., and Moreau, E. Electric Wind Produced by a Surface Dielectric Barrier Discharge Operating Over a Wide Range of Relative Humidity, *AIAA 2009-488*, 2009.
- [19] Bartnikas, R. Partial Discharges Their Mechanism Detection and Measurement, *IEEE Trans. on Dielectrics and Electrical Insulation*, v. 9, n. 5, Oct. 2002, pp. 763-808.
- [20] Guo, H., Meador, M.A.B., McCorkle, L., Quade, D.J., Guo, J., Hamilton, B., and Cakmak, M. Tailoring Properties of Cross-Linked Polyimide Aerogels for Better Moisture Resistance, Flexibility and Strength, *ACS Applied Materials and Interfaces*, 2014, 5422-5429.
- [21] Meador, M.A.B., McMillon, E., Sandberg, A., Barrios, E., Wilmoth, N.G., Mueller, C.H., and Miranda, F.A. Dielectric and Other Properties of Polyimide Aerogels Containing Fluorinated Blocks, *ACS Applied Materials and Interfaces*, January 31, 2014, DOI:10.1021/am405106h.
- [22] Durscher, R., and Roy, S. Aerogel and Ferroelectric Dielectric Materials for Plasma Actuators, *J. Phys. D: Appl. Phys.* 45 (2012) 012001.
- [23] Baytekin, H. T., Baytekin, B., Hermans, T.M., Kowalczyk, B., and Grzybowski, B.A. Control of Surface Charges by Radicals as a Principle of Antistatic Polymers Protecting Electronic Circuitry, *Science*, Vol. 341, 20 September 2013, pp. 1368-1371.
- [24] ASTM D149, Standard Test Method for Dielectric Breakdown Voltage and Dielectric Strength of Solid Electrical Insulating Materials at Commercial Power Frequencies, 2013.
- [25] ASTM D638-10, Standard Test Method for Tensile Properties of Plastics, 2010.
- [26] ASTM D1708-13, Standard Test Method for Tensile Properties of Plastics by Use of Microtensile Specimens, 2013.

- [27] Dyre, J.C., and Schröder, T.B. (2000), Universality of AC Conduction In Disordered Solids, Review of Modern Physics, 72(3), 873-892.
- [28] Hrubesh, L.W., and Pekala, R.W. Dielectric Properties and Electronic Applications of Aerogels, Lawrence Livermore National Laboratory Report UCRL-JC-113378, CONF-9308158-2, presented at International Symposium on Advances in Sol-Gel Processing and Applications, Chicago, Illinois, August 24-28, 1993.
- [29] Ashpis, D.E., and Laun, M.C. Dielectric Barrier Discharge (DBD) Plasma Actuators Thrust – Measurement Methodology Incorporating New Anti-Thrust Hypothesis, AIAA Paper 2014-0486, 2014.
- [30] Kwok, P.L.C., Trietsch, S.J., Kumon, M., and Hak-Kim Chan, H.-K. Electrostatic Charge Characteristics of Jet Nebulized Aerosols, J. Aerosol Medicine and Pulmonary Drug Delivery Volume 23, Number 3, 2010.
- [31] ASTM D-570 -98, Standard Test Method for Water Absorption of Plastics, 2010.
- [32] Attwood, S.S. Electric and Magnetic Fields, 3rd Edition, John Wiley & Sons, Inc, New York, 1949, pp 141-144 (out-of-print). See also Dover Publication edition, 1967, ISBN 048661753X or 978-0486617534 (out-of-print).
- [33] Wheeler, H.A. Transmission-Line Properties of a Strip on a Dielectric Sheet on a Plane, IEEE Trans. on Microwave Theory and Technique, Vol. MMT-25, No. 8, August 1977, pp. 631-647.
- [34] Enloe, C.L., McLaughlin, T.E., VanDyken, K.D., Kachner, K.D., Jumper, E.J., and Corke, T.C. Mechanisms and Responses of a Single Dielectric Barrier Discharge, AIAA Paper 2003-1021.
- [35] Hayt, W.H. Jr. Engineering Electromagnetics, 5th Ed., McGraw-Hill, Inc., ISBN 0-07-027406-1, 1989, pp. 147-150.
- [36] Kogelschatz, U. Filamentary, Patterned, and Diffuse Barrier Discharges, IEEE Transactions on Plasma Science, vol. 30, no. 4, August 2002, pp. 1400-1408.
- [37] Kriegseis, J., Möller, B., Grundmann, S., and Tropea, C. Capacitance and Power Consumption Quantification of Dielectric Barrier Discharge (DBD) Plasma Actuators, Journal of Electrostatics 69 (2011), pp. 302-312.
- [38] Falkenstein, Z., and Coogan, J.J. Microdischarge Behaviour in the Silent Discharge of Nitrogen-Oxygen and Water-Air Mixtures, J. Phys. D: Appl. Phys. 30 (1997), pp. 817-825.
- [39] QucsTeam. (n.d.). Qucs (Quite Universal Circuit Simulator). Retrieved from <http://qucs.sourceforge.net/>.
- [40] Linear Technology. (n.d.). Linear Technology/Software. Retrieved from http://www.linear.com/design_tools/software/.
- [41] Akaike, H. A New Look at the Statistical Model Identification, IEEE Transactions on Automatic Control, 19(6), 1974, pp. 716-723.

- [42] Press, W.H., Teukolsky, S.A., Vetterling, W.T., and Flannery B.P. Numerical Recipes in C++, 2nd edition, Cambridge University Press, 2003.
- [43] Nelder, J.A. A Simplex Method for Function Minimization, Computer Journal, 7, 1965, pp.308-313.
- [44] Powell, M.J. On Search Directions for Minimization Algorithms, Mathematical Programming, 4, 1973, pp. 193-201.



Annex A – A SUMMARY OF PAPERS ON THE TOPIC OF SPECIAL SESSION: NATO-RTO-AVT-190: STANDARDIZATION OF DBD ACTUATORS, DELIVERED AT THE 2014 AVIATION CONFERENCE (AIAA)

A special AIAA session devoted to NATO-AVT-190 DVD Actuators was held during the 2014 Aviation Conference held in Atlanta, Georgia. Six papers were presented at that time and summaries are included here in numerical order for completeness and for the reader's convenience. Copies of the papers may be obtained from the AIAA.

AIAA 2014-2668

In the paper, **Development of a Multilevel Plasma Generator for Dielectric Barrier Discharge Actuators, AIAA2014-2668, Carlo A. Borghi et al., University of Bologna, Italy**, describe the development and the testing of a high voltage – high frequency (HVHF) plasma generator to supply Dielectric Barrier Discharge (DBD) actuators for control of aerodynamic flows. The generator provides a wide set of arbitrary voltage waveforms with peak-to-peak electrical tension up to 30 kV at frequencies up to 20 kHz. Operating frequencies are independent of the load characteristics and are not subject to requirements on impedance matching.

In still air, the flow induced in the region above the surface of a DBD actuator has been investigated and the Electro-Hydro-Dynamic (EHD) efficiency determined. A sinusoidal voltage waveform, simulated by the HVHF generator, and a sinusoidal voltage waveform by a conventional generator obtained comparable EHD effects and efficiencies. Of the wave forms investigated, the sinusoidal and the inverse saw-tooth voltage waveforms had the best efficiencies with regard to the EHD interaction.

AIAA 2014-2807

In the next paper, **Characterization of the Time-Dependent Behaviour of Dielectric Barrier Discharge Plasma Actuators, AIAA 2014-2807, Rogerio Pimentel, DRDC Valcartier, Canada**, a phase-locked PIV is used to investigate the time-dependent behaviour of a Di-electric Barrier Discharge (DBD) plasma actuator. Excited by a sine-wave signal with peak- to-peak amplitudes between 7.2 kV and 10 kV, at frequencies of 2.5 kHz and 4 kHz. The results indicate that the maximum induced velocity and body force occur during the negative half-cycle of the excitation signal, with a phase lag relative to the excitation signal that grows when excitation voltage or frequency is increased. A smaller, secondary peak is observed in the induced body force, occurring during the positive half-cycle of the excitation signal. The results suggest that this peak is due to formation of a secondary high-velocity region due to local discharges near the grounded electrode. Analysis of the induced body force, estimated using momentum balance in a control volume surrounding the actuator, indicates the significant role of the shear force acting on the actuator surface for the present configuration. The variability in the results of different methods for determining the shear force, the difference observed in certain conditions between the estimated body forces and those measured directly using a balance, highlight the need for further methodology improvements for body force prediction based on PIV measurements.

AIAA 2014-2808

In the third paper, **Numerical Simulation of sinusoidal driven DBD actuators and Comparisons with Experiments, AIAA 2014-2808, F. Rogier et al., ONERA, France**, present their numerical investigation of the body force induced by DBD actuator on the standardized configuration proposed by the AVT-190 group. Their simulated total body force results are in good agreement with measured forces for a large range of operating voltages and for some values of the working frequency. The body force variations in time and in space obtained by numerical simulation shows a good correlation with the observations noticed in other experimental works. However, some differences such as the presence of a negative force for a 14 kHz SDBD actuator, are noted that lead to some discrepancy on the induced velocity results. Further experimental and modeling studies are recommended to improve the accuracy-range of the results and thereby increase confidence in the simulation as a prediction tool.

AIAA 2014-2809

In the paper **Electromagnetic and Ozone Emissions from Dielectric Barrier Discharge Plasma Actuators (RTO), Nicole M. Houser et al., University of Toronto, Canada**, evaluate the electromagnetic and the ozone emissions generated by typical plasma actuator operation for flow control and the effects on human health. A significant implementation challenge is the high voltage signal required for their operation and the effects of high voltage exposure on humans. A second risk is posed by the ozone produced during plasma discharge. To assess these effects, the electric and magnetic fields were characterized and the locations surrounding an active plasma actuator at which the maximum safety exposure were met or exceeded known limits. The rate of ozone production was determined in an enclosed area and compared to safety standards for human exposure to ozone. Operating voltages and frequencies were used within the range of values commonly reported in plasma actuator research. The dielectric barrier discharge (DBD) plasma actuator was made of conventional materials (copper electrodes on acrylic dielectric). It was shown that electromagnetic field strength increases with operating voltage and proximity to the active device. Field strengths were independent of operating frequency. Ozone production, however, increased with both applied voltage and frequency. The results reinforce the importance of developing safe operating procedures for plasma actuator research.

AIAA 2014-2810

In the contribution **Evaluation of Dielectric-Barrier-Discharge Actuator Substrate Materials, Stephen P. Wilkinson et al., NASA LRC, United States**, material characteristics for actuators are discussed. An enabling element of a dielectric barrier discharge (DBD) actuator is the dielectric substrate material. While many investigators have studied the performance of different homogeneous materials, often in the context of related DBD experiments, fundamental studies focused solely on the dielectric materials are few. In an attempt to fill this shortcoming, the authors performed a cross-disciplinary study of DBD actuator dielectric materials with the objective of improving DBD actuator performance. A variety of existing dielectric materials and new polyimide aerogel were tested. Differences in actuator performance attributed to each dielectric material were assessed on volume and surface properties that included static induced thrust, electrical circuit parameters for 2D surface discharges and 1D volume discharges. Lumped-parameter circuit simulations for the 1D case corresponded well to experimental data provided that stray capacitances are included. After extensive testing, it was determined that the chemical composition and the structure of the material had no significant effect on DBD body force generation when actuator impedance is properly accounted for over the range of input energies tested. The secondary test outcome of the study was the observation that normal levels of atmospheric humidity has a strong influence on DBD thrust measurements. This represents a source of uncertainty when comparing 2D

surface-discharge thrust data between different laboratories, even on identical models, and has important implications for acquisition of CFD code-validation data.

AIAA 2014-2811

In the paper **Understanding SDBD Actuators: An Experimental Study on Plasma Characteristics**, **R. Geuns, Pénélope Leyland et al.**, *Ecole Polytechnique Federale de Lausanne, Switzerland*, the authors investigated the working mechanisms of surface dielectric barrier discharge (SDBD) plasma actuator, as aerodynamic control devices, on the NATO-AVT-RTO-190 common test platform. It is through this testing done at multiple locations that a better understanding of the working principle and characteristics of SDBD may lead the way for more efficient and safer use of these devices in aerodynamic applications. In this study, the experimental plasma characterization is done by current measurements, fast-camera plasma imaging and force measurements. Advanced plasma characterization, such as reduced electric field and excited species population, are found by Optical Emission Spectroscopy. Study results indicate that the force generated by the actuator increases as the driven frequency or voltage increases. An optimal condition for operating the SDBD plasma actuator was found eliminating the need for higher voltage levels. Detailed fast-camera imaging and spectroscopy facilitates understanding of the plasmas' transitions and their temporal evolution with respect to different operating conditions of voltage, frequency and ambient pressure. Optical emission spectroscopy detected the excited species in the plasma allowing reduced electric field calculations. These results are in agreement with trends noticed during current measurements and plasma imaging. The collective goal of the AVT190 task group research is to contribute to a database which can also be used for numerical variation and validation by varying the key parameters such as frequency and voltage.

AIAA 2014-2812

The last paper of this session was **Flow Control at Subsonic Speeds using Serpentine Plasma Actuators**, **K. Kontis et al.**, *University of Glasgow, United Kingdom*. The authors examine the use of a three-dimensional serpentine plasma actuator design to improve the relatively low flow speeds induced by surface dielectric barrier discharges. It is used as an active flow control device to manipulate the flow over a backwards facing step. A serpentine actuator is characterized by two geometric features, namely the pinch, and the spread. PIV was used to examine the influence of the actuator on the separated shear layer. At the pinch location, the induced jet from opposing sides collide and a strong upwards jet is created. At the spread location, because there is no cancelling effect of the induced jet from opposite sides of the actuator, a greater stream wise influence is achieved due to the three-dimensional flow and shear layer induced by the actuator. Further studies are underway to understand in greater detail the influence of such three-dimensional actuators on the flow properties, such as the flow reattachment downstream of the step as well as the vortical structures inside the recirculation bubble.



REPORT DOCUMENTATION PAGE			
1. Recipient's Reference	2. Originator's References	3. Further Reference	4. Security Classification of Document
	STO-TR-AVT-190 AC/323(AVT-190)TP/866	ISBN 978-92-837-2190-1	PUBLIC RELEASE
5. Originator	Science and Technology Organization North Atlantic Treaty Organization BP 25, F-92201 Neuilly-sur-Seine Cedex, France		
6. Title	Plasma Based Flow Control for Performance and Control of Military Vehicles		
7. Presented at/Sponsored by	Final report of NATO STO Task Group AVT-190.		
8. Author(s)/Editor(s)	Multiple		9. Date August 2021
10. Author's/Editor's Address	Multiple		11. Pages 142
12. Distribution Statement	There are no restrictions on the distribution of this document. Information about the availability of this and other STO unclassified publications is given on the back cover.		
13. Keywords/Descriptors	Aerodynamics; Computational fluid dynamics; Dielectric barrier discharge; Electromagnetics; Electron energy distribution function; Electrostatics; Energy; Filtered Rayleigh scattering; Flow control; Laser; Microwave; Particle image velocimetry; Plasma; Shock wave; Spectroscopy		
14. Abstract	<p>AVT-190 focused on understanding the capability for plasma flow control using dielectric barrier discharge, laser and microwave discharge. A series of benchmark experiments were established combining previously published data and new experiments conducted during the course of the AVT-190 activity. The experimental diagnostics provide detailed analysis of the dynamic effects of plasma actuation on the flowfield structure. Experimental configurations varied from plasma generation in quiescent air using dielectric barrier discharge to the interaction of a laser or microwave discharge with hemisphere-cylinder at supersonic speeds. Computational fluid dynamic simulations were performed for each experiment to assess the accuracy of the modeling and to analyze the details of the flowfield structure. Experiments were also performed to assess the effect of different dielectric materials on the effectiveness of dielectric barrier discharge devices.</p>		





BP 25

F-92201 NEUILLY-SUR-SEINE CEDEX • FRANCE
Télécopie 0(1)55.61.22.99 • E-mail mailbox@cs0.nato.int



**DIFFUSION DES PUBLICATIONS
STO NON CLASSIFIEES**

Les publications de l'AGARD, de la RTO et de la STO peuvent parfois être obtenues auprès des centres nationaux de distribution indiqués ci-dessous. Si vous souhaitez recevoir toutes les publications de la STO, ou simplement celles qui concernent certains Panels, vous pouvez demander d'être inclus soit à titre personnel, soit au nom de votre organisation, sur la liste d'envoi.

Les publications de la STO, de la RTO et de l'AGARD sont également en vente auprès des agences de vente indiquées ci-dessous.

Les demandes de documents STO, RTO ou AGARD doivent comporter la dénomination « STO », « RTO » ou « AGARD » selon le cas, suivi du numéro de série. Des informations analogues, telles que le titre et la date de publication sont souhaitables.

Si vous souhaitez recevoir une notification électronique de la disponibilité des rapports de la STO au fur et à mesure de leur publication, vous pouvez consulter notre site Web (<http://www.sto.nato.int/>) et vous abonner à ce service.

CENTRES DE DIFFUSION NATIONAUX

ALLEMAGNE

Streitkräfteamt / Abteilung III
Fachinformationszentrum der Bundeswehr (FIZBw)
Gorch-Fock-Straße 7, D-53229 Bonn

BELGIQUE

Royal High Institute for Defence – KHID/IRSD/RHID
Management of Scientific & Technological Research
for Defence, National STO Coordinator
Royal Military Academy – Campus Renaissance
Renaissancelaan 30, 1000 Bruxelles

BULGARIE

Ministry of Defence
Defence Institute “Prof. Tsvetan Lazarov”
“Tsvetan Lazarov” bul no.2
1592 Sofia

CANADA

DGSIST 2
Recherche et développement pour la défense Canada
60 Moodie Drive (7N-1-F20)
Ottawa, Ontario K1A 0K2

DANEMARK

Danish Acquisition and Logistics Organization
(DALO)
Lautrupbjerg 1-5
2750 Ballerup

ESPAGNE

Área de Cooperación Internacional en I+D
SDGPLATIN (DGAM)
C/ Arturo Soria 289
28033 Madrid

ESTONIE

Estonian National Defence College
Centre for Applied Research
Riia str 12
Tartu 51013

ETATS-UNIS

Defense Technical Information Center
8725 John J. Kingman Road
Fort Belvoir, VA 22060-6218

FRANCE

O.N.E.R.A. (ISP)
29, Avenue de la Division Leclerc
BP 72
92322 Châtillon Cedex

GRECE (Correspondant)

Defence Industry & Research General
Directorate, Research Directorate
Fakinos Base Camp, S.T.G. 1020
Holargos, Athens

HONGRIE

Hungarian Ministry of Defence
Development and Logistics Agency
P.O.B. 25
H-1885 Budapest

ITALIE

Ten Col Renato NARO
Capo servizio Gestione della Conoscenza
F. Baracca Military Airport “Comparto A”
Via di Centocelle, 301
00175, Rome

LUXEMBOURG

Voir Belgique

NORVEGE

Norwegian Defence Research
Establishment
Attn: Biblioteket
P.O. Box 25
NO-2007 Kjeller

PAYS-BAS

Royal Netherlands Military
Academy Library
P.O. Box 90.002
4800 PA Breda

POLOGNE

Centralna Biblioteka Wojskowa
ul. Ostrobramska 109
04-041 Warszawa

PORTUGAL

Estado Maior da Força Aérea
SDFA – Centro de Documentação
Alfragide
P-2720 Amadora

REPUBLIQUE TCHEQUE

Vojenský technický ústav s.p.
CZ Distribution Information Centre
Mladoboleslavská 944
PO Box 18
197 06 Praha 9

ROUMANIE

Romanian National Distribution
Centre
Armaments Department
9-11, Drumul Taberei Street
Sector 6
061353 Bucharest

ROYAUME-UNI

Dstl Records Centre
Rm G02, ISAT F, Building 5
Dstl Porton Down
Salisbury SP4 0JQ

SLOVAQUIE

Akadémia ozbrojených síl gen.
M.R. Štefánika, Distribučné a
informačné stredisko STO
Demänová 393
031 01 Liptovský Mikuláš 1

SLOVENIE

Ministry of Defence
Central Registry for EU & NATO
Vojkova 55
1000 Ljubljana

TURQUIE

Milli Savunma Bakanlığı (MSB)
ARGE ve Teknoloji Dairesi
Başkanlığı
06650 Bakanlıklar – Ankara

AGENCES DE VENTE

**The British Library Document
Supply Centre**
Boston Spa, Wetherby
West Yorkshire LS23 7BQ
ROYAUME-UNI

**Canada Institute for Scientific and
Technical Information (CISTI)**
National Research Council Acquisitions
Montreal Road, Building M-55
Ottawa, Ontario K1A 0S2
CANADA

Les demandes de documents STO, RTO ou AGARD doivent comporter la dénomination « STO », « RTO » ou « AGARD » selon le cas, suivie du numéro de série (par exemple AGARD-AG-315). Des informations analogues, telles que le titre et la date de publication sont souhaitables. Des références bibliographiques complètes ainsi que des résumés des publications STO, RTO et AGARD figurent dans le « NTIS Publications Database » (<http://www.ntis.gov/>).



BP 25
F-92201 NEUILLY-SUR-SEINE CEDEX • FRANCE
Télécopie 0(1)55.61.22.99 • E-mail mailbox@cs.o.nato.int



**DISTRIBUTION OF UNCLASSIFIED
STO PUBLICATIONS**

AGARD, RTO & STO publications are sometimes available from the National Distribution Centres listed below. If you wish to receive all STO reports, or just those relating to one or more specific STO Panels, they may be willing to include you (or your Organisation) in their distribution.

STO, RTO and AGARD reports may also be purchased from the Sales Agencies listed below.

Requests for STO, RTO or AGARD documents should include the word 'STO', 'RTO' or 'AGARD', as appropriate, followed by the serial number. Collateral information such as title and publication date is desirable.

If you wish to receive electronic notification of STO reports as they are published, please visit our website (<http://www.sto.nato.int/>) from where you can register for this service.

NATIONAL DISTRIBUTION CENTRES

BELGIUM

Royal High Institute for Defence –
KHID/IRSD/RHID
Management of Scientific & Technological
Research for Defence, National STO
Coordinator
Royal Military Academy – Campus
Renaissance
Renaissancelaan 30
1000 Brussels

BULGARIA

Ministry of Defence
Defence Institute “Prof. Tsvetan Lazarov”
“Tsvetan Lazarov” bul no.2
1592 Sofia

CANADA

DSTKIM 2
Defence Research and Development Canada
60 Moodie Drive (7N-1-F20)
Ottawa, Ontario K1A 0K2

CZECH REPUBLIC

Vojenský technický ústav s.p.
CZ Distribution Information Centre
Mladoboleslavská 944
PO Box 18
197 06 Praha 9

DENMARK

Danish Acquisition and Logistics Organization
(DALO)
Lautrupbjerg 1-5
2750 Ballerup

ESTONIA

Estonian National Defence College
Centre for Applied Research
Riia str 12
Tartu 51013

FRANCE

O.N.E.R.A. (ISP)
29, Avenue de la Division Leclerc – BP 72
92322 Châtillon Cedex

GERMANY

Streitkräfteamt / Abteilung III
Fachinformationszentrum der
Bundeswehr (FIZBW)
Gorch-Fock-Straße 7
D-53229 Bonn

GREECE (Point of Contact)

Defence Industry & Research General
Directorate, Research Directorate
Fakinos Base Camp, S.T.G. 1020
Holargos, Athens

HUNGARY

Hungarian Ministry of Defence
Development and Logistics Agency
P.O.B. 25
H-1885 Budapest

ITALY

Ten Col Renato NARO
Capo servizio Gestione della Conoscenza
F. Baracca Military Airport “Comparto A”
Via di Centocelle, 301
00175, Rome

LUXEMBOURG

See Belgium

NETHERLANDS

Royal Netherlands Military
Academy Library
P.O. Box 90.002
4800 PA Breda

NORWAY

Norwegian Defence Research
Establishment, Attn: Biblioteket
P.O. Box 25
NO-2007 Kjeller

POLAND

Centralna Biblioteka Wojskowa
ul. Ostrobramska 109
04-041 Warszawa

PORTUGAL

Estado Maior da Força Aérea
S DFA – Centro de Documentação
Alfragide
P-2720 Amadora

ROMANIA

Romanian National Distribution Centre
Armaments Department
9-11, Drumul Taberei Street
Sector 6
061353 Bucharest

SLOVAKIA

Akadémia ozbrojených síl gen
M.R. Štefánika, Distribučné a
informačné stredisko STO
Demänová 393
031 01 Liptovský Mikuláš 1

SLOVENIA

Ministry of Defence
Central Registry for EU & NATO
Vojkova 55
1000 Ljubljana

SPAIN

Área de Cooperación Internacional en I+D
SDGPLATIN (DGAM)
C/ Arturo Soria 289
28033 Madrid

TURKEY

Milli Savunma Bakanlığı (MSB)
ARGE ve Teknoloji Dairesi Başkanlığı
06650 Bakanlıklar – Ankara

UNITED KINGDOM

Dstl Records Centre
Rm G02, ISAT F, Building 5
Dstl Porton Down, Salisbury SP4 0JQ

UNITED STATES

Defense Technical Information Center
8725 John J. Kingman Road
Fort Belvoir, VA 22060-6218

SALES AGENCIES

The British Library Document Supply Centre

Boston Spa, Wetherby
West Yorkshire LS23 7BQ
UNITED KINGDOM

Canada Institute for Scientific and Technical Information (CISTI)

National Research Council Acquisitions
Montreal Road, Building M-55
Ottawa, Ontario K1A 0S2
CANADA

Requests for STO, RTO or AGARD documents should include the word 'STO', 'RTO' or 'AGARD', as appropriate, followed by the serial number (for example AGARD-AG-315). Collateral information such as title and publication date is desirable. Full bibliographical references and abstracts of STO, RTO and AGARD publications are given in “NTIS Publications Database” (<http://www.ntis.gov>).